Tree-Based Radiative Transfer of Diffuse Sources: A Novel Scheme and its Application in Massive Star Formation

INAUGURAL-DISSERTATION

zur

Erlangung des Doktorgrades
der Mathematisch-Naturwissenschaftlichen Fakultät
der Universität zu Köln

vorgelegt von

Andre Klepitko
aus Leverkusen, Deutschland

Köln, 2022

Berichterstatter (Gutachter):
Prof. Dr. Stefanie Walch-Gassner
Prof. Dr. Cristiano Porciani

Für meine Eltern.

ZUSAMMENFASSUNG

Elektromagnetische Strahlung spielt eine essenzielle Rolle in der Entwicklung astrophysikalischer Prozesse. Das Lösen der Strahlungstransportgleichung in numerischen Simulationen der Strahlungshydrodynamik ist aufwendig. Diese Arbeit beschreibt eine neue Methode namens TreeRay/RadPressure zur Lösung der Strahlungstransportgleichung für diffuse Quellen wie etwa interstellarer Staub. Die Methode basiert auf einem Ansatz, dem eine sogenannte Baumdatenstruktur in Kombination mit Strahlverfolgung zu Grunde liegen. Auf diese Weise wird es jeder numerischen Einheit ermöglicht zur Strahlung beizutragen oder diese abzuschwächen. Die Methode wurde in einem Finite-Volumen-Verfahren implementiert, lässt sich generalisieren und damit auch auf zum Beispiel die Smoothed-Particle-Hydrodynamics-Methode anwenden.

TreeRay/RadPressure eignet sich zur Berechnung von Strahlungsdruck auf Staub und Gas. Zusammen mit einem chemischen Netzwerk lassen sich mit der neuen Methode Heiz- und Kühlprozesse durch Staub modellieren. Eine Anwendung des neuen Algorithmus zeigt, dass sich durch Eigengravitation verursachte Fragmentation in Verbindung mit genaueren Heiz- und Kühlprozessen reduziert. Insbesondere durch Selbstabschirmung kann Staub nur an der Oberfläche optisch dicker Regionen kühlen.

Unter der Verwendung von TreeRay/RadPressure wurde der Kollaps stark gebundener Klumpen mit verschiedener Metallizität berechnet. Die Klumpen haben eine Masse von 150 Sonnenmassen, einen Radius von 0.1 Parsec und bilden einen massiven Stern. Zusammen mit TreeRay/OnTheSpot lies sich so die relative Stärke von Strahlungsdruck und ionisierender Strahlung untersuchen. Das Ergebnis zeigt, dass Strahlungsdruck stärker ist als ionisierende Strahlung, während der massereiche Stern von einer ultrakompakten HII region umgeben ist. Strahlungsdruck stoppt nicht die Akkretion von Masse auf den Stern und seine Stärke verringert sich sobald sich eine Akkretionsscheibe bildet. Größere Metallizität fördert Fragmentation durch stärkere Kühlung. Dadurch erhöht sich die Multiplizität im Falle höherer Metallizität. Strahlungsdruck bewirkt den Ausstoß von Gas und Staub entlang der Rotationsachse der Scheibe.

Der durch TreeRay/RadPressure berechnete Strahlungsdruck wurde mit dem einer unabhängigen Methode verglichen. Die Methode basiert auf der RADMC-3D Software und modelliert Strahlungstransport basierend auf der Monte-Carlo-Methode. Hierbei liegen Dichtekonfigurationen aus Simulationen zugrunde, anhand derer sich ein überwiegend übereinstimmendes Ergebnis gezeigt hat. Vereinfachte theoretische Modelle, die nur die optische Tiefe verwenden, scheitern an der Beschreibung des tatsächlich berechneten Strahlungsdrucks.

ABSTRACT

Electromagnetic radiation plays an essential role in the evolution of astrophysical phenomena. Solving radiative transfer in numerical radiation hydrodynamics simulations is expensive and challenging. This work presents a novel method called TreeRay/RadPressure employing a tree-based backwards ray-tracing approach to compute radiative transfer of non-ionizing radiation on diffuse sources such as interstellar dust. The novel scheme allows for every computational entity to be a source of radiation and a contributor towards extinction. The scheme is implemented and tested for a finite volume method and can be generalized to work with particles of, for example, a Smoothed-Particle-Hydrodynamics method.

The scheme developed in this thesis is suitable to compute radiation pressure on dust and gas. Coupled to a chemical network, the method allows to accurately model radiative cooling and heating of dust. An application of the scheme in the context of massive star formation shows that fragmentation induced by self-gravity is reduced by the scheme's more accurate teatmennt of cooling and heating. In particular, self-shielding of dust allows efficient cooling only from the surface of optically thick regions.

With the help of TreeRay/RadPressure, the role of metallicity in the collapse of a subvirial turbulent core forming a massive stars is investigated. The core has a radius of 0.1 parsec and a mass of 150 solar masses. Along with ionizing radiation computed by TreeRay/OnTheSpot, the relative strength of radiation pressure and ionizing feedback are examined. Radiation pressure is the dominant feedback mechanism during the formation of the massive star while it hosts an ultra-compact HII region. Radiation pressure does not halt accretion onto the massive star and its strength is reduced once a disk establishes. Greater metallicities favour fragmentation by enhancing cooling. This results in a greater multiplicity with increased metallicity. Radiation pressure manages to launch bipolar outflows along the rotational axis of the disk.

TreeRay/RadPressure is compared to a multi-wavelength scheme based on RADMC-3D to compute radiation pressure. The comparison is done using non-trivial density distributions generated by radiation hydrodynamics simulations with TreeRay/RadPressure. The comparison shows the radiation pressure calculations of both schemes to agree for the majority of density and luminosity configurations. Simplfied theoretical modelling using the optical depth as a proxy for the momentum boost fails to estimate the radiation pressure.

CONTENTS

1 INTRODUCTION **1**

2 FROM GIANT MOLECULAR CLOUDS TO MASSIVE STARS **3**

2.1 Giant Molecular Clouds 3

2.2 Initial Mass Function 5

2.3 Massive Stars and their Formation 6

2.4 Dust 9

3 HIGH-PERFORMANCE COMPUTING IN ASTROPHYSICS **15**

4 RADIATIVE TRANSFER IN NUMERICAL SIMULATIONS **17**

5 THEORETICAL AND NUMERICAL MODELLING **20**

5.1 Fluid Dynamics 20
- 5.1.1 Finite Volume Method 22
- 5.1.2 Adaptive Mesh Refinement 22
- 5.1.3 Octree 24

5.2 Modelling of Long Range Interactions 25
- 5.2.1 Gravity 25
- 5.2.2 Tree-Solver as an All-purpose Tool 25

5.3 Radiative Transfer and Radiation Pressure 26

6 RESEARCH QUEST **29**

7 TREE-BASED SOLVERS FOR ADAPTIVE MESH REFINEMENT CODE FLASH - III: A NOVEL SCHEME FOR RADIATION PRESSURE ON DUST AND GAS AND RADIATIVE TRANSFER FROM DIFFUSE SOURCES. **31**

7.1 Publication 32

7.2 Failed Ansätze 61

7.3 Shared Memory Extension 63

7.4 Further Comparison of TREERAY/RADPRESSURE 65

8 THE IMPACT OF METALLICITY ON MASSIVE STAR FORMATION: IT IS ALL ABOUT THE DUST! **72**

8.1 Publication 73

9 RADIATION PRESSURE BOOST FACTOR **89**

9.1 RADMC-3D-RP 89

9.2 Boost Factor with RADMC3D-RP 90

9.2.1 Constant Opacity Case 91

9.2.2 λ^{-2} Opacity Case and Realistic Opacity Models 93

9.3 Comparing RADMC-3D-RP to TREERAY/RADPRESSURE 99

9.4 Conclusion 108

10 CONCLUSION AND OUTLOOK **110**

10.1 Summary 110

10.2 Conclusion 111

10.3 Outlook and Discussion 112

1

INTRODUCTION

Relating humankind, the Sun and massive stars. Trapped on Earth and gazing into the night sky, humankind has been curious about what is out there. Like a goldfish in its bowl, we observed our surroundings for millennia and eventually realised how small and insignificant our habitat truly is. Our planet Earth orbits the Sun which has a mass of 1.99×10^{33} g = 1 $M_\odot$ at an average distance of 1.496×10^{13} cm = 1 AU. Our Sun, a G-type main-sequence star, is small and lightweight compared to the most massive stars out there. The Sun formed about 4.6 Gyr ago [Bonanno et al., 2002]. These characteristics of the Sun and its long steady-state on the main sequence may have benefited the development of life on Earth as we know it. The most massive stars reach masses a hundred times that of our Sun, and some of them are located in the Large Magellanic Cloud (LMC) [see Doran et al., 2013, Hainich et al., 2014, Bestenlehner et al., 2020], a satellite galaxy of the Milky Way. Fig. 1 shows the Tarantula Nebula (also known as 30 Doradus) inside the LMC. The bright spots are stars shaping their environment via feedback, such as ionising radiation resulting in so-called HII regions. The ionised gas heats up and tends to expand due to its greater thermal pressure, removing additional dust and gas with it. The dark features are dust which may radiate in the infrared (orange). The precise mechanism by which these stars influence their formation remains unclear and is a part of ongoing research [Kuiper and Hosokawa, 2018, Rosen et al., 2019, Rosen and Krumholz, 2020, Rosen, 2022, Menon et al., 2022a].

This thesis in particular. In this work, I develop the necessary numerical tools to study the effects of radiation pressure (RP) on massive star formation (MSF) in numerical simulations. The scheme I present in this thesis is a so-called backwards ray-tracing scheme allowing to account for every cell in the computational domain being a source of radiation. Here, the focus lies on reprocessed radiation through dust and with dust being a diffuse source permeating the entire domain, radiation can originate from anywhere. With the novel scheme at hand, I study the effects of metallicity in combination with RP during the collapse of isolated molecular cloud cores resulting in the formation of massive star(s). To summarise, this thesis investigates the following points:

- Development of a radiative transfer (RT) scheme to model infrared radiation of dust based on ray-tracing,
- Metallicity and its impact on massive star formation following both its influence on fragmentation and the relative strength of ionising feedback and radiation pressure,
- Comparing the RP generated by the novel backwards ray-tracing scheme to a Monte-Carlo RT method included the momentum boost of RP.

Structure of this thesis. Chapter 2 introduces massive stars starting from giant molecular clouds and going down in spatial scales towards massive stars.

Figure 1: Image showing the heart of the Large Magellanic Cloud, a satellite galaxy of the Milky Way. The Large Magellanic cloud hosts the Tarantula Nebula and is the birthplace of the most massive stars currently known. Dark features in the center are caused by dust. The data of this image was revealed by Josh Lake in Hubble's Hidden Treasures image processing competition. *Credit: ESA/NASA/Hubble*

Subsequently, the relevance for high-performance computing and general RT techniques in numerical simulations are introduced in Chapters 3 and 4. Chapter 5 summarises theoretical and numerical modelling relevant to this thesis ranging from fluid dynamics to the modelling of long-range interactions in numerical codes and an overview of RT and RP. The following chapters compose the main scientific content generated by this thesis. The overarching theme and reasoning behind the main scientific Chapters is given in Chapter 6. Chapter 7 explains the novel scheme forming the core of this thesis within Paper I (see §7.1), followed by details about the development process and shared-memory optimisations. Chapter 8 presents an application of the novel scheme in massive star formation. In particular, the impact of metallicity on fragmentation and feedback is measured. The resulting radiation pressure from the novel scheme is compared to a Monte-Carlo method in Chapter 9. Finally, this thesis is summarized and concluded in Chapter 10.

2

FROM GIANT MOLECULAR CLOUDS TO MASSIVE STARS

Description. Astrophysical phenomena range in scales of space, time and energy across many orders of magnitude. This chapter introduces astrophysical phenomena relevant to this thesis. Giant molecular clouds (GMCs) form the starting point. Following the spatial scale downwards, smaller objects and concepts present inside GMCs are introduced thereafter.

2.1
Giant Molecular Clouds

The first detection. Detecting the presence of carbon monoxide (CO) in the Orion Nebula [Wilson et al., 1970] triggered studies of other objects looking for the CO transition line $J = 1$ to $J = 0$ with radio telescopes [Lada, 1976, Blair et al., 1978]. Today these objects are referred to as giant GMCs having masses of 10^4 to 10^6 $M_\odot$ and temperatures of around 10 K [Dame et al., 1987, Scoville et al., 1987, Solomon et al., 1987]. Regions hosting molecules that are less massive than 10^4 $M_\odot$ are referred to as just molecular clouds (MCs). Moving on from the realm of our galaxy to the LMC, GMCs have been found in other galaxies as well [Fukui et al., 2001]. Also other galaxies of the local group contain GMCs [Blitz et al., 2007].

Formation of GMCs. The review article by Dobbs et al. [2014] lists mechanisms by which GMCs might form. They argue that individual mechanisms dominate on specific scales and their combined effort brings GMCs into existence. GMCs are surrounded by less dense atomic gas of the interstellar medium (ISM). One might argue that GMCs must have formed from the less dense parts of the ISM by some form of converging flow that drives mass towards the regions of future GMCs. Numerical studies by Audit and Hennebelle [2005] show turbulent flows to generate condensations of molecular gas, forming a filamentary network. Once formed, the molecular gas, in particular, allows for fast cooling, removal of thermal support and the growth of condensations in their simulations. In fact, large scale flows can cause turbulent motions on smaller scales through the energy cascade [Klessen and Hennebelle, 2010]. These large scale flows may be caused by global galactic motions [Wada, 2008, Nusser and Silk, 2022]. Flows on smaller scales can be caused by, for example, stellar feedback such as expanding HII regions [Bania and Lyon, 1980, Vazquez-Semadeni et al., 1995] and supernova blast waves [McCray and Kafatos, 1987, Walch et al., 2015, Girichidis et al., 2016, Lu et al., 2020] where the injected momentum may sweep up gas. Observations in the Milky Way and the LMC have found MCs (less massive than 10^4 $M_\odot$) on the edges of swept-up gas [Dawson et al., 2011, 2013]. These clouds may at some point be governed by large-scale flows and combine to form more massive clouds in cloud-cloud collisions. In particular, spiral arms may catalyse the collisions of clouds [Casoli and Combes, 1982, Dobbs, 2008].

Characteristic quantities of GMCs. GMCs can be described with additional parameters besides their mass, M, and their radius, R. One such parameter capturing the strength of turbulence inside a GMC is the velocity dispersion, σ_v, given by

$$\bar{\mathbf{v}} = \frac{1}{V_{\mathrm{GMC}}} \int_{V_{\mathrm{GMC}}} \mathbf{v} \, \mathrm{d}V \,, \tag{2.1}$$

$$\sigma_v = \left(\frac{1}{V_{\mathrm{GMC}}} \int_{V_{\mathrm{GMC}}} (\mathbf{v} - \bar{\mathbf{v}})^2 \, \mathrm{d}V \right)^{1/2} \,, \tag{2.2}$$

where $\mathbf{v}$, $\bar{\mathbf{v}}$ and V_{GMC} are the velocity, the mean of the velocity and the volume of the GMC, respectively. In observations, the velocity dispersion is typically determined from the line width of molecular emission lines [Larson, 1981]. To mitigate effects introduced by optically thick saturation, one can resort to less optically thick lines in observations of, for example, ^{13}C^{16}O (short ^{13}CO) or ^{12}C^{18}O (short C^{18}O), instead of the more abundant ^{12}C^{16}O (short CO) [Phillips et al., 1979]. Using the virial theorem, one can estimate how well bound a structure is via the virial parameter,

$$\alpha_{\mathrm{vir}} = \frac{2E_{\mathrm{kin}}}{E_{\mathrm{grav}}} \,, \tag{2.3}$$

where E_{kin}, E_{grav} are the kinetic energy and the potential energy, respectively. Eq. 2.3 only accounts for the turbulence stabilizing the cloud and the gravity causing the collapse. Recent work by Ganguly et al. [2022] shows that additional contributions by magnetic fields and thermal pressure stabilize fluffy atomic structures while turbulence is the main contributor for dense structures. For $\alpha_{\mathrm{vir}} \approx 1$, a structure is expected to be stabilized and will neither collapse nor expand. Given that $\alpha_{\mathrm{vir}} < 1$, a structure is prone to collapse, while $2 > \alpha_{\mathrm{vir}} > 1$ indicates stable structures. The virial parameter for a spherical cloud can be computed like such:

$$\alpha_{\mathrm{vir}} = \frac{5\sigma_v^2 R}{GM} \,, \tag{2.4}$$

where G is the gravitational constant [Bertoldi and McKee, 1992]. The work of Larson [1981] states the following empirical relation between the velocity dispersion and the radius of a cloud:

$$\sigma_v = \sigma_0 \left(\frac{R}{1\,\mathrm{pc}} \right)^{\beta_{\mathrm{size}}} \,, \tag{2.5}$$

where one finds $\sigma_0 = 0.7\,\mathrm{km\,s^{-1}}$ [Solomon et al., 1987] and $\beta_{\mathrm{size}} = 0.5$ [Heyer and Dame, 2015] inside the Milky Way. In addition, one finds similar molecular column densites, $\Sigma_{\mathrm{mol}} \approx 10^2\,\mathrm{M_\odot\,pc^{-2}}$, among GMCs which can be used to relate the sizes and masses of GMCs [Solomon et al., 1987] via

$$M = \Sigma_{\mathrm{mol}} \pi R^2 \,. \tag{2.6}$$

The cloud mass distributions is given by [Dame et al., 1987, Solomon et al., 1987, Scoville et al., 1987, Heyer and Dame, 2015]

$$\frac{\mathrm{d}N}{\mathrm{d}M} \propto M^{\eta_M} \,, \tag{2.7}$$

where N describes the number of GMCs and $-2.5 < \eta_M - 1.5$. Eq. 2.7 indicates, that GMCs with increasing mass are less frequent.

STRUCTURE OF GMCS. The internal conditions of GMCs have been linked to sites of ongoing star formation (SF) [Mooney and Solomon, 1988] which has made them integral parts in the quest of understanding SF. The combined effects of gravity, magnetic fields, cooling and heating, stellar feedback and most importantly turbulence, give rise to the typical structure of GMCs. Inside GMCs, one finds the mass density function's probability density function (PDF) to follow a log-normal distribution indicating the GMCs' turbulent nature. The PDF has a linear power-law tail [see Collins et al., 2012, Burkhart et al., 2017, and others] where the transition from the log-normal distribution to the linear power-tail is referred to as the *post-shock density*. The post-shock density describes the density where the turbulent energy density,

$$P_{\mathrm{turb}} \;=\; \bar{\rho}\left(\frac{1}{M_{\mathrm{GMC}}}\int_{V_{\mathrm{GMC}}}\rho \times (\mathbf{v}-\bar{\mathbf{v}})^2\,\mathrm{d}V\right)^{1/2}, \tag{2.8}$$

for a given mean density, $\bar{\rho}$, is comparable to the thermal pressure [defined here as the critical density Li et al., 2015]. Beyond the post-shock density, structures inside GMCs transition from being turbulently dominated to being gravitationally dominated and more or less thermal pressure supported. Once gravity has taken over, it forms filamentary structures inside GMCs [André et al., 2014, Hacar et al., 2022] along which mass flows into hubs connecting multiple filaments. These hubs act as sinkholes for gas and are ultimately the place where SF happens within GMCs.

2.2
INITIAL MASS FUNCTION

DEFINITION. The initial mass function (IMF), $\xi(m)\mathrm{d}m$, describes the number of stars with masses between m and $m + \mathrm{d}m$. The IMF is a direct outcome of the complex SF process itself. The early work of Salpeter [1955] suggested a power-law relation given by

$$\xi(m)\mathrm{d}m \propto \left(\frac{m}{M_\odot}\right)^{-2.35}\left(\frac{\mathrm{d}m}{M_\odot}\right), \tag{2.9}$$

for masses in the range of 0.1 $M_\odot$ and 10 $M_\odot$. This single power-law was later improved by Kroupa [2002] and Chabrier [2003] to account for a flattening in the low-mass regime of stars. Here, the exponent changes to -1.3 for $0.08\ M_\odot < m < 0.5\ M_\odot$ and to -0.3 for $m < 0.08\ M_\odot$ in the work of Kroupa [2002]. Chabrier [2003] formulates the IMF as a log-normal distribution up to 1 $\mathrm{M}_\odot$ beyond which it follows the power-law of -2.35. So far, the IMF appears to be universal and an outcome of the statistical process of SF arising from random large-scale super-sonic flows [Padoan et al., 1997]. Though, this statement is part of current research and is further elaborated below.

MISSING EXPLANATION. A conclusive explanation for the observed shape of the IMF is part of current research. Chabrier [2003] proposed the flattening occurring for lower-mass stars to be linked to the decreasing probability associated with the gravitational collapse of low-mass-star-forming clumps. In particular, the so called jeans-mass, referring to the work of Jeans [1902], proposes a minimum mass prone

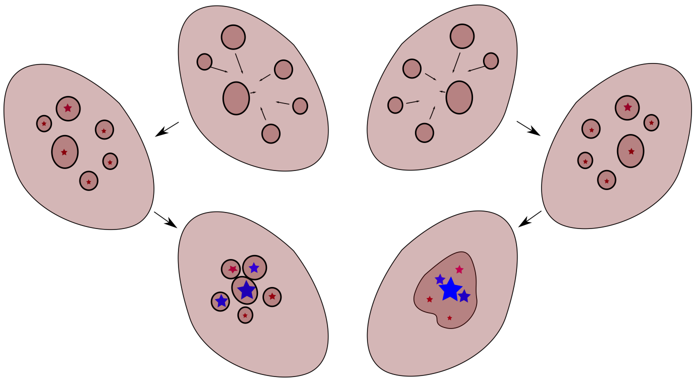

Figure 2: Schematic overview of Core Accretion (left) and Competitive Accretion (right) in the context of massive star formation. In the model of Core Accretion, individual cores within molecular clouds collapse and form stars where their masses are to some extent determined by the mass of their natal core. This picture changes in the competitive accretion model, where individual stars compete for mass outside of the core they formed in. Stars may combine their mass reservoir to host a cluster of stars. Here, massive stars are preferably located at the potential minimum such that they accrete from the densest parts.

to collapse for given conditions on the density and temperature. Objects of masses near or below their jeans-mass are less likely to collapse in the turbulent conditions associated with SF. Additionally, two main ingredients may contribute to the shape of the ISM as we see it today. These are environmental factors and the SF process across different mass scales themselves. The metallicity and its impact on the fragmentation via cooling can be associated with an environmental factor and has been studied in many early works [see, e.g. Omukai, 2000a, Schneider et al., 2003, Omukai et al., 2005, and others]. Observational evidence suggests that increased densities and lower metallicities yield a more top-heavy IMF [Marks et al., 2012] meaning that the number of heavy stars deviates to the top of the slope resulting in more heavy stars than usual. Numerical investigations by Chon et al. [2021] show that the IMF transitions to a Chabrier-like like IMF for metallicities reaching 0.1 $Z_\odot$ and beyond. They conclude that cooling inherent with increased metallicities leads to fragmentation, limiting stars to accrete from their local mass reservoir. SF is accompanied by the release of energy back into the environment through different mechanisms – so-called feedback processes. Individual feedback processes may act negligibly, equally or dominantly on particular scales of SF. For regions forming lower-mass stars, outflows act as the dominant feedback mechanism [see e.g. Nakamura and Li, 2007, Federrath et al., 2014, Guszejnov et al., 2022, and others]. For sites of MSF, ionising radiation, RP, and stellar winds become important [see, e.g. Tanaka et al., 2017]. The work of Guszejnov et al. [2022] finds radiative feedback to be important in the disruption of clouds and the reduction of SF therein. Further, the IMF shows no change concerning the initial cloud mass, turbulence and cloud surface densities in their work.

2.3
Massive Stars and their Formation

Introducing massive stars. Massive stars (MS) live by the credo *'live big - die* *big'*. They are generally defined by having masses greater than 8 $M_\odot$ [see review of Rosen et al., 2020] and preferably form out of gas inside star-forming clumps contained inside GMCs [see review of Tan et al., 2014]. During their life, MSs dominate over low-mass stars by their feedback and the enrichment of heavy elements [see reviews of Tan et al., 2014, Rosen et al., 2020]. MSs ionize their surroundings which eventually starts out as an hyper-compact HII region ($\approx 10^{-2}$ pc scales [Kurtz, 2005]) if they are deeply embedded [e.g. see Murphy et al., 2010]. Eventually, these HII regions may grow to span multiple parsecs. At the end of their life, MSs result in a supernova releasing enormous amounts of energy and metals into their environment.

THEORIES OF MASSIVE STAR FORMATION. The leading theories of MSF are referred to as *Core Accretion* [extension of turbulent core collapse, Shu et al., 1987, towards MSs] and *Competitive Accretion* [Bonnell et al., 2001, Bonnell and Bate, 2006]. In essence, massive stars form out of a single gravitationally bound core according to the core accretion theory. Thus, each core's mass would predetermine the star's resulting mass. Therefore, one would expect to find a similar distribution of cores with specific masses described by a core-mass function (CMF) that would translate to the distribution one finds in the IMF [Motte et al., 1998, Testi and Sargent, 1998]. Furthermore, one finds similarities between the CMF and the IMF that show agreeing power-laws [Motte et al., 1998, Testi and Sargent, 1998, Alves et al., 2007]. However, the CMF shows no flattening within the GMC Cygnus X as it is observed for low mass stars in the IMF [Cao et al., 2021]. In addition, the CMF seems to steepen towards the high-mass regime, contradicting the top-heavy IMF found in Cygnus X [Cao et al., 2021]. Competitive accretion was described by Bonnell et al. [2001] as an extension of the measured differences in accretion rates of stars within smaller stellar clusters based on their position [Bonnell et al., 1997] towards general star formation. This mechanism was suggested to explain the high mass end of the IMF [Bonnell and Bate, 2006]. Fig. 2 illustrates the process of core accretion on the left and competitive accretion on the right. Starting from a region prone to forming clumps (top row), we end up with two different outcomes. Following the core accretion model, each star forms out of an isolated clump that, to some extent, determines the final mass of the resulting star (bottom row, left side). On the right, the clumps interact such that they combine while having formed stars individually beforehand. The stars and gas are subject to the combined gravitational effects resulting in higher densities near the combined potential minimum. Heavier stars tend to be located near dense regions and therefore experience higher accretion rates. This process leaves room for chaotic randomness as the n-body interactions between stars are of chaotic nature. As long as gas is accreting onto the cluster, mass preferably flows to the stars located in a local potential minimum.

ACCRETION THROUGH DISKS. Zooming in on individual MSs, the consensus is that MSs host disks during their formation from which they accrete mass [see, e.g. Vaidya et al., 2009, and others]. Within disks, angular momentum is transported outwards by gravitational torques [see Toomre, 1977, Kuiper et al., 2011, and others] and magneto-rotational instabilities [see Kratter et al., 2010, and others], allowing for accretion onto the central star. Molecular outflows are observed to originate from disks around MSs [Beuther et al., 2002b]. Outflows along the angular momentum axis and their launching mechanism have extensively been studied in low mass star formation (see, e.g. review by Pudritz et al. [2007]). Numerical simulations by Seifried et al. [2012] show magneto-centrifugally launched collimated outflows for disks around MSs. Given these similarities between low- and high-mass star formation, the considered time scales, energetic scales and mass scales are very different. Time scales concerning MSF have been measured to be on the order of 5×10^5 yr [Bovino et al., 2021] and typical accretion rates via disc accretion reach $10^{-4} - 10^{-3}\,M_\odot\,\mathrm{yr}^{-1}$ [see, e.g., McKee and Tan, 2003, Hosokawa et al., 2010]. Lower-mass stars typically accrete with rates on the order of $10^{-7} - 10^{-9}\,M_\odot\,\mathrm{yr}^{-1}$ once they are out of their Class 0 phase and start hosting a disk [see, e.g., Motte and André, 2001]. With that in mind, MSF can not be considered a scaled up version of the low-mass star-formation process given that more energy is released in a shorter time frame generating more extensive feedback in the form of luminosity. Disks around MSs have formed fragments as massive as 1 $\mathrm{M}_\odot$ in numerical simulations by Oliva and Kuiper [2020]. Some of those fragments have hosted their own disks within their gravitational sphere of influence and some where destroyed by interacting with other fragments. Yorke and Bodenheimer [1999] carried out numerical studies that suggest radiative signatures to be dependent on the orientation of the disk. Here, the bolometric luminosity may vary by a factor of 30, depending on the viewing angle. Moreover, individual features like the 10 μm feature may vary by orders of magnitude. Said mechanism is referred to as the *flashlight effect* [Yorke and Bodenheimer, 1999].

Feedback processes. Feedback processes generated by mature MSs are capable of disrupting MCs [Inutsuka et al., 2015]. MSs form deeply embedded and reach the zero-age main sequence while still accreting mass. During their protostellar phase, massive protostars' feedback processes are more destructive than that of their low-mass siblings. Similar to their low-mass siblings, massive young stellar objects show collimated outflows during their accretion time [see, e.g. Beuther et al., 2002a, Garay et al., 2007, and others]. Numerical studies by Rosen and Krumholz [2020] show that outflows dominate the momentum input compared to RP in the early stage of MSF. However, this may change at later stages as the momentum input by outflow feedback is proportional to the accretion rate, and the square root of the stellar mass and accretion may eventually fade [Rosen and Krumholz, 2020]. The exact mechanism by which collimated outflows are generated has not been reproduced self-consistently in numerical simulations across an entire star formation process on the smallest scales[1]. Numerical efforts in doing so are costly and current methods, and hardware allow to model 1 year feasibly [see, e.g. Tomida et al., 2013, 2015]. A different feedback mechanism is so-called stellar winds. Here, radiation pressure drives material directly from the stellar surface contributing to a continuous mass loss where resonance in emission and absorption lines of ions cause additional boosts [see, e.g. Lucy and Solomon, 1970, Castor et al., 1975]. As these winds drift away from their natal star, they produce hot bubbles when they shock against the surrounding material. The work of Weaver et al. [1977] describes the expansion of a corresponding bubble as energy-driven due to the high thermal pressure generated by the shock-heated gas. Recent studies suggest that the cooling maintaining the thermal balance of the interior takes place on a fractal surface due to turbulent mixing [Lancaster et al., 2021a,b]. With the surface being larger in a fractal case, cooling is more potent than assumed by the work of Weaver et al. [1977] suggesting the expansion of wind-driven bubbles to be momentum driven once mixing becomes efficient. In addition, MSs release an enormous amount of ionising radiation into the environment. This ionising radiation ionises the surrounding gas, which tends to expand due to its high-pressure [Spitzer, 1978]. For the dynamics of GMCs, ionising radiation is argued to be the main constituent for turbulence driving [Matzner, 2002]. Self-shielding plays an essential role in the removal of gas through ionising radiation and can introduce a delay in the destruction of the star's natal environment [Haid et al., 2019]. MSs located near the border of MCs can evaporate MCs effectively once their HII region breaks out of the cloud allowing gas to stream into rarefied space [Whitworth, 1979]. Given that recombinations of ions and electrons are more efficient at greater densities resulting in effectively less ionised material, the impact of ionising radiation may be boosted by any of the other previous feedback mechanisms and radiation pressure. The work of Rosdahl and Teyssier [2015] [and also **Klepitko** et al., 2023, taking into account mean molecular weights] compares direct RP from ionising radiation to the D-type driven expansion of an HII region, finding ionising feedback to be more assertive on larger scales. Observations estimating the relative importance of direct radiation pressure and pressure generated by ionising radiation show equal importance in HII regions of sizes of around 0.2 pc to 2 pc, with direct radiation pressure dominating at smaller scales and ionising radiation dominating at larger scales [see, e.g. Lopez et al., 2014, Barnes et al., 2020, Olivier et al., 2021]. In this way, it is meaningful to think of a cascade of feedback mechanisms that all together result in the dispersal of MCs.

---

[1] This holds to my knowledge and is hard to prove given the vast number of publications.

RP in particular. The modelling and understanding of RP and its role in MSF lie at the heart of this thesis. Early theories suggest a maximum stellar mass of 40 $M_\odot$ limited by RP if stars were to form due to spherical accretion [Kahn, 1974]. This limit was softened by considering non-spherical accretion through a disk allowing for radiation to escape without interacting with in-falling gas [Nakano, 1989, Nakano et al., 1995]. This was followed by complex numerical investigations on large and small scales with the advent of suitable computer hardware. On large scales, recent numerical work of Menon et al. [2022a] finds RP to be unlikely to influence SF in the ISM and launching galactic winds [see also Krumholz and Thompson, 2012]. The investigated scales, however, are larger than the scales on which RP is thought to dominate compared to ionising feedback [see, e.g., Barnes et al., 2020, Olivier et al., 2021]. The work of Ali [2021] shows RP to be stronger than ionizing feedback at around 0.5 pc for solar metallicity. They find lower metallicities to increase the strength of ionizing feedback due to the higher temperatures present in HII regions. Larger metallicities are considered to trap radiation released by stars especially in the infrared through increased dust-to-gas ratios. This trapped radiation is reprocessed multiple times may generate a multitude of the momentum that is injected by the initial radiation and thus boost the net momentum generated by RP [see Hopkins et al., 2011, Krumholz and Thompson, 2012, Kuiper and Hosokawa, 2018, Rosen et al., 2019, and many others]. The RT scheme developed in the course of this thesis is employed to study the influence of varying the metallicity in MSF. Further, the role of RP is therein is investigated.

2.4
DUST

DEFINITION AND ORIGIN. Dust forms out of heavier elements generated through nucleosynthesis by stars. Once these elements are ejected from stars, they may form dust. Sources of dust-forming elements are red giants, supernovae and Wolf-Rayet stars [Gehrz, 1989]. Dust is categorised into two branches which are labelled carbonaceous dust and silicates. The former type is a product of carbon-rich zones ($C/O > 1$) while the latter forms in oxygen-rich zones [Tielens, 2005]. The main contributors towards carbonaceous grains are C-rich giants, whereas Supernovae

Star-Forming Region S106
NASA, ESA, and the Hubble Heritage Team (STScI/AURA) • HST WFC3/UVIS • STScI-PRC11-38
Hubble Heritage

Figure 3: Looking into the heart of the star-forming region S106 at Sharples 2 reveals hot gas (blue) being expelled from the central young massive star in a horizontal, bipolar fashion. Dust (red) accumulates in a disk surrounding the massive star and squeezes the hot gas into an hourglass shape. *Credit: NASA, ESA, and the Hubble Heritage Team (STScI/AURA)*

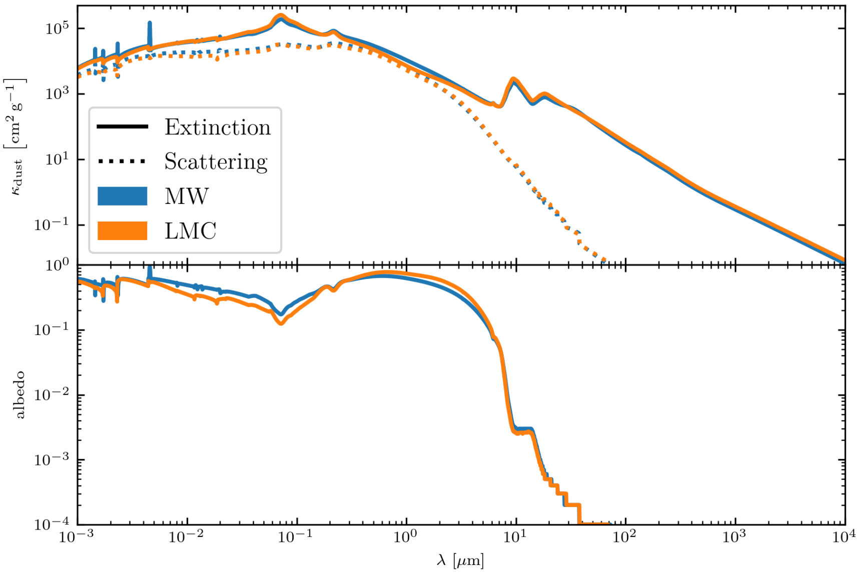

Figure 4: The top panel shows the dust extinction (solid line) and scattering (dotted line) cross sections per grams of dust as a function of the wavelength for two different dust model representing the Milky Way (MW, blue) and the LMC (orange) [Weingartner and Draine, 2001b]. The bottom panel shows the corresponding albedo to for both models.

Table 2.1: Radical-radical dust-grain surface reactions as shown in the book of Tielens [2005]. The list shown here can be extended as more complex organic molecules can form by adding carbon atoms. This table highlights the chemical richness provided by the dust-grain surface reactions. The reactions presented in this table do not cover all possible reactions.

reactants		products
H + O	$\longrightarrow$	OH
H + OH	$\longrightarrow$	H_2O
H + C	$\longrightarrow$	CH
H + CH	$\longrightarrow$	CH_2
H + CH_2	$\longrightarrow$	CH_3
H + CH_3	$\longrightarrow$	CH_4
H + N	$\longrightarrow$	NH
H + NH	$\longrightarrow$	NH_2
H + NH_2	$\longrightarrow$	NH_3
H + O_2H	$\longrightarrow$	H_2O_2
H + NO	$\longrightarrow$	HNO
H + CN	$\longrightarrow$	HCN
H + CNO	$\longrightarrow$	HCNO
H + HCO	$\longrightarrow$	H_2CO
H + HCOO	$\longrightarrow$	HCOOH
H + CH_3O	$\longrightarrow$	CH_3OH
H + NCHO	$\longrightarrow$	NHCHO
H + NHCHO	$\longrightarrow$	NH_2CHO
H + CCHO	$\longrightarrow$	CHCHO
H + CHCHO	$\longrightarrow$	CH_2CHO
H + CH_2CHO	$\longrightarrow$	CH_3CHO
H + N_2H	$\longrightarrow$	N_2H_2
O + O	$\longrightarrow$	O_2
O + N	$\longrightarrow$	NO
O + C	$\longrightarrow$	CO
O + CN	$\longrightarrow$	OCN
O + HCO	$\longrightarrow$	HCOO
C + N	$\longrightarrow$	CN
C + HCO	$\longrightarrow$	CCHO
N + N	$\longrightarrow$	N_2
N + NH	$\longrightarrow$	N_2H
N + HCO	$\longrightarrow$	NCHO

and O-rich giants contribute towards the formation of silicates [Tielens, 2005]. For dust to ultimately form, the temperature of the forming material must drop below the sublimation temperature of 1500 K. Individual grains may form through two processes. These include the accretion of individual atoms resulting in nearly spherical grains and the coagulation of larger grains to form irregular shapes [Weitz and Oliveria, 1984]. These two processes may independently contribute to the growth of individual grains, as shown by the lab experiments of Praburam and Goree [1995]. The resulting size distribution of dust grains can be approximated by

$$\frac{\mathrm{d}n_{\mathrm{gr}}}{\mathrm{d}a} = C n_{\mathrm{H}} a^{-3.5} , \tag{2.10}$$

where n_{gr}, a, C and n_{H} are the number density of grains, the grain-size, a normalization constant and the hydrogen number density, respectively [Mathis et al., 1977]. Additional constraints are $5\,\mathrm{nm} < a < 0.25\,\mu\mathrm{m}$. The work of Mathis et al. [1977] derived this distribution by demanding that it reproduces absorption features seen in stellar spectra passing through dark clouds.

Grain surface chemistry. Dust is an integral part of the chemical evolution of the ISM. Dust allows molecular hydrogen to form more easily by trapping individual hydrogen atoms on its surface where they can form more effectively [McCrea and McNally, 1960, Tielens, 2005]. Given a relatively high metallicity present in our local surroundings, almost all H_2 formation has been catalysed by dust grains [Ballesteros-Paredes et al., 2020]. Besides hydrogen, dust may also trap heavier elements [Tielens, 2005] and aid in the formation of complex molecules on its surface [Hasegawa et al., 1992, Tielens, 2005]. Table 2.1 shows an exemplary portfolio of radical-radical surface reactions on dust grains as displayed in the work of Tielens [2005] and underlines the chemical richness brought forth by dust grain surface chemistry. Overall, dust can increase the rate at which molecules form by two orders of magnitude [e.g. see reactions given in Hollenbach and McKee, 1979].

Dust and radiation. Dust interacts with radiation across a wide range of the electromagnetic spectrum. The wavelength-dependent dust opacity, $\kappa_{dust}(\lambda)$, gives a metric for the strength of interaction with radiation by dust. Fig. 4 shows dust opacities as a function wavelength. The dust opacities are based on the work of Weingartner and Draine [2001b] and show the extinction opacity and the scattering opacity for dust models of the Milky Way and the LMC. Dust shows high opacities towards ultraviolet radiation (from $10^{-2}\,\mu$m to $4 \times 10^{-1}\,\mu$m) which decreases towards higher wavelengths with a power-law of roughly $\propto \lambda^{-2}$. In ultra-luminous infrared galaxies (ULIRGs), for example, dust absorbs light of shorter wavelengths emitted by massive stars and reemits radiation in the infrared giving these galaxies their typical infrared excess [see e.g. Genzel et al., 1998]. Distinct features like the peak around 10 μm in the spectrum of dust continuum emission are caused by metals contained in the dust grains. The peak around 10 μm in particular is caused by silicate (Si_xO_y) [see for example absorption lines of NGC 1068 by Rieke and Low, 1975]. As dust in space is a compound of different grain sizes, small grains will contribute to Rayleigh scattering if their size is smaller than the wavelength. For small grains, however, absorption and reemission are the dominant process for interactions with photons [Draine, 2011]. On the other hand, larger particles will contribute through the mechanism of Mie scattering.

Forces acting on dust. Besides gravity, dust is subject to forces of different origins. One of these forces is RP, generated by the interaction with radiation. In ULIRGs, RP on dust may provide additional support to the galactic plane against gravity, thus reducing the star formations rate described by the Kennicutt-Schmidt law [Kennicutt, 1998] for star formation in the optically thick limit [Thompson et al., 2005]. Additional scattering, absorption and reemission of light through dust may boost the departed momentum through radiation pressure [see, e.g. Hopkins et al., 2011, Krumholz and Thompson, 2012, Kuiper and Hosokawa, 2018, Rosen et al., 2019, and others]. Given an anisotropic radiation field, dust may experience additional forces generated by anisotropically ejected particles [Weingartner and Draine, 2001a]. Dust and gas can experience relative velocities to each other. Collisions between dust and gas equalize the relative velocity component between the two species causing a drag [see, e.g. Moseley et al., 2022, and others].

Dust as a cooling agent. Dust can be understood as a thermodynamic subsystem within the ISM that interacts with a wide range of the electromagnetic spectrum. In the limit of blackbody radiation, one can calculate a Planck-weighted opacity of dust, $\kappa_{\mathrm{P,dust}}(T)$, that is temperature-dependent in the following way

$$\kappa_{\mathrm{P,dust}}(T) = \frac{\int \kappa_{\mathrm{dust}}(\lambda) B_\lambda(T,\lambda)\,\mathrm{d}\lambda}{\int B_\lambda(T,\lambda)\,\mathrm{d}\lambda}\,, \tag{2.11}$$

where $B_\lambda(T,\lambda)$ is Planck's law for a given temperature T. The Planck-weighted opacity roughly scales with T^2 for temperatures less than 150 K and is constant beyond 150 K depending on the model [see e.g. Semenov et al., 2003, Krumholz and Thompson, 2012]. The mean energies absorbed, $\Gamma_{\mathrm{dust,BB}}$, and emitted, $\Lambda_{\mathrm{dust,BB}}$, by dust per unit volume and unit time are given by

$$\begin{aligned} \Gamma_{\mathrm{dust,BB}} &= \rho_{\mathrm{dust}}\sigma\kappa_{\mathrm{dust}}(T_{\mathrm{dust}})T_{\mathrm{dust}}^4\,, && (2.12)\\ \Lambda_{\mathrm{dust,BB}} &= \rho_{\mathrm{dust}}4\pi\kappa_{\mathrm{dust}}(T_{\mathrm{dust}})J\,, && (2.13) \end{aligned}$$

where ρ_{dust}, σ, J are the dust density, the Stefan-Boltzmann constant and the mean radiative intensity per steradian, respectively [see e.g. Tielens, 2005, **Klepitko** et al., 2023, and others]. From these one can conclude a temperature, T_J, associated with radiative equilibrium written as

$$T_J = \left(\frac{\pi J}{\sigma}\right)^{1/4}\,. \tag{2.14}$$

Radiative heating and cooling of dust are two processes among many which determine the dust temperature. In the case where $\Gamma_{\mathrm{dust,BB}}$ and $\Lambda_{\mathrm{dust,BB}}$ are dominating, the dust temperature will tend towards T_J. Emission by dust as well as emission by stars may contribute to J and thus lift the radiation temperature. Another process by which dust grains interact thermodynamically is the collisional coupling of dust and gas. This process scales with the dust number density, n_{dust}, and the gas number density, n, and the difference between the dust temperature and the gas temperature, T_{gas}. The following expression yields the change of energy per unit volume and unit time onto dust:

$$\Gamma_{\mathrm{dust-gas}} = n n_{\mathrm{dust}}\sigma_{\mathrm{dust}}v_{\mathrm{p}}f 2k_{\mathrm{B}}(T_{\mathrm{gas}} - T_{\mathrm{dust}})\,, \tag{2.15}$$

where σ_{dust}, v_{p}, f and k_{B} are the dust cross-section, the thermal speed of a proton at a given temperature, a correction factor for the coupling strength and the Boltzmann constant, respectively [Hollenbach and McKee, 1979]. Eq. 2.15 describes as positive energy flow towards dust if $T_{\mathrm{gas}} > T_{\mathrm{dust}}$ and in return thermal energy is drained from gas such that it is effectively cooled. In the opposite case where $T_{\text{dust}} > T_{\text{gas}}$, gas will drain energy from dust and thus be heated.

IMPACT ON GAS DYNAMICS VIA COOLING. The work of Omukai [2000b] investigates the role of radiative cooling at different metallicities for protostellar cores, including continuum radiation from dust. They find higher temperatures for diffuse gas in the case of lower metallicities. Towards greater densities, they find similar temperatures once metals and dust are embedded and lose their ability to cool. The final size of the protostellar core does not change as it is pressure stabilised by the embedded material. Throughout their simulations, they use an approximation to assess whether a region is embedded or not based on local quantities. Besides that, they neglect radiation treatment, contributing to T_J.

3

HIGH-PERFORMANCE COMPUTING IN ASTROPHYSICS

REASON FOR HIGH-PERFORMANCE COMPUTING. With humanity being on the way to becoming a Type I civilisation on the Kardashev scale [Kardashev, 1964] (approx. $10^{19}\,\mathrm{erg\,s^{-1}}$), we will at some point manage a power equivalent to that, reaching Earth from the Sun via radiation. With that, we are nowhere near to perform experiments on the energetic scales of star formation. Type Ia supernovae, for example, release an energy equivalent of roughly 10^{51} erg [see, e.g. Ostriker and McKee, 1988, Khokhlov et al., 1993, and others]. The significant difference between the energetic scales of SF and humanity underlines that the energetic scales of SF are beyond that of current and foreseeable technologies of humanity. We would simply not be capable of constructing suitable initial conditions in nature ourselves. Additionally, SF's timescales are beyond human civilisation's lifetimes (estimated to be 10 kyr for the first cities to appear [Tudge et al., 1999]), rendering experiments impractical. In a similar way, observations appear to be static in time given the large spatial scales of SF, albeit great velocities present. For these reasons, one turns to simulations on supercomputers to study astrophysical problems interactively. Here, interactively describes the situation in that we as humans can construct an experiment that can be evolved in time either by nature itself or by a given set of rules that mimic nature as best as possible.

ANALYTICAL SOLUTIONS. One might argue that analytical solutions are a more desired solution strategy due to their superior accuracy compared to numerical approaches. However, the realm covered by analytical solutions is often full of simplifications and, therefore, far from reality. Looking at the problem of an expanding HII, one can find a spectrum of analytical solutions of varying complexity [see Strömgren, 1939, Spitzer, 1978, Dyson and Williams, 1980, Raga et al., 2012]. These solutions have in common that they assume a homogeneous background density resulting in spherical HII regions. Observations, however, show deviations from purely spherical HII regions [see, e.g. Sibille et al., 1975] and their causes have been discussed in further models by Kandel and Sibille [1978]. An example of such an HII region is given in Fig. 3 where the blue colours show gas ionised by a source sitting in the centre. Nonetheless, analytical solutions present a helpful approach toward building intuition and understanding of the impact of astrophysical mechanisms.

NUMERICAL SOLUTIONS. Where analytical approaches reach their limits, numerical techniques *can* push further and help to obtain an insightful solution. This is especially true in the chaotic nature of astrophysical problems where analytical solutions are hard to find. Note that constraints on their applicability limit most numerical techniques. Solutions obtained outside of these limits should not be trusted.

HIGH-PERFORMANCE COMPUTING – HARDWARE. High-performance computing (HPC) refers to solving demanding and complex problems by allocating powerful hardware resources in combination with numerical techniques. The machines used in the context of HPC are called supercomputers which contain multiple compute nodes, each equipped with a processor and memory. Individual nodes can then be allocated to share the workload of a computational problem. A biannually updated list of the 500 most powerful, publicly[1] known supercomputers on our planet is provided on the TOP500 website[2]. According to the list for June 2022, the most powerful machine is capable of performing 1,102.0 PFlop/s. This performance is roughly eight times more powerful than it was a decade ago. In return, this allows tackling more demanding problems through advances in the hardware by simply allocating more powerful resources.

High-performance computing – Software. The software used in the context of HPC must highly opt for distributed computing such that multiple processors can work simultaneously on independent sub-problems. In addition, the software must be efficient in communicating solutions of sub-problems among processors if needed. Generally, such software consists of parts that can be executed by multiple processors simultaneously and parts that can not. For a given fraction of time, p, that is spent in parts which can be executed in parallel during the runtime of software, one can achieve a maximum theoretical speedup, S, according to Amdahl's law [Amdahl, 1967] in the following way

$$S = \frac{1}{1-p}, \tag{3.1}$$

by allocating infinitely many processors. Here, the time spent communicating solutions between processors and the time taken for I/O operations is neglected, presenting an ideal upper limit to the possible speedup. As a corollary, it is therefore desirable to keep p as high as possible when designing HPC software to achieve maximum speedup.

Message Passing Interface. Typically, HPC software employs the Message Passing Interface (MPI) standard in order to compute on multiple processors and, therefore, nodes simultaneously. A single processor is composed of multiple compute cores in present-day computer architecture such that each core is assigned an MPI rank, a unique identifier during runtime. MPI ranks are natural numbers from zero to $N-1$, where N is the number of total ranks. Out of all MPI ranks, one usually takes a unique role and is referred to as the master rank, defined by its rank equalling zero. Each rank is aware of the whole program during runtime, and the workload may be split among ranks equally. The workload division is typically accomplished by splitting the entire work into N work packages of similar runtime costs. Once a rank has finished its package, it enters a synchronisation barrier and waits until all ranks have arrived at the barrier. Afterwards, solutions are exchanged or combined if necessary, and the workflow continues. In this particular instance, the master processor often directs data gathering and does non-parallelisable computations. However, the exact details of the implementation rely on the problem to be solved and the team or person writing the software.

---

[1] There might be more powerful supercomputers classified for the general public due to strategic reasons.

[2] `https://top500.org/`

4

RADIATIVE TRANSFER IN NUMERICAL SIMULATIONS

Motivation. Radiative processes are of significant importance for the physical processes in the ISM. Cooling through metals [Smith et al., 2008] and dust [Dopcke et al., 2011] even at low metallicities as small as $10^{-5}\,Z_\odot$ has shown to pronounce fragmentation and may contribute to the formation of lower-mass fragments. These fragments may eventually lead to the abundance of low mass stars we see in the Chabrier IMF today [Chon et al., 2021]. Radiation, however, may also lower the formation of stars through ionising feedback in their proximity and may trigger star formation elsewhere [Haid et al., 2019]. The broad implications make RT a desired additive in recent numerical simulations.

Numerical solutions. Solving RT, however, is costly in numerical simulations and only feasible due to advances in both computer hardware technology and novel algorithms. In order to obtain solutions in a feasible time frame, one generally makes use of approximations when dealing with RT. Three widely used flavours of solving RT will be introduced in the following course of this section.

Moment methods. One such flavour is the so-called flux-limited-diffusion (FLD) approximation in which radiation is modelled to be an energy density that permeates the computational domain via diffusion [Levermore and Pomraning, 1981]. This approach has the benefit of rendering RT into a local problem where fluxes in a limited volume need to be considered. This approach was adapted and improved by many works in the scientific community [e.g. Krumholz et al., 2007, Rosen et al., 2017, Kuiper and Hosokawa, 2018, Kannan et al., 2019, and others]. This method was improved by Levermore [1984] by including one more moment during the advection of the energy density. The method was coined M1 closure and is also still in use [e.g. González et al., 2007, Skinner and Ostriker, 2013, Rosdahl and Teyssier, 2015, and others]. By comparison to other methods of RT, it was found that the FLD and M1 closure scheme may yield unphysical results. FLD shows difficulties in casting shadows, such that radiation may creep behind objects where it should not. The M1 closure scheme, however, shows a significant improvement in that regard but suffers from collisions between streams of radiation in the presence of multiple sources. Both FLD and M1 closure are discussed in the work of Menon et al. [2022b], where they also show the implementation of a more improved moment method, the variable Eddington tensor (VET) method [e.g. Stone et al., 1992, and others]. Their approach does not show the collision of radiation streams and faithfully captures shadows from obscuring objects.

Monte-Carlo methods. A conceptually completely different approach is given by the application of the Monte-Carlo method on RT (MCRT). This approach makes use of random sampling to obtain a converged solution eventually. Similar to FLD, MCRT is present in many codes used in astrophysics where some codes model RT in post-processing [see Lucy, 1999, Dullemond et al., 2012, Ferland et al., 2013, and others] and others to improve the physics in numerical simulations of hydrodynamics [see Harries et al., 2019, Smith et al., 2020, and others]. Here, radiation is split

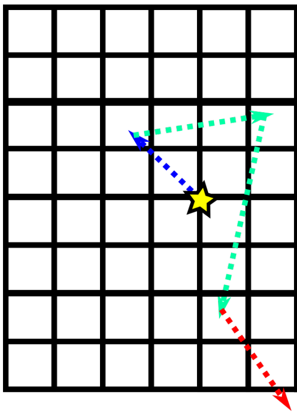

Figure 5: Exemplary path of a single photon package during MCRT drawn out by arrows. The package was launched from the central source (star) and permeated the computational domain. During its journey, the photon package changes its direction and associated wavelength (indicated by the color) depending on the nature of the interaction. Finally, the packages leave the computational domain.

into packages of photons carrying energy and momentum. Packages are launched individually and travel the computational domain until they either escape or are terminated given by the exact algorithm. At their launch, each package is assigned a wavelength which sets the properties for the package to interact with matter. Upon interaction, the path of a package may change due to physical processes involving scattering or absorption and immediate reemission. Physics, to an arbitrary degree, can be implemented by changing, for example, the likelihood of interactions and how the direction is changed on a microphysical level. Fig. 5 shows an exemplary path of a single photon package through a computational domain.

Ray-Tracing methods. Last but not least, one finds methods that solve RT via ray-tracing. Here, light propagates along straight lines, so-called rays, in the form of an intensity. Along its path, the intensity may decrease due to absorption events or increase due to emission and scattering events along the ray's direction. Ray-tracing may conceptually be approached by two ansatzes (*German translation: Ansätze*). For the first ansatz, we start from a point source, for example, a star viewed from a great distance, emitting light in all directions. Light is then propagated along rays, where each ray has an angular size, $d\Omega_{\rm ray}$, associated with it. The rays are launched such that they cover the entire angular space of a unit sphere. Obscuring material reduces the intensity along rays either by absorption or scattering. However, additional emission or scattering of material along the path directed into the ray's path may increase the radiative intensity along it. This approach is generally referred to as forward-ray-tracing. The naive approach, as described here, may become unfeasible for large distances as objects far away require rays with small $d\Omega$ to be resolved. Fig. 6 illustrates forward ray-tracing in the example on the left, where two sources (yellow stars) cast rays at a clump (brown structure). With the clump at an increasingly larger distance, more rays are required to fully resolve it. A more efficient way to the naive approach can be found in the work of Abel and Wandelt [2002] where they introduce additional rays at certain distances to enhance the resolution. The intensities of the inner, more coarse rays are forwarded to rays further out with smaller angular sizes, where they continue to be propagated. By doing this, the resolution is selectively applied where it is needed such that the compu-

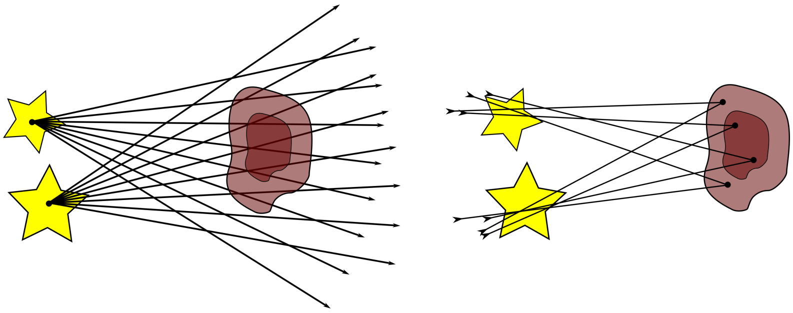

Figure 6: A sketch showing the concepts of forward-ray-tracing on the left and backwards ray-tracing on the right. Both examples include two sources of radiation marked by stars and the material on which the radiation is acting given by the red-brown blob. During forward-ray-tracing, one tries to propagate radiation from the sources via rays, which requires great angular resolutions for distant objects. Backwards ray-tracing casts rays from a target position directed at sources and can obtain results with coarser angular resolutions at greater distances by mapping, for example, multiple sources to a ray.

tational cost overall is decreased. This approach is widely used in astrophysical simulation codes and continues to inspire other works [see Baczynski et al., 2015, Rosen et al., 2017, Kuiper et al., 2020, and others]. The second ansatz is generally referred to as backwards ray-tracing. In this instance, rays are cast from target positions toward radiation sources. Fig. 6 illustrates backwards ray-tracing on the right. Here, a limited number of target positions (dots) cast rays at the two sources to their left (yellow stars), where each ray has an opening angle. If multiple sources or obscuring material appear close to each other in an angular direction, contributions may be merged to generate a speedup [Kessel-Deynet and Burkert, 2000, Okamoto et al., 2012, Grond et al., 2019]. A somewhat similar approach has been applied to solve gravity with an octree (see §5.1.3) [Barnes and Hut, 1986, Wünsch et al., 2018] allowing to merge contributions of individual resolution elements within numerical simulations. Recently it has been put forward to solve RT of ionising radiation via backwards ray-tracing [Okamoto et al., 2012, Wünsch et al., 2021].

5

THEORETICAL AND NUMERICAL MODELLING

The application of numerical methods is key to modern advancements in the field of astronomy, and this thesis in particular. This chapter summarises relevant numerical techniques and briefly touches on analytical descriptions relevant to this thesis. More extensive descriptions can be found in the works of Tielens [2005], Bodenheimer et al. [2006], Toro [2013] and Mihalas and Mihalas [2013]. This chapter presents basic concepts of fluid dynamics along with data structures found in numerical codes in §5.1. Tree-based solvers and their relevance towards computing gravity and RT numerically are shown in §5.2. Finally, the modelling of RT and RP are presented in 5.3.

5.1
Fluid Dynamics

Relevance for astrophysics. The dynamics of the gas composing the ISM can be modelled to follow that of a continuous fluid, as long as a the mean free path of gas particles between interactions, $\lambda_{\text{particle}}$, is much smaller than the characteristic length scale of the problem, l_{problem} [Bodenheimer et al., 2006]. Clouds composed of neutral hydrogen (HI), so-called Spitzer-type clouds, have number densities of around $n_{\text{HI}} \approx 50\,\text{cm}^{-3}$ [Tielens, 2005]. Combined with an average scattering cross section per atom of $\sigma_{\text{HI}} \approx 10^{-15}\,\text{cm}^2$ [Bodenheimer et al., 2006], one can estimate the mean free path to be

$$\lambda_{\text{HI}} = \frac{1}{n_{\text{HI}}\sigma_{\text{HI}}} = 2 \times 10^{13}\text{cm} \tag{5.1}$$

inside a Spitzer-type cloud. Given that such clouds are comparable in size of $10\,\text{pc} \approx 3.086 \times 10^{19}\,\text{cm}$ [Tielens, 2005], one can conclude that modelling the dynamics of gas in an astrophysical context as a continuous fluid is well suited.

Euler-Equations. The Euler-Equations describing the evolution of an ideal fluid read

$$\begin{aligned}
\frac{\partial \rho}{\partial t} + \nabla \cdot (\rho \mathbf{v}) &= 0\,, && (5.2)\\
\frac{\partial \rho \mathbf{v}}{\partial t} + \nabla \cdot (\rho \mathbf{v} \otimes \mathbf{v} + P) &= \rho \mathbf{a}\,, && (5.3)\\
\frac{\partial E}{\partial t} + \nabla \cdot (E \mathbf{v}) &= -P\,\nabla \cdot \mathbf{v}\,, && (5.4)
\end{aligned}$$

where ρ, t, $\mathbf{v}$, P, $\mathbf{a}$ and E are the mass density $[\text{g}\,\text{cm}^{-3}]$, time [s], velocity $[\text{cm}\,\text{s}^{-1}]$, thermal pressure $[\text{erg}\,\text{cm}^{-3}]$, accelerations acting on the fluid $[\text{cm}\,\text{s}^{-2}]$ and internal energy per unit volume $[\text{erg}\,\text{cm}^{-3}]$ [Bodenheimer et al., 2006]. Each of the Euler-

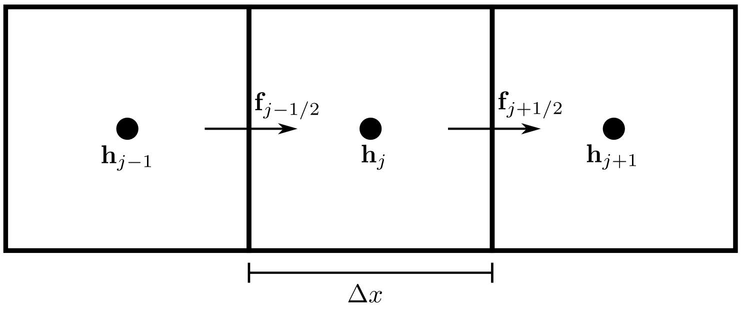

Figure 7: Sketch of the finite volume method applied to cells in a one dimensional space with conserved quantities, $\mathbf{h}_j^n$, and fluxes, $\mathbf{f}_{j-1/2}^n$ and $\mathbf{f}_{j+1/2}^n$, where n and j identify the corresponding timestep and cell, respectively. All cells are of width Δx and spaced uniformly apart.

Equations by itself is written in the form

$$\frac{\partial \mathbf{h}}{\partial t} + \mathbf{g}\left(\mathbf{h}, \nabla \cdot \mathbf{h}\right) = \mathbf{S}\,, \tag{5.5}$$

where **h**, **g** and **S** represent a physical quantity that is conserved, a function of that quantity and its divergence, and a so-called source term, respectively [Bodenheimer et al., 2006]. Note, that **S** may very well equal to zero, as it does for Eq. 5.2 which indicates that mass is conserved. The source term describes how the physical quantity may change locally over time [Bodenheimer et al., 2006]. Especially the source term of Eq. 5.3, the momentum equation, is an entry point physical phenomena to generate a change in momentum. Such phenomena, like gravity, radiation pressure, etc., may be arbitrarily included by modifying the source term of the momentum equation.

LAGRANGIAN DESCRIPTION. The Euler-Equations (see Eq. 5.2 to 5.4) describe the evolution of a fluid at a fixed position while the fluid moves with respect to a resting coordinate system [Bodenheimer et al., 2006]. One can find an equivalent alternative description, where the coordinate system is co-moving to a given fluid-element [Bodenheimer et al., 2006]. This approach is widely referred to as the Lagrangian picture, contrary to the Eulerian picture discussed earlier [Bodenheimer et al., 2006]. The entire thesis builds on the Eulerian description such that further discussion of the Lagrangian picture is omitted.

NUMERICAL SOLUTION. One can find analytical solutions to the Euler-Equations in the case of a few simple problems. Unfortunately, simple problems rarely capture the full complexity the natural world has to offer, but understanding them allows us to build intuition for more complex settings. In the interest of tackling more complicated problems, one often turns to numerical approaches. Solutions are generated with the help of software opted to run on powerful machines, referred to as supercomputers. One particular example of such a program is the highly scalable and modular hydrodynamics code FLASH4 [Fryxell et al., 2000], which forms a huge building block of this thesis towards solving fluid dynamics in the Eulerian picture.

5.1.1

Finite Volume Method

Scope of application. The finite volume method (FVM) is a numerical approach towards solving partial differential equations numerically [Bodenheimer et al., 2006]. flash4 makes use of the FVM to model the evolution of fluids (see Eq. 5.2 to Eq. 5.4).

General approach. The general idea of the FVM is to generate several evaluation points inside a domain and associate sub-volumes of the domain with each evaluation point. Each sub-volume contains one, and only one, evaluation point, without any overlapping between any two sub-volumes. The entire sub-volume ensemble maps out the domain gaplessly, so no additional point inside the domain can be found without being contained inside a sub-volume. A single sub-volume may be referred to as a cell. Numerical fluxes describing the flow of conserved quantities are computed on the boundaries of cells with the help of Riemann solvers. The evaluation points are then evolved in time in incremental steps by integrating the contributions received from the fluxes of each cell. Two consecutive steps, t^n and t^{n+1}, are separated by a positive time interval, $\Delta t = t^{n+1} - t^n$, which may vary in length. The value of Δt is chosen such that the Riemann solver maintains accuracy and stability during its evolution. A suitable choice of Δt is given by the Courant–Friedrichs–Lewy condition [Courant et al., 1928].

Cubic 1D mesh as an example. Consider cubic cells, c_1, c_2, c_3, ... c_j, ... c_N in a one dimensional space with coordinates $x_j = x_0 + j\Delta x$ and conserved quantities $\mathbf{h}_j$ associated with a cell, c_j, as depicted in Fig. 7. Given a flux $\mathbf{f}^n_{j-1/2}$ that is directed into cell c_j at the boundary to cell c_{j-1} and a flux $\mathbf{f}^n_{j+1/2}$ that is directed outwards at the boundary to cell c_{j+1}, one can update the value of $\mathbf{h}^n_j$ by computing

$$\mathbf{h}^{n+1}_j = \mathbf{h}^n_j + \Delta t \frac{\mathbf{f}^n_{j-1/2} - \mathbf{f}^n_{j+1/2}}{\Delta x}\,, \tag{5.6}$$

where the superscript n denotes the association to a given timestep labeled n [Toro, 2013].

FVM in flash4. The hydrodynamics code flash4 uses a structured mesh FVM supporting spherical, cylindrical and cartesian coordinates. Within the scope of this thesis, the latter is used, while individual cells are taken to be cubic in 3D. In flash4 $8 \times 8 \times 8$ cells form a so-called block. Fig. 8 shows a single block (red) formed by 8×8 cells in two dimensions.

5.1.2

Adaptive Mesh Refinement

Motivation. This section is appositely motivated with cost-effectiveness in mind. While nothing may stop us from using arbitrarily many cells from the algorithm's perspective when studying a problem involving hydrodynamics, we will eventually encounter limitations due to using an actual computer to generate a numerical solution. One may be limited by the memory of the machine, which will only allow a certain number of cells to be calculated. Additionally, an increased number of cells will take longer for the computer to obtain a solution since the processor can only do a certain amount of instruction cycles per time, and each cell will take a certain number of instructions to be updated. So it is in the best interest to keep the number of cells present in the simulation as low as possible. Some regions are

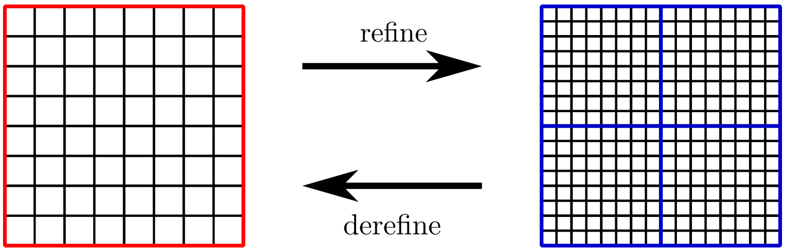

Figure 8: Illustration of the refinement and derefinement process for a block in $N = 2$ dimensions. A single block with eight cells along each dimension is shown on the left side. The red lines highlight the block boundaries. During a refinement process, cell sizes are halved in each direction creating 2^N blocks from the original block. The blue lines highlight each block created during a refinement process.

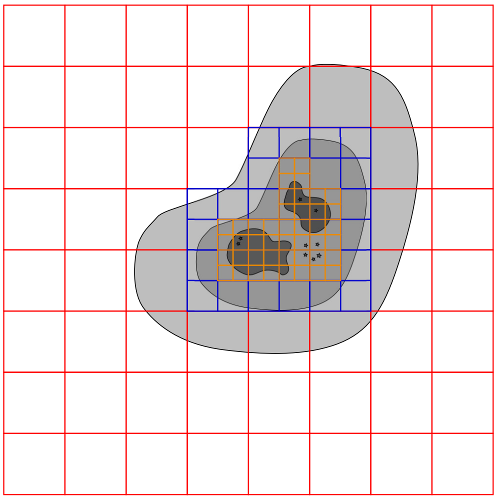

Figure 9: Schematic overview of applying adaptive mesh refinement in an astrophysical simulation. Refinement can be put selectively into regions of interest, which are marked by the grey shaded areas.

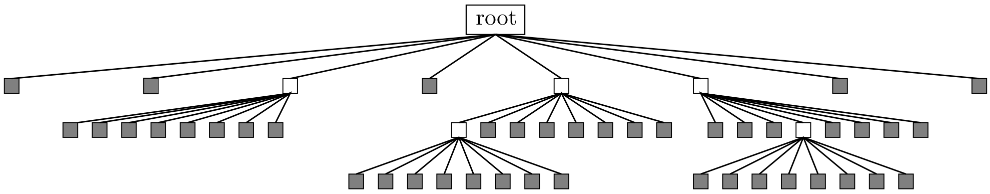

Figure 10: Sketch of an octree where data is organized hierarchically on different levels. The root node is labelled 'root' and has eight associated nodes, one level beneath. Each of those nodes may have additional eight children if so desired. Nodes without children are called leaf nodes and are shaded grey.

physically motivated and more interesting than others, depending on the question one is trying to answer. See, for example, Fig. 9 which schematically shows a cloud hosting a cluster of stars. In this instance, the stars and the denser regions can be considered to be of greater interest.

Approach. Allowing cells to be of different sizes allows selectively putting more cells in regions of interest, giving those regions a better refinement. This process is generally called adaptive mesh refinement (AMR). A block in flash4 can be replaced by eight blocks half the original size. This process is called refining. The opposite may also take place and is referred to as derefining. Both are shown in Fig. 8. Refining a block causes the newly spawned blocks to have half the original block length along one coordinate axis. During a simulation flash4 will dynamically refine and derefine regions in space, based on the local conditions. Fig. 9 shows how refinement is put selectively around the denser, darker grey coloured regions and the stars. The structure of the AMR is shown as an overlaid grid which gets finer as colours cycle through red, blue and orange. In this particular example, refinement is selectively put around denser regions and regions hosting stars.

5.1.3

Octree

Definition. An octree organizes data hierarchically in a tree-like way. Starting from a root and representing the entire data, the data may be subdivided into eight smaller chunks called nodes. Any of the nodes may be subdivided again recursively until the structure of the octree is satisfactory. Nodes that do not have children are often referred to as leaves, like the leaves on a tree that do not have any additional branches. Fig. 10 shows an octree. The root is shown at the top with eight nodes attached to it. The leaves are shaded in a dark grey, and nodes with children are shaded white.

Application. Octrees are well suited as a data structure for AMR grids discussed in 5.1.2. Given that a refinement of a block will spawn eight new blocks, one can translate this to attaching eight new nodes to an existing leaf node. In the event of a derefinement, one deletes the eight children of a node, such that said node becomes a leaf node. By doing so, the octree can dynamically adapt to the changing structure of the underlying AMR grid.

Space filling curve. In this particular instance, where the octree models some distribution in three dimensions, one often employs a space-filling curve. Such a curve will map out the entire three-dimensional space while taking only a one-dimensional parameter as an input. In addition, these curves can be designed to maintain the locality of the data, such that a small distance in the input will translate to a small distance in the generated output for two evaluation points. The hydrodynamics code FLASH4 uses the Morton space-filling curve for its octree that manages the AMR structure [Fryxell et al., 2000]. Within FLASH4, the leaf blocks of the octree are connected through the space filling curve allowing to conveniently distribute them among different processors.

5.2
MODELLING OF LONG RANGE INTERACTIONS

HYDRODYNAMICS VS LONG-RANGE. The equations of hydrodynamics are purely local in the sense that the equations themselves only depend on local quantities and their derivatives. This locality makes hydrodynamics relatively cheap to compute compared to long-range interactions (LRIs) such as gravity and RT. This section explains how LRIs are treated in this thesis.

5.2.1
GRAVITY

DIRECT SUMMATION. LRIs are difficult to compute in numerical simulations involving astrophysics due to their often costly time complexity. To further elaborate, one can consider gravitational interaction between mass elements in a numerical simulation. If one were to compute the gravitational acceleration of one cell, c_j, naively one has to sum over all force contributions caused by all other cells, $\{c_k | k \neq j, 1 \leq k \leq N\}$. Now, for a total number of cells, N, one needs to compute a total of $N \times (N-1)$ interactions in order to know the resulting force at every position. This approach gives a time complexity of $\mathcal{O}(N^2)$. The local force can then be considered by the momentum equation's source term (see, e.g., Eq. 5.3) to include gravity in a simulation. With gravity being essential in modelling the dynamics of astrophysical objects, one is interested in obtaining a fast way to compute gravitational effects.

UTILIZING A TREE. The algorithm of Barnes and Hut [1986] manages to reduce the time complexity to $\mathcal{O}(N \log(N))$ by computing the gravitational interactions between a given cell and nodes of a tree data structure. In the case of three dimensions, an octree (see §5.1.3) poses a suitable data structure. Wünsch et al. [2018] have implemented a similar tree-based approach to solve the problem of gravity in the hydrodynamics code FLASH4.

5.2.2
TREE-SOLVER AS AN ALL-PURPOSE TOOL

TREE-SOLVER APPLICATIONS. In addition to gravity, the work of Wünsch et al. [2018] allows to compute the optical depth along different lines of sight from everywhere inside the computational domain, named TREERAY/OPTICALDEPTH, which they based on a method named TREECOL [Clark et al., 2012]. With the optical depth at hand, one can model the extinction of external radiation affecting the local chemistry [Glover and Clark, 2012]. In a next step, Wünsch et al. [2021] developed the module TREERAY/ONTHESPOT enabling the computation of RT of ionizing radiation on the fly in numerical simulations. The method they developed is independent of the number of ionizing sources.

General approach of TreeRay. At its essence, TreeRay calculates the radiative flux received along different lines of sight (LOS) at every position in the simulation, called a target. TreeRay follows a reverse ray-tracing approach. The different LOS are generated by the HEALPix algorithm [Górski et al., 2005] such that each LOS occupies an equal area in the angular space of the unit sphere. Along each LOS, a ray is cast to which contributions are mapped. Data from the octree is taken and mapped onto the ray such that it fulfils the minimum required resolution. Finally, each ray is integrated, generating a flux or a similarly helpful quantity. Note that this general approach is effective in probing the computational domain and can be used to compute other effects of type LRI.

Importance for this thesis. This thesis builds on the work of Wünsch et al. [2018], and Wünsch et al. [2021] to expand the applicability of the TreeRay onto infrared radiative transport on dust. In addition, the ionizing and non-ionizing radiative flux will be used to account for radiation pressure in numerical simulations.

5.3
Radiative Transfer and Radiation Pressure

Radiation field. Solving RT is challenging. Conceptionally different approaches towards solving RT in numerical settings have been discussed in §4. Here, within this section, essential quantities important for RT are presented. One such quantity is the radiation intensity. It can be understood as a quantity defined everywhere in space and throughout time [Mihalas and Mihalas, 2013]. Further, this function holds a distribution for different directions and frequencies at every position [Mihalas and Mihalas, 2013]. RT deals with the evolution of the radiation field. The radiation intensity, $I(\mathbf{r}, t; \mathbf{n}, \nu)$, can be understood as the radiation field and describes the amount of energy, $\mathrm{d}E$, flowing through a surface, $\mathrm{d}\mathbf{S}$, per unit time, $\mathrm{d}t$, in a frequency interval, $[\nu, \nu + \mathrm{d}\nu]$, in a solid angle, $\mathrm{d}\omega$, in the following way

$$\mathrm{d}E = I(\mathbf{r}, t; \mathbf{n}, \nu)\mathrm{d}\mathbf{S}\cos(\alpha)\,\mathrm{d}\omega\mathrm{d}\nu\mathrm{d}t\,, \tag{5.7}$$

where α is the angle between $\mathrm{d}\mathbf{S}$ surface element and $\mathbf{n}$, the direction along which radiation travels [Mihalas and Mihalas, 2013]. From $I(\mathbf{r}, t; \mathbf{n}, \nu)$, one can compute the radiative flux, $\mathbf{F}(\mathbf{r}, t; \nu)$, measuring the net flow of radiation at a given position and the mean radiative intensity, $J(\mathbf{r}, t; \nu)$, describing the average intensity for randomly placed surface elements at a given position. Both quantities can be calculated as

$$\mathbf{F}(\mathbf{r}, t; \nu) = \oint_{4\pi} I(\mathbf{r}, t; \mathbf{n}, \nu)\mathbf{n}\,\mathrm{d}\omega\,, \tag{5.8}$$

$$J(\mathbf{r}, t; \nu) = \frac{1}{4\pi}\oint_{4\pi} I(\mathbf{r}, t; \mathbf{n}, \nu)\,\mathrm{d}\omega\,. \tag{5.9}$$

The quantities $\mathbf{F}(\mathbf{r}, t; \nu)$ and $J(\mathbf{r}, t; \nu)$ are useful to compute radiation pressure and radiative heating (see Eq. 2.13).

Time dependent radiative transfer equation. The equation by which $I(\mathbf{r}, t; \mathbf{n}, \nu)$ evolves is given by

$$\left(\frac{1}{c}\frac{\partial}{\partial t} + \mathbf{n}\cdot\nabla\right) I(\mathbf{r}, t; \mathbf{n}, \nu) = -\epsilon(\mathbf{r}, t; \mathbf{n}, \nu) I(\mathbf{r}, t; \mathbf{n}, \nu) + j(\mathbf{r}, t; \mathbf{n}, \nu)\,, \tag{5.10}$$

where ϵ is the extinction coefficient and j the emission coefficient [Mihalas and Mihalas, 2013]. The extinction coefficient, ϵ, can be attributed to absorption and scattering where both effects combined remove radiative intensity propagating along the direction, **n**. Generally, ϵ is dependent on the material through which radiation travels and for known absorption and scattering opacities, κ_{abs} and κ_{scat}, respectively, ϵ is calculated as

$$\epsilon = (\kappa_{\mathrm{abs}} + \kappa_{\mathrm{scat}})\rho \, , \tag{5.11}$$

where ρ is the mass density of the material through which radiation travels [Mihalas and Mihalas, 2013]. Here, both opacities have units of area per unit mass giving ϵ the unit of one over length. In Eq. 5.10, ϵ is dependent on space and time as well as the direction and the frequency of the radiation. These dependencies are directly inherited from the underlying material and its density as shown in Eq. 5.11. The very material removing radiative intensity along a path may also contribute radiative intensity towards it. Thermal emission along a path as well as scattering of incoming radiation into the direction of the path may increase I. Both effects can be summarized in the following way

$$j = j_{\mathrm{thermal}} + j_{\mathrm{scat}} \, , \tag{5.12}$$

$$j_{\mathrm{thermal}} = \kappa_{\mathrm{abs}}\rho\frac{\sigma}{\pi}T^4 \, , \tag{5.13}$$

$$j_{\mathrm{scat}} = \kappa_{\mathrm{scat}}\rho J \, , \tag{5.14}$$

where j_{thermal} and j_{scat} denote contributions caused by thermal emission and scattering towards the emission coefficient, respectively.

Radiative transfer in this thesis. For the development of the RT scheme in this thesis, the so-called infinite speed of light approximation is assumed. Here, c is approaching infinity such that the time derivative in Eq. 5.10 vanishes. A resulting drawback is the inability to model any time-resolved propagation of light and thus with this approach one ends up with the equilibrium solution. Given that a radiation source can potentially influence the entire domain with its radiation at an instant, this approximation is costly to realize numerically. Even more challenging is the fact that thermal emission or scattering generates additional sources that need to be considered to solve Eq. 5.10. However, this thesis will neglect scattering, focusing on thermal reemission. Further, thermal reemission is considered only for dust grains which pose the challenge that its emission and absorption characteristics are tied to its spatial distribution making dust a so-called diffuse source. In addition, dust may be located everywhere inside a computational domain, requiring an efficient algorithm to probe the spatial distribution of dust and infer a resulting radiation field from it. The algorithm generated in this thesis makes use of a tree-based approach as presented in 5.2.

Radiation pressure from flux. An elegant approach to understanding radiation pressure is given by the idea that radiation consists of photons in the particle picture where each photon carries momentum [Mihalas and Mihalas, 2013]. As a consequence of momentum conservation, interactions with radiation necessitate a change of momentum in the interacting part. This mechanism ultimately causes RP. A single photon of energy, E_{ph}, has a momentum of

$$D_{\mathrm{ph}} = \frac{E_{\mathrm{ph}}}{c} = \frac{h\nu_{\mathrm{ph}}}{c} \, , \tag{5.15}$$

where ν_{ph} and are the photon's frequency and Planck's constant, respectively. By combining individual photons, a radiative intensity can be constructed as an average rate of photons travelling along a direction inside a solid angle through a unit surface per unit time, each carrying E_{ph}. Thus, one receives the momentum rate associated with the radiative intensity as I/c. The connection of RP to the radiative flux is then given by Eq. 5.8. By integrating along all directions, an effective sum over all incident radiative intensities is computed. The net momentum per unit time streaming through a unit area at a given position is then given as

$$\mathbf{p}_{\mathrm{rad}} = \frac{\mathbf{F}}{c}\,. \tag{5.16}$$

6

RESEARCH QUEST

Massive star formation. The previous chapters have introduced the astrophysical phenomena of GMCs, the IMF and MSs. MSs form deeply embedded in MCs making observations difficult [see reviews by, e.g. Tan et al., 2014, Rosen et al., 2020]. Thus, in the interest of understanding the complex nature of MSF, numerical simulations play a vital role. Given the vast variety of feedback mechanisms involved in MSF, faithful modelling requires the development of novel methods to include these mechanisms in HPC simulations. This thesis is particularly aimed at modelling radiative processes and their role in MSF.

Radiation pressure boost. Radiation generates RP. Reprocessed radiation may generate a momentum boost caused by multiple interactions with, for example, dust [see, e.g. Krumholz et al., 2009, Hopkins et al., 2011, and others]. The role of RP has been studied on galactic scales [Krumholz and Thompson, 2012] and on smaller scales of clumps forming MSs [see, e.g. Rosen et al., 2019, Kuiper and Hosokawa, 2018, Ali, 2021]. Yet, the importance of RP is debated. To approach RP from an independent angle, a novel method to compute RP is developed in the course of this thesis.

Radiative transfer. One needs to treat RT to model RP faithfully. A perk of including RT in numerical simulations is studying the role of heating and cooling processes without making compromises by employing approximations. Such approximations can be justified in specific settings, for example, done by Omukai [2000b] to circumvent the expensive computation of RT. In their work, they base the cooling strength on local approximations. Moreover, in some settings, where radiation can escape almost freely, it is custom to employ cooling without any limitations Chon et al. [2021]. The RT method developed in this thesis is aimed at studying problems in numerical simulations that require solving RT.

Numerical development. The publication of §7 achieves a major step towards the goal of this thesis. It lays the foundation, by developing a scheme capable of computing radiation pressure from direct radiation and dust-reprocessed radiation. The scheme is capable of handling a great number of sources. In fact, every cell can be a radiation source. This makes the scheme inherently strong at computing the formation of clusters hosting massive stars involving many sources of radiation.

Application of the scheme. In this thesis, the application of the scheme focuses on the formation of a single star out of a collapsing core. The core has a mass of 150 $M_\odot$ and a radius of 0.1 pc. The setup makes it easier to assess the performance of the novel method by keeping the problem simple in the sense a single star dominates the scene. The setup, however, is still complex as the principal star interacts with its non-trivial surroundings composed of dust. The setup has been introduced in §7 and is expanded in the publication of §8 by taking into account different metallicities. The outcome of §8 shows that increased metallicity favors fragmentation and thus influences the multiplicity of the collapsing core. Further, ionizing feedback plays a subordinate role on the simulated scales compared to RP.

Further benchmarks. Finally in §9, the novel scheme is benchmarked against an independent method to assess its performance in computing RP. Both schemes are applied to the same density distributions which are the results generated in §8. In addition, theoretical estimates are compared to model the computed momentum boost. These models do not recover the momentum boost in the non-trivial density distributions. The formation of the disk reduces the momentum input to orders of unity in the proximity of the star.

7

TREE-BASED SOLVERS FOR ADAPTIVE MESH REFINEMENT CODE FLASH - III: A NOVEL SCHEME FOR RADIATION PRESSURE ON DUST AND GAS AND RADIATIVE TRANSFER FROM DIFFUSE SOURCES.

DESCRIPTIVE METADATA. This chapter forms the foundation of this thesis and presents a novel RT scheme to model absorption and reemission of infrared radiation by dust. The scheme is thoroughly presented within the first publication of this thesis in §7.1. The scheme is based on the preliminary work of Klepitko [2018] which failed to produce physically correct results when applied to setups including point sources representing stars in its original form. Details regarding the previous iterations of the scheme are explained in §7.2 including Ansätze that were tried to mitigate the unphysical behaviour. Optimizations towards a better memory footprint via shared memory are presented in §7.3. These optimizations were necessary to meet the demands of current HPC hardware and maintain a high core count per node.

7.1
Publication

A. Klepitko, S. Walch, R. Wünsch, D. Seifried, F. Dinnbier, and S. Haid. Tree-based solvers for adaptive mesh refinement code FLASH - III: a novel scheme for radiation pressure on dust and gas and radiative transfer from diffuse sources. MNRAS, 521 (1):160–184, May 2023. doi: 10.1093/mnras/stad385

Within the first publication of this thesis, I present a novel scheme to compute RT of infrared radiation from dust in numerical simulations on-the-fly. I implemented the scheme in the existing tree-solver TreeRay [Wünsch et al., 2018, 2021]. The scheme is novel, in the sense that it is the first and only scheme to this day that computes RT from diffuse sources via backwards ray-tracing, in particular from dust. I use the resulting infrared radiation-field to compute radiation pressure on dust as well as the resulting radiation field of ionizing radiation provided by the scheme of Wünsch et al. [2021] to compute RP on both dust and gas. Further, I improved the dust temperature calculation within an existing chemical network [Walch et al., 2015] by taking into account the infrared radiation field provided by the novel scheme. I crafted and performed tests to verify the scheme's accuracy and I employ the novel scheme in a star forming setup which I briefly analyse.

Contribution overview of Co-Authors
Prof. Dr. Stefanie Walch-Gassner provided helpful counseling in the design of the scheme, engaged in implementation discussions and edited the paper. Dr. Richard Wünsch, Dr. Daniel Seifried, Dr. František Dinnbier and Dr. Sebastian Haid helped me familiarize myself with the large code base initially, engaged in code review discussions later on and edited the paper. Within a peer-reviewed process, the referee, Dr. Joaki Rosdahl, gave valuable comments to improve the quality of the paper. All implementations, the data analysis and the underlying simulations where carried out by **Andre Klepitko**. The manuscript has largely been written by **Andre Klepitko**.

MNRAS **000**, 1–27 (2023) Preprint 25 June 2023 Compiled using MNRAS LaTeX style file v3.0

Tree-based solvers for adaptive mesh refinement code FLASH - III: a novel scheme for radiation pressure on dust and gas and radiative transfer from diffuse sources.

A. Klepitko[1★], S. Walch[1,2†], R. Wünsch[3], D. Seifried[1,2],
F. Dinnbier[4], S. Haid[1]
[1] *I. Physikalisches Insitut, Universität zu Köln, Zülpicher Str. 77, 50937 Köln, Germany*
[2] *Center for data and simulation science, University of Cologne, www.cds.uni-koeln.de*
[3] *Astronomical Institute, Academy of Sciences of the Czech Republic, Bocni II 1401, 141 31 Prague, Czech Republic*
[4] *Astronomical Institute, Faculty of Mathematics and Physics, Charles University, V Holešovičkách 2, 180 00 Praha 8, Czech Republic*

Accepted 2023 January 30. Received 2023 January 29; in original form 2022 April 19

ABSTRACT

Radiation is an important contributor to the energetics of the interstellar medium, yet its transport is difficult to solve numerically. We present a novel approach towards solving radiative transfer of diffuse sources via backwards ray tracing. Here we focus on the radiative transfer of infrared radiation and the radiation pressure on dust. The new module, TreeRay/RadPressure, is an extension to the novel radiative transfer method TreeRay implemented in the grid-based MHD code Flash. In TreeRay/RadPressure, every cell and every star particle is a source of infrared radiation. We also describe how gas, dust and radiation are coupled via a chemical network. This allows us to compute the local dust temperature in thermal equilibrium, leading to a significantly improvement over the classical grey approximation. In several tests, we demonstrate that the scheme produces the correct radiative intensities as well as the correct momentum input by radiation pressure. Subsequently, we apply our new scheme to model massive star formation from a collapsing, turbulent core of 150 $M_\odot$. We include the effects of both, ionizing and infrared radiation on the dynamics of the core. We find that the newborn massive star prevents fragmentation in its proximity due to radiative heating. Over time, dust and radiation temperature equalize, while the gas temperature can be either warmer due to shock heating or colder due to insufficient dust-gas coupling. Compared to gravity, the effects of radiation pressure are insignificant for the stellar mass on the simulated time scale in this work.

Key words: radiative transfer – radiation hydrodynamics – backwards ray tracing – dust cooling – massive star formation

1 INTRODUCTION

Radiation provides a channel through which energy and momentum may be transported independently from the flow of mass. This makes it an integral part of the physical processes of the interstellar medium (ISM). The impact of radiation ranges from peaceful processes such as line emission cooling, continuum radiation cooling and heating – to violently driven HII regions (Spitzer 1978) and radiation pressure (RP) driven outflows. This enables radiative processes to regulate the star formation efficiency both ways – increasing it through cooling processes, enabling gas to collapse, and decreasing it through explosive expansion resulting in the removal of gas. Especially in recent works, RP is discussed as a mechanism to limit star formation. Matzner (2002) argues that giant molecular clouds are supported by the feedback of their most massive stars. Sites of massive star formation are those with column densities greater than 0.1 $\mathrm{g\,cm^{-2}}$ (Tan et al. 2014). Thompson et al. (2005) discuss the importance of RP on galactic scales and argue that RP from dust acts as an anti-catalyst for the star formation rate in ultra-luminous infrared galaxies.

The combination of photoionization and RP is discussed by Kuiper & Hosokawa (2018) in the context of massive star formation, where they find that RP plays a role at later stages and may limit the final mass of a massive star. Rosen et al. (2019) find that RP may lead to cavities, which only

---

★ E-mail: klepitko@ph1.uni-koeln.de
† E-mail: walch@ph1.uni-koeln.de

© 2023 The Authors

allow for disk accretion onto the star at later stages. Eventually the mass flow onto the disk is cut off resulting in starvation of the disk and limiting the total accretion onto the star.

Solving radiative transfer (RT) numerically is difficult to accomplish, because RT can be considered a non-local problem to solve in the context of hydrodynamical simulations. This makes solving RT to a certain degree similar to the problem of solving gravity, where its numerical solution requires a lot of communication. However, unlike gravity, radiation may be shielded or reprocessed, rendering the problem even more difficult than solving gravity numerically. Recent improvements in computer hardware, ever-growing supercomputers, and the development of numerical methods enabled RT to be treated on the fly in state-of-the-art numerical simulations. Bisbas et al. (2015) show benchmarks of 11 independent approaches towards solving the D-type expansion of an HII region driven by a single source. This highlights the effort that is put into solving RT in current numerical codes.

The pioneering work of Levermore & Pomraning (1981) formulates a flux-limited diffusion (FLD) theory, of which core concepts are still used in state-of-the-art numerical simulations and codes today (e.g. Krumholz et al. 2007; Kuiper & Hosokawa 2018, and many others). Here, radiation is treated in the form of an energy density and evolved according to the diffusion equation. This formalism transforms RT into a local problem, which is beneficial from a computational perspective as very little communication is required during the computation. As a trade-off the timestep is limited through the speed of light. This limitation can be partially overcome in a reduced speed of light approximation.

M1 closure builds on the FLD method and introduces more accuracy to the solution by taking into account one more moment to advect its radiation energy density. This leads to M1 closure capturing shadows more accurate than FLD (Levermore 1984; Rosdahl & Teyssier 2015; Kannan et al. 2019). However, M1 closure may result in colliding flows of radiation if mulitiple sources are present (Menon et al. 2022). The work of Menon et al. (2022) employs a variable Eddington tensor method which greatly improves the result of the radiation field. Their algorithm, VETTAM, uses ray-tracing to compute the variable Eddington tensor in a hybrid characteristics approach.

A different approach to solving RT is ray tracing, where multiple rays are cast to probe the environment along different lines of sight. Ray tracing yields more accurate results in terms of shadow casting than moment methods. This is especially the case if the radiation originates from many pointlike sources, with the trade-off of being computationally more demanding compared to moment methods or FLD. Examples of ray tracing can be found in the works of Baczynski et al. (2015) and also Kim et al. (2018) where they solve the forward propagation of ionizing radiation based on the methods of Abel & Wandelt (2002). Forward ray tracing (FRT) may quickly become infeasible if the number of sources grows, limiting the applicability of FRT. For this reason FRT is not suited for modelling reprocessed radiation, because of the sheer number of sources involved i.e. each gaseous or dusty cell can be a source of radiation. Rosen et al. (2017) and Kuiper et al. (2020) use a hybrid solution where radiation originating from pointlike sources is modelled with FRT while the reprocessed radiation is modelled with FLD. The early work of Kessel-Deynet & Burkert (2000) shows a different approach to ray tracing, where they use backwards ray tracing to solve RT of ionizing radiation. Similarly, the work of Altay & Theuns (2013) shows an application of backwards ray tracing to treat ionizing radiation in the context of smoothed particle hydrodynamics. Another example can be found in the work of Grond et al. (2019) where a single ray from each point in space is cast to every source of radiation along which RT is solved. Their approach, named TREVR, merges sources and adaptively refines on extincting material to save on computational effort. Over all, TREVR scales with an ($N\ \log^2(N)$) relation. Following this approach calculations on taking into account emission from dust may become infeasible.

Wünsch et al. (2018) solve gravity in adaptive mesh refinement (AMR) simulations with a tree-solver operating on an octal-spatial tree (Octtree). In a next step, Wünsch et al. (2021) expand the method to treat ionizing radiation from pointlike sources in a backwards ray tracing approach, called TreeRay/OnTheSpot. This work will build on both these papers and will expand the applicability of TreeRay to treat reprocessed radiation from dust. Or more general, this work will explore solving radiative transfer from macroscopic sources via backwards ray tracing.

This work discusses three types of radiation: ionising radiation from point sources (e.g. stars), non-ionising radiation from point sources, and non-ionising radiation from dust. The transport of the first one is treated by the TreeRay/OnTheSpot module described in Wünsch et al. (2021), calculating its absorption by gas through the case B recombination and the gas heating. Here, we add the interaction of ionising radiation with dust, specifically, its radiation pressure on dust and gas. The absorption of ionising radiation by dust is neglected. The TreeRay/RadPressure module described here calculates the transport of the non-ionising radiation from point sources and from dust. Both types of the non-ionising radiation interact directly only with the dust. In the latter we assume that dust and gas are always dynamically coupled and the momentum inserted by the radiation pressure to the dust is immediately transferred to the gas.

This manuscript is structured as follows. In §2 we recall basics and simplifications on radiative transfer relevant to this work. In §3 we summarize the numerical methods used in this work followed by a detailed explanation of the novel radiative transfer scheme given in §4. We show tests verifying the correctness of the scheme in §5. We follow this up with two more sophisticated setups covering the expansion of an HII region in §6 and a star forming setup in §7.

2 SIMPLE, DUSTY RADIATIVE TRANSFER

In this section we briefly define the essentials of radiative transfer while focussing on dust. We employ simplifications to aid the speedup of the algorithm.

The radiative transfer equation for the frequency-dependent radiation intensity, I_ν, propagating along a unit vector, $\hat{\mathbf{n}}$, reads

$$\left(\frac{1}{c}\frac{\partial}{\partial t} + \hat{\mathbf{n}} \cdot \nabla\right) I_\nu = -a_\nu I_\nu + j_\nu, \quad (1)$$

where t, ν, a_ν and j_ν are the unit time, the frequency of the light and the extinction and emission coefficient, respectively (Mihalas & Mihalas 2013). In the following we will assume c to approach infinity in eq. 1. As a consequence, contributions from the time derivative vanish, such that one arrives at an equilibrium solution. By doing this, we can not model the propagation of light within a small time window $\mathrm{d}t$ accurately. However, given that the sound crossing time is much larger than the light crossing time on astrophysical scales, this is a reasonable approximation. Further we drop all frequency dependencies by introducing a Planck weighting.

By doing so we arrive at a formulation of eq. 1 that is greatly simplified, namely

$$\hat{\mathbf{n}} \cdot \nabla I = -aI + j\,, \tag{2}$$

where a and j are the Planck-weighted mean extinction and emission coefficient, respectively, and I is the total radiation intensity. We summarize

$$\begin{aligned} I &= \int_0^\infty I_\nu d\nu\,, && (3)\\ a &= \kappa_\mathrm{P}\rho\,, && (4)\\ j &= \frac{\sigma}{\pi}\kappa_\mathrm{P}\rho T^4\,, && (5)\\ \kappa_\mathrm{P} &= \frac{\int_0^\infty \kappa_\nu B_\nu \mathrm{d}\nu}{\int_0^\infty B_\nu \mathrm{d}\nu}\,, && (6) \end{aligned}$$

where κ_P, σ are the Planck mean opacity and Stefan-Boltzmann constant, respectively. Throughout this work, we employ the Planck mean dust opacity based on Semenov et al. (2003). The model description we choose is the same as stated by Krumholz & Thompson (2012):

$$\kappa_\mathrm{P}(T) = 10^{-1}\frac{\mathrm{cm}^2}{100\,\mathrm{K}^2\,\mathrm{g}} \times \begin{cases} T^2 & \text{for } T < 150\,\mathrm{K} \\ (150\,\mathrm{K})^2 & \text{else} \end{cases}\,. \tag{7}$$

In the following we drop the index P such that $\kappa := \kappa_\mathrm{P}$.

We define the radiative flux, $\mathbf{F}$, and the mean radiative intensity, $\bar{J}$, in the following way

$$\begin{aligned} \mathbf{F} &= -\oint_\mathcal{S} I\,\hat{\mathbf{n}}_\mathrm{rad}\,\mathrm{d}\Omega\,, && (8)\\ \bar{J} &= \frac{1}{4\pi}\oint_\mathcal{S} I\,\mathrm{d}\Omega\,. && (9) \end{aligned}$$

Here, $\hat{\mathbf{n}}_\mathrm{rad}$ is the radial unit vector pointing from the origin towards the surface of a unit sphere, $\mathcal{S}$, and $\mathrm{d}\Omega$ is the solid angle around $\hat{\mathbf{n}}_\mathrm{rad}$. The minus sign in Eq. 8 defines the flux in the opposite direction of $\hat{\mathbf{n}}_\mathrm{rad}$.

Note that our approximation for the radiative transfer scheme does not account for scattering. Hence, also the momentum of RP is caused only by first absorption and reemission by thermal photons but not by scattering. However, in the infrared regime the scattering albedo is very small (e.g. for the dust models of Weingartner & Draine 2001) and hence absorption and reemission events are significantly more frequent than scattering events.

2.1 Effective area of an infinitesimal volume of dust

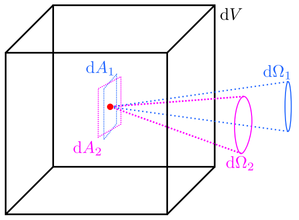

Figure 1. Schematic picture of an infinitesimal volume, $\mathrm{d}V$, from which radiation is emitted into solid angles, $\mathrm{d}\Omega_1$ and $\mathrm{d}\Omega_2$. The associated areas of the solid angles, $\mathrm{d}\Omega_1$ and $\mathrm{d}\Omega_2$, are labeled $\mathrm{d}\mathbf{A}_1$ and $\mathrm{d}\mathbf{A}_2$, respectively. The relation $|\mathrm{d}\mathbf{A}_1| = |\mathrm{d}\mathbf{A}_2|$ holds. The source radiates with $L^0_\Omega = \frac{\sigma}{\pi}T^4$ into every solid angle (see Eq. 12).

In this section we discuss the emission properties of dust in the context of three-dimensional emission. In the following, we argue that the effective area, $\mathrm{d}A$, from which dust inside an infinitesimal volume, $\mathrm{d}V$ of mass density ρ emits radiation into a solid angle $\mathrm{d}\Omega$, is given by

$$\cos\vartheta\,\mathrm{d}A\mathrm{d}\Omega = \kappa\rho\,\mathrm{d}V\mathrm{d}\Omega\,, \tag{10}$$

where ϑ is the angle between the surface normal of $\mathrm{d}A$ and solid angle $\mathrm{d}\Omega$.

Following Eq. 2, the decrease in radiation intensity as a function of distance from the radiation source is governed by the extinction coefficient. Both the effects of scattering and absorption contribute to a. If we neglect scattering, we can express a as the product of the mass density and the dust opacity (Eq. 4). Following its dimensionality, L^2M^{-1}, the dust opacity can be understood as an associated area per unit mass. It is the effective area through which dust interacts with radiation.

For the cubic, infinitesimal volume, $\mathrm{d}V = (\mathrm{d}r)^3$, filled with material of mass density ρ, we can express the contained mass as $\mathrm{d}m = \rho\,\mathrm{d}V$. A one-dimensional ray penetrating $\mathrm{d}V$ and traveling through its length, $\mathrm{d}r$, would act on an area $\mathrm{d}A = \kappa\,\mathrm{d}m = \kappa\rho\,\mathrm{d}V = (\mathrm{d}r)^2(\kappa\rho\,\mathrm{d}r)$. The last term

$$\tau = \kappa\rho\,\mathrm{d}r \tag{11}$$

represents the optical depth, τ, through the volume element. Here, in this instance, we only consider volumes which are so small that they are certainly optically thin (in the numerical implementation we separately treat optically thin and thick volumes; see §4).

At the same time, $\mathrm{d}A$ is the effective area from which thermal radiation is emitted by the volume into the path of the ray. Note, that $\mathrm{d}A$ is invariant under rotation, since the spatial distribution of dust within $\mathrm{d}V$ is assumed to be homogeneous (i.e. $|\mathrm{d}\mathbf{A}_1| = |\mathrm{d}\mathbf{A}_2| =: \mathrm{d}A$ in Fig. 1). For this reason, $\mathrm{d}V$ emits and absorbs radiation isotropically. Because of the isotropic emission behaviour of such a volume of dust, we can neglect the $\cos\vartheta$ factor as there always exists an area $\mathrm{d}\mathbf{A}$ which is normal to a choosen $\mathrm{d}\Omega$. This yields $\vartheta = 0$ and therefore $\cos\vartheta = 1$.

2.2 Thermal emission of an infinitesimal volume

We model the radiation of dust to be of thermal nature. Let $L^0_\Omega(T)\cos\vartheta\,\mathrm{d}A\,\mathrm{d}\Omega$ measure the luminosity of thermal radiation emitted from an effective surface element, $\mathrm{d}A$, at

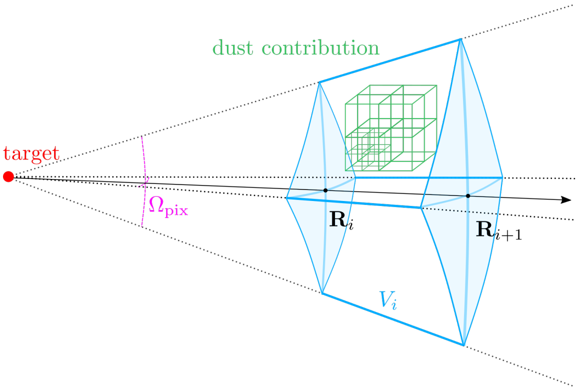

Figure 2. Graphical representation of a single HEALPIX ray. The ray is of angular size Ω_{pix} (pink) and has multiple evaluation points along its radial direction. One such evaluation point is labeled with i and has an associated distance $\mathbf{R}_i$ from the target point (black dot). The volume V_i (blue) associated with evaluation point i is bound by $\mathbf{R}_i$ and $\mathbf{R}_{i+1}$ in radial direction. The dust contributions (green) exist on an octree structure and can be mapped to rays adaptively.

temperature T into a solid angle $\mathrm{d}\Omega$. The following equation holds (Mihalas & Mihalas 2013):

$$L^0_\Omega\,(T)\cos\vartheta\,\mathrm{d}A\,\mathrm{d}\Omega \quad = \quad \frac{\sigma}{\pi}T^4\cos\vartheta\,\mathrm{d}A\,\mathrm{d}\Omega\,. \tag{12}$$

Combining eq. 10 and eq. 12 yields

$$L^0_\Omega\,(T)\,\kappa\rho\,\mathrm{d}V\,\mathrm{d}\Omega \quad = \quad \frac{\sigma}{\pi}\kappa\rho T^4\,\mathrm{d}V\,\mathrm{d}\Omega\,, \tag{13}$$

where σ is the Stefan-Boltzmann constant. Fig. 1 schematically shows how an area $\mathrm{d}\mathbf{A}_1$ represents a fraction of the surface area of $\mathrm{d}V$.
Since we aim to model radiative transfer from dust and we assume the dust to be distributed smoothly within $\mathrm{d}V$, we can use $\mathrm{d}A$ to model the emission from a small volume $\mathrm{d}V$.

3 NUMERICAL METHODS

We use the highly scalable code FLASH 4.3 (Fryxell et al. 2000) to solve the ideal hydrodynamics equations. The equations are solved with a directionally split scheme based on the 5-wave Bouchut solver HLL5R (Bouchut et al. 2007, 2010). Gravity is accounted for using the tree-based solver described in the work of Wünsch et al. (2018). Additionally, we include the treatment of ionizing (Wünsch et al. 2021) and non-ionizing radiation in this work. For the first time we present results from our backwards ray tracing infrared radiative transfer method, TREERAY/RADPRESSURE, implemented in FLASH4.3[1]. These numerical methods form the baseline upon which we will benchmark TREERAY/RADPRESSURE.

TREERAY/RADPRESSURE allows to compute radiation fields from both pointlike (e.g. stars represented by sink particles) and macroscopic sources (e.g. radiation from dust) taking into account absorption and emission on the fly. The latter is accomplished by allowing for every cell to be a source. With the radiation fields at hand we can treat the effects of radiation pressure and radiative heating and cooling through dust. Here, TREERAY/RADPRESSURE is coupled to a chemical non-equilibrium network (Nelson & Langer 1997; Walch et al. 2015). We explain the details of TREERAY/RADPRESSURE throughout section 4 and how we treat heating and cooling of gas through dust in section 4.6.

4 RADIATIVE TRANSFER ALGORITHM

The algorithm presented in this work builds on TREERAY (Wünsch et al. 2021) as a framework. The general approach uses backwards ray tracing to solve radiative transfer. For the algorithm to work efficiently, it is necessary that the information of the computational domain is stored in a volume dividing tree. To do this, we employ an octree in the current implementation. From each point of interest we cast rays aligned with the pixel defined by the HEALPIX algorithm (Górski et al. 2005). Fig. 2 illustrates the shape and components of a ray originating from a point of interest (target position, red dot). For each ray we map contributions to the ray based on their geometric intersection. The contributions are mapped on a node basis, as they naturally occur in an oct-tree. If the nodes appear larger than an angle, θ_{lim}, while being mapped to a ray, they are rejected and opened instead. This refinement process is repeated until we eventually reach leaves of the tree, in which case they are guaranteed to be accepted. In a final step we integrate the rays to obtain useful quantities. In our case we focus on dust, a macroscopic source potentially permeating the entire computational domain. Applications of TREERAY solving radiative transfer for ionizing radiation can be found in the works of Haid et al. (2018), Haid et al. (2019) and Dinnbier & Walch (2020).

In the general spirit of TREERAY, we will solve radiative transfer for infrared radiation with backwards ray tracing. The method consists of multiple conceptual parts: (1) we save necessary quantities on the tree (see §4.1); (2) we cast rays from our target point in order to probe the surroundings, tree-nodes are mapped to the rays (see §4.2); (3) we integrate individual rays (see §4.3); (4) perform final calculations after knowing results from all rays (see §4.4). In §4.5 we compute the momentum from our flux. The additional features presented in this work recover the same computational strong and weak scaling as presented in the work of Wünsch et al. (2021). A derivation of the performance was carried out by Grond et al. (2019) where they conclude a scaling of $N_{\text{sink}}\log(N)$, where N_{sink} and N are the number of sink particles and cells, respectively. In our scheme, the scaling is the same as in the work of Grond et al. (2019) except that N_{sink} is substituted by the number of cells, N.

The main goals of this module are to calculate both the acceleration caused by RP, $\mathbf{a}_{\text{RP}}$, projected onto the cartesian coordinates x, y, and z as well as the radiation intensity, J. The accelerations are stored in 3 fields within FLASH named `RPAX`, `RPAY` and `RPAZ` and have units cm s^{-2} each. We explain the calculation of $\mathbf{a}_{\text{RP}}$ starting in §4.1 and arrive at the final expression in §4.5. The calculation of the mean radiative intensity, J, which is stored in the field variable `IRXE` of units erg s^{-1} cm^{-2} sr^{-1}, is finalized in section §4.4. The directly deposited radiation pressure due to first absorption within a cell, $P_{\rm src}$, is stored in the field `PRAD` and has the units dyn cm^{-2}. We use this quantity to account for RP due to direct absorption of radiation from a point source (like a star) within a cell. The dust temperature, $T_{\rm dust}$, is stored in the field `TDUS` with units K.

---

[1] The method has been transferred to FLASH4.6 as well.

Due to the difference of radiation being emitted from an optically thin volume compared to that of an optically thick volume, we need to treat either case inherently separate. While optically thin material can radiate from its entire volume, optically thick material can only radiate from its surface. Since we use backwards ray tracing that adaptively refines the grid, we need to make simplifications, as the exact geometry of the material is unknown. For our simplifications we assume a complete mixing for the optically thin material and assume a compact geometry for optically thick material at given radial distances for the entire solid angle of the rays.

4.1 Tree build

Information about regions in space is stored in an oct-tree structure. We use the term *node* whenever we talk about data stored inside the tree. The nodes that represent the AMR grid at the highest local refinement are called *bottom nodes* (:= *b-node*). *Higher level nodes* (:= *h-node*) are all nodes that are not bottom nodes. By our definition, bottom nodes correspond to leaf nodes of a tree such that they have the highest resolution meaning that they resolve the smallest structures. On the other hand, higher level nodes correspond to branches of a tree structure, therefore offering less resolution.

4.1.1 Bottom nodes

We store different quantities on a b-node depending on the b-node being optically thin or thick. A node is labeled optically thin if its optical depth, $\tau_{\rm b-node}$, is less than 1 and optically thick otherwise. We calculate $\tau_{\rm b-node}$ for our nodes of cubic shape with volume $\mathrm{d}V = \mathrm{d}r^3$ as such:

$$\tau_{\rm b-node} = \rho\kappa \mathrm{d}r\,. \tag{14}$$

For an optically thin node we store:

$$\begin{aligned} L_{\rm b-node,\,thin} &= 4\sigma\rho\kappa(T_{\rm dust})^4 \mathrm{d}V, & (15)\\ \widetilde{A}_{\rm b-node} &= \rho\kappa \mathrm{d}V, & (16)\\ S_{\rm b-node} &= L_{\rm src,\,IR} \times e^{-\tau_{\rm b-node}/2}, & (17) \end{aligned}$$

where $L_{\rm b-node,\,thin}$ is the optically thin luminosity of the node and $\widetilde{A}$ is the associated area, $S_{\rm b-node}$ are luminosity contributions from pointlike sources like sink particles. $L_{\rm src}$ is the non ionizing luminosity of pointlike particles present in a bottom node (see eq. 70). The complement of the pointlike sources contributions is used to heat the node and added as a trapped radiation pressure. $\widetilde{A}$ can be interpreted as an associated area for a volume to interact with radiation analogue to the concept discussed in §2.1. Fig. 1 shows the associated area of an optically thin volume. Later on $\widetilde{A}$ will be used to compute extinction along the ray.

For an optically thick node we store:

$$\underline{L}_{\rm b-node,\,thick} = \frac{\sigma}{\pi}(T_{\rm dust})^4, \tag{18}$$

$\widetilde{A}_{\rm b-node}$ and $S_{\rm b-node}$, where $\underline{L}_{\rm b-node,\,thick}$ is the luminosity per area emitted from a solid black body into a solid angle. Note that we indicate the different units between the luminosities stored on optically thin and thick nodes by an underline (compare Eq. 15 and Eq. 18). In our implementation we toggle the bit responsible for storing the ±-sign of $L_{\rm b-node}$ in the memory to indicate whether a node is optically thin or thick on the bottom layer. By doing this we keep the memory footprint of the bottom nodes small by containing only 3 floats. This enhancement is doable because a negative luminosity is not meaningful in our scheme.

4.1.2 Higher level nodes

Higher level nodes are created by joining 8 subvolumes together into a bigger volume. We refer to a subvolume of a higher level node as a *sub-node*. The edge length of a node is twice that of its sub-node in our implementation.

We propagate the information from the bottom of the tree upwards to each h-node by summation over all subnodes. The details can be found in §A of the appendix. The quantities are stored separately for optically thin and thick material in h-nodes, so that we can trace the optically thin and thick content of L, $\widetilde{A}$ and V inside each h-node.

Each of the h-nodes holds $\mathbf{r}_{\rm COL}$ pointing from the geometric center of the h-node to its center of luminosity (COL). We find that taking into account $\mathbf{r}_{\rm COL}$ while mapping nodes helps improving errors introduced by coarsening at greater distances. Again the details can be found in §A of the appendix.

4.2 Ray mapping

Each target is equipped with a set of rays defined by the pixels generated by the HEALPix algorithm (Górski et al. 2005). We will distinguish the rays with the index h. The total number of rays is given by $N_{\rm pix}$. Note that each cell in our computation is considered to be a target point.

A single ray has multiple evaluation points along its direction, which will be labeled with the index i. Their spacing from the target, $\mathbf{R}_i$, grows quadratically. We choose this spacing because it is on par with the angular resolution criterion, where we satisfy that nodes are opened until they appear to be smaller than a certain angle. A more detailed discussion can be found in the work of Wünsch et al. (2021). The volume, V_i, associated with evaluation point i is the space between evaluation point i and $i+1$. Fig. 2 illustrates the shape of a ray and all the quantities just mentioned.

Two kernels in the form of lookup tables are used in order to map nodes to rays. First, the angular overlapping fraction, $\alpha_{\rm node}(h)$, of a node with a ray, h, is looked up in the corresponding kernel. The kernel holds montecarlo precalculated values for nodes of different node sizes at discrete angles ,$\vartheta_{{\rm fine},j}$ and $\varphi_{{\rm fine},j}$, and discrete distances, $R_{{\rm fine},\,j}$. These discrete coordinates are chosen such that they closely represent the true position of the node (i.e. by taking the closest matching discrete value for either value). The second kernel treats radial mapping. It ensures that quantities affected by the inverse square law stay conserved, when they are mapped from their true position, $\mathbf{r}_{\rm node}$, to an evaluation point at distance R_i. The kernel holds pre-calculated correction values for nodes at discrete distances $R_{\mathrm{fine},\,j}$. By choosing a large set of $R_{\mathrm{fine},\,j}$ we approximate the true correction factor, $\beta^*_{\mathrm{node}}(i)$, with, $\beta_{\mathrm{node}}(i)$, such that

$$\beta_{\mathrm{node}}(i) = \frac{R^2_{\mathrm{fine},\,j}}{R^2_i} \approx \frac{r^2_{\mathrm{node}}}{R^2_i} = \beta^*_{\mathrm{node}}(i). \tag{19}$$

For a given node at distance r_{node}, $R_{\mathrm{fine},\,j}$ is choosen so that

$$(R_{\mathrm{fine},\,j} < r_{\mathrm{node}}) \wedge (R_{\mathrm{fine},\,j+1} > r_{\mathrm{node}}) \tag{20}$$

hold. We allocate the radial kernel inside shared memory, because of its large size. This allows us to keep the memory footprint small while allowing for great precision.

We implement periodic boundary conditions during ray mapping by considering periodic copies of nodes. Out of all periodic copies, only the closest ones are considered. This treatment is analogous to that described by Wünsch et al. (2021).

4.2.1 Optically thin nodes

We correct inverse square law sensitive quantities in the following way:

$$\hat{L}_{\mathrm{node}} = \beta_{\mathrm{node}}\, L_{\mathrm{node}}, \tag{21}$$

$$\hat{A}_{\mathrm{node}} = \beta_{\mathrm{node}}\, \widetilde{A}_{\mathrm{node}}. \tag{22}$$

This way the flux seen from the luminosity $\hat{L}_{\mathrm{node}}$ at distance R_i approximates the flux seen from L_{node} at distance r_{node}. The same holds for $\hat{A}_{\mathrm{node}}$.

Each evaluation point, i, of a ray, h, holds

$$\hat{L}^h_{\mathrm{thin},\,i} = \sum^{\mathrm{nodes}(i)} \alpha_{\mathrm{node}}(h) \hat{L}_{\mathrm{node,\,thin}}, \tag{23}$$

$$\hat{A}^h_{\mathrm{thin},\,i} = \sum^{\mathrm{nodes}(i)} \alpha_{\mathrm{node}}(h)\, \hat{A}_{\mathrm{node}}, \tag{24}$$

$$\hat{V}^h_{\mathrm{thin},\,i} = \sum^{\mathrm{nodes}(i)} \alpha_{\mathrm{node}}(h)\, V_{\mathrm{node}}, \tag{25}$$

where nodes(i) describes the set of nodes mapped to evaluation point i. $\hat{L}^h_i$ can be understood as the total unextincted luminosity of segment i of ray h. In section 4.3 we will use $\hat{A}^h_i$ to compute the corrected luminosity of our segment i. V_{node} is the volume of the node volume (which is known).

4.2.2 Optically thick nodes

For optically thick nodes we map the following quantities to rays:

$$\hat{L}^h_{\mathrm{thick},\,i} = \sum^{\mathrm{nodes}(i)} \alpha_{\mathrm{node}}(h)\, \underline{L}_{\mathrm{node,\,thick}} V_{\mathrm{node}}, \tag{26}$$

$$\hat{A}^h_{\mathrm{thick},\,i} = \sum^{\mathrm{nodes}(i)} A_{\mathrm{node}}, \tag{27}$$

$$\hat{V}^h_{\mathrm{thick},\,i} = \sum^{\mathrm{nodes}(i)} \alpha_{\mathrm{node}}(h)\, V_{\mathrm{node}}, \tag{28}$$

$$\hat{Q}^h_{\mathrm{thick},\,i} = \sum^{\mathrm{nodes}(i)} \alpha_{\mathrm{node}}(h)\, \beta_{\mathrm{node}}(i)\, V_{\mathrm{node}}. \tag{29}$$

Similar to eq. 23, 24 and 25 in the optically thin case we map the luminosity, area and volume in the optically thick case as well. A fourth quantity is mapped, $\hat{Q}^h_{\mathrm{thick},\,i}$, which will later on be used to compute the angular size of the optically thick material. $\hat{Q}^h_{\mathrm{thick},\,i}$ is the only quantity that holds information about the inverse square law corretions concerning the treatment of optically thick nodes.

4.3 Ray integration

In the following we will benefit from eq. 2 being 1 dimensional and aligned with our radial direction. We will apply eq. 2 to integrate each ray individually from the inside out. For each ray segment, i, along a pixel, h, we will compute extinction (see section 4.3.1) and emission (see section 4.3.2) from thin and thick material. Finally we will obtain the radiative flux, $\mathbf{F}$, and mean intensity, $\bar{J}$, in section 4.4 below.

To simplfify, we focus on one ray and drop the labeling of individual pixels, h, throughout this section.

If optically thick material of a node is detected to be spread across 2 adjacent segments in radial direction, then those segments are merged to one segment instead. To account for errors introduced by the inverse square law, we multiply by the factor $T(i,j) = R^2_i/R^2_j$ before adding the inverse square law sensitive content of segment j into segment i. These quantities are $\hat{L}_{\mathrm{thin}}$, $\hat{A}_{\mathrm{thin}}$ and $\hat{Q}_{\mathrm{thin}}$. All other quantities are not affected by the inverse square law and can simply be added together during merging. This step is required, since we assume the optically thick material to take the shape of a compact object.

4.3.1 Optical Depth and Extinction

We assume that the optically thin matter is evenly mixed within one segment and spread over the whole volume of that segment. Together with the angular size of a ray, $\omega = 4\pi/N_{\mathrm{pix}}$, we can compute the optical depth of a ray segment i accounting for optically thin matter, $\tau_{\mathrm{thin},i}$, with the following equation:

$$\tau_{\mathrm{thin},i} = \begin{cases} 0\,, & \text{for} \quad i = 0 \\ \frac{\hat{A}_{\mathrm{thin},\,i}}{\omega R^2_i}\,, & \text{for} \quad i > 0 \end{cases}. \tag{30}$$

Concerning the optically thick matter, we assume that the volume forms a compact sphere. Assuming a perfect mixing for optically thick material is overestimating the luminosity output at greater distances drastically.[2] To be self-consistent with respect to previous assumptions, we compute the optical depth of the optically thick material, $\tau_{\mathrm{thick},i}$, of segment i by

$$\omega_{\mathrm{thick},i} = \min\left(\frac{\hat{Q}_{\mathrm{thick},i}}{\hat{V}_{\mathrm{thick},i}} \frac{(\hat{V}_{\mathrm{thick},i})^{2/3}}{R^2_i}, \omega \right), \tag{31}$$

$$\tau_{\mathrm{thick},i} = \begin{cases} 0\,, & \text{for} \quad i = 0 \\ \frac{\hat{A}_{\mathrm{thick},\,i}}{\omega_{\mathrm{thick},i} R^2_i}\,, & \text{for} \quad i > 0 \end{cases}. \tag{32}$$

Eq. 31 computes the angular size, $\omega_{\mathrm{thick},i}$, of our compact volume limited to be less or equal to the angular size of a ray, ω.

The ray is integrated starting from the target position

---

[2] Changing the shape of an optically thick body also changes its luminosity, as $L \propto A$ if a body is optically thick.

(see Fig. 2) going radially outwards. For the optically thin material we compute the extinction in the following way

$$\tau_{\mathrm{thin},\,0\to i} = \sum_{j=0}^{i-1} \tau_{\mathrm{thin},j}\,, \tag{33}$$

$$\epsilon_{\mathrm{thin},\,0\to i} = \exp(-\tau_{\mathrm{thin},\,0\to i})\,. \tag{34}$$

Concerning the extinction caused by the optically thick material we take into account its angular size. First we compute the fraction of a ray occupied by optically thick matter, $f_{\mathrm{thick},\,i}$, and its complement, $\bar{f}_{\mathrm{thick},\,i}$. Secondly we compute the cumulative effects of extinction of all segments between the target and segment i, $\epsilon_{\mathrm{thick},\,0\to i}$.

$$f_{\mathrm{thick},\,i} = \frac{\omega_{\mathrm{thick},i}}{\omega}\,, \tag{35}$$

$$\bar{f}_{\mathrm{thick},\,i} = 1 - f_{\mathrm{thick},\,i}\,, \tag{36}$$

$$\epsilon_{\mathrm{thick},\,0\to i} = \prod_{j=0}^{i-1}\left(\bar{f}_{\mathrm{thick},\,j} + f_{\mathrm{thick},\,j}\,\exp(-\tau_{\mathrm{thick},\,j})\right) \tag{37}$$

The combined extinction of optically thin and thick material working together is then straight forward computed by

$$\epsilon_{0\to i} = \epsilon_{\mathrm{thin},\,0\to i}\cdot\epsilon_{\mathrm{thick},\,0\to i}\,. \tag{38}$$

4.3.2 Emission

In this section we explain how we compute the flux at our target position arising from optically thin and thick material within each segment i. The equations stating the received flux (eq. 39, eq. 40 and finally eq. 41) already account for the self extinction within segment i.

The flux received from optically thin material without extinction from inner material is given by

$$F^{*}_{\mathrm{thin},i} = \frac{1-\exp(-\tau_{\mathrm{thin},i})}{\tau_{\mathrm{thin},i}} \times \frac{\hat{L}_{\mathrm{thin},i}}{4\pi R_i^2}\,. \tag{39}$$

Eq. 39 takes into account self extinction of the material inside segment i. We direct the reader to section B for discussion of the limits of eq. 39.

The flux received from optically thick material without extinction from inner material is given by

$$F^{*}_{\mathrm{thick},i} = \omega_{\mathrm{thick},i}\frac{\hat{L}_{\mathrm{thick},i}}{\hat{V}_{\mathrm{thick},i}}\,. \tag{40}$$

Finally we compute a linear combination of both source types based on the optical depth:

$$F^{*}_{i} = \frac{F^{*}_{\mathrm{thin},i}\cdot\hat{A}_{\mathrm{thin},i} + F^{*}_{\mathrm{thick},i}\cdot f_{\mathrm{thick},i}\hat{A}_{\mathrm{thick},i}}{\hat{A}_{\mathrm{thin},i} + f_{\mathrm{thick},i}\hat{A}_{\mathrm{thick},i}}\,. \tag{41}$$

In order to account for the extinction of the inner part, we use $\epsilon_{0\to i}$ from eq. 38 to compute

$$F_i = \epsilon_{0\to i}F^{*}_{i}\,. \tag{42}$$

and finally sum up over all evalutation points by taking the sum

$$F = \sum_{i} F_i\,. \tag{43}$$

F is now the final flux we receive from our pixel.

4.4 Ray finalization

After section 4.3 we know the flux received from each pixel, F^h (eq. 43). To compute the net flux, $\mathbf{F}$, at our target position we sum up all pixels taking into account the orientation of each ray, $\hat{\mathbf{n}}^h$. Note that $||\hat{\mathbf{n}}^h|| = 1$. Since the radiation is antiparallel with the ray, we have to introduce a minus sign. Finally we compute

$$\mathbf{F} = \sum_{h=1}^{N_{\mathrm{pix}}} -F^h\,\hat{\mathbf{n}}^h\,. \tag{44}$$

Similar, the mean intensity, $\bar{J}$, can be computed by summation over all pixels and by including the local heating intensity generated by a source, J_{src}. We summarize

$$J_{\mathrm{src,\,IR}} = \left(1-e^{-\tau_{\mathrm{b-node}}/2}\right)\frac{L_{\mathrm{src,\,IR}}V_{\mathrm{b-node}}}{V_{\mathrm{b-node}}^{2/3}V_{\mathrm{src}}}\,, \tag{45}$$

$$\bar{J} = \frac{1}{4\pi}\sum_{h=0}^{N_{\mathrm{pix}}} F^h + J_{\mathrm{src,\,IR}}\,, \tag{46}$$

where $\tau_{\mathrm{b-node}} = \rho\kappa\mathrm{d}x$ and $V_{\mathrm{b-node}}$ are the optical depth and volume of the bottom node containing the point source, respectively. Note that $J_{\mathrm{src}} = 0$ if the bottom node does not contain a source. We use $\bar{J}$ in order to heat the dust with radiation coming from surrounding material and point sources as explained in section 4.6. $\bar{J}$ is then stored in the field `IRXE` in units erg s^{-1} cm^{-2} sr^{-1}.

4.5 Momentum from Flux

The momentum equation reads

$$\frac{\partial\rho\mathbf{v}}{\partial t} + \nabla\left(\rho\mathbf{v}\otimes\mathbf{v} + (P + P_{\mathrm{src}})\right) = \frac{\kappa\rho}{c}\mathbf{F}\,, \tag{47}$$

where we obtain the trapped radiation pressure, P_{src}, as discussed below and the flux, $\mathbf{F}$, as discussed in section 4.4. ρ, $\mathbf{v}$, P, κ and c are the density, velocity, thermal pressure and speed of light, respectively. P_{src} is the radiation pressure that is generated by the absorption of radiation within the hosting bottom node of the point source. P_{src} is computed in the following way

$$P_{\mathrm{src}} = \left(1-e^{-\tau_{\mathrm{b-node}}/2}\right)\frac{L_{\mathrm{src}}}{cA_{\mathrm{src}}}\,, \tag{48}$$

where L_{src} and A_{src} are the luminosity and the area of the volume containing the source. Eq. 48 does not account for the multiscattering limit which is expected to boost RP by the optical depth for IR photons (see eg. Hopkins et al. 2011). Instead, Eq. 45 generates additional boosting of RP by heating the dust locally around the source in a given b-node and therefore increases the received flux for surrounding cells.

In the following we will explain how we compute the rate of momentum, $\dot{\mathbf{P}}$, absorbed by a cell of volume, $\mathrm{d}V$, from an incoming flux, $\mathbf{F}$. We assume the cell to be cubic with an edge length $\mathrm{d}x$. Density ρ and opacity of the cell are given by ρ and κ, respectively.

If the cell's optical depth, $\tau = \rho\kappa\mathrm{d}x$, is low so that we can neglect extinction within the cell, we can assume the flux through the cell to be constant. In that particular case $\dot{\mathbf{P}}$ can be computed as follows

$$\dot{\mathbf{P}}_{\tau<<1} = \frac{\mathbf{F}}{c}\,\kappa\rho\mathrm{d}V. \tag{49}$$

In the limit where the cell is optically thick, we must have

$$\dot{\mathbf{P}}_{\tau>1} \leq \frac{\mathbf{F}}{c}\,\mathrm{d}A, \tag{50}$$

where $\mathrm{d}A = (\mathrm{d}x)^2$ is the geometric surface of the cell.

One can compute $\dot{\mathbf{P}}$ in a scenario where $\mathbf{F}$ is not affected by the inverse square law and hits the cube face on. In this case we find $\dot{\mathbf{P}}$ can be expressed in the following way

$$\dot{\mathbf{P}} = \frac{\mathbf{F}}{c}\kappa\rho\frac{1-e^{-\tau}}{\tau}\mathrm{d}V\,. \tag{51}$$

Note that eq. 51 recovers booth limits mentioned by eq. 49 and eq. 50. Finally we store the acceleration, $\mathbf{a}_{\mathrm{RP}} = \dot{\mathbf{P}}/(\rho\mathrm{d}V)$, in x, y, and z direction in the fields `RPAX`, `RPAY` and `RPAZ`. Eq. 51 may be prone to under- and over-flows during its numerical evaluation. We approximate the fraction holding τ to be 1 if $\tau < 10^{-4}$.

The deposition of momentum by ionizing radiation onto dust is treated in an analogous manner. We receive a flux of ionizing radiation at our target position provided by TreeRay/OnTheSpot (Wünsch et al. 2021) and assume a constant kappa, $\sigma_{\mathrm{d}} = 1.5\times10^{-21}\,\mathrm{cm}^2$ per hydrogen atom, for UV photons. We explain the exact details of how gas and dust receive their momenta from ionized radiation in §C.

4.6 Heating and Cooling of Dust Grains

For each cell we compute the equilibrium temperature of dust by taking into account heating and cooling rates of dimension $\left[\mathrm{erg\,cm^{-3}\,s^{-1}}\right]$ for multiple physical processes. These processes are:

- $\Gamma_{\mathrm{dust-gas}}$: dust grain and gas collisional interactions (Hollenbach & McKee 1979, given by eq. 3.25 of theirs),
- Γ_{ISRF}: heating by an interstellar radiation field (Bakes & Tielens 1994, given by eq. 42 of theirs) which we set to 0 here,
- Γ_{H2}: heating from H_2 formation on grain surface (Hollenbach & McKee 1979; Glover & Mac Low 2007, their eq. 45),
- $\Lambda_{\mathrm{BB-cool}}$: cooling by thermal emission,
- $\Gamma_{\mathrm{BB-heat}}$: heating by thermal radiation.

We list the equations for $\Gamma_{\mathrm{dust-gas}}$, Γ_{ISRF} and Γ_{H2} in appendix D. During the dust temperature calculation we do not allow dust to cool beyond $T_{\mathrm{dust,\,floor}} = 2.7\mathrm{K}$.

The rates of the thermal radiative processes are modelled in the following way:

$$\begin{aligned}\Lambda_{\mathrm{BB-cool}} &= \rho\xi4\sigma\kappa T_{\mathrm{dust}}^4, & (52)\\ \Gamma_{\mathrm{BB-heat}} &= \rho\xi4\pi\kappa\bar{J}, & (53)\end{aligned}$$

where ρ and ξ are the density and dust to gas ratio respectively. Eq. 52 and eq. 53 together model cooling and heating due to thermal radiation accurately. In the limit, where we consider dust being embedded inside an optically thick medium, the mean intensity, J, will resemble the mean temperature of the surroundings. This is the temperature the dust will attempt to converge to. However, if the medium is optically thin along one or more HEALPix generated surfaces, $\bar{J}$ will have contributions of 0 K allowing the dust to cool and thus remove energy from the computational domain.

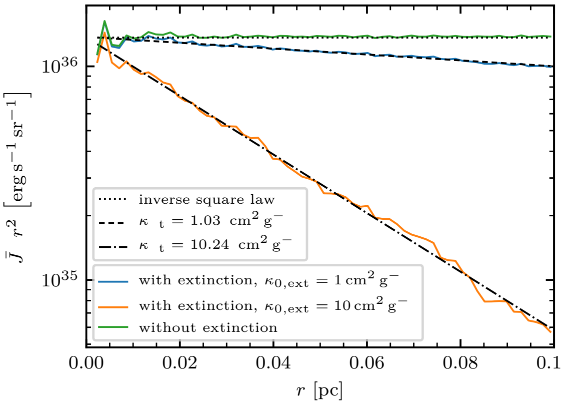

Figure 3. A single point source inside a homogeneous density medium. We compare three scenarios, two with extinction where $\kappa_{0,\,\mathrm{ext}} = 1\,\mathrm{cm}^2\,\mathrm{g}^{-1}$ (solid blue line) and $\kappa_{0,\,\mathrm{ext}} = 10\,\mathrm{cm}^2\,\mathrm{g}^{-1}$ (solid orange line) and one without extinction (solid green line). We show the mean intensity times the distance squared as a function of distance. Without extinction the inverse-square law is recovered. For the runs with extinction we fit an exponential to the simulation results

. We recover a dust opacity of $\kappa_{\mathrm{fit}} = 1.03\,\mathrm{cm}^2\,\mathrm{g}^{-1}$ and $\kappa_{\mathrm{fit}} = 10.24\,\mathrm{cm}^2\,\mathrm{g}^{-1}$ as shown by the dashed and dash-dotted lines.

In combination with the effects of $\Gamma_{\mathrm{dust-gas}}$, dust may drain energy from the gas and radiate it away given the right circumstances. These circumstances are given if the gas is substantially hotter than the dust temperature according to the mean radiatiave intensity, $\bar{J}$. We can assign a temperature to the radiation field by solving for the equilibrium between $\Lambda_{\mathrm{BB-cool}}$ and $\Gamma_{\mathrm{BB-heat}}$, which yields

$$T_{\bar{\mathrm{J}}} = \sqrt[4]{\frac{\pi\bar{J}}{\sigma}}\,. \tag{54}$$

5 BENCHMARK OF TREERAY/RADPRESSURE

We will present results of TreeRay/RadPressure and verify them against analytically known solutions. The tests performed within this scope include a single radiating point source (see §5.1), an optically thick blob of dust radiating thermal emission (see §5.2), dust chemistry (see §5.3) and a radiation pressure driven expansion of a bubble to verify the correct momentum deposition (see §5.4). We perform all tests with TreeRay set to 48 rays. Note that we perform an additional test in §7.6 with an increased number of rays using a more realistic setup of star formation.

5.1 Point source inside a homogeneous medium

We consider a point source with a luminosity of $5.7\times10^4\,L_\odot$ inside a $(0.1\,\mathrm{pc})^3$ computational domain of homogeneous density $\rho_0 = 10^{-18}\,\mathrm{g\,cm^{-3}}$. Background radiation is set to 0 K and the boundary conditions are isolated such that there is no effect from the ambient medium. We disable reemission from dust and only consider radiation from the principal source so that we can validate the radiative transfer for a single point source in a simplified way. We perform three runs with a constant dust opacity of $\kappa_{0,\mathrm{ext}} = 1\,\mathrm{cm}^2\,\mathrm{g}^{-1}$, $\kappa_{0,\mathrm{ext}} = 10\,\mathrm{cm}^2\,\mathrm{g}^{-1}$ and $\kappa_{0,\mathrm{no\,ext}} = 0\,\mathrm{cm}^2\,\mathrm{g}^{-1}$. The two groups of runs are labeled with and without extinction, respectively.

We expect the radial profile of the radiation field to follow a combination of the inverse square law and the Beer-Lambert law, namely

$$\bar{J} = \bar{J}_0 \times \frac{e^{-\tau}}{4\pi r^{-2}} \,. \tag{55}$$

Fig. 3 shows the mean radiative intensity times the distance squared, $\bar{J} \cdot r^2$, effectively disposing the effects of the inverse square law. Here, we expect the inverse square law to be a horizontal line as shown by the black dotted line. Our run without extinction is in agreement with the inverse square law, while the runs with extinction decreases exponentially according to the Beer-Lambert law. By fitting an exponential to the runs with extinction we recover the dust opacities with a value of $\kappa_{\mathrm{fit}} = 1.03\,\mathrm{cm}^2\,\mathrm{g}^{-1}$ and $\kappa_{\mathrm{fit}} = 10.24\,\mathrm{cm}^2\,\mathrm{g}^{-1}$, respectively. The dashed and dash-dotted lines in Fig. 3 show the fitted curves. Note that the momentum input is given by Eq. 51 which means that an accurate radiation field will yield the correct momentum input caused by radiation pressure in this test. This is because $\mathbf{F}$ and $4\pi\bar{J}$ can be considered to have the same magnitude, as the single point source is the only source of radiation. In our case we are overshooting the extinction by $\sim 3\,\%$ and thus underestimating the momentum input from our point source. This behaviour results from inaccuracies introduced by not tracking the material in front of the source accurately. Rather, all of the material including the source appear to be mixed inside each radial volume along the ray.

5.2 Optically thick blob of dust

In this section we want to show that the superposition of optically thin and thick contributions add up to the correct solution.

Let us consider a spherical, optically thick body with radius r_c and density $\rho_\mathrm{c} = 10^{-17}\,\mathrm{g\,cm}^{-3}$ at temperature $T_\mathrm{c} = 30\,\mathrm{K}$. The blob is placed inside a low density ambient medium with temperature $T_\mathrm{a} = 10\,\mathrm{K}$ and density $\rho_\mathrm{a} = 10^{-19}\,\mathrm{g\,cm}^{-3}$ and the background radiation temperature is set to zero. The density field of a blob with radial size r_c is given by the following equation

$$\rho\left(\mathbf{r}\right) = \begin{cases} \rho_\mathrm{c} & \text{if } r \leq r_\mathrm{c} \\ \rho_\mathrm{a} & \text{else} \end{cases} \quad , \tag{56}$$

where r is the distance measured from the centre of the blob. Such a scenario is difficult to handle for backwards ray tracing, as the geometric size of an optically thick object has to be tracked accurately, because the luminosity scales with area.

We realise 3 different blob sizes each inside a $(15\,\mathrm{pc})^3$ sized computational domain and label them S, M and L in an increasing order. The blobs S, M and L are of size 0.75 pc, 1.5 pc and 3 pc in diameter, respectively. For each blob size we perform a run taking into account emission and absorption from the surrounding ambient medium.

Fig. 4 shows $\bar{J}$ in a slice through $z = 0$ for S, M and L. The blobs are 2, 4 and 8 grid cells wide. The radiation field produced by the blob of hot dust are spherically symmetric in all three cases.

We perform two additional runs for S, which we label S^- and S^+. S^- is run without emission and absorption from the ambient medium, so that $\bar{J}$ as a function of distance approximately follows an r^{-2} profile, because the blob can be approximated by a point source at large distance. The run S^+ has an increased density of the ambient medium by a factor of 10. This causes the ambient medium to be optically thick on the length scale of the computational domain. We expect $\bar{J}(r)$ to converge to a value of 10 K, which is the equilibrium temperature, of greater distances. For the other runs, S, M and L, we expect the profile to drop below the $\bar{J}(T = 10\,\mathrm{K})$ value, because the outer regions cool radiatively since we set the background temperature to zero.

Fig. 5 shows the mean radiation intensity, $\bar{J}$, as a function of distance for our five runs. The black dotted line shows the analytic solution for a point particle with a luminosity corresponding to the central dense object in the run labelled S. The analytic expression we use to model the small blob of radius R_S is given by

$$\bar{J}_\mathrm{S}(r) = \frac{1}{4\pi}\sigma T^4 \frac{R_\mathrm{S}^2}{r^2} \,. \tag{57}$$

Additionally, black horizontal lines mark the values $\bar{J}(T = 10\,\mathrm{K})$ and $\bar{J}(T = 30\,\mathrm{K})$.We can see that the runs S, S^+ and S^- agree with the r^{-2} profile of the black dotted line for small distances. Note that S does not reach the full 30 K value of $\bar{J}$ because the core is only realised by $2 \times 2 \times 2$ cubic cells. Evaluating the radiation field at one of those 8 cells will create HEALPix pixel which are not populated with 30 K material so that we do not reach the full $\bar{J}(T = 30\,\mathrm{K})$ value. For greater distances only S^- follows the r^{-2} profile, while the ambient medium contributes additional radiation in the case of S and S^+ causing deviation. S^+ does enter the expected plateau phase in the ambient medium, similar to M and L which plateau in the optically dense core at $\bar{J}(T = 30\,\mathrm{K})$. However outside we do not see a flattening caused by the ambient medium for M and L.

From this test we conclude that the method of splitting material in optically thin and thick contributions (see section 4) converges to the correct $\bar{J}$ in an optically thick embedded case. Also note that the interior of the core remains at constant temperature, hence there is acceleration caused by radiation pressure, because $\mathbf{F} = 0$ is the case inside. Additionally, there is no trapped radiation pressure inside, since a source of radiation does not exist. Outside in close proximity, there is a region where we can model the blob to be a point source, such that $\mathbf{F} \propto r^{-2}\mathbf{e}_r$ is roughly satisfied. Further outwards, we reach a state where the ambient medium shields the radiation from the blob and dominates in emission. Again we find $\mathbf{F} = 0$ in that region.

5.3 Dust Chemistry

We show results from our method discussed in section 4.6 in this section. We setup a homogeneous density field of density $\rho_0 = 10^{-16}\,\mathrm{g\,cm}^{-3}$ at a gas temperature of $T_{\mathrm{gas}} = 2000\,\mathrm{K}$. Initially, the dust temperature is set to $T_{\mathrm{dust}} = 150\,\mathrm{K}$. The entire domain is $(30\,\mathrm{pc})^3$ at a resolution of $(8)^3$ grid cells.

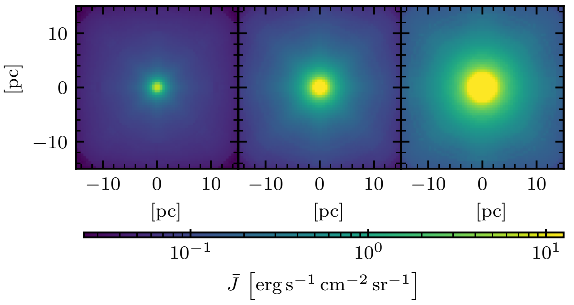

Figure 4. Slice through $z = 0$ of small (S), medium (M) and large (L) sized blobs with central temperature 30 K showing the mean radiation intensity, $\bar{J}$. The blobs are 2, 4 and 8 grid cells in diameter.

The background radiation field is set to $T_{\mathrm{BG}} = 0\,\mathrm{K}$. We disable any hydrodynamical evolution and focus on the interactions of dust and the non-equilibrium chemical network.

Dust tends to cool to the background temperature, $T_{\mathrm{BG}} = 0\,\mathrm{K}$, and is floored at 2.7 K. We use a dust to gas ratio of $\frac{1}{100}$. Heating of dust originates from dust-gas coupling given by $\Gamma_{\mathrm{dust-gas}}$ within this setup. In addition, emission of dust from elsewhere may contribute to the local $\bar{J}$ (see eq. 53) and partially stall the cooling process of dust.

Fig. 6 shows the temperature of dust and gas as a function of time for different densities, $f \times \rho_0$, where $f = 10^0, 10^{-2}, 10^{-4}, 10^{-5}, 10^{-7}, 10^{-10}$. At low densities dust and gas remain uncoupled and the dust quickly cools down to T_{min} while the gas remains warm. As the density increases, dust begins to have an impact on the gas temperature through the collisional interaction terms and vice versa. Gas and dust are heated by additional H_2 formation as the gas starts cooling down. As a function of density, the H_2 formation process happens on different timescales. Dust and gas remain at a temperature greater than 10 K as long as this process is ongoing in our test (see red, green and orange lines in fig. 6). Once this process has finished, the mixture of gas and dust is able to cool below 10 K (see orange line in fig. 6). In our test the H_2 formation is still ongoing for densities smaller than $\rho_0 \times 10^{-4}$ at the end of the simulation time resulting in temperatures between 19 K and 16 K. At densities greater than $\rho_0 \times 10^{-4}$ the formation of H_2 is completed before the simulation ends and thus the temperature is able to drop below 10 K. We show the H_2 fraction in E.

We conclude that the non-equilibrium chemical modelling may influence the dust and gas temperatures depending on the simulated timescale and densities. For example, chemical reactions may heat the gas, which may in return influence the dust temperature through collisional coupling. Thus, dust may also be indirectly heated by chemical reactions.

5.4 Radiation pressure driven bubble

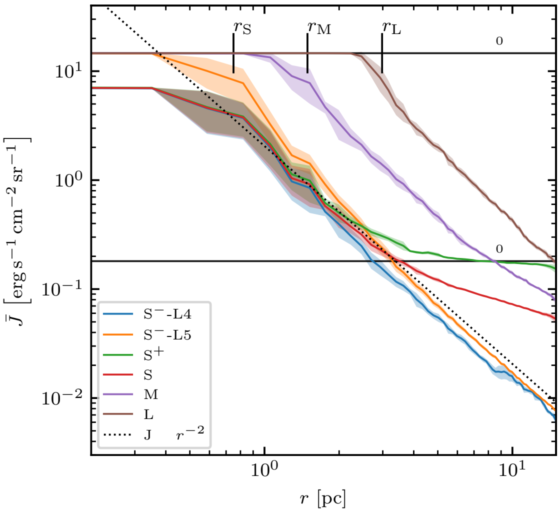

Figure 5. Radial average of the the mean intensity, $\bar{J}$, for different optically thick blobs of hot dust at $T_{\mathrm{dust}} = 30\,\mathrm{K}$ inside a 10 K cold optically thin medium. Small (S, red solid line), medium (M, purple solid line) and large (L, brown solid line) sized blobs with have a density of $\rho_{\mathrm{c}} = 10^{-17}\,\mathrm{g\,cm^{-3}}$. Three additional runs for the small blobs are shown, one where the background medium is turned optically thick (S^{+}, green solid line) and two where it is removed (S^{-}-L4, blue solid line, and S^{-}-L5, orange solid line). The run S^{-}-L4 is run at $(64)^3$ resolution and the run S^{-}-L5 at $(128)^3$. The shadows of the respective curves indicate the $1\,\sigma$ region. The black dotted line shows the Inverse-square law for an object of luminosity equal to that of model S. The black solid horizontal lines show the value of $\bar{J}$ corresponding to 30 K and 10 K, respectively. The vertical marks labeled r_{S}, r_{M} and r_{L} mark the radius of the blobs S, M and L, respectively.

In this section, we want to verify that the momentum injected through radiation pressure is correct. We consider a single point source of luminosity, $L = 1/8 \times 10^6\,L_{\odot}$, embedded inside a small compact spherical core of radius, $r_{\mathrm{core}} = 0.15\,\mathrm{pc}$, at density $\rho_{\mathrm{c}} = 1.08 \times 10^{-16}\,\mathrm{g\,cm^{-3}}$. The mass of the core is given as $M_{\mathrm{c}} = \frac{4}{3}\pi r_{\mathrm{c}}^3 \rho_{\mathrm{c}}$. The ambient density is $1.08 \times 10^{-28}\,\mathrm{g\,cm^{-3}}$. The entire setup is placed inside a $(3.0\,\mathrm{pc})^3$ sized computational domain so that the centre of the cloud, as well as the source are positioned in one of the corners. We set the faces adjacent to the source to be reflecting (see Wünsch et al. (2021) for details on the boundary condition). By doing so we only have to simulate 1/8 of the entire setup due to symmetry. The entire mass of the cloud is $M = 2.2 \times 10^4\,M_{\odot}$, where we also take into account the mass that is not actually simulated. Faces that are not reflecting have contributions of $T_{\mathrm{BG}} = 0\,\mathrm{K}$.

The source is expected to inject radial momentum per unit time at a rate of $\dot{p} = L/c$ given that all of its radiation is absorbed. If the line of sight from the source outwards is optically thin, we expect the rate to decrease by a factor $f(r) = 1 - e^{-\tau(r)}$, where $\tau(r)$ measures the optical depth along the line of sight from the source through a thin shell at distance r. The optical depth can be calculated as the product of the surface density, $\Sigma(r) = M/4\pi r^2$, and the dust opacity, $\kappa(T)$. We compute $\Sigma(r)$ by assuming that the cloud behaves like a thin shell, where all its mass is concentrated at a radial distance, $\bar{r}$, and distributed smoothly across the

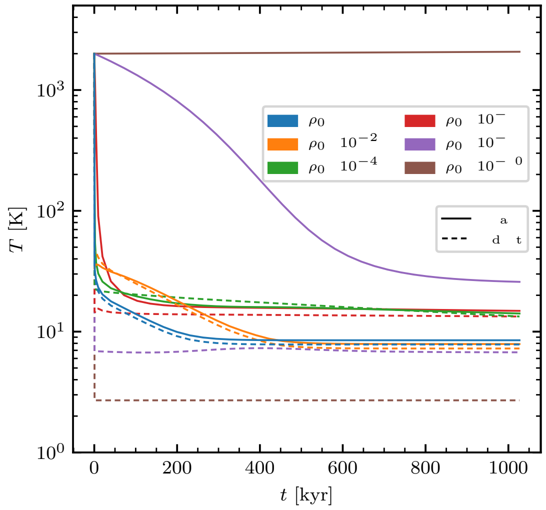

Figure 6. Dust temperature calculation showing the effects of dust cooling on the gas temperature. The initial gas temperature is set to 2000 K with $\rho_0 = 10^{-16}\,\mathrm{g\,cm^{-3}}$. The dust temperature is calculated according to §4.6. Dust tends to cool to $T_{\mathrm{dust,floor}} = 2.7\,\mathrm{K}$ radiatively but the gas dust coupling heats the dust, preventing the dust from reaching $T_{\mathrm{dust,floor}}$. Because $\Gamma_{\mathrm{dust-gas}} \propto \rho^2(T_{\mathrm{gas}} - T_{\mathrm{dust}})$ is the case, dust gas coupling is effective at high densities and high temperature differences. Thus in the early stage dust is able to impact the gas temperature more effectively due to larger differences in temperature. In the run $\rho_0 \times 10^{-10}$ the radiative cooling of dust is stronger than the gas-dust coupling and so that dust reaches $T_{\mathrm{dust,floor}}$.

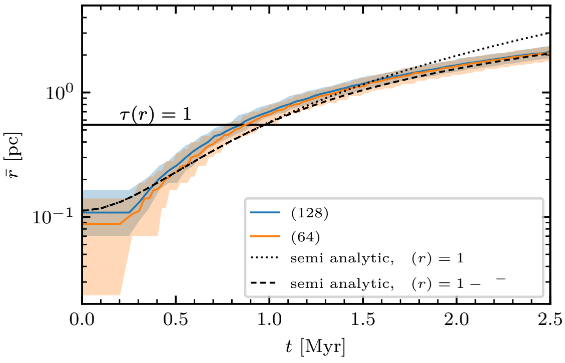

Figure 7. Mean radius of the shell, $\bar{r}$, vs. time of a single source driving a bubble through radiation pressure. The blue and orange solid lines show the numerical solutions obtained through TreeRay/RadPressure running with $(128)^3$ and $(64)^3$ cells, respectively. The black dotted and dashed lines show semi-analytic solutions of eq. 58 with $f(r) = 1$ and $f(r) = 1 - e^{-\tau(r)}$, respectively. For $f(r) = 1 - e^{-\tau(r)}$ (dashed line), radiation can escape the shell once it gets optically thin resulting in a momentum conserving phase above the $\tau(r) = 1$ line. The other case, $f(r) = 1$ (dotted line), does not account for leakage resulting in a greater $\bar{r}$ compared to $f(r) = 1 - e^{-\tau(r)}$.

entire angular space. The temperature, T, for $\kappa(T)$ is computed by solving for the equilibrium between the two rates given by eq. 52 and eq. 53.The equation of motion reads

$$\ddot{r} = f(r) \cdot \frac{L}{cM}, \tag{58}$$

where M denotes the mass of the shell.

Two black lines in Fig. 7 show the radius of the thin shell, $\bar{r}$, as a function of time for two numerically integrated solutions of Eq. 58. Both lines employ $f(r) = 1$ (black dotted line) and $f(r) = 1 - e^{-\tau(r)}$ (black dashed line), respectively. The two semi-analytic solutions deviate past the point, where $\tau(r) < 1$ (above black solid horizontal line). The initial radius of the thin shell has been set to match the center of mass along the radial direction for the cloud at $\frac{3}{4} r_{\mathrm{core}}$.

Additionally, we show two runs performed with TreeRay/RadPressure, where we use $(64)^3$ and $(128)^3$ cells for the simulated domain, respectively. For these runs, the radius is determined by taking the radial distance of maximum density along 48 rays. The rays are cast along different directions that originate from the source. We compute the mean among all the rays to determine the average radius, $\bar{r}$. Additionally, we estimate the error of the shell by also tracking the location of half the maximum density. The two locations in front and behind $\bar{r}$ are shown as shadows of both curves Comparing the analytical solutions, we find the solution taking into account leaking of radiation to match the computational results of TreeRay/RadPressure. With this, the radial momentum carried by the light may also escape, as very little is absorbed, since $\tau(r)$ tends towards 0 for large values of r. Here, the shell enters a momentum conserving phase as $f(r) = 1 - e^{-\tau(r)}$ approaches zero for decreasing τ.

6 EXPANDING HII REGION

This section features a D-type expansion of an HII region that is radiation pressure assisted. We compare the importance of the thermal driving caused by ionisation to the radiation pressure driving for two cases. In one instance, radiation pressure will play a minuscule role for the dynamics of the HII region and in the other instance, radiation pressure will play the dominating part. Either case will be run with radiation pressure turned off and on, respectively, to highlight a direct comparison. We use similar setups to those of Rosdahl & Teyssier (2015) in their §3.

For the setup, we initiate a single source inside a computational domain of homogeneous number density, n. The source radiates at a luminosity of L corresponding to a rate of $\dot{N}_{\mathrm{LyC}} = L/E_{\mathrm{LyC}}$ photons in the Lyman continuum, where $E_{\mathrm{LyC}} = 13.6\,\mathrm{eV}$. We place the ionizing source in one corner of the computational domain and set the boundary conditions of the cube to be reflecting on all faces connected to said corner. Table 1 summarizes the parameters we use for our simulations. Radiation pressure from non-ionizing radiation is neglected and turned off. In addition, we reduce the density of cells within a distance of 2 grid cells of the source by a factor of 100. This is to ensure that an HII region is spawned immediately, since TreeRay/OnTheSpot can not resolve the R-type expansion of an HII region. In particular, the Strömgren-radius must exceed one grid cell

Table 1. This table organizes the parameters used in §6 across the two different setups in rows. The symbols n, L and t_f represent the number density, luminosity and normalization time, respectively. The variables r_D and r_RP are the radii the ionisation front will expand to based on the effects of D-type and RP driven expansion, respectively. Both setups run with RP turned on and off. The normalisation of time, t_f, is calculated as explained in eq. 65.

Case	$n\ \left[\mathrm{cm^{-3}}\right]$	$\dot{N}_\mathrm{LyC}\ \left[\mathrm{s^{-1}}\right]$	$L\ [L_\odot]$	r_RP [pc]	r_D [pc]	t_f [Myr]
D-type dominated	10^3	10^{49}	5.64×10^4	1.86	1.64×10^1	9.2
RP dominated	10^9	10^{52}	5.64×10^7	5.87×10^{-2}	1.64×10^{-2}	0.014

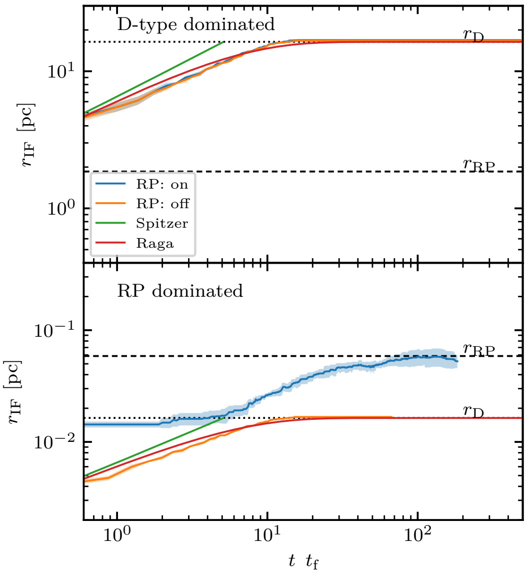

Figure 8. Radius of the ionisation front, r_IF, measured from the central source vs normalised time. The blue and orange lines show the runs with and without radiation pressure, respectively. The green line shows the Spitzer solution. The black dashed and dotted horizontal lines show the expected radiation pressure and ionisation driven radii r_RP (eq. 61) and r_D (eq. 64), respectively. The red line is the numerical solution to eq. 8 of Raga et al. (2012). The upper and lower panel show the case where D-type and RP are dominating, respectively.

for an HII region to spawn. We set the number of rays within TreeRay to be 48 and $T_\mathrm{BG} = 0\,\mathrm{K}$.

The Strömgren radius (Strömgren 1939) is given by

$$R_\mathrm{s} = \left(\frac{3\dot{N}_\mathrm{LyC} m_\mathrm{p}^2}{4\pi\alpha_\mathrm{B} X^2 \rho_0^2}\right)^{1/3}, \tag{59}$$

where m_p, $\alpha_\mathrm{B} = 2.5\cdot10^{-13}\,\mathrm{cm^3\,s^{-1}}$ and X are the mass of a proton, the case B recombination rate and the mass fraction of hydrogen in the neutral medium (Wünsch et al. 2021), respectively. The equation of motion for an ionisation front expanding into a neutral homogeneous medium through time, t, is given by the Spitzer solution, namely

$$r_\mathrm{i} = R_\mathrm{s}\left(1 + \frac{7}{4}\frac{c_\mathrm{i} t}{R_\mathrm{s}}\right)^{4/7}, \tag{60}$$

where r_i measures the radius of the ionisation front and c_i the sound speed of the ionised medium.

One can express equilibrium radii at which the driving through radiation pressure and thermal expansion stalls, similar to the work of Rosdahl & Teyssier (2015). The radiation pressure is expected to be in pressure balance, if the thermal ambient medium pressure, $P_{\mathrm{T}_0} = n_0 k T_0$, is comparable to that of the radiation pressure at the bubble surface, $P_\mathrm{RP} = L/4\pi c r_\mathrm{RP}^2$. Here, n_0, k, T_0 and r_RP are the number density and temperature of the neutral medium, the Boltzmann constant and the radius of the radiation pressure bubble, respectively. In that case we find the radius to be

$$r_\mathrm{RP} = \sqrt{\frac{L m_\mathrm{p}\mu_0}{4\pi c \rho_0 k T_0}}. \tag{61}$$

A similar argument can be used to determine the final radius of the HII region driven by its D-type expansion. We expect the bubble to expand until the pressure between the ionised and neutral medium are equal, $P_\mathrm{i} = P_0$. This relation is given by

$$n_\mathrm{i} T_i = \frac{\rho_\mathrm{i}}{\mu_\mathrm{i} m_\mathrm{p}} T_\mathrm{i} = \frac{\rho_0}{\mu_0 m_\mathrm{p}} T_0 = n_0 T_0\,, \tag{62}$$

$\rho = m_\mathrm{p} n \mu$, μ and T are the mass density, mean molecular mass and temperature, respectively, and we label the ionised and neutral medium with the subscript i and 0. Our source is able to keep a specified amount of hydrogen atoms ionised, according to eq. 59. Using eq. 59 and solving for the expected ionized number density, $n_\mathrm{i} = \rho_0/(m_\mathrm{p}\mu_\mathrm{i})$, yields

$$n_\mathrm{i} = \frac{1}{X\mu_\mathrm{i}}\sqrt{r_\mathrm{D}^{-3}\frac{3\dot{N}_\mathrm{LyC}}{4\pi\alpha_\mathrm{B}}}\,. \tag{63}$$

We can use this constraint to express n_i in terms of a corresponding radius, r_D, for the equilibrium radius of the HII region driven by heating through ionization. By combining the pressure constraint given by Eq. 62 and the ionized number density, n_i, from Eq. 63, we arrive at

$$r_\mathrm{D} \quad = \quad \left(\frac{T_\mathrm{i}}{T_0}\frac{\mu_0}{\mu_\mathrm{i}}\right)^{2/3} R_\mathrm{s}|_{\rho_0}\,. \tag{64}$$

We find a slightly altered description taking into account the mean molecular weight of the neutral and ionised species in our calculations (compare their eq. 65 to our eq. 64).

We construct two cases corresponding to $r_\mathrm{D} > r_\mathrm{RP}$ and $r_\mathrm{RP} < r_\mathrm{D}$ where we turn RP on and off for each instance. We expect the presence of RP to have no effect on the run where $r_\mathrm{D} > r_\mathrm{RP}$ holds. On the other hand, we expect RP to drastically change the outcome of the runs where $r_\mathrm{RP} > r_\mathrm{D}$.

Fig. 8 shows the radial distance of the ionisation front, r_IF, vs. time for our different setups using TreeRay/RadPressure. We determine r_IF as the mean distance along multiple rays aligned with the HEALPix algorithm. The time is normalised by

$$t_{\rm f} = \frac{r_{\rm D}}{c_{\rm i}}, \tag{65}$$

where $c_{\rm i}$ is the sound speed of the ionised medium. The top panel shows the runs where the expansion is thermal pressure dominated (i.e. $r_{\rm D} > r_{\rm RP}$). Both runs, regardless of RP being present, show almost identical dynamics of the ionisation front in the upper panel. This is because, the dominating effect is the D-type expansion itself. Their solution follows the solution of Raga et al. (2012) and converges to the limit given by $r_{\rm D}$. The Spitzer solution is capped at $r_{\rm D}$ (dotted line) which corresponds to the D-type expansion radius from the semi-analytical solution by Raga et al. (2012) (red line). The lower panel shows the RP dominated setup. The run with RP expands more quickly and further than the run without RP. The run without RP stalls at a size in agreement with the solution of Raga et al. (2012). The run with RP in the lower panel reaches a final radius matching $r_{\rm RP}$ given by Eq. 61 and has clearly surpassed the limits provided by $r_{\rm D}$ and the solution of Raga et al. (2012).

7 STAR FORMING SETUP

In this section, we show results from a molecular clump undergoing gravitational collapse where we form stars self-consistently. The setup is a similar setup to the one presented by Rosen et al. (2019), except for the initial turbulent velocity field.

7.1 Initial Conditions

We model the evolution of a $150\,{\rm M}_\odot$ massive molecular clump with an initially seeded turbulent velocity field with a power spectrum, $P(k) \propto k^{-2}$, such that the clump is subvirial with a virial parameter of $\alpha = 0.14$. The density, ρ, follows a radial power-law profile of $\rho(r) \propto r^{-1.5}$ up to an outer cloud radius of 0.1 pc. The free fall time of the core is $t_{\rm ff} = 42.3$kyr. The cloud is pressure confined by a hot low density ambient medium of temperature $T_{\rm amb} = 2000\,{\rm K}$ such that the density of the ambient medium is a factor of 100 lower than the density at the edge of the cloud. The gas temperature is set to 20 K throughout the cloud. The entire setup is housed inside a $(0.4\,{\rm pc})^3$ computational domain with von Neumann boundary conditions, allowing for matter to flow in and out smoothly. We set the background infrared radiation field to $J_{\rm BG} = 1.205 \cdot 10^{-2}\,{\rm erg\,s^{-1}\,cm^{-2}\,sr^{-1}}$ which corresponds to an equilibrium dust temperature of $T_{\rm BG} = 5\,{\rm K}$.

We start with a base resolution of $(128)^3$ for the density and use 48 rays within TreeRay. We adaptively refine the grid to ensure that the Jeans length is refined by at least 8 grid cells following the conditions of Truelove et al. (1997) to prevent artificial fragmentation. We allow for up to 5 additional levels of refinement such that the highest resolution of this simulation is 20 AU. If the Jeans length is refined by 16 or more cells, we derefine. Condensations within our core arise self-consistently through gravitational collapse. Eventually, they may form sink particles.

7.2 Sink Formation and Radiation from Protostars

We only allow sink formation for cells with densities greater than $\rho_{\rm thresh} = 5.2 \times 10^{-14}\,{\rm g\,cm^{-3}}$ which corresponds to 4 grid cells per Jeans-length (Truelove et al. 1997) at the highest resolution, 20 AU. We employ additional criteria for sink formation following Federrath et al. (2011) and Clarke et al. (2017). These criteria are listed below. All volumes, $V_{\rm sink}$, which have a density greater than $\rho_{\rm thresh}$ qualify to form sink particles. We set $\rho_{\rm thresh}$ to be the Jeans density for a Jeans length corresponding to 4 grid cell sizes at highest refinement, fulfilling the conditions of Truelove et al. (1997). Additionally, we allow for the formation of a sink particle inside $V_{\rm sink}$ if and only if all of the following conditions are met:

(i) $V_{\rm sink}$ is on maximum refinement,
(ii) $V_{\rm sink}$ is free of sink particles,
(iii) gas inside $V_{\rm sink}$ is infalling,
(iv) $V_{\rm sink}$ is located on a gravitational potential minimum,
(v) gas inside $V_{\rm sink}$ is gravitationally bound,
(vi) gas inside $V_{\rm sink}$ will collapse within its own free fall time before it has the chance of being accreted by another sink particle (see Clarke et al. (2017), their eq. 4 and 5).

Conditions (i) to (v) are taken from Federrath et al. (2010) and condition (vi) has been taken from Clarke et al. (2017). We find that (vi) substantially reduces the number of sinks formed in accordance with Clarke et al. (2017).

We allow sink particles to model protostars, where we use the implementation of Klassen et al. (2012) on GitHub[3]. From the model we obtain an internal luminosity, $L_{\rm int}$, as well as an accretion luminosity, $L_{\rm acc}$. We assign each of these luminosities, $L_{\rm int}$ and $L_{\rm acc}$, a temperature, $T_{\rm int}$ and $T_{\rm acc}$, respectively, in the following way

$$T_{\rm int} = \left(\frac{L_{\rm int}}{\sigma 4\pi r_{\rm star}^2}\right)^{1/4}, \tag{66}$$

$$T_{\rm acc} = \left(\frac{L_{\rm acc}}{f_{\rm filling}\sigma 4\pi r_{\rm star}^2}\right)^{1/4}, \tag{67}$$

where $r_{\rm star}$ and $f_{\rm filling}$ are the stellar radius and the fraction of the area of the star upon which the star is accreting. We obtain $r_{\rm star}$ from the protostellar model and set $f_{\rm filling} = 0.1$ (Calvet & Gullbring 1998). Finally we split each luminosity, $L_{\rm X}$ (where X = int or X = acc, based on its temperature, $T_{\rm X}$, to contribute towards ionizing radiation with a fraction, $\gamma(T_{\rm X})$, and its complement, $(1 - \gamma(T_{\rm X}))$, to contribute towards non ionizing radiation. We compute the fraction $\gamma(T_{\rm X})$ by computing the ratio of luminosity emitted in the Lyman band and the bolometric luminosity at temperature $T_{\rm X}$. This is computed as such

$$\gamma(T_{\rm X}) = \frac{\int_{\nu_{\rm LyC}}^{\infty} {\rm d}\nu B_\nu(T_{\rm X})}{\int_0^{\infty} {\rm d}\nu B_\nu(T_{\rm X})}, \tag{68}$$

where $\nu_{\rm LyC}$ marks the lower frequency of the Lyman continuum, and B_ν is Planck's law of black body radiation.

---

[3] https://github.com/mikhailklassen/protostellar_evolution

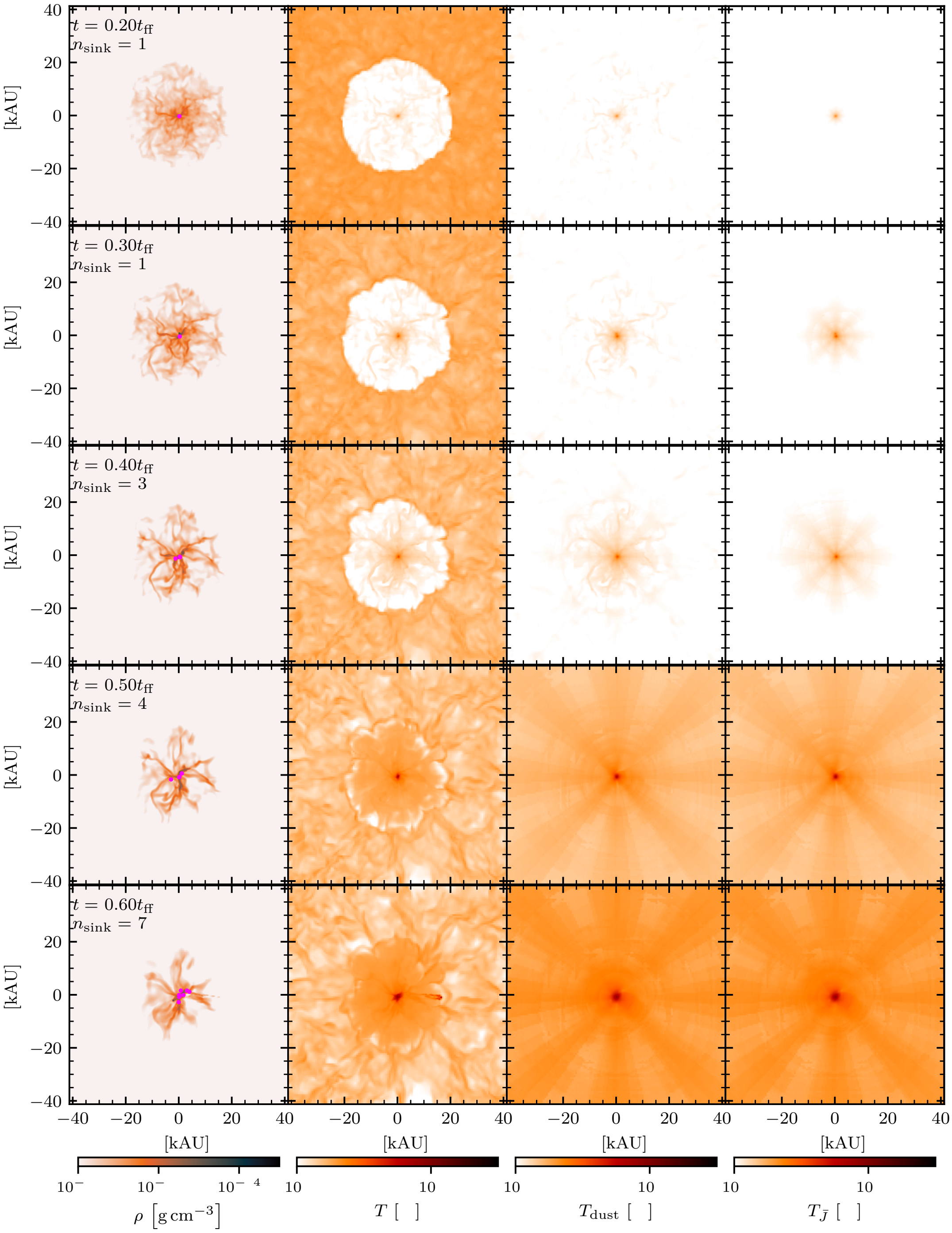

Figure 9. Slices through $z = 0$. Organized in rows we show from left to right density, gas temperature, dust temperature and radiation temperature across different times. The time, t, is measured in free-fall times, $t_{\mathrm{ff}} = 42.3\,\mathrm{kyr}$. The number of sink particles present is labeled n_{sink}. This figure pertains to the SF core setup of §7.

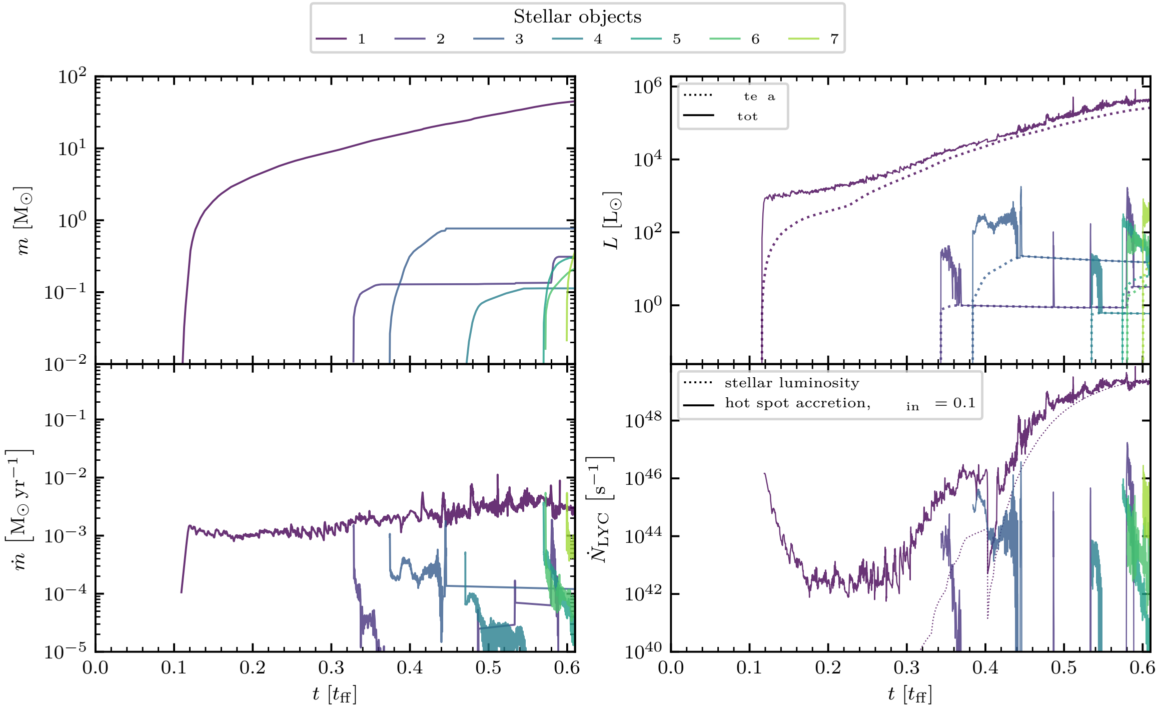

Figure 10. We show the mass, m, luminosity, L, accretion rate, $\dot{m}$, and rate of ionizing photons, $\dot{N}_{\rm LYC}$, vs time in this plot. In total we form 7 stellar objects represented by sink particles. The most massive star, labeled 1, forms early on embedded in the center (see Fig. 11) It is the most massive star (see left upper panel) and the dominating source of radiation (see upper right panel) throughout time.

In total one can state the ionizing luminosity, $L_{\rm src,\,UV}$, and the non-ionizing luminosity, $L_{\rm src,\,IR}$, of a sink particle as:

$$L_{\rm src,\,UV} = \gamma(T_{\rm int})L_{\rm int} + \gamma(T_{\rm acc})L_{\rm acc}\,, \tag{69}$$

$$L_{\rm src,\,IR} = L_{\rm int} + L_{\rm acc} - L_{\rm src,\,UV}\,. \tag{70}$$

We discuss the treatment of the non ionizing luminosity, $L_{\rm src,\,IR}$, in this work and treat the ionizing luminosity, $L_{\rm src,\,UV}$, as discussed by Wünsch et al. (2021).

In total, we include two bands of radiation. A non-ionizing band acting on dust with the novel scheme TREERAY/RADPRESSURE and an ionizing band with the module TREERAY/ONTHESPOT (Wünsch et al. 2021). Both bands are emitted by sink particles, while the non-ionizing radiation may additionally be emitted by dust from everywhere inside the computational domain.

7.3 Morphology across time

The initial spherically symmetric configuration is quickly disturbed by the turbulent velocity field. Local high density regions are forming where streams of momentum, $\rho\mathbf{v}$, collide. In those regions the gas is heated through pdV work (adiabatic compression). The dust is heated by the gas through collisional interactions, whilst trying to cool by radiating in the continuum infrared. As a result, the dust temperature is settling in between the gas temperature, $T_{\rm gas}$, and the radiation temperature, $T_{\bar{J}}$ (see eq. 54), as described in §4.6. Fig. 9 shows the density, ρ, gas and dust temperatures, and the radiation temperature, $T_{\bar{J}}$, across different times for the entire computational domain. We can see that $T_{\bar{J}}$ is hottest at the central hub and decreases further out. This indicates that the central hub is dominating the IR luminosity output. As the simulation evolves, the radiation temperature increases globally, which can be seen most significantly comparing the times $0.4\,t_{\rm ff}$ and $0.5\,t_{\rm ff}$. The increased radiation temperature also heats the dust and therefore indirectly the gas at greater distances further out.

7.4 Stellar population

Fig. 10 shows an overview over the stellar population, showing the mass, accretion rate, luminosity and number of ionising photons vs. time. Early on, at around $0.1\,t_{\rm ff}$ the first stellar object, labeled '1', forms in the central dense hub. Throughout the simulation '1' stays the most massive object and with that it is the most dominant source of stellar feedback. After its formation the simulation enters a quiescent phase, where no stars are formed for about another 0.2 $t_{\rm ff}$. This is followed by a phase of frequent star formation taking place outside of the central hub in the dense filamentary material accreting onto the central hub.

Fig. 11 shows the column density, Σ, and the density-weighted temperatures of gas, dust, and radiation at 0.2 $t_{\rm ff}$,

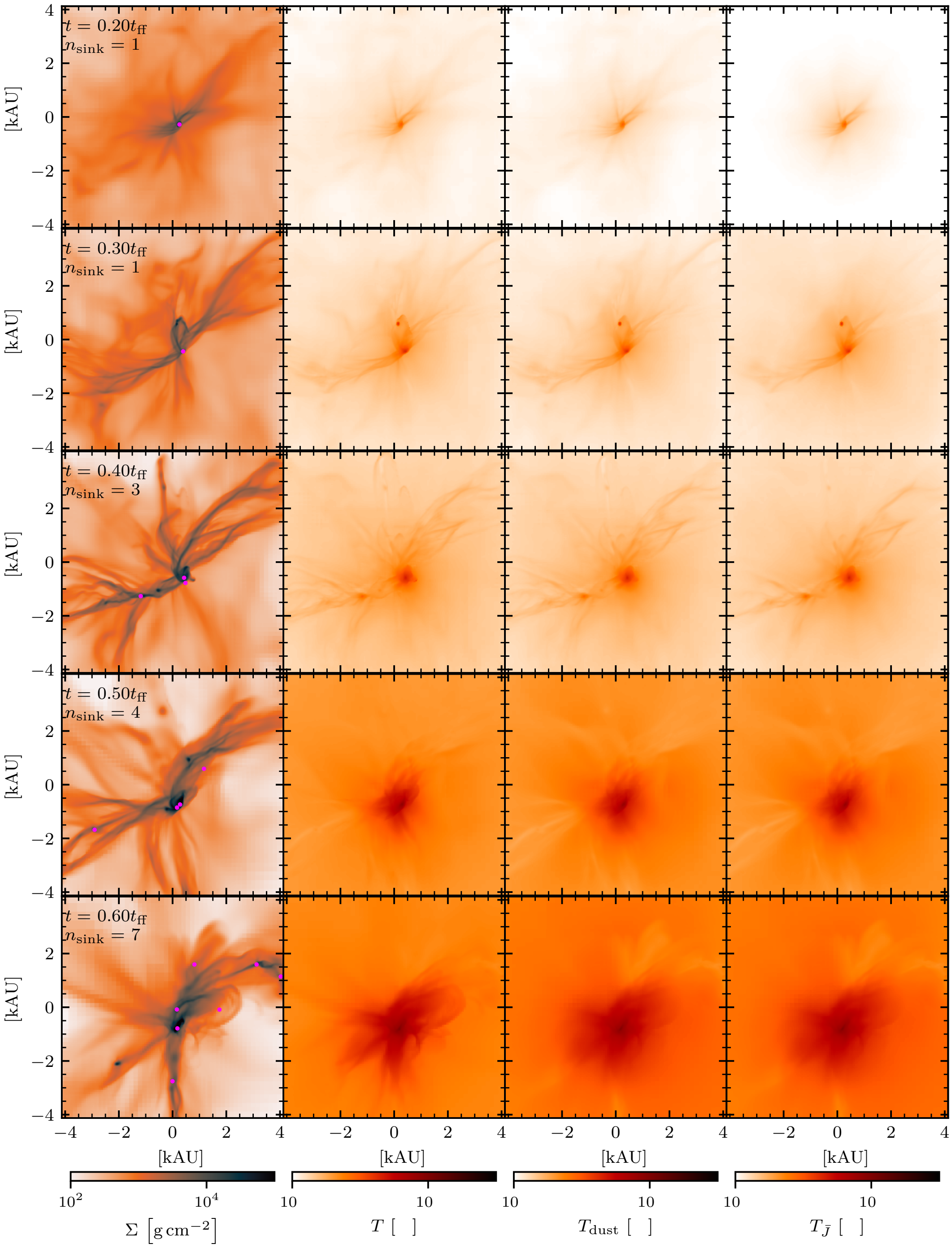

Figure 11. Projections along the z-coordinate axis of an $(8\ \mathrm{kAU})^3$ cube around the origin for the turbulent star forming test (see §7). Organized in rows we show, from left to right, the column density and the density-weighted gas temperature, dust temperature and radiation temperature across different times (top to bottom). The time, t, is measured in free-fall times, $t_{\rm ff} = 42.3\,\mathrm{kyr}$. The number of formed sink particles present is labeled $n_{\rm sink}$. We can see stars forming in the central hub initially and later on forming in dens structures connected to the hub further out. The central hub is hotter than the ambient medium with gas and dust temperatures of around 100 K to 1000 K. At around $t = 0.5\,t_{\rm ff}$ the luminosity output of the central hub increases, heating up the surrounding material. Other stars than the primary do not cause visible changes in the radiation temperature as $T_{\bar{J}}$ is dominated by the most massive star.

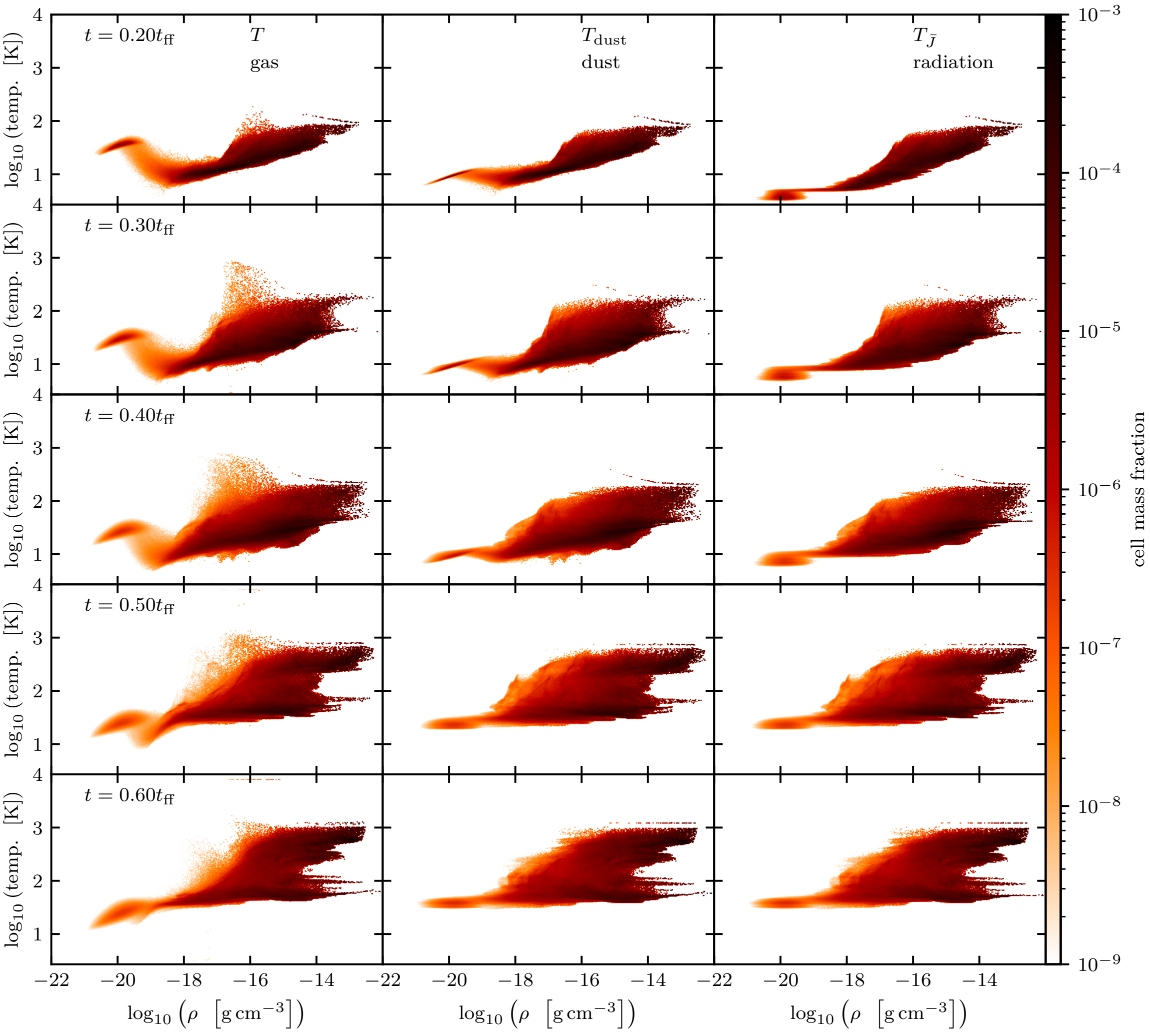

Figure 12. Phase diagrams of the gas, dust and radiation temperature (from left to right) for different times (from top to bottom). All cells are normalised by the total mass in the computational domain. The clump at $\rho \approx 10^{-20}\,\mathrm{g\,cm^{-3}}$ and $T \approx 10^{2}\mathrm{K}$ represents the background medium which is slowly cooled by dust. The very dense part at around $\rho \approx 10^{-14}\,\mathrm{g\,cm^{-3}}$ and $T \approx 10^{2}\mathrm{K}$ shows the central hub getting hotter over time. For $t \leq 0.4t_{\mathrm{ff}}$, we find $T > T_{\mathrm{dust}} > T_{\bar{J}}$ for some of the diffuse gas enabling dust to cool gas by radiating thermal energy away. Eventually, the global minimum radiation temperature increases and with it the gas and dust temperature follow.

0.3 t_{ff}, 0.4 t_{ff}, 0,5 t_{ff} and 0.6 t_{ff}. One can see that the filamentary structure develops over time and feeds gas into the central hub. Stellar objects forming in the filamentary outskirts follow the general trend of the infalling gas and migrate to the central hub (see Fig. 11). Inside the central hub their accretion rate is minuscule compared to the primary star embedded in the center. It is only a brief time during which the secondary sink particles accrete and after which their accretion drops significantly. Looking at their luminosity in the upper right panel of Fig. 10 one can see that the luminosity output of the secondary sink particles is dominated by their stellar luminosity due to the lack of accretion. Overall, the motion of the secondary sink particles is governed by the gravity of the central star and gas. The lower right panel of Fig. 10 shows the rates of photons emitted in the Lyman continuum, $\dot{N}_{\mathrm{LYC}}$, both from the stellar and hot spot accretion separately. The most massive star manages to form a very compact HII region between $0.4t_{\mathrm{ff}}$ and $0.5t_{\mathrm{ff}}$ (looking at the phase diagram, Fig. 12). We show an exemplary spectral emission diagram in the appendix F.

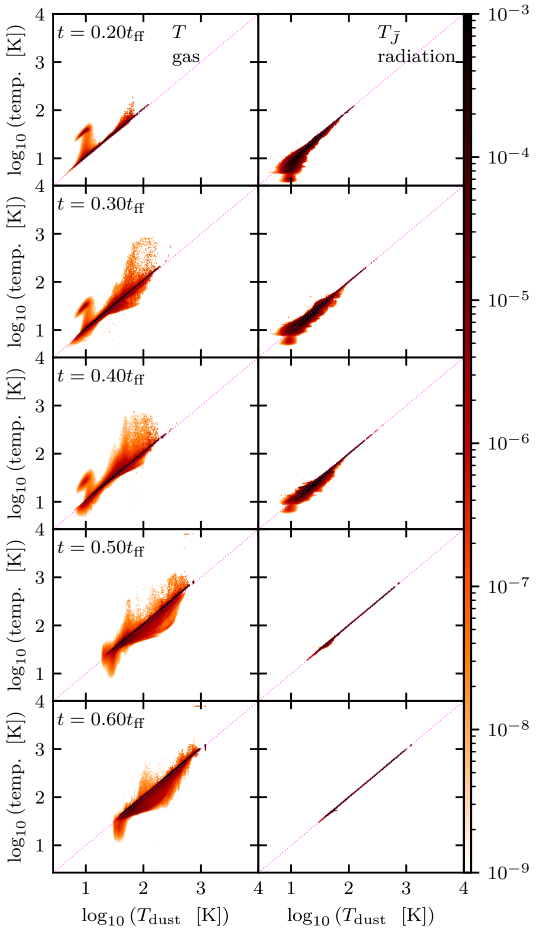

Figure 13. Phase diagrams of gas and radiation temperature vs dust temperature organized in columns. The phase diagrams are grouped into rows for different times. The dotted magenta line shows the one-to-one line. The cells are normalised to the current mass present in the entire computational domain. Most of gas and dust follow the one-to-one line with slight deviation (left column). The accretion shock heated gas is in a state able to be cooled by gas effectively ($T_{\rm dust} < T$). Dust is mostly hotter than the local radiation temperature (right column), which allows dust to cool radiatively.

7.5 The Role of Dust

7.5.1 Heating and Cooling

With TreeRay/RadPressure and our chemistry network (see §4.6) we can follow the dust temperature evolution. Fig. 12 shows phase diagrams of gas, dust and radiation across different times.

We consider gas with $\rho < 10^{-19}\,{\rm g\,cm^{-3}}$ to be part of the initial background medium. Throughout time the background medium is cooling down. Gas at densities $10^{-19}\,{\rm g\,cm^{-3}} < \rho < 10^{-16}\,{\rm g\,cm^{-3}}$ behaves mostly isothermal and is able to cool down over time via dust, since the radiation temperature is lower than the dust temperature. One can see this in Fig. 12 where $T_{\bar{J}}$ is lower than the dust temperature at $t = 0.2\,t_{\rm ff}$ for the most diffuse gas. Over time $T_{\bar{J}}$ increases and hence the ability of dust to cool efficiently fades. The forming stars become more embedded as time progresses because of gravitational collapse, which forms compact structures. The average optical depth along all lines of sight at a given position increases. This causes the radiation temperature to increase due to contributions from hotter surrounding material. At later times one finds the luminosity output of the central object to be significant enough to influence $T_{\rm dust}$ even at greater distances, where the densities are lower. Here we find $T_{\bar{J}} \approx T_{\rm dust} > T$. We can also see the effects of accretion shock heating in the gas temperature at intermediate densities. Initially only a subtle characteristic can be found at $t = 0.2\,t_{\rm ff}$ at around $\rho = 10^{-16}\,{\rm g\,cm^{-3}}$, where the temperature spikes for a small fraction of the gas. At later times we find the feature of accretion shock heating to be more pronounced and shifted towards lower densities. This is because gas from the outer parts of the cloud starts hitting the central hub, which is at lower density due to the power-law profile. In addition, the kinetic energy with which the gas from the outside is accreting onto the central hub is increasing, resulting in more thermal energy upon impact. This results in the growing peak of accretion shock heating as seen in the evolution of the gas temperature for densities around $10^{-16}\,{\rm g\,cm^{-3}}$ in Fig. 12. Because dust is coupled to the gas in this density regime (see Fig. 6), we expect dust to be heated by the accretion shock heated gas. This is further elaborated in the following paragraph.

Fig. 13 shows phase diagrams for the gas and radiation temperature vs. dust temperature at different times. The dotted, magenta line indicates the one-to-one line. We can see that most of the gas is located around the one-to-one line in the left column at $t = 0.2\,t_{\rm ff}$. Any deviations from the one-to-one line during $t = 0.2\,t_{\rm ff}$ appear above the one-to-one line which allows gas to be cooled through dust, as $T > T_{\rm dust}$. In particular, this is the case for higher temperatures, most likely caused by accretion shock heating. For $t = 0.3\,t_{\rm ff}$ and beyond, we find gas that may also be heated by dust ($T_{\rm dust} > T$). Looking at the right column for $T_{\bar{J}}$ vs. $T_{\rm dust}$, most deviations from the one-to-one line indicate that dust is preferably hotter than the radiation temperature and therefore capable of cooling radiatively until $0.4\ t_{\rm ff}$. This difference shrinks with increasing time, so that $T_{\rm dust} \approx T_{\bar{J}}$ indicating radiative cooling becomes less effective. The decrease in cooling efficiency allows both dust and gas to move upward along the one-to-one line reaching higher temperatures with time. The accretion shocked gas can be seen at high gas temperatures at around 10^2 K to 10^3 K while being far from the one-to-one line. Typically one finds this type of gas on the boundary of dense structures, giving the gas suitable conditions to be cooled by radiation. We expect that dust in this regime is also heated by the gas given that gas is up to ten times hotter in some instances (see $t = 0.4\,t_{\rm ff}$ of Fig. 13). We find dust and radiation to follow the one-to-one line in the center of the core. Here dust can not cool as efficiently as on the boundary thus resulting in accumulation near the one-to-one line. This behaviour can be seen in Fig. 13 in the right column at $t \geq 0.5\,t_{\rm ff}$. Here dust is surrounded by optically thick material radiating at its own temperature making

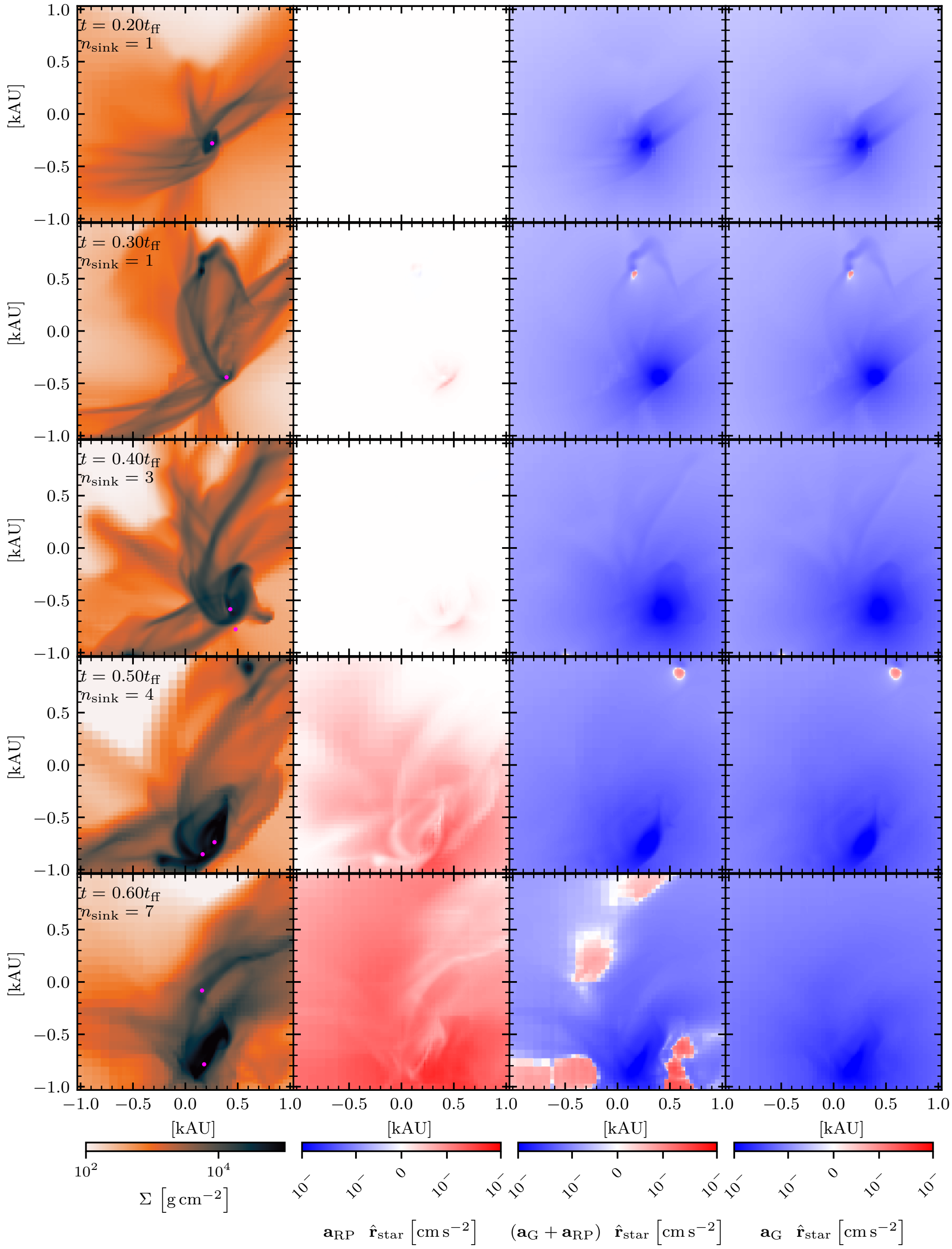

Figure 14. Projections along the z-axis of a $(2\ \mathrm{kAU})^3$ cube around the origin. From left to right we show again the column density (for reference) and 3 different radial accelerations. All 3 acceleration vectors are density-weighted along the line of sight and projected on the line of sight towards the most massive star. Going from left to right we have the RP acceleration, the acceleration due to gravity and RP combined, and the gravitational acceleration. We can see that RP manages to oppose gravity in the diffuse gas close to the central star over time.

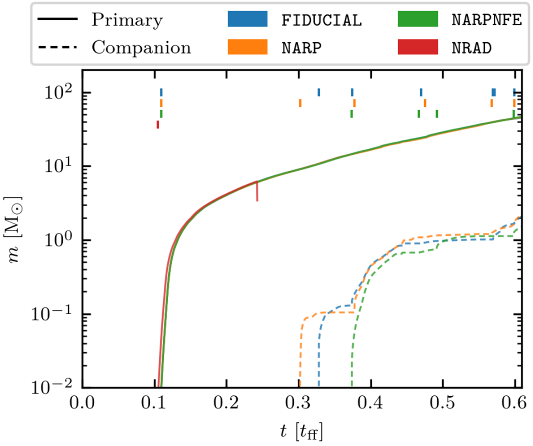

Figure 15. Mass vs. time of the central primary star and its companions for all performed runs. Tick marks at the top represent the formation of further sink particles. The primary mass does not change across different runs indicating that RP does not impact the accretion of the central star in our simulation.

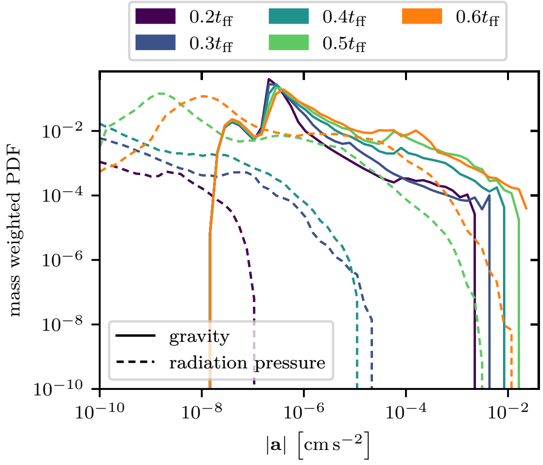

Figure 16. Mass weighted PDF of acceleration exerted as a consequence of gravity and radiation pressure across time. The impact of radiation pressure is increasing over time towards higher accelerations while the spectrum of gravity does not change by a lot.

it unable to cool. Sitting at $T_{\mathrm{gas}} \approx 10^4$ K and $T_{\mathrm{dust}} \approx 10^3$K one finds few cells that represent ionized gas contained in a hypercompact HII region around the most massive star for $t \geq 0.5\,t_{\mathrm{ff}}$. Besides that, we find radiation from the Lyman-Continuum to have no dynamical impact in the star forming setup for the simulated timescales. In our implementation, absorbed Lyman-Continuum radiation is immediately reprocessed by dust into IR radiation, thus contributing to heating the gas and dust which surrounds the young stars.

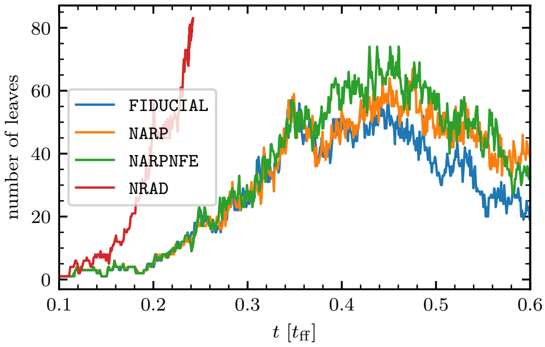

Figure 17. Number of leaves in a dendogram vs. time for all four runs. After $0.15\ t_{\mathrm{ff}}$ `NRAD` deviates from the runs `NARP`, `NARPNFE` and `FIDUCIAL` owing to its lack of both radiative heating from dust and stars, and RP. All other runs coincide until roughly $0.35\ t_{\mathrm{ff}}$ after which fragmentation is more suppressed the more physics is included. We can see that the addition of both RP and radiative heating suppresses fragmentation towards $0.6\ t_{\mathrm{ff}}$.

Following the TreeRay/OnTheSpot method, ionizing radiation is locally ionising hydrogen that constantly recombines. Here, in particular, we reemit the consumed ionizing radiation as IR radiation in an energy conserving manner, taking into account the heating by absorbed UV radiation in the chemical network. We note that in this way TreeRay/OnTheSpot faithfully recovers temperatures inside HII regions (see comparison with the code MOCASSIN (Ercolano et al. 2003) as shown by Haid et al. (2018)).

7.5.2 Additional runs

To further investigate the effect of heating and cooling (see §4.6) and RP on gas dynamics and fragmentation, we employ three additional runs. In the first run, we disable all radiation effectively turning TreeRay/RadPressure off. This run is called `NRAD`. Here, dust will always cool optically thin and without any background radiation, $\bar{J} = 0$. The other two runs we label `NARP` and `NARPNFE`. For both runs, we do not apply accelerations from RP and in addition, we disable stellar feedback in the case of run `NARPNFE`. By comparing all runs including the original run (hereafter **`FIDUCIAL`**) to one another, we will benchmark the impact of TreeRay/RadPressure on the star forming setup in §7.5.3 and §7.5.4.

7.5.3 Radiation Pressure

We find that gravity dominates over RP in the early stages of the **`FIDUCIAL`** run. Fig. 14 shows a projection of the density along the line of sight and density-weighted acceleration due to RP, $\mathbf{a}_{\mathrm{RP}}$, gravity and RP, $\mathbf{a}_{\mathrm{RP}} + \mathbf{a}_{\mathrm{G}}$, and gravity, $\mathbf{a}_{\mathrm{G}}$. All accelerations shown are projected in the radial direction of the most massive star, where positive values of $\mathbf{a}_{\mathrm{RP}} \cdot \hat{\mathbf{r}}_{\mathrm{star}}$ and $\mathbf{a}_{\mathrm{G}} \cdot \hat{\mathbf{r}}_{\mathrm{star}}$ point away from the star. We can see that the region only close to the star is affected by radiation pressure and turns super-Eddington, $\mathbf{a}_{\mathrm{RP}} \cdot \hat{\mathbf{r}}_{\mathrm{star}} > -\mathbf{a}_{\mathrm{G}} \cdot \hat{\mathbf{r}}_{\mathrm{star}}$, in the diffuse gas at later times. But still, RP does not manage to overcome gravity very close to the central star. From this, we conclude that RP will not influence the accretion of mass onto the central before $0.6\,t_{\rm ff}$. The spherical fragment seen in the column density at 0.5 $t_{\rm ff}$ is collapsing. It shows red features in both, $\mathbf{a}_{\rm RP}+\mathbf{a}_{\rm G}\cdot\hat{\mathbf{r}}_{\rm star}$ and $a_{\rm G}\cdot\hat{\mathbf{r}}_{\rm star}$, indicating that the blob is self-gravitating. However, this blob does not go on to form a sink particle because it is sheared apart before it can collapse (see §7.2).

The mass of the principal star and all its companions is shown in Fig. 15 for the four runs. Vertical tick marks on the top mark the formation of new sink particles for all simulations. Again, a direct comparison of the primary masses for the different runs as shown in Fig. 15 underlines that RP is unable to impact the accretion rate onto the central star. The principal mass agrees in all three (four) runs (for the simulated time).

Fig. 16 shows the mass-weighted probability density function (PDF) of RP and gravitational acceleration at different times. As a function of time, the change in the PDF of the gravitational acceleration is minuscule, while the RP PDF changes significantly. The RP PDF shows higher accelerations with increasing luminosity output of the central hub. It is only after 0.5 $t_{\rm ff}$ that the maximum accelerations reached by RP are comparable to those caused by gravity within an order of magnitude. Yet, gravity dominates over RP in the high-acceleration regime. Given that these high accelerations are expected to occur close to the central hub, it is unlikely that RP from the central star has a substantial impact on accretion up to $0.6\,t_{\rm ff}$.

7.5.4 Gas dynamics and Fragmentation

Next, we investigate the effect of radiative heating of gas via dust. This requires the dust to be heated in the first place. In our method, dust may be heated by radiation originating from stars as well as by infrared radiation from the surrounding dust. Otherwise, the dust may cool indefinitely (run `NRAD`). In particular for run `NRAD`, one expects more fragmentation to occur as the overall temperature and the corresponding Jeans mass should be lower. We measure the degree of fragmentation in the density field using dendrograms[4]. Dendrograms construct a tree that shows the structural hierarchy inside a given dataset. By counting the resulting leaves generated by a dendrogram tree, we can assess the degree of fragmentation.

Fig. 17 shows the number of leaves as a function of time for each run. The run `NRAD` shows the most fragmentation as it cools the gas via optically thin dust emission standing in contrast to the other runs which do account for infrared radiation by dust (red line vs. others). Going a step further, the addition of radiation from stars reduces the number of leaves past 0.4 $t_{\rm ff}$ (compare the green and orange lines). After 0.45 $t_{\rm ff}$, RP provides an additional mechanism by which fragmentation is slightly suppressed. We show slices of the density and all three temperatures in Fig. 18 for `FIDUCIAL` and `NRAD`. Here, we can see a major difference in T and $T_{\rm dust}$ being lower for the run `NRAD` as TreeRay/RadPressure is turned off. This reduction in temperature is caused by the fact that dust is allowed to cool optically thin ($T_{\bar{J}}=0$). From this we conclude that RP and thermal feedback contribute towards reducing fragmentation in the star forming setup.

7.6 Discussion: TreeRay/RadPressure and the Star Forming Setup

The star forming setup presents an application of TreeRay/RadPressure using a more realistic and ultimately more demanding setup other than the tests presented in §5 and §6. The setup is identical to the one presented in the work of Rosen et al. (2019) except for its treatment of radiative transfer, the initial velocity seed and chemistry, including dust thermo-chemistry.

On large scales, TreeRay/RadPressure shows artifacts that form a ray-like pattern in the radiation temperature. This pattern is concentric around the embedded source (see Fig. 9). To investigate how TreeRay/RadPressure would perform against a perfectly accurate $\mathcal{O}(N^2)$-method we increase the number of rays sequentially. By doing so, h-nodes are opened further in comparison to the fiducial setup running with 48 rays, such that in the limit of a very high number of rays all nodes would be fully opened (i.e. all bottom nodes would be considered). We increase the number of rays and perform two additional restarts of the `FIDUCIAL` run (48 rays) at $t=0.6\,t_{\rm ff}$ using 192 and 768 rays, respectively. We find a relative cost increase of (1.00 : 4.39 : 15.98) for the algorithm with (48 rays : 192 rays : 768 rays) (i.e. close to the theoretical expectation). Fig. 19 shows $T_{\bar{J}}$ in a slice through $z=0$ for the three different ray resolutions. The upper row shows slices, which are half of the domain size in width, while the lower row shows the entire domain. TreeRay/RadPressure captures the temperature features at distances of 10 kAU to the central hub well with only 48 rays. On scales of the entire domain, one finds a star-like pattern surrounding the central hub. This pattern becomes more whispy as the number of rays increases, and it is expected to vanish in the perfect $\mathcal{O}(N^2)$ limit.

The resulting pattern may originate from splitting optically thick labeled volumes onto rays linearly followed by a non-linear way of generating an angular size of the mapped optically thick volume (see Eq. 31). In this way, the perceived total area may oscillate as one circles an optically thick clump at a fixed distance. The radiative intensity is the lowest if all material is contained in one ray and the greatest if all material is split among many rays resulting in a star-like pattern. The resulting oscillations are expected to be on the order of 26% for the following reasons. A single optically thick control volume, $V_{\rm control}$, mapped to a single ray produces an area equivalent to $A_{\rm control}=V_{\rm control}^{2/3}$. If $V_{\rm control}$ is mapped to two rays equally instead, the equivalent area is $A_{\rm two\ rays}=(0.5V_{\rm control})^{2/3}+(0.5V_{\rm control})^{2/3}=1.26\times A_{\rm control}$, thus producing a maximum overestimate of 26%. For three rays involved, the overestimate reaches up to 44%. The previous estimates assume that the rays are not saturated, corresponding to the angular size of $V_{\rm control}$ being smaller than that of a ray. Therefore, the pattern in Fig. 19 only appears for large distances where rays are not saturated. To counteract this problem, we shift the nodes towards their center of emission during mapping to rays. It may also occur that

---

[4] We use the following implementation:https://github.com/dendrograms/astrodendro/

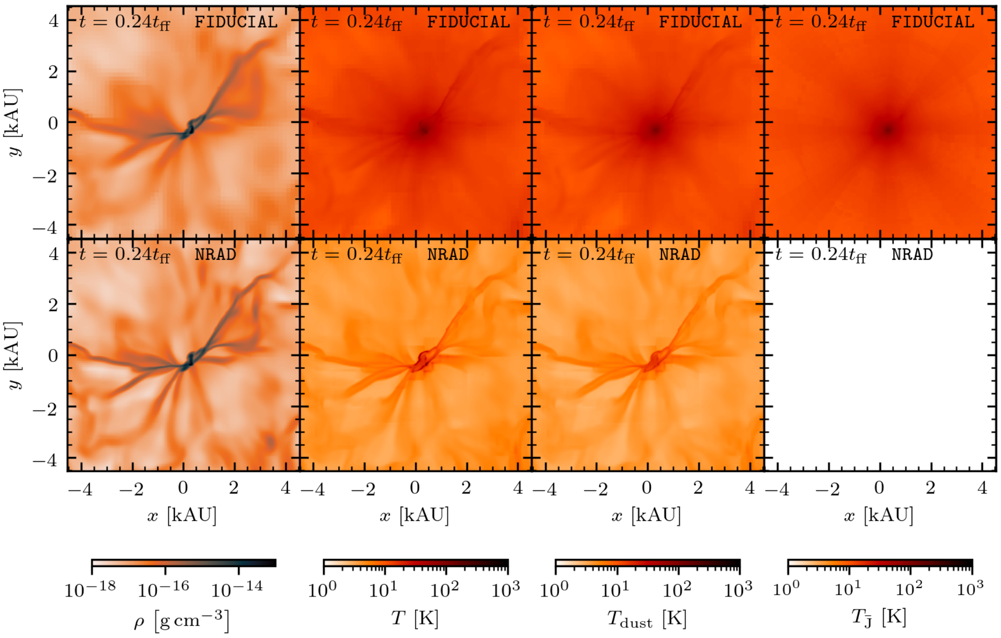

Figure 18. Slices through $z = 0$ showing the density, gas temperature, dust temperature and radiation temperature from left to right at similar times. From top to bottom we show two different runs where we include all physics (`FIDUCIAL`) and no radiative transfer at all (`NRAD`). Comparing the densities one can see more fragmentation occurring in run `NRAD`. This is linked to optically thin cooling behaviour of dust ($T_{\bar{J}} = 0$ everywhere). We find more heating in the center for runs with stellar radiation (`FIDUCIAL` and `NARP` vs. `NARPNFE` although not shown here). Radiation pressure does not affect the early dynamics of the setup (`FIDUCIAL` vs. `NARP`).

shielding of a luminous sink particle will oscillate in a similar manner. These effects will be less pronounced if additional sources contribute to $T_{\rm rad}$ or dust provides additional shielding in the line of sight. Thus, the error estimate is a drastic overestimation of the real deviation. We find a mean residual of $-15.4\% \pm 14\%$ and $-3.77\% \pm 5.31\%$ when comparing 48 rays and 192 rays with 768 rays, respectively, for the domain shown in the upper panel of Fig. 19. In the lower panel, we find $-31.0\% \pm 17.9\%$ and $-13.2\% \pm 10.5\%$ for the same comparison. We note that this star formation simulation, where all radiating sources are located very close to the center, is basically the worst-case setup for TreeRay. If other sources were present in the surroundings, those would dominate the radiation field locally, and hence the artifacts would be much smaller. Despite the presence of mild artifacts, we believe that 48 rays are the preferred setting given the significantly reduced computational cost (factor 4 compared to 192 rays).

Currently, all rays have the same orientation leading to pronounced artifacts. A single orientation has been implemented because the ray intersection list is tabulated in the beginning of the simulation, and these tables are used every time when walking the tree to compute the contributions of tree nodes to ray segments. Different orientations require a number of these tables, which of course need to be communicated to, and stored on, all cores, which increases the memory footprint of the method and is hence not ideal for a pure MPI scheme. In a preliminary implementation, we find that introducing different HEALPix orientations mitigates the ray-like features while introducing some noise. However, the resulting physical properties of the gas and dust are better because the different orientations prevent the dust to locally heat up in a ray-like pattern and influence the dynamics and density distribution. This will be discussed in follow-up work.

Given that TreeRay/RadPressure only tracks information of a single monopole on each node, the scheme can not distinguish a source to be embedded or not. This may cause over- or under-extinction of sources and anisotropic emission characteristics to be lost at large distances. This uncertainty in shielding may also contribute to the ray structures discussed above. The accuracy of TreeRay/RadPressure can be improved by introducing higher order terms containing information about the geometry within both h-nodes and the volumes of rays. We defer such improvements to later works.

8 CONCLUSION

This work presents a novel method to compute the radiative transfer of the infrared radiation by dust and stars on-the-fly in three-dimensional simulations of e.g. star formation. In particular, every cell in the computational domain and any number of present (sink) particles can be a source of radiation.

The general idea of the method can be transferred to compute radiative transfer on other macroscopic sources of

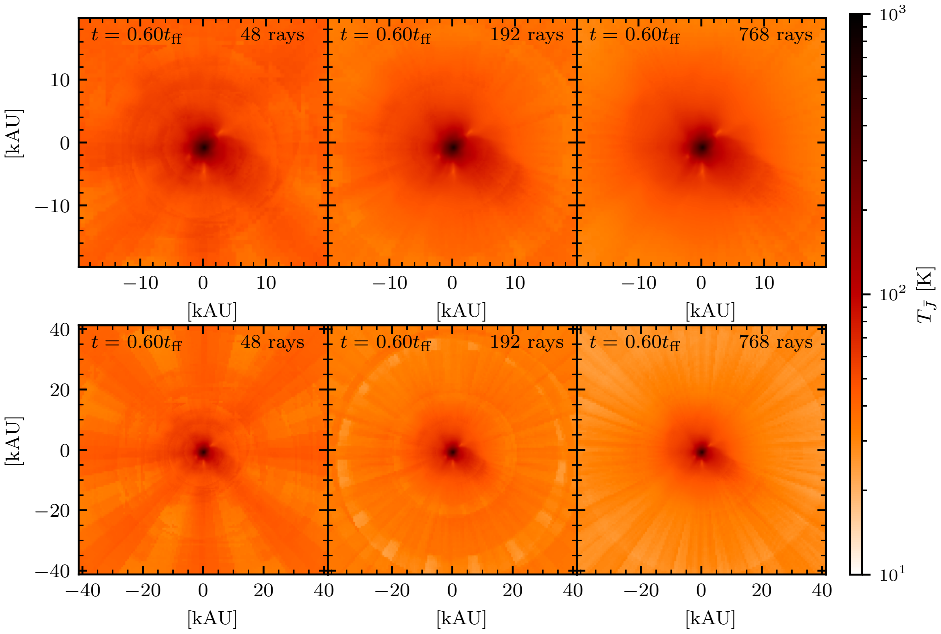

Figure 19. Slices through $z = 0$ showing the radiation temperature, $T_{\bar{J}}$. From left to right, $T_{\bar{J}}$ is computed with 48, 192 and 768 rays, respectively. From top to bottom we vary the size of the shown region. Sink particles are not shown in this figure. By increasing the number of rays used, we tend towards an $\mathcal{O}(N^2)$ method as h-nodes are further opened to be comparable to the ray size. $T_{\bar{J}}$ changes mildly in the upper row showing that the scheme performs well scales of half a domain size. On scales of the full domain however, $T_{\bar{J}}$ shows ray artefacts that change with the number of rays used. We find the ratio of computational cost to be (1.00 : 4.39 : 15.98) for (48 rays : 192 rays : 768 rays). Additionally, we find a residual of $-15.4 \pm 14\%$ and $-3.77 \pm 5.31\%$ when comparing 48 rays and 192 rays with 768 rays, respectively, for the domain shown in the upper panel. In the lower panel, we find $-31.0 \pm 17.9\%$ and $-13.2 \pm 10.5\%$ for the analogous comparison.

radiation (e.g. sources that can not be considered as point sources like stars in a numerical simulation). We find that with a computational expense of $N\log(N)$, where N is the number of grid cells (as for the original implementation in Wünsch et al. (2021)), TreeRay/RadPressure is applicable to solve large scale problems.

In a first step, for each grid cell, TreeRay/RadPressure maps contributions from dust and point sources (e.g. stars) onto rays along different directions, where each ray has an associated angular size similar to the shape of a cone. The rays span the surface of the unit sphere according to the HEALPix algorithm (typically we use 48 rays). Subsequently, each ray is integrated to compute a radiative intensity along its line of sight. With all rays integrated, a radiative flux and mean intensity are calculated. We take into account that the Planck-mean dust opacity is temperature-dependent. Finally, we compute the radiation pressure on dust by infrared radiation and its heating rate.

The novel approach presented in this work also couples the infrared radiative transfer to a chemical network (see §4.6). In particular, the mean intensity of the infrared radiation serves as an input for the thermal equilibrium calculation of the dust temperature, i.e. the dust is heated by IR radiation. In this way, we are able to model the interplay of dust and gas in a self-consistent way. Given that a region is not deeply embedded, dust may cool gas through collisional interactions and radiate thermal energy away. In that case we recover an almost isothermal behavior. On the other hand, an embedded region behaves close to adiabatic if radiation can not escape efficiently. Our method allows to model radiative cooling in both embedded and exposed conditions.

The tests presented in §5 show that we can reproduce the Beer-Lambert law and correct radiative energy profiles in optically thin and thick regimes. We are able to compute radiative transfer from macroscopic objects such as dense blobs as presented in §5.2. We verify the correct momentum transfer caused by radiation pressure onto dust and show that the method allows for the leakage through optically thin media as shown in §5.4.

Next, we connect the TreeRay/RadPressure module with the TreeRay/OnTheSpot module (Wünsch et al. 2021), which treats the transport of ionizing radiation and the associated momentum input on gas and dust. In §6, we show that the combined method faithfully models the expansion of an HII region in two different environments. We find that RP drives the expansion of an ultra-compact HII region over its limitation given by the pressure balance of the ionised medium and its surroundings.

In addition to the tests, we simulate massive star formation in a collapsing, turbulent prestellar core. The star forming setup highlights accretion shock heated gas on the boundary of filaments and the central hub. We find that dust is picking up thermal energy through collisional coupling with gas, resulting in dust temperatures slightly below 100 K. Under those circumstances, where dust is not fully surrounded by other hot dust, dust is able to radiatively cool. On the other hand, dust is not able to cool in the dense region close to the central star, where the local radiation temperature and dust temperature are equal. For times later than 0.5 $t_{\rm ff}$ gas may be warmer than dust due to accretion shock heating and in other instances, gas may be colder than dust due to insufficient dust-gas coupling where dust is radiatively heated. We find that the dust temperature is in agreement with the radiation temperature past 0.5 $t_{\rm ff}$. RP is minuscule compared to the effects of gravity in the early stage as the central star is not luminous enough to provide relevant feedback. The luminosity output of the central hub grows with the mass of the stellar population over time and with it the relative strength of RP compared to gravity. On the simulated timescales, however, RP does not manage to influence the dynamics of gas near the central star. Eventually, gas may be blown away through stellar feedback in the later evolution of this setup, once the ram pressure generated by the infalling gas decreases.

Our method, TreeRay/RadPressure, is a first approach towards solving RT of extended sources and we plan on improving it further in future works, e.g. we plan to treat the effects of scattering on dust in future works. We aim at analysing the star forming setup in greater detail in a separate publication.

ACKNOWLEDGEMENTS

We thank the referee J. Rosdahl for his valuable comments that helped to improve the quality of this work. AK, SW, and SH gratefully acknowledge the European Research Council under the European Community's Framework Programme FP8 via the ERC Starting Grant RADFEEDBACK (project number 679852). SW and SH further thank the Deutsche Forschungsgemeinschaft (DFG) for funding through SFB 956 "The conditions and impact of star formation" (sub-project C5). DS acknowledges the DFG for funding through SFB 956 "The conditions and impact of star formation" (sub-project C6). RW acknowledges support by project 19-15008S of the Czech Science Foundation and by the institutional project RVO:67985815. FD gratefully acknowledges funding from the Grant Agency of the Czech Republic under grant number 20-21855S. The software used in this work was in part developed by the DOE NNSA-ASC OASCR Flash Center at the University of Chicago. The authors gratefully acknowledge the Gauss Centre for Supercomputing e.V. (www.gauss-centre.eu) for funding this project by providing computing time through the John von Neumann Institute for Computing (NIC) on the GCS Supercomputer JUWELS at Jülich Supercomputing Centre (2021) (JSC). We particularly thank the Regional Computing Center Cologne for providing the computational facilities for this project by hosting our supercomputing cluster "Odin".

DATA AVAILABILITY

The data underlying this article will be shared on reasonable request to the corresponding author.

REFERENCES

Abel T., Wandelt B. D., 2002, MNRAS, 330, L53
Altay G., Theuns T., 2013, MNRAS, 434, 748
Baczynski C., Glover S. C. O., Klessen R. S., 2015, MNRAS, 454, 380
Bakes E. L. O., Tielens A. G. G. M., 1994, ApJ, 427, 822
Bisbas T. G., et al., 2015, MNRAS, 453, 1324
Bouchut F., Klingenberg C., Waagan K., 2007, Numerische Mathematik, 108, 7
Bouchut F., Klingenberg C., Waagan K., 2010, Numerische Mathematik, 115, 647
Calvet N., Gullbring E., 1998, ApJ, 509, 802
Clarke S. D., Whitworth A. P., Duarte-Cabral A., Hubber D. A., 2017, MNRAS, 468, 2489
Dinnbier F., Walch S., 2020, MNRAS, 499, 748
Draine B. T., 2011, ApJ, 732, 100
Ercolano B., Barlow M. J., Storey P. J., Liu X. W., 2003, MNRAS, 340, 1136
Federrath C., Banerjee R., Clark P. C., Klessen R. S., 2010, ApJ, 713, 269
Federrath C., Banerjee R., Seifried D., Clark P. C., Klessen R. S., 2011, in Alves J., Elmegreen B. G., Girart J. M., Trimble V., eds, IAU Symposium Vol. 270, Computational Star Formation. pp 425–428 (`arXiv:1007.2504`), doi:10.1017/S1743921311000755
Fryxell B., et al., 2000, The Astrophysical Journal Supplement Series, 131, 273
Glover S. C. O., Mac Low M.-M., 2007, ApJS, 169, 239
Górski K. M., Hivon E., Banday A. J., Wandelt B. D., Hansen F. K., Reinecke M., Bartelmann M., 2005, ApJ, 622, 759
Grond J. J., Woods R. M., Wadsley J. W., Couchman H. M. P., 2019, MNRAS, 485, 3681
Haid S., Walch S., Seifried D., Wünsch R., Dinnbier F., Naab T., 2018, MNRAS, 478, 4799
Haid S., Walch S., Seifried D., Wünsch R., Dinnbier F., Naab T., 2019, MNRAS, 482, 4062
Hollenbach D., McKee C. F., 1979, ApJS, 41, 555
Hopkins P. F., Quataert E., Murray N., 2011, MNRAS, 417, 950
Jülich Supercomputing Centre 2021, Journal of large-scale research facilities, 7
Kannan R., Vogelsberger M., Marinacci F., McKinnon R., Pakmor R., Springel V., 2019, MNRAS, 485, 117
Kessel-Deynet O., Burkert A., 2000, MNRAS, 315, 713
Kim J.-G., Kim W.-T., Ostriker E. C., 2018, ApJ, 859, 68
Klassen M., Pudritz R. E., Peters T., 2012, MNRAS, 421, 2861
Krumholz M. R., Thompson T. A., 2012, The Astrophysical Journal, 760, 155
Krumholz M. R., Klein R. I., McKee C. F., Bolstad J., 2007, ApJ, 667, 626
Kuiper R., Hosokawa T., 2018, A&A, 616, A101
Kuiper R., Yorke H. W., Mignone A., 2020, arXiv e-prints, p. arXiv:2009.12374
Lepp S., Shull J. M., 1983, ApJ, 270, 578
Levermore C. D., 1984, J. Quant. Spectrosc. Radiative Transfer, 31, 149

Levermore C., Pomraning G., 1981, The Astrophysical Journal, 248, 321

Martin P. G., Schwarz D. H., Mandy M. E., 1996, ApJ, 461, 265

Matzner C. D., 2002, ApJ, 566, 302

Menon S. H., Federrath C., Krumholz M. R., Kuiper R., Wibking B. D., Jung M., 2022, MNRAS, 512, 401

Mihalas D., Mihalas B. W., 2013, Foundations of radiation hydrodynamics. Courier Corporation

Nelson R. P., Langer W. D., 1997, ApJ, 482, 796

Raga A. C., Cantó J., Rodríguez L. F., 2012, MNRAS, 419, L39

Rosdahl J., Teyssier R., 2015, Monthly Notices of the Royal Astronomical Society, 449, 4380

Rosen A. L., Krumholz M. R., Oishi J. S., Lee A. T., Klein R. I., 2017, Journal of Computational Physics, 330, 924

Rosen A. L., Li P. S., Zhang Q., Burkhart B., 2019, ApJ, 887, 108

Semenov D., Henning T., Helling C., Ilgner M., Sedlmayr E., 2003, Astronomy & Astrophysics, 410, 611

Shapiro P. R., Kang H., 1987, ApJ, 318, 32

Spitzer L., 1978, Physical processes in the interstellar medium. New York Wiley-Interscience, 1978. 333 p.

Strömgren B., 1939, ApJ, 89, 526

Tan J. C., Beltrán M. T., Caselli P., Fontani F., Fuente A., Krumholz M. R., McKee C. F., Stolte A., 2014, in Beuther H., Klessen R. S., Dullemond C. P., Henning T., eds, Protostars and Planets VI. p. 149 (`arXiv:1402.0919`), doi:10.2458/azu_uapress_9780816531240-ch007

Thompson T. A., Quataert E., Murray N., 2005, The Astrophysical Journal, 630, 167

Truelove J. K., Klein R. I., McKee C. F., Holliman John H. I., Howell L. H., Greenough J. A., 1997, ApJ, 489, L179

Walch S., et al., 2015, MNRAS, 454, 238

Weingartner J. C., Draine B. T., 2001, ApJ, 548, 296

Wünsch R., Walch S., Dinnbier F., Whitworth A., 2018, MNRAS, 475, 3393

Wünsch R., Walch S., Dinnbier F., Seifried D., Haid S., Klepitko A., Whitworth A. P., Palouš J., 2021, arXiv e-prints, p. arXiv:2105.09644

APPENDIX A: INFORMATION PROPAGATION UPWARDS THE TREE

In this section we explain how quantities are propagated upwards the octtree. The crucial part is to store optically thin and thick contributions separately to maintain accuracy. In our implementation we propagate b-nodes and h-nodes differently in order to save memory on the biggest layer, made up of b-nodes. If the sub-node is a bottom node, we do the following:

$$\underline{L}_{\rm h-node,\,thick} = \sum_{k}^{\tau_{\rm b-node}\geq 1} \underline{L}_{\rm b-node,\,thick},_{k}, \quad \text{(A1)}$$

$$V_{\rm h-node,\,thick} = \sum_{k}^{\tau_{\rm b-node}\geq 1} V_{\rm b-node},_{k}, \quad \text{(A2)}$$

$$\widetilde{A}_{\rm h-node,\,thick} = \sum_{k}^{\tau_{\rm b-node}\geq 1} \widetilde{A}_{\rm b-node},_{k}, \quad \text{(A3)}$$

$$L_{\rm h-node,\,thin} = \sum_{k}^{\tau_{\rm b-node,\,thick}<1} L_{\rm b-node,\,thin},_{k}, + S_{\rm b-node,\,k} \quad \text{(A4)}$$

$$V_{\rm h-node,\,thin} = \sum_{k}^{\tau_{\rm b-node}<1} V_{\rm b-node},_{k}, \quad \text{(A5)}$$

$$\widetilde{A}_{\rm h-node,\,thin} = \sum_{k}^{\tau_{\rm b-node}<1} \widetilde{A}_{\rm b-node},_{k}. \quad \text{(A6)}$$

Otherwise, if the sub-nodes consist of h-nodes, we simply compute

$$X_{\rm h-node,\,Y} = \sum_{k}^{\rm b-node} X_{{\rm b-node},Y,k}, \quad \text{(A7)}$$

where X may be, L, $\widetilde{A}$, V or S and Y, thin or thick, respectively.

Since a higher level node may contain optically thin and thick contributions at the same instance, we need to store them seperately. Eq. A1, eq. A2 and eq. A3 trace optically thick quantities, while eq. A4, A5, and eq. A6 trace optically thin contributions.

In addition we compute the centre of luminosity (COL), $\mathbf{r}_{\rm COL}$, as seen from the geometric centre of the node, $\mathbf{r}_{\mathcal{O}}$, for higher level nodes. Again we distinguish if the sub-nodes are b-nodes or h-nodes. In the former case we compute

$$\xi_{\rm b-node} = L_{\rm b-node}, \quad \text{(A8)}$$

if the b-node is optically thin and

$$\xi_{\rm b-node} = L_{\rm b-node} \cdot (V_{\rm b-node})^{2/3}, \quad \text{(A9)}$$

otherwise. If the sub-nodes are h-nodes we use

$$\xi_{\rm h-node} = L_{\rm h-node,thin} + \underline{L}_{\rm h-node,\,thick} \cdot (V_{\rm h-node,\,thick})^{2/3} \quad \text{(A10)}$$

Finally we compute:

$$\Xi_{\rm h-node} = \sum_{k}^{\rm sub-nodes} \xi_{\rm sub-node,\,k}\,, \quad \text{(A11)}$$

$$\mathbf{r}_{\rm h-node,\,COL} = \frac{1}{\Xi} \sum_{k}^{\rm sub-nodes} \xi_{{\rm sub-node},k} \mathbf{r}_{{\rm sub-node},k}, \quad \text{(A12)}$$

where $\mathbf{r}_{\rm sub-node,\,k}$ is the position of the sub-node relative to $\mathbf{r}_{\mathcal{O}}$.

APPENDIX B: LIMITS OF AN OPTICALLY THIN AND THICK SEGMENT

Here we want to show, that eq. 39 has the correct limits if the material inside segment i becomes optically thin or thick. To do this we consider $\tau_{{\rm thin},i} << 1$ and $\tau_{{\rm thin},i} >> 1$.

By using a Taylor expansion series one can show that all terms involving $\tau_{\rm thin,\mathit{i}}$ collapse to unity in the former case. We arrive at

$$\text{eq. (39)} \quad \overset{\tau_{\rm thin,\mathit{i}}<<1}{\approx} \quad \frac{\hat{L}_{\rm thin,\mathit{i}}}{4\pi R_i^2}\,. \tag{B1}$$

Expression B1 is as expected, as would indeed see all luminosity content of segment i to be radiating. This solution is similar to that of a point source.

In the latter case all terms involving $\tau_{\rm thin,\mathit{i}}$ can be approximated by $1/\tau_{\rm thin,\mathit{i}}$. The complete relation can be expressed in the following way

$$\text{eq. (39)} \quad \overset{\tau_{\rm thin,\mathit{i}}>>1}{\approx} \quad \frac{1}{\tau_{\rm thin,\mathit{i}}} \times \frac{\hat{L}_{\rm thin,\mathit{i}}}{4\pi R_i^2}\,. \tag{B2}$$

Next we can introduce a factor of unity of the form $\frac{A_i}{A_i}$, where $A_i = \omega R_i^2$ is the area of segment i measured in angular direction. Together with $1/\tau_{\rm thin,\mathit{i}}$ we can express this as

$$\frac{A_i}{A_i} \times \frac{1}{\tau_{\rm thin,\mathit{i}}} = \frac{A_i}{\hat{A}_{\rm thin,\mathit{i}}} \tag{B3}$$

by using the definition of eq. 30. Substituting eq. B3 into eq. B2 results in the following expression

$$\text{eq. (39)} \quad \overset{\tau_{\rm thin,\mathit{i}}>>1}{\approx} \quad \frac{\omega R_i^2}{4\pi R_i^2} \times \frac{\hat{L}_{\rm thin,\mathit{i}}}{\hat{A}_{\rm thin,\mathit{i}}}\,. \tag{B4}$$

The left factor yields $1/N_{\rm pix}$. The factor on the right hand side can be understood as optical depth weighted mean temperature by considering that each segment sums over the each node's quantities described by eq. 15 and eq. 16. Finally we arrive at

$$\text{eq. (39)} \quad \overset{\tau_{\rm thin,\mathit{i}}>>1}{\approx} \quad \frac{4\pi}{N_{\rm pix}} \times \frac{\sigma}{\pi}\,\langle T^4_{\rm dust}\rangle_{\rho{\rm dV}\kappa}\,. \tag{B5}$$

Note that eq. B5 is in agreement with eq. 40 which describes the flux seen from optically thick material contained within a ray's segment. The difference is that the optically thin material is stretched over the entire pixel and thus shining over the full ray's solid angle $\omega = \frac{4\pi}{N_{\rm pix}}$ while the optically thick material is not, but compact instead. This approximates the optically thick material to radiate from its surface.

APPENDIX C: RADIATION PRESSURE ON DUST AND GAS BY UV RADIATION

For a given flux of ionizing photons per unit time and area, $\dot{N}_{\rm ph}$, with an average energy per photon, $\bar{E}$, we compute the momentum input per time caused by RP from UV radiation in the following way:

$$\dot{\mathbf{P}}_{\rm UV,\,dust} = \sigma_{\rm d} n \frac{\bar{E}_{\rm ph}}{c} \dot{N}_{\rm ph}\,\mathbf{u}_{\rm ph} {\rm d}V\,, \tag{C1}$$

$$\dot{\mathbf{P}}_{\rm UV,\,H} = \sigma_{\rm H} n_{\rm H} \frac{\bar{E}_{\rm ph}}{c} \dot{N}_{\rm ph}\,\mathbf{u}_{\rm ph} {\rm d}V\,, \tag{C2}$$

$$\dot{\mathbf{P}}_{\rm UV,\,H+} = n^2 \alpha_{\rm B} \frac{\bar{E}_{\rm ph}}{c}\,\mathbf{u}_{\rm ph} {\rm d}V\,, \tag{C3}$$

where $\dot{\mathbf{P}}_{\rm UV,\,dust}$, $\dot{\mathbf{P}}_{\rm UV,\,H}$ and $\dot{\mathbf{P}}_{\rm UV,\,H+}$ are the momentum deposition per unit time on dust, atomic hydrogen and ionized hydrogen, respectively. The quantities $\sigma_{\rm H}$, $\bar{E}_{\rm ph}$, $\dot{N}_{\rm ph}$ and $\mathbf{u}_{\rm ph}$ are the hydrogen cross section, the mean energy per photon, the incoming photon number per unit time per unit area and the normalised flux vector of the photons, respectively.

APPENDIX D: EQUATIONS FOR HEATING AND COOLING OF DUST

The gas-dust coupling is given by the following expression Hollenbach & McKee (1979):

$$\Gamma_{\rm dust-gas} = n n_{\rm dust} \sigma_{\rm dust} v_{\rm p} f 2 k_{\rm B} \left(T - T_{\rm dust}\right), \tag{D1}$$

where n and $n_{\rm dust}$ are the number density of gas and dust, $\sigma_{\rm dust}$ is the dust cross section and $v_{\rm p}$ is the thermal speed of protons for a given temperature T. f corrects the coupling strength for different ionization fractions and temperatures.

We compute the heating by the interstellar radiation field with the following equation (Bakes & Tielens 1994):

$$\Gamma_{\rm pe} = 10^{-24} \epsilon_{\rm pe} G_0 n_{\rm H}\,{\rm erg\,s^{-1}\,cm^{-3}}, \tag{D2}$$

where G_0 is the flux normalized to the Habing field for the solar neighborhood and $\epsilon_{\rm pe}$ is the photoelectric heating efficiency and $n_{\rm H}$ is the hydrogen number density. $\epsilon_{\rm pe}$ is given by eq. 43 of Bakes & Tielens (1994).

The H_2 formation heating is calculated as such (Glover & Mac Low 2007)

$$\Gamma_{\rm H_2} = 7.2 \times 10^{-12} \frac{R_{\rm H_2}}{1 + n_{\rm cr}/n}\,{\rm erg\,s^{-1}\,cm^{-3}}, \tag{D3}$$

where $R_{\rm H_2}$ measures the rate of H_2 formation on dust grains and $n_{\rm cr}$ is the critical density given by

$$\frac{1}{n_{\rm cr}} = \frac{x_{\rm H}}{n_{\rm cr,H}} + \frac{x_{\rm H_2}}{n_{\rm cr,H_2}}. \tag{D4}$$

$x_{\rm H}$ and $x_{\rm H_2}$ are the abundances of atomic and molecular hydrogen. As discussed by (Glover & Mac Low 2007) we take the values for $x_{\rm H}$ from Lepp & Shull (1983) with the modification from Martin et al. (1996) and the value for $x_{\rm H_2}$ from Shapiro & Kang (1987).

APPENDIX E: ADDITIONAL FIGURES: DUST CHEMISTRY

We show the corresponding molecular hydrogen fraction, $f_{\rm H2} = 2n_{\rm H2}/(n_{\rm H+} + n_{\rm H} + 2n_{\rm H2})$, vs. time in Fig. E1. The formation timescale of H_2 is given by $T_{\rm H2} = 1{\rm Gyr}/(n_{\rm H}/{\rm cm}^{-3})$ and for the density ρ_0 it is roughly 1 yr. We can see that both the blue and orange line of Fig. E1 complete the formation of H_2 well within the simulated time period.

APPENDIX F: ADDITIONAL FIGURES: STAR FORMING SETUP

Fig. F1 shows the emitted energy rate at a given wavelength for a stellar particle modeled according to §7. Everything part of the Lyman-continuum is left of the blue vertical line and emitted in the ionizing band. Everything to the right of the blue line is emitted in the non-ionising band. Although the hot spot accretion is emitted from a smaller area it dominates in the bolometric luminosity output due to its higher temperature (see fig. 10 upper right panel). γ is the fraction that is emitted in the ionising regime from the total luminosity output.

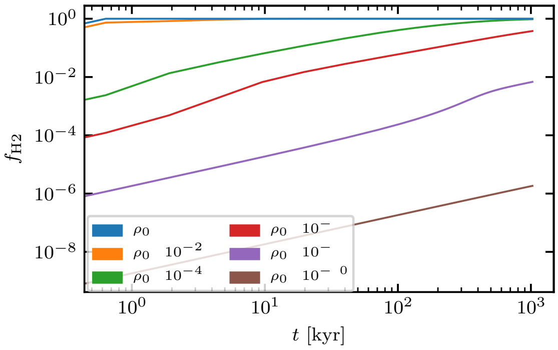

Figure E1. Molecular hydrogen fraction vs. time for dust chemistry setup in §5.3. The different lines show different densities used for the dust chemistry setup. Higher densities form molecular hydrogen faster than lower ones.

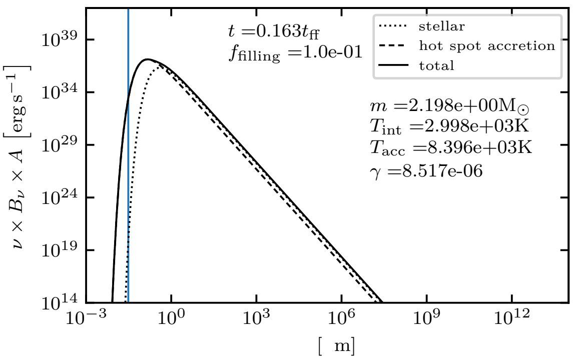

Figure F1. Stellar spectrum of the primary stellar particle at simulation time t. The y-axis is the resulting product of frequency, ν, Planck's law, B_ν, and the respective area from which the radiation is emitted, A. In the case of hot spot accretion we assume that the emission originates from f_{filling} times the area of the stellar object. The dotted line shows the purely stellar component and the dashed line shows the component due to hot spot accretion. The sum of both components is shown by the solid line. T_{int} and T_{acc} are calculated based on eq. 66 and eq. 67, respectively. γ is the fraction of the power that is emitted in the ionising regime from both the internal and accretion luminosity combined (see eq. 68).

APPENDIX G: RADIATION PRESSURE ACTING ON THE INTERIOR OF HII REGIONS

In this section we apply our scheme to the scenario of dusty HII regions and see if the scheme is producing expected outcomes. The work by Draine (2011) provides semi-analytical descriptions for such cases and we will use these as a reference.

Draine (2011) describe the interior of dusty HII regions in static equilibrium based on the following equation

$$n\sigma_d \frac{L_{\mathrm{n}} e^{-\tau} + L_{\mathrm{i}}\Phi(r)}{4\pi r^2 c} + \alpha_{\mathrm{B}} n^2 \frac{\langle h\nu\rangle_{\mathrm{i}}}{c} - \frac{\mathrm{d}}{\mathrm{d}r}(2nk_{\mathrm{B}}T) = 0\,, \quad \text{(G1)}$$

where n, σ_{d}, L_{n}, L_{i}, τ and $\Phi(r)$ are the proton density, dust opacity, neutral and ionizing luminosity, the optical depth and extinction of ionizing radiation, respectively. The quantity $\langle h\nu\rangle_i$ is the mean energy of a photon which is 18 eV in our case and r measures the radial distance from the source of ionizing photons. Eq. G1 assumes a constant dust to gas ratio everywhere and takes into account the radiation pressure on dust by ionizing and non-ionizing radiation (first term) and radiation pressure on gas gas by ionizing radiation (second term). Radiation pressure is opposed by thermal pressure (third term) which governs the static equilibrium.

Fig. G1 shows both semi-analytic predictions based on the work of Draine (2011) in dotted lines and the result from our code in solid line. While our solution has not reached its steady state, it matches the semi-analytic prediction (in-between red and purple dotted lines; $10^3 < Q_0 n_{\mathrm{rms}} < 10^4$; for $\gamma = 20$). The spikes are minor waves in the density field which is still adjusting for true static equilibrium. The different semi-analytic solutions are categorized based on the product of the number of ionising photons per second normalized to $10^{49}\,s^{-1}$ and the root mean square number density, which are labeled Q_0 and n_{rms}, respectively. The latter is calculated in the following way according to the work of Draine (2011)

$$n_{\mathrm{rms}} = n_0 \left(\frac{3}{y_{\mathrm{max}}^3} \int_0^{y_{\mathrm{max}}} \frac{1}{u^2} y^2 \mathrm{d}y \right)^{1/2}\,, \quad \text{(G2)}$$

where n_0 is the characteristic density scale,

$$n_0 = \frac{4\pi\alpha_{\mathrm{B}}}{Q_0} \left(\frac{2ckT}{\alpha_{\mathrm{B}} \langle < h\nu \rangle} \right)^3 . \quad \text{(G3)}$$

The dimensionless quantities u and y refer to the density and length scale

$$u = \frac{n_0}{n} \quad \text{(G4)}$$

$$y = \frac{r}{\lambda_0} \quad \text{(G5)}$$

with λ_0 being the characteristic length scale defined as

$$\lambda_0 = \frac{Q_0}{4\pi\alpha_{\mathrm{B}}} \left(\frac{\alpha_{\mathrm{B}} \langle h\nu \rangle}{2ckT} \right)^2 . \quad \text{(G6)}$$

Further the quantity γ is calculated in the following way

$$\gamma = \left(\frac{2ckT}{\alpha_{\mathrm{B}} \langle h\nu \rangle} \right) \sigma_{\mathrm{d}}, \quad \text{(G7)}$$

where our value of γ is roughly 15. The quantity γ refers to the dust opacity towards ionizing radiation. Note that we do not employ a constant dust opacity for non ionizing radiation in our scheme, which is a significant difference to the assumptions made by Draine (2011). Our dust opacity for ionizing radiation however is constant, namely $\sigma_{\mathrm{d}} = 1.5 \times 10^{-21}\,\mathrm{cm}^2\,\mathrm{H}^{-1}$. Our setup compares to the setup $10^3 < Q_0 n_{\mathrm{rms}} < 10^4$ and features $\gamma \approx 15$. We can see that our solution recovers features of both the purple and red dotted line.

This paper has been typeset from a TEX/LATEX file prepared by the author.

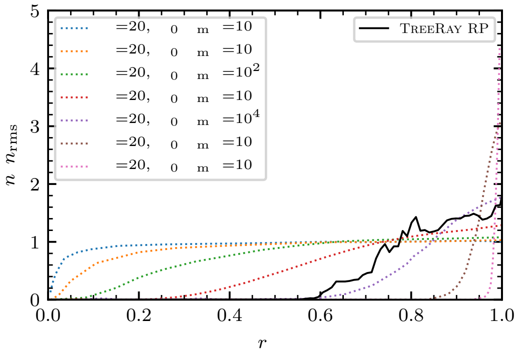

Figure G1. Radial profile showing the interior of an HII region taking into account radiation pressure. The plot shows the number density vs. radial distance. The solid line shows the curve obtained from our code and the dotted lines show semi-analytic models from Draine (2011) (see their Fig. 2).

7.2
Failed Ansätze

Flaws of the original scheme. The scheme as presented by Klepitko [2018] could not account for the fact that optically thick structures emit from their surface. This caused optically thick structures to artificially generate more emission than physical because these structures were smeared out over the entire angular size of individual rays. This problem occurred particularly at larger distances where the structures were small compared to the angular size of rays. Similarly, the approach overestimates extinction generated by optically thick structures as these should only contribute to extinction according to their geometric size. In the following, this behaviour is further elaborated. For a given spherical structure of radial size, R_s, and mass, M_s, one can estimate the surface density, Σ_s, as

$$\Sigma_\mathrm{s} = \frac{M_\mathrm{s}}{4\pi R_\mathrm{s}^2} \,. \tag{7.1}$$

Given an opacity, κ, the optical depth, τ_s, of the structure can again be estimated to be roughly

$$\tau_\mathrm{s} = \Sigma_\mathrm{s}\kappa \,. \tag{7.2}$$

Here, radiation traveling through the structure would experience an extinction, ϵ_s, by the structure to the following degree

$$\epsilon_\mathrm{s} = \exp\left(-\tau_\mathrm{s}\right) . \tag{7.3}$$

Assuming this structure to be smeared out over the solid angle of a single ray, $\omega_\mathrm{pix} = 4\pi/N_\mathrm{pix}$, for a total number of rays, N_pix, overestimates the extinction along the ray for the following reason. Given the structure to be located at a distance, D_s, its angular size, ω_s, can be approximated as

$$\omega_\mathrm{s} = 4\pi \times \frac{\pi R_\mathrm{s}^2}{4\pi D_\mathrm{s}^2} = \pi \times \frac{R_\mathrm{s}^2}{D_\mathrm{s}^2} \,, \tag{7.4}$$

where $R_\mathrm{s} < D_\mathrm{s}$ and ω_s is certainly smaller than ω_pix. If ω_s is now stretched to ω_pix, the perceived radius of the structure, R_pix, would translate to

$$R_\mathrm{pix} = D_\mathrm{s}\sqrt{\frac{4}{N_\mathrm{pix}}} \,. \tag{7.5}$$

From Eq. 7.5 one can again compute a perceived optical depth, τ_pix, of the smeared out structure and compare it to τ_s yielding

$$\frac{\tau_\mathrm{pix}}{\tau_\mathrm{s}} = \frac{R_\mathrm{s}^2}{D_\mathrm{s}^2} \times \frac{N_\mathrm{pix}}{4} \,. \tag{7.6}$$

The problem can be approached by switching to an idealized setup, as illustrated by Fig. 11. A ray is cast towards a group of stars providing radiation to compute the radiation field at the target position (red dot). Without any extinction one would receive a radiative intensity, $I_{\mathrm{no-ext}}\omega_\mathrm{pix} = I_0\omega_\mathrm{s}$ from the stars for the entire ray, where I_0 $\left[\mathrm{erg\,s^{-1}\,cm^{-2}\,sr^{-1}}\right]$ is the average radiative intensity per steradian caused by all

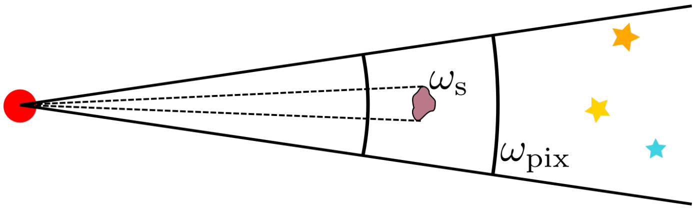

Figure 11: Idealized setup of a single clump of angular size, ω_s, sitting between a target point (red dot) and sources of radiation (stars) in a backwards ray-tracing scheme. The ray has a solid angle of size, ω_pix.

stars when smeared out over ω_pix. An optically thick object appearing smaller than ω_pix as shown in Fig. 11 (brown clump) should only affect the intensity contribution blocked by its "shadow". The expected intensity caused by the optically thick structure for the whole ray, $I_\mathrm{s}\omega_\mathrm{pix}$, can be stated as

$$I_\mathrm{s}\omega_\mathrm{pix} \quad = \quad I_0\left((\omega_\mathrm{pix}-\omega_\mathrm{s}) + \exp\left(-\tau_\mathrm{s}\right)\omega_\mathrm{s}\right) \ , \tag{7.7}$$

where one recovers $I_{\mathrm{no-ext}}\omega_\mathrm{pix}$ for ω_s approaching zero. Computing the intensity received from the entire ray for a smeared out structure, $I_\mathrm{pix}\omega_\mathrm{pix}$, yields

$$I_\mathrm{pix}\omega_\mathrm{pix} \quad = \quad I_0 \exp\left(-\tau_\mathrm{pix}\right)\omega_\mathrm{pix} \, . \tag{7.8}$$

The right hand side of Eq. 7.8 approaches zero as τ_pix increases indefinitely. Eq. 7.7 approaches $I_0(\omega_\mathrm{pix}-\omega_\mathrm{s})$ as τ_s grows on the right hand side. The outcome of Eq. 7.8 leads to an overestimation of extinction for compact, dense structures at large distances. Note that this behaviour is not pronounced for optically thin structures where $\tau_\mathrm{s} < 1$. One can compare both, Eq. 7.7 and Eq. 7.8 with the help of a Taylor series to first order in τ_s and τ_pix, respectively. One receives

$$\begin{aligned}
I_\mathrm{s}\omega_\mathrm{pix} &\approx I_0\left((\omega_\mathrm{pix}-\omega_\mathrm{s}) + \left(1-\tau_\mathrm{s}+\mathcal{O}\left(\tau_\mathrm{s}^2\right)\right)\omega_\mathrm{s}\right) && (7.9)\\
&\approx I_0\left(\omega_\mathrm{pix}-\tau_\mathrm{s}\omega_\mathrm{s}+\mathcal{O}\left(\tau_\mathrm{s}^2\right)\omega_\mathrm{s}\right) \ , && (7.10)\\
I_\mathrm{pix}\omega_\mathrm{pix} &\approx I_0\left(\omega_\mathrm{pix}-\tau_\mathrm{pix}\omega_\mathrm{pix}+\mathcal{O}\left(\tau_\mathrm{pix}^2\right)\omega_\mathrm{pix}\right) && (7.11)\\
&\approx I_0\left(\omega_\mathrm{pix}-\tau_\mathrm{s}\omega_\mathrm{s}+\mathcal{O}\left(\tau_\mathrm{pix}^2\right)\omega_\mathrm{pix}\right) \ , && (7.12)
\end{aligned}$$

where Eq. 7.10 and Eq. 7.12 show the same behaviour for optically thin structures when stretched and maintained in size, respectively[1]. From this, one can conclude that optically thick material requires a different treatment while optically thin material shows the correct behaviour.

ADAPTIVE RADIAL CONTAINERS. With the problem identified a promising solution are containers that catch these problematic optically thick structures as they occur during ray mapping (see §7.1 and §4.2 therein). These containers can be spawned along individual rays at arbitrary radial positions. The angular size of optically thick structures could then be inferred from the volume mapped to these containers such that adequate emission and absorption behaviours could be reproduced. Such an algorithm has been implemented in the course of the thesis, and it was observed that it performs well for isolated optically thick structures. However,

---

[1] The set of Eq. 7.9 to 7.12 have only been mentioned in this theses and so is the whole idea of this paragraph.

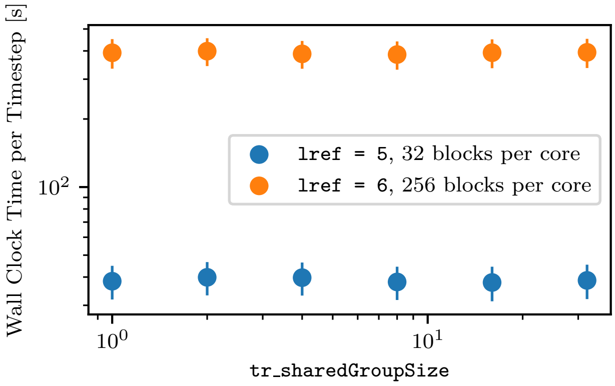

Figure 12: Wall-clock time per timestep vs. the number of shared memory allocations per compute node given by the parameter `tr_sharedGroupSize`. Using fewer shared memory allocations may cause performance issues due to cache conflicts while more processors try to access the same memory space. The performance test was run on the HPE Apollo (HAWK) cluster of the High-Performance Computing Center in Stuttgart running the AMD EPYC™ 7742 processors. Overall, the performance is not affected by the number of processors sharing their memory in this example.

this idea was rejected as more complicated setups as, for example, the star-forming setup of §7.1 requires many such containers to be employed. Thus, an additional search is necessary during mapping to find the correct radial container for a given contribution of optically thick material. This additional search is infeasible if many such containers are employed, resulting in potentially worse computational complexity than $N\log(N)$. At the expense of additional memory, the search can be omitted by tracking both the optically thin and thick content within nodes and mapping both to rays simultaneously. This approach is the final result of this thesis, as presented in §7.1.

7.3
SHARED MEMORY EXTENSION

MEMORY PROBLEM. In the course of Paper I, optimizations towards better memory efficiency of TREERAY were necessary to continue running on recent supercomputers in a feasible way. TREERAY uses kernels to map contributions from the AMR grid onto rays. These kernels are expensive to compute on-the-fly such that they are computed once in the beginning and stored in memory for discrete values instead. This technique is referred to as a ’lookup table’ and replaces complex runtime calculations with simple array index operations. To maintain accuracy, the kernels must be stored in great detail. Because FLASH is using the MPI standard, each of the kernels is allocated once per core of a given CPU. Thus, each core will lose a significant portion of its memory budget due to the allocation of kernels. A typical memory budget per core is 2 GB on recent machines (see JUWELS at the Jülich Supercomputing Centre, SuperMuc-NG at the Leibniz Rechenzentrum or HAWK at the High-Performance Computing Center in Stuttgart). Making use of the shared memory feature of the recent MPI versions, one achieves to lower the memory consumption per core to meet the demands of 2 GB per core.

TOTAL MEMORY SAVINGS. In total, two groups of kernels aid the mapping process of nodes in TreeRay. One group holds coefficients to split nodes across different rays during node mapping, and the other holds coefficients for the radial evaluation points along individual rays. The former is rather small in memory and has the following number of entries

$$N_{\text{angular}} = N_{\text{pix}} \times (N_{\phi} + 1) \times (N_{\theta} + 1) \times N_{\text{node-size}}, \tag{7.13}$$

where N_{pix}, N_{ϕ}, $N_{\backprime}$ and $N_{\text{node-size}}$ are the number of rays, number of precalculated points along ϕ-direction and θ-direction and the number of relative node sizes, respectively. The array entries N_{ϕ} and N_{θ} encode the position in angular space similar to (ϕ, θ) in spherical coordinates and the relative node size is accounted for by $N_{\text{node-size}}$ to track accurate mapping of nodes on different levels. The first parameter, N_{pix}, holds coefficients to individual rays for instances of the three previously mentioned parameters. A typical value is $N_{\text{angular}} = 1272960$ entries which corresponds to roughly 10 MB per core at double precision (for 48 rays). Given the small size of the angular lookup table, the memory savings would be on the order of 470 MB for the entire node if all processors of a node with 48 cores would share a single allocation in their memory. Upon sharing the angular lookup table, a strong performance drop was observed caused by high traffic on small regions in memory. It is the very memory that was shared across different processors. The other group of kernels dealing with intersections in radial directions are larger; therefore, such a bottleneck is not likely. Each ray has a total number of evaluation points, N_{rad}, given by

$$N_{\text{R}} = \left\lceil N_{\text{ray-rad}} \sqrt{2 * \frac{D_{\text{ray-max}}}{D_{\text{min-cell}}}} \right\rceil, \tag{7.14}$$

where $N_{\text{ray-rad}}$, $D_{\text{ray-max}}$ and $D_{\text{min-cell}}$ are a user-defined resolution (typically $_{\text{ray-rad}} = 2$), the maximum ray length and the minimum cell size present in the computational domain. The bracket around the expression of N_{R} indicates that its interior is rounded up. By default, $D_{\text{ray-max}}$ is set to the maximum distance found inside the computational domain. In this instance and for a cubical domain, one can approximate the square-root as

$$\sqrt{2 \frac{D_{\text{ray-max}}}{D_{\text{min-cell}}}} = \sqrt{\sqrt{3} \times 2^{l_{\text{ref}}+3}}, \tag{7.15}$$

where l_{ref} is the refinement level inside FLASH[2]. Especially for high-resolution runs, N_{R} can become large. In total, the radial kernel has a size of N_{radial}, and its size is given as

$$N_{\text{radial}} = N_{\text{R}} \times (N_{\text{fine-R}} N_{\text{R}}) \times (l_{\text{ref}} + 3), \tag{7.16}$$

where $N_{\text{fine-R}}$ is the number of distances between two radial points. Typical production scale simulations reach l_{ref} greater than 10. At $l_{\text{ref}} = 10$, N_{radial} holds 56857500 entries which yields 454 MB for a single allocation in double precision (64 bit accuracy). Thus, on a typical node consisting of 48 processors (see JUWELS or SuperMUC), the saved memory is as high as almost 21.5 GB per node by employing shared memory. Fig. 12 shows a benchmark for different allocations per node used in shared memory. The parameter, `tr_sharedGroupSize`, denotes

---

[2] The number of cells along one dimension is $8 \times 2^{l_{\text{ref}}-1}$.

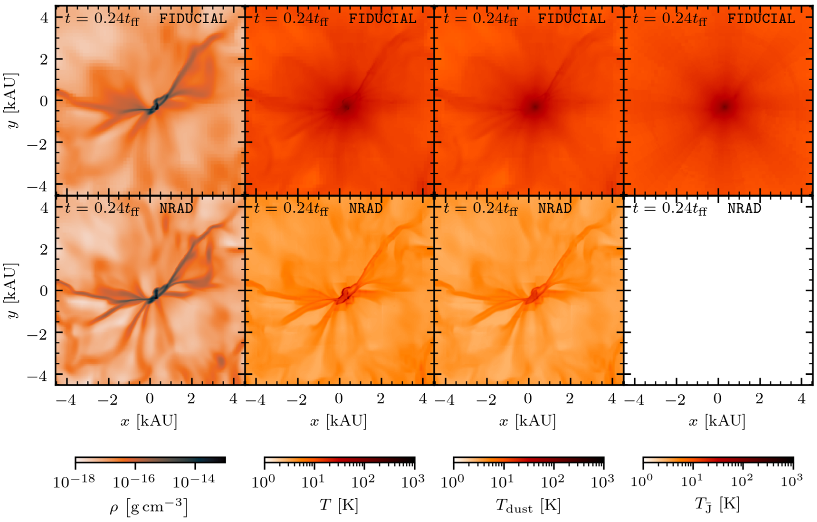

Figure 13: Slices showing the density and three different temperatures for gas, dust and radiation of two runs presented in §7.1. The runs are organized in rows showing the `FIDUCIAL` run and the `NRAD` run in the top and bottom row, respectively. The `FIDUCIAL` run uses TreeRay/RadPressure while `NRAD` does not. With that, dust is allowed to cool in an optically thin manner in the run `NRAD` resulting in colder dust and, thus, colder gas temperatures. Ultimately, the run `NRAD` shows greater densities and finer structure due to lower Jeans masses.

the number of allocations per shared memory space, such that lower values of `tr_sharedGroupSize` correspond to more processors accessing the same allocation. The points presented in Fig. 12 show no impact on performance concerning the parameter `tr_sharedGroupSize` and therefore highlight a performance conserving enhancement of the memory consumption.

7.4
Further Comparison of TreeRay/RadPressure

Purpose of this section. To highlight the scheme's impact, additional runs were performed in the course of §7.1. Further comparison of the different runs is carried out within this section to understand the novel scheme's impact. In total, three additional runs were performed. These include a run without radiation pressure acceleration, `NARP`, a run without radiation pressure acceleration and any radiation from stars, `NARPNFE`, and a run without any RT at all, `NRAD`. All these runs stand in contrast to the `FIDUCIAL` run having all available physics enabled.

Removing dust RT. The biggest contrast with respect to the `FIDUCIAL` is seen if all of the RT is turned off. In this instance, dust is allowed to cool as if it was optically thin. This translates to an optically thin cooling rate, $\Lambda_{\rm thin}$, of

$$\Lambda_{\rm thin} = \rho 4\sigma\kappa_{\rm P}(T_{\rm dust})T_{\rm dust}^4, \tag{7.17}$$

where we emphasize that the Planck-opacity is dependent on $T_{\rm dust}$ as stated in §7.1. With TreeRay/RadPressure, however, dust is reheated by emission from elsewhere. In return, the net cooling rate is muffled or may even flip its sign and

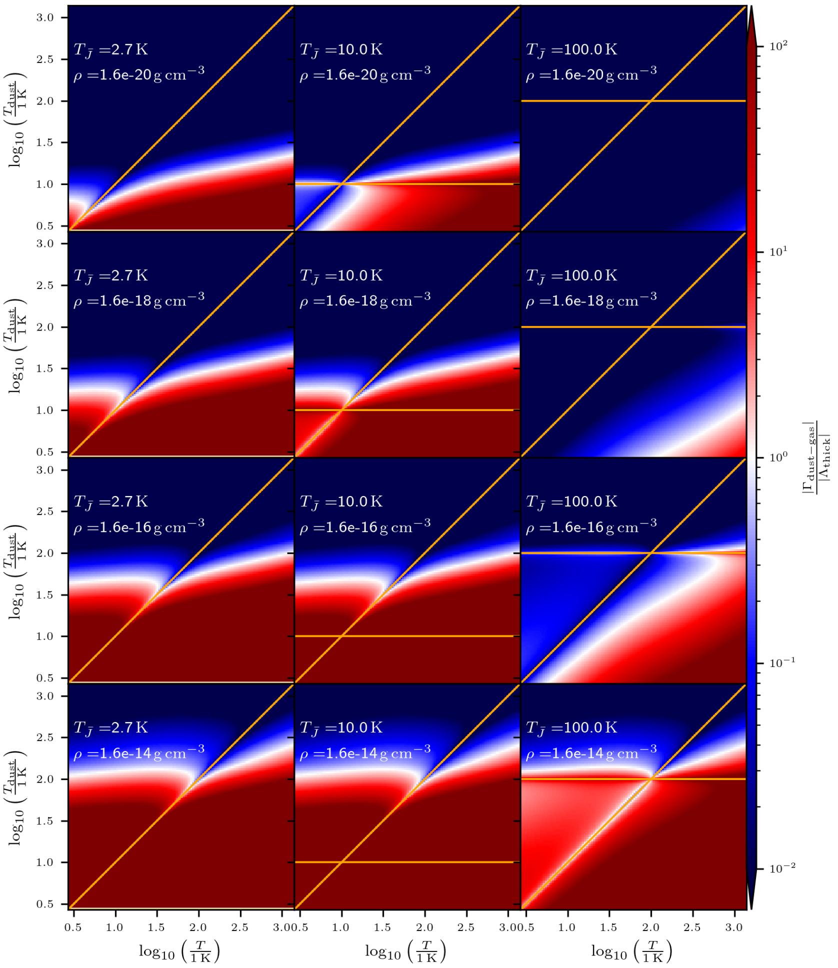

Figure 14: Diagrams comparing the strength of dust gas coupling and radiative heating and cooling for different pairs of dust and gas temperatures. Different panels show different environmental conditions given by the density and radiation temperature. The qualitative shape of the plot changes for different environmental parameters. The orange lines show the radiation temperature (horizontal) and the dust and gas temperature 1-to-1 line (diagonal), respectively. Regions of equal rates (white) show comparable rates where only the two narrow cones (angel less than 90 degrees) formed by the orange lines are allowed physical solutions.

turn into a heating rate. This more accurate cooling rate, Λ_{thick}, is given by

$$\Lambda_{\text{thick}} = \rho 4\sigma\kappa_{\text{P}}(T_{\text{dust}})(T_{\text{dust}}^4 - T_{\bar{J}}^4)\,, \tag{7.18}$$

where $T_{\bar{J}}$ is the radiation temperature. Eq. 7.18 is derived by taking the difference of the thermal cooling and heating rates $\Lambda_{\text{BB-cool}}$ and $\Gamma_{\text{BB-heat}}$ from §7.1, where $\bar{J}$ has been expressed in terms of the radiation temperature, $T_{\bar{J}}$. Eq. 7.17 and Eq. 7.18 will contribute to the dust temperature calculation in different ways. Eq. 7.17 will overestimate radiative cooling by dust immensely. In fact, it will be larger by the term $\Gamma_{\text{BB-heat}}$. Given that $\Gamma_{\text{BB-heat}}$ is a result of the RT calculation and therefore not a local approximation, the resulting cooling rate, Λ_{thick}, models radiative interactions of dust more realistic. In addition, dust is coupled to gas via collisional coupling, as mentioned in 7.1. This mechanism transfers thermal energy from gas to dust or vice versa and is given by Eq. 2.15 as a heating rate, $\Gamma_{\text{dust-gas}}$. Fig. 13 shows the `FIDUCIAL` run and the `NRAD` run where the latter is lacking RT of non-ionizing radiation following Eq. 7.17. The resulting dust temperature is substantially lower and therefore cools gas via collisional coupling more efficiently. In the further course of this section, the relative strength of Λ_{thick} and $\Gamma_{\text{BB-heat}}$ towards a final dust temperature are analyzed.

Comparing optically thin and thick cooling with collisional coupling. A comparison of Λ_{thick} and $\Gamma_{\text{dust-gas}}$ is shown in Fig. 14 for different densities, ρ, and different radiation temperatures, $T_{\bar{J}}$. The colours show the absolute values of the ratio of $\Gamma_{\text{dust-gas}}$ and Λ_{thick} as a function of the dust and gas temperature, where red regions highlight dust-gas coupling to dominate while blue regions show the opposite. In each panel, two orange lines are shown to guide the eye. Regions located above the horizontal line, marking $T_{\text{dust}} = T_{\bar{J}}$, show where dust can cool radiatively. Dust is radiatively heated for values below the horizontal line. The orange 1-to-1 line divides the parameter space into regions where dust is colder (below the line) and hotter (above the line) than gas, respectively. As energy is transferred from the hotter to the colder medium, these regions correspond to gas being cooled or heated by dust. As the density increases in the panels from top to bottom, the role of dust gas-coupling becomes more important, showing more regions associated with greater absolute values of $\Gamma_{\text{dust-gas}}$. Going to higher values of $T_{\bar{J}}$ from left to right, the relative strength of $\Gamma_{\text{dust-gas}}$ gets muffled, indicated by regions of fully red saturation getting fainter and even shifting to blue. Out of all regions shown in the panels, only those regions where T_{dust} is squeezed between $T_{\bar{J}}$ and T are physically allowed regions for the dust temperature to settle. These regions can be identified as the two narrow cones formed by the two lines (lower left and upper right cones formed by the intersection point of the two lines). Inside these cones, dust will take the solution where $|\Gamma_{\text{dust-gas}}| = |\Lambda_{\text{thick}}|$, namely its equilibrium temperature between the heating and cooling rates (white line). For cones that are only blue, the solution is given by the horizontal line where $T_{\text{dust}} = T_{\bar{J}}$, and therefore Λ_{thick} approaches zero such that the two rates become comparable. For red cones, equilibrium is given by the 1-to-1 line because $\Gamma_{\text{dust-gas}}$ approaches zero, and both rates become comparable, again. From this plot, one can see that the dust temperature does not always follow the 1-to-1 line at densities greater than $10^{-18}\,\text{g}\,\text{cm}^{-3}$. Rather, it is a matter of column densities setting whether a region is saturated in radiation temperature along all directions (embedded) or not. In addition, one can see the difference in the resulting dust temperature for no RT and, therefore, optically thin cooling ($T_{\bar{J}} = 2.7\,\text{K}$) by comparing the left column with the other two columns. In the case of no RT, dust will follow the 1-to-1 line until radiative cooling is stronger than the dust gas coupling. In this way, dust cooling by radiation is overestimated. Given that, $\Gamma_{\mathrm{dust-gas}} \propto (T - T_{\mathrm{dust}})$, lower dust temperatures will gas the dust gas coupling to be overestimated as well, such that too much cooling is acting on gas.

Dust RT vs stellar particles. In the following, RT from dust alone is compared to the addition of protostellar sources. Fig. 15 to Fig. 17 show slices of the radiation, dust and gas temperatures for the runs `FIDUCIAL`, `NARP` and `NARPNFE`. Comparing the radiation temperature among all three runs in Fig. 15, one finds similar appearances across the three runs at larger distances. This suggests that the radiation generated by dust through collisional coupling to gas is the dominant radiation source during the simulated times. The energy for this radiation is generated by converting gravitational energy to thermal energy. At $t = 0.2\,t_{\mathrm{ff}}$, `FIDUCIAL` and `NARP` show a slightly hotter $T_{\bar{J}}$ within the central hub hosting the most massive star when compared to then run without any stellar feedback, `NARPNFE`. However, this difference does not translate to hotter radiation temperatures further out. Proceeding to the dust temperature, as shown in Fig. 16, one sees a similar behaviour suggesting that the dust is dominated by the radiative interaction heating-cooling rate given by Λ_{thick} (see Eq. 7.18). This behaviour is consistent with the gas temperature being different to the dust and radiation temperature. Looking at Fig. 17, one finds colder gas further out and hotter gas near the central part deviating from the dust temperature.

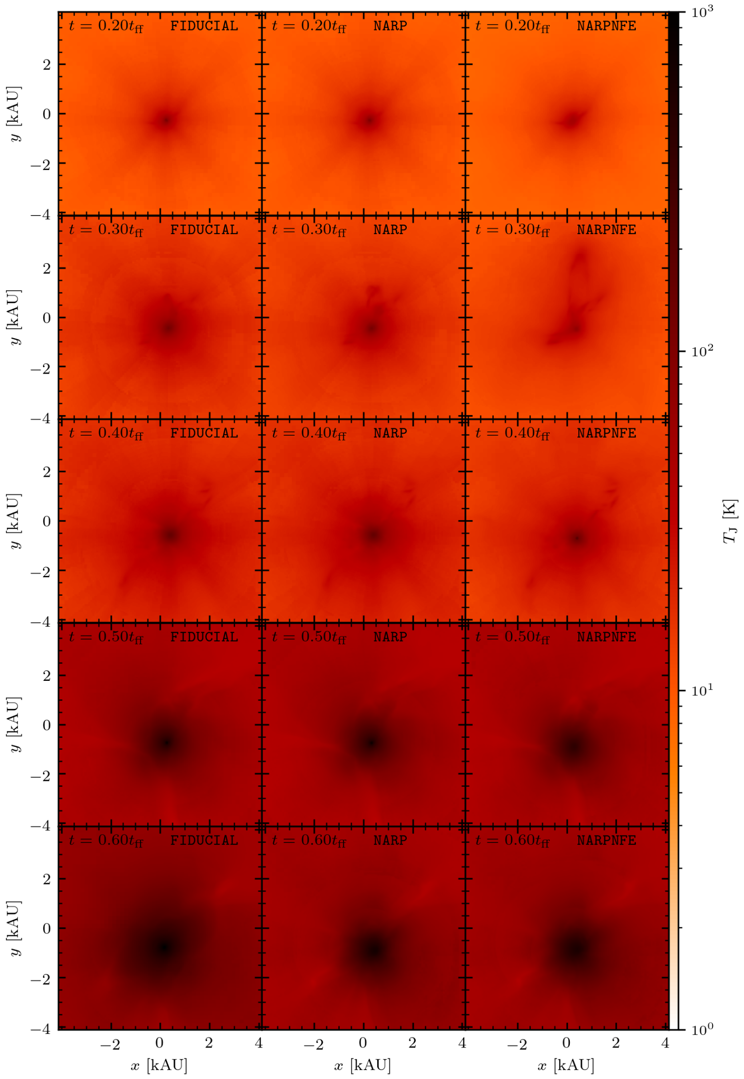

Figure 15: Slices showing the radiation temperature of the radiation field for the star forming setup presented in §7.1. The panels are organized in rows for similar times and show runs with different physics included across columns. These runs include a run with all physics (`FIDUCIAL`), a run where accelerations from RP are disabled (`NARP`) and a run where both accelerations from RP and any type of radiation from stars is switched off (`NARPNFE`). The runs `FIDUCIAL` and `NARP` are similar throughout time. `NARPNFE` is similar for $t \leq 0.4t_{\rm ff}$ but shows lower radiation temperatures throughout for later times. This is especially the case for $t \geq 0.5t_{\rm ff}$ in the central region once the most massive star located in the center reaches greater luminosities.

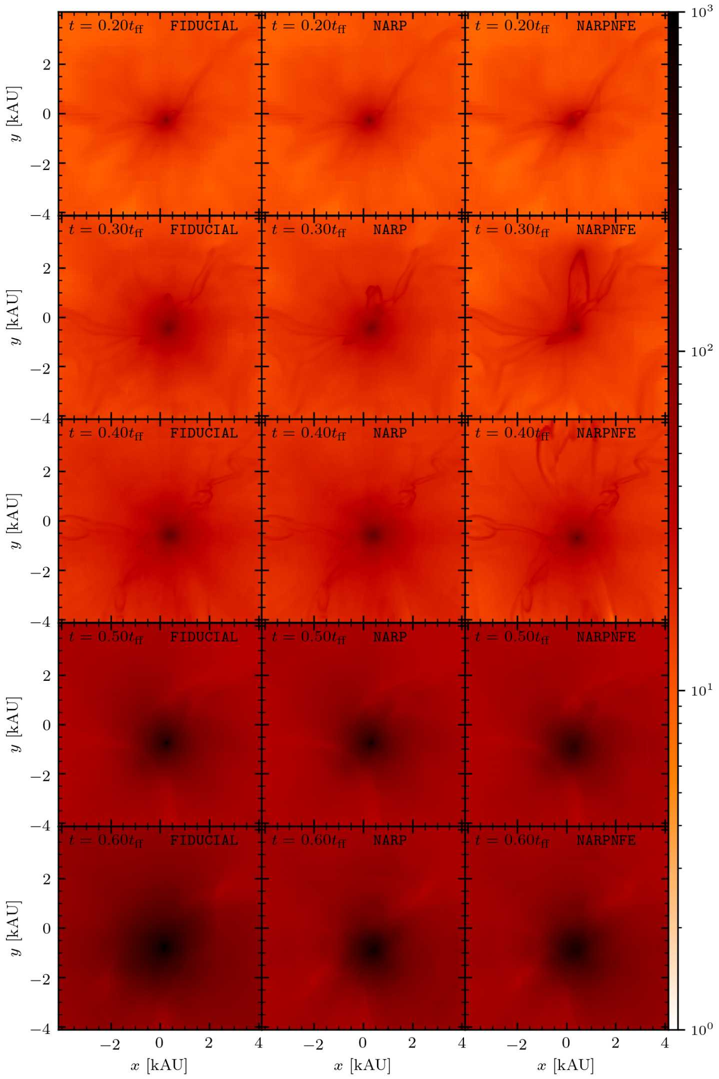

Figure 16: Same as Fig. 15 except that the dust temperature is shown here. Similar to Fig. 16 the run `NARPNFE` appears colder than `FIDUCIAL` and `NARP`. As described in §7.1, the dust temperature is coupled to both the radiation field and the gas. The influence of radiation heating the dust can be seen clearly by comparing the radiation temperatures in Fig. 15 to the corresponding panels of this Fig.

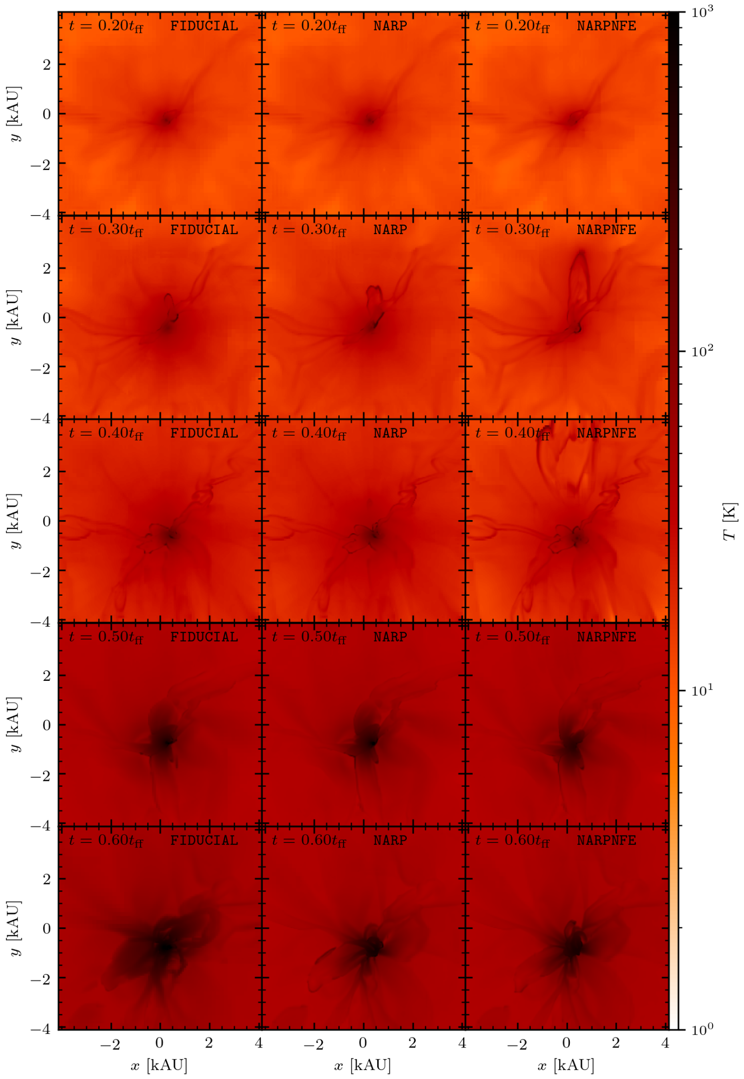

Figure 17: Same as Fig. 15 but the gas temperature is shown here. Gas is coupled to dust in an exchange of thermal energy which makes it indirectly coupled to the radiation field provided by TreeRay/RadPressure (see §7.1. We can see slightly hotter gas at $t \geq 0.5t_{\rm ff}$ for the runs that include stellar feedback from the stars (`FIDUCIAL` and `NARP`) compared to the runs that do not include it (`NARPNFE`). However, at times $t \leq 0.4t_{\rm ff}$ all runs have similar temperatures as the central star is not liminous enough.

8

THE IMPACT OF METALLICITY ON MASSIVE STAR FORMATION: IT IS ALL ABOUT THE DUST!

Descriptive metadata. Within this chapter, the scheme developed in §7 is employed to investigate the role of metallicity in massive star formation on the scales of cores. The star-forming setup of §7 is taken and varied in metallicity. The numerical simulations and scientific conclusions part of this chapter are only possible through the scheme developed in §7.

8.1
PUBLICATION

A. **Klepitko** and S. Walch. The Impact of Metallicity on Massive Star Formation: It is all about the Dust! Unpublished Manuscript, 2022

Within the second publication of this thesis, I present a scientific application of the RT scheme developed in §7 [**Klepitko** et al., 2023]. Here, the aim lies in understanding the impact of metallicity in the context of MSF. In particular, its impact on fragmentation via cooling and the relative strength of RP and ionizing feedback are of interest.

Contribution overview of Co-Authors
Prof. Dr. Stefanie Walch-Gassner engaged in helpful discussions. All implementations, the data analysis and the underlying simulations where carried out by **Andre Klepitko**. The manuscript has largely been written by **Andre Klepitko**.

MNRAS **000**, 1–15 (2022) Preprint 25 June 2023 Compiled using MNRAS LATEX style file v3.0

The Impact of Metallicity on Massive Star Formation: It is all about the Dust!

A. Klepitko[1]★, S. Walch[1,2]†
[1] *I. Physikalisches Insitut, Universität zu Köln, Zülpicher Str. 77, 50937 Köln, Germany*
[2] *Center for data and simulation science, University of Cologne, www.cds.uni-koeln.de*

Manuscript in preparation.

ABSTRACT

The impact of metallicity on the formation of massive stars and the shape of the initial mass function is not fully understood. We investigate the role of metallicity on massive star formation in highly subvirial collapsing cores of 150 $\mathrm{M}_\odot$. We model radiation pressure on dust and gas along with ionising radiation. We employ a chemical network to compute the chemical evolution of hydrogen and equilibrium dust temperatures. The radiative transfer algorithm TreeRay accounts for the self-shielding and emission of dust during RT. We find greater metallicities to enhance fragmentation. Numerical evidence supports that increased metallicities lead to the formation of more "low-mass" stars. We find radiation pressure to be stronger for greater metallicities and, therefore, higher dust-to-gas ratios. At the considered scales, radiation pressure presents the dominant feedback compared to ionising radiation. Radiation pressure may aid ultra-compact HII regions to grow beyond what is achieved by a D-type expansion. In our simulations, disks around the principal star form at all metallicities, and the disk in the lowest metallicity case is the most stable.

Key words: Massive Star Formation – Metallicity – Radiation Pressure – Ionizing Radiation – Fragmentation – Isolated Core Collapse

1 INTRODUCTION

Massive star formation. Massive star formation (MSF) takes place deeply embedded in the densest parts of molecular clouds under extreme conditions. Sites of MSF are rare and far away from our solar system compared to places of low mass star formation, so observations of the ongoing process are difficult. One of MSF's most well-known and closest sites is the Orion Nebula (M42, or NGC1976), where Fujita et al. (2021) propose cloud-cloud collisions to cause fruitful conditions for MSF. The most massive stars currently known are located in the Tarantula Nebula (30-Doradus) within the Large Magellanic Cloud (see Doran et al. 2013; Hainich et al. 2014; Bestenlehner et al. 2020) reaching masses of 200 $\mathrm{M}_\odot$. Typical timescales and accretion rates present in MSF are on the order of 10^5 yr and upwards of 10^{-4} $\mathrm{M}_\odot\,\mathrm{yr}^{-1}$ (McKee & Tan 2003).

Feedback during formation. To this day, it is not understood how feedback from massive stars regulates their own formation process. During their formation, massive stars impact their environment via protostellar outflows, stellar winds, photoionization, radiative heating and radiation pressure (RP) (see Matzner & McKee 2000; Kuiper et al. 2012; Rosen et al. 2020; Klepitko et al. 2023, and others). In addition, the habitat in which massive stars form may also host companion stars. These stars may prevent fragmentation through radiative heating in their surroundings and assist in feeding the principal star gas that would otherwise form stars (Krumholz & McKee 2008). Eventually, the feedback of massive stars may disrupt their natal environment and remove gas from it by driving HII regions on 100 pc scales. Before that, however, massive stars spend a significant lifetime of their main-sequence hosting ultra-compact HII regions (Wood & Churchwell 1989). The hot ionized gas is thought to be confined by in-falling material, stopping the further expansion of the ionized bubble. Indeed, other feedback processes may be involved in boosting the expansion of such ultra-compact HII bubbles beside the thermal pressure of the ionized gas.

Metallicity and massive star formation. We study the environmental parameter of metallicity, Z, which is expected to favour fragmentation via cooling by metal lines and dust (see Omukai 2000; Schneider et al. 2003; Omukai et al. 2005, and others). The stellar initial mass function (IMF) (see Salpeter 1955; Kroupa 2002; Chabrier 2003) shows a tendency towards more massive stars at lower metallicities in numerical simulations (Clark et al. 2008; Dopcke et al. 2011) in accordance with the theory and early predictions (Abel et al. 2002; Bromm et al. 2002). The work of Chon et al. (2021) suggests a return from a top-heavy IMF, an IMF where MSs are more abundant than usual, to the present day IMF for $Z < 0.1\,Z_\odot$. Because metallicities above $0.1\,Z_\odot$ may ultimately limit the mass reservoir of massive stars through the formation of low mass stars in their proximity (Chon et al. 2021). We also investigate the role of the dust-to-gas ratio (DGR). In particular, its influence on the trapping of infrared radiation and the implied boosting factor with it, as greater DGR increases the infrared opacity per unit mass of gas. At higher dust to gas ratios, additional trapping of infrared radiation may ultimately boost RP from reprocessed radiation. To our knowledge, no such study exists on the scales of individual cores of sizes 0.2 pc in diameter.

★ E-mail: klepitko@ph1.uni-koeln.de
† E-mail: walch@ph1.uni-koeln.de

© 2022 The Authors

Table 1. Table of simulation parameters.

Name	velocity dispersion [km/s]	mass [$M_\odot$]	radius [pc]	virial parameters	$t_{\rm ff}$ [kyr]	Z	$f_{\rm d}$
`SMC`	0.42	150	0.1	0.14	42.3	0.1	1×10^{-3}
`LMC`	0.42	150	0.1	0.14	42.3	0.4	4×10^{-3}
`SOL`	0.42	150	0.1	0.14	42.3	1	1×10^{-2}

Boost factor for radiation pressure. RP originating from reprocessed radiation of dust has been put forward to play an important role in MSF. While direct radiation from stars with luminosity, L, may inject momentum per unit time directed radially outwards on the order of

$$\dot{P}_{\rm direct} \approx \frac{L}{c}\,, \tag{1}$$

with c being the speed of light, reprocessed radiation may boost the strength of RP by a factor of the optical depth, τ (see, e.g. Hopkins et al. 2011; Costa et al. 2018, and others). We can express τ as a product of the opacity, κ, and the surface density, Σ, such that we can state the radial momentum injected per unit time from reprocessed radiation as

$$\dot{P}_{\rm reprocessed} \approx \tau \dot{P}_{\rm direct} \approx \kappa \Sigma \dot{P}_{\rm direct}\,. \tag{2}$$

The optical depth may become larger depending on the compactness of the material embedding the massive stars. The same mass distributed over a smaller volume would lead to a higher surface density. Similarly, the opacity may be enhanced by a more compact geometry as hotter dust and gas lead to reemission in shorter wavelengths with greater opacity than longer wavelengths. A more direct variable in setting the infrared opacity per unit mass of dust-gas mixture is given by the DGR, $f_{\rm d}$, since dust is a major reacting agent for interactions with infrared radiation.

Outline of this work. We explain the numerical methods and initial conditions relevant to this work in §2. We present the results in §3, where we link cooling via radiation to fragmentation in §3.1 and show the aftermath of fragmentation on multiplicity and accretion rates §3.2. Next, we highlight differences in RP and ionising feedback across metallicities in §3.3. Finally, we show a disk forming around the principal massive star in all runs and its destruction by RP in §4.

2 NUMERICAL METHODS AND INITIAL CONDITIONS

Broad summary. We use the same numerical methods as described by Klepitko et al. (2023) in this work. These methods are opted to model star formation under self-gravity and arising radiative feedback processes self-consistently. The radiative feedback processes encompass ionising radiation and infrared radiation from stars and reprocessing infrared radiation from dust. RP on gas from ionising radiation and RP on dust from both ionising and non-ionising radiation are included.

Brief overview of the methods. We use the hydrodynamics code flash 4.3 (Fryxell et al. 2000) along with a tree-based gravity module (Wünsch et al. 2018) and the radiative transfer module TreeRay (see Wünsch et al. 2021; Klepitko et al. 2023) for both ionising and non-ionising radiation and RP. We model the evolution of H_2, H, H^+, CO, C^+ and O with a non-equilibrium chemical network based on (Glover & Mac Low 2007) and described in detail by Walch et al. (2015). We have introduced modifications to the dust thermochemistry that allows for modelling of cooling by infrared radiation by taking into account emission from surrounding dust and therefore limiting the cooling efficiency in embedded regions (see their section 7.3.1 in Klepitko et al. 2023). In addition, regions which are not embedded are free to cool in an optically thin manner. The chemical reaction rates of the network are based on Nelson & Langer (1997). We allow for the self-consistent formation of sink particles which are evolved in time using a Hermite integrator as described by Dinnbier & Walch (2020). We combine the sink formation criteria from Federrath et al. (2010) with an additional criterium from Clarke et al. (2017), which guarantees that the local free-fall-time of a volume is smaller than the time for the volume to be accreted by any other sink particle (see Klepitko et al. 2023, for the complete set of criteria). Sink particles forming within our simulation are modelled to be protostellar objects (Klassen et al. 2012). We split their luminosity into an ionising and non-ionising contributions. We accomplish this by taking the Stefan-Boltzmann temperature of the radiation and computing the respective fraction that would be emitted in ionising and non-ionising radiation as described in Klepitko et al. (2023). Note that an individual temperature is calculated for both the stellar and accretion luminosity. The latter luminosity assumes a hotspot accretion model with a filling factor of 0.1 in agreement with Calvet & Gullbring (1998). Details on the splitting of luminosities are given by Klepitko et al. (2023).

Emphasise on radiative transfer. The radiative transfer method TreeRay computes the radiation field via backwards ray-tracing using the HEALPix algorithm from Górski et al. (2005). For ionising radiation, we consider only protostellar objects to be sources. They are represented by sink particles within our simulation. The ionising radiation is treated in the On-The-Spot approximation and is extincted by gas. Regarding non-ionising radiation, we consider both protostellar objects and dust to be sources of radiation. Here, dust is assumed to be perfectly mixed with gas throughout the computational domain at a constant dust-to-gas mass ratio, everywhere, $f_{\rm d} = \frac{1}{100} Z$. The algorithm TreeRay allows us to efficiently obtain a radiation field by considering all cells in the domain as a source. That way, we include RP on dust and gas and radiative cooling and heating by dust. The method allows us to recover both limits for radiative cooling by dust. In one instance, dust can cool gas due to a lower surrounding radiation temperature. In the other instance, dust cannot do so because it is sufficiently embedded in equally hot dust. We use a Planck-weighted mean opacity based on the work of Semenov et al. (2003) and stated in the work of Krumholz & Thompson (2012). We apply a slight modification to account for varying DRGs, where we assume that the dust to gas ratio is proportional to the metallicity. The opacity per gram of gas is given by

$$\kappa_{\rm P}(T, Z) = 10^{-1}\,\frac{Z}{Z_\odot}\,\frac{\rm cm^2}{100\,{\rm K}^2\,{\rm g}} \times \begin{cases} T^2 & \text{for } T < 150\,{\rm K} \\ 150^2 & \text{else} \end{cases}\,, \tag{3}$$

where T and Z are the dust temperature and metallicity, respectively.

Initial Conditions. The setup used in this work is similar to that of Rosen et al. (2019) and is the same as used in the work of Klepitko et al. (2023). We model the collapse of a 150 $M_\odot$ massive core that follows an initial density power-law $\rho(r) \propto r^{-3/2}$ out to a radius of $r_{\rm c} = 0.1$ pc. The power-law is evaluated at the center of each cell inside the computational domain. The computational domain is 0.4 pc across and initially refined by 128 cells in each direction. We allow for five additional levels of adaptive refinement such that we resolve 20 AU. The initial gas temperature is set to 20 K inside and 2000 K outside of the core. We set the density of the ambient medium such that the core is pressure confined at the boundary ($P(r_c) = P(r > r_c)$). We set the initial velocity to a turbulent field with a one dimensional velocity dispersion of $\sigma_{1D} = 0.42\,\mathrm{km\,s^{-1}}$, such that we recover a virial parameter of 0.14. Using these initial conditions, we generate 3 different setups, with metallicities $Z_{\mathrm{SMC}} = 0.1\,Z_\odot$, $Z_{\mathrm{SMC}} = 0.4\,Z_\odot$, and $Z_{\mathrm{SOL}} = 1.0\,Z_\odot$, respectively. These metallicities correspond to the Small Magellanic Cloud (SMC) (Choudhury et al. 2016), the Large Magellanic Cloud (LMC) (Choudhury et al. 2018) and solar metallicity, respectively. The metallicities could also be representative for for massive-star-forming regions outside of the solar circle. The DGR in each of the three setups is taken such that

$$f_d = \frac{Z}{Z_\odot} \times \frac{1}{100}, \tag{4}$$

where Z is the respective metallicity of the setup. We summarize the most important simulation parameters in Tab. 1.

3 RESULTS

Morphological evolution. The three different runs, `SMC`, `LMC` and `SOL`, start with the same initial conditions including the tubulent velocity seed except for their metallicity and DGR. Doing it this way allows us to study the differences induced by changing the metallicity. The turbulent velocity field disturbs the initial spherically symmetric density distribution such that gas is compressed or rarefied depending on converging or diverging velocity streams. Early on, all three runs form a sink particle in the densest region in the centre at around $t = 0.1\,t_{\mathrm{ff}}$. This central hub is continuously fed by infalling gas via filamentary concentric streams. We show column density plots for different times in Fig. 1. Here, we can qualitatively see more fragmentation in the higher metallicity runs, which can be explained by the enhanced cooling at greater metallicities (see Omukai 2000; Schneider et al. 2003; Omukai et al. 2005, and others). Fig. 2 shows the total gas mass available for all three runs. The total gas mass is converted to stellar mass with comparable efficiency for all three runs. In further detail, we analyse the degree of fragmentation associated with each metallicity in §3.1. At later times we find feedback from the central star shaping the hub. The primary feedback of RP is catalysed by higher metallicities and a greater DGR. RP tends to be more powerful than ionising feedback on the considered scales. We find a slightly more efficient trapping of radiation resulting in a boost of RP in the higher metallicity runs. We show a detailed analysis in §3.3.

3.1 Temperature Regulated Fragmentation

Radiation temperature. To aid the analysis of this work concerning radiative cooling, we define the radiation temperature, T_{rad}, in the following way

$$T_{\mathrm{rad}} = \left(\frac{\pi J}{\sigma}\right)^{1/4}, \tag{5}$$

where J is the mean radiative intensity in $\mathrm{erg\,s^{-1}\,cm^{-2}\,sr^{-1}}$ and σ is the Stefan-Boltzmann constant. The radiation temperature allows us to compare the radiation intensity to a radiative equilibrium temperature directly. The mean radiative intensity, J, is known from the radiative transfer method TreeRay-RP everywhere in our computational domain. By locally comparing the temperatures of gas T_{gas}, dust, T_{dust}, and radiation, we can determine whether the local conditions allow for radiative cooling ($T_{\mathrm{rad}} \leq T_{\mathrm{dust}} < T_{\mathrm{gas}}$) or radiative heating ($T_{\mathrm{rad}} \geq T_{\mathrm{dust}} > T_{\mathrm{dust}}$).

Temperatures across metallicities. We find less structure and fragmentation in the runs with lower metallicity and propose this to be caused by the less efficient cooling associated with the lack of metals and lower dust-to-gas ratios. Fig. 3 shows the gas temperature, T_{gas}, for all three runs at comparable times to Fig. 1. The temperature is hottest in the central hub for all three runs. At $t = 0.35\,t_{\mathrm{ff}}$, gas outside of the central hub is hotter for lower metallicities. Fig. 4 shows the mass fraction of gas with temperatures of gas, T_{gas}, dust, T_{dust}, and radiation, T_{rad} separated in three intervals. These intervals are defined by temperatures lower than 100 K, between 100 K and 500 K and above 500 K. We find the mass fraction of gas present in either of the three intervals to be similar for all three runs across time. Yet we find a higher multiplicity, more stars, towards higher metallicities (see Fig. 1). To further investigate this, we show the mass averaged temperature phase diagrams for our three runs at different times in Fig. 5. We find hotter gas, dust and radiation temperatures for lower metallicity runs. This holds especially true for material in the density range $10^{-18}\,\mathrm{g\,cm^{-3}}$ to $10^{-14}\,\mathrm{g\,cm^{-3}}$. It is said density range out of which the stellar particles may form in the later course of the simulation. Grey dashed lines in Fig. 5 indicate the adiabatic temperature density relation. We find the profile of the lines to match the adiabatic relation in the densest parts for $\rho > 10^{-14}\,\mathrm{g\,cm^{-3}}$. This match suggests that cooling is inefficient for these dense regions. From the work of Jeans (1902), we know that lower temperatures benefit fragmentation, which may result in less massive fragments. To follow up on this, we show the 10^{th} percentile temperatures, T_{10}, for gas, dust and radiation as a function of time for all our runs in Fig. 6. A fraction of 0.9 of the total gas mass is hotter than T_{10} at the corresponding time. We include only cells that are at a gas density $10^{-16}\,\mathrm{g\,cm^{-3}}$ or greater. Overall we find lower gas, dust and radiation temperatures in runs with higher metallicity. Because the three runs share similar initial conditions, they also share similar features across time. These features, however, become more smoothed out towards higher metallicity, e.g. at $0.25\,t_{\mathrm{ff}}$ or at $0.4\,t_{\mathrm{ff}}$ in Fig. 6. Common across all runs is the sudden increase in T_{10} past $0.45\,t_{\mathrm{ff}}$. We find lower temperatures, which benefit fragmentation, for higher metallicities.

Jeans mass as a proxy for fragmentation. We show the Jeans mass, M_{Jeans}, vs. time in Fig. 7. The Jeans mass is calculated in the following way

$$c_s = \sqrt{\frac{\gamma k T}{\mu m_{\mathrm{H}}}}, \tag{6}$$

$$M_{\mathrm{Jeans}} = \frac{\pi}{6} c_s^3 \frac{1}{\sqrt{G^3 \rho}}, \tag{7}$$

where c_s, γ, k, T, μ, m_{H}, G and ρ are the sound speed, the heat capacity ratio, the Boltzmann constant, the gas temperature, the mean molecular weight, the mass of a single hydrogen atom, the gravitational constant and the density, respectively. Similar to T_{10}, the Jeans-mass increases with lower metallicities due to reduced cooling. The Jeans mass is almost constant in the `SOL` run in-between $0.15\,t_{\mathrm{ff}}$ and $0.45\,t_{\mathrm{ff}}$ and increases only at later times, when the luminosity output of the central hub increases and the floor radiation temperature is lifted. The runs `SMC` and `LMC` undergo a similar behaviour but show

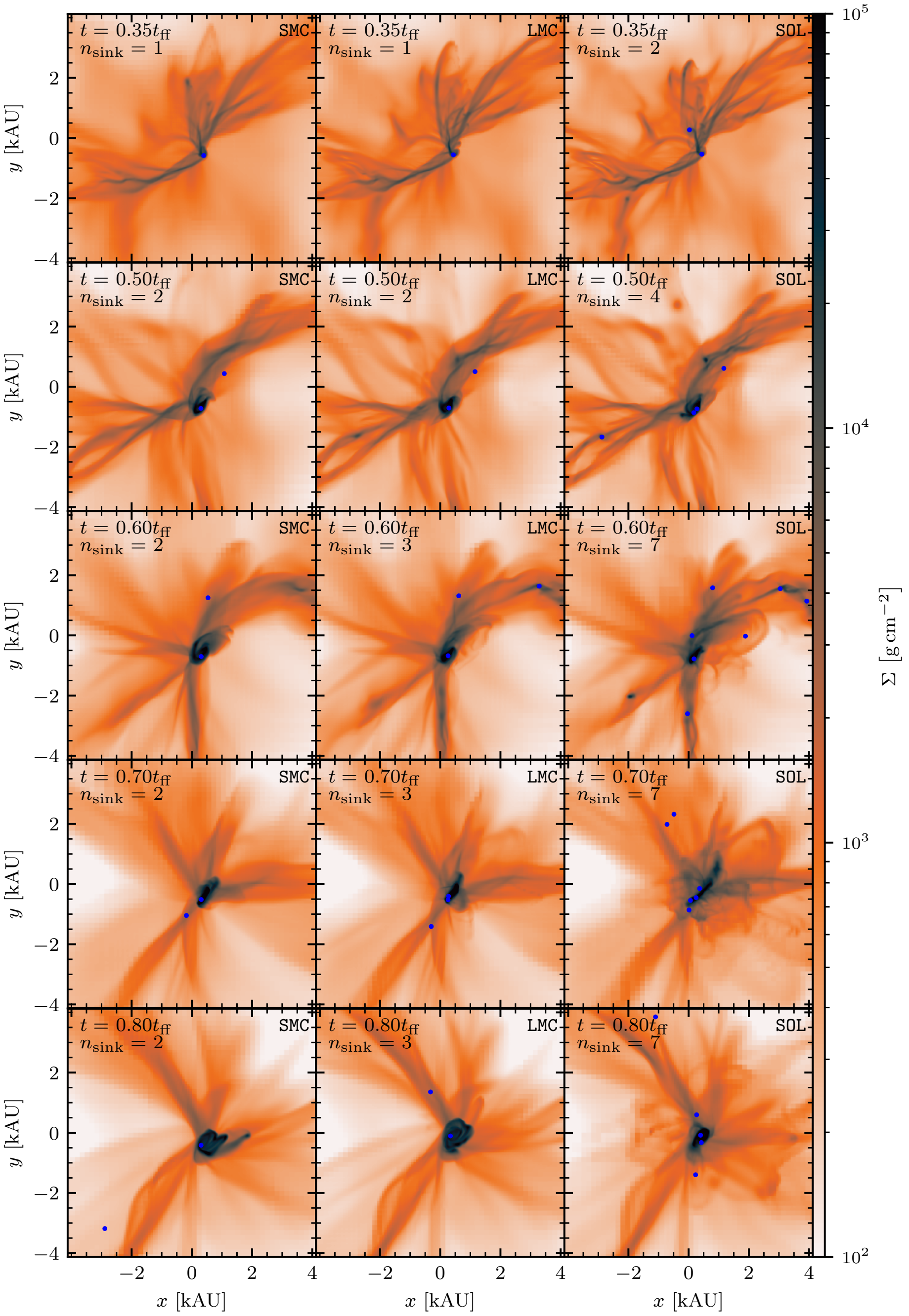

Figure 1. Column density plots for all three runs (left to right shows `SMC`, `LMC` and `SOL`) at different times organized in rows. Blue dots represent sink particles and $n_{\rm sink}$ gives the total number of sink particles in the computational domain. Each sink particle is a single proto-stellar object and the most massive one is deeply embedded in the center. The higher metallicity runs tend to form more fragments and with it more stellar particles. Starting at 0.6 $t_{\rm ff}$, the `SOL` run repels diffuse gas from surroundings of the central hub. This event, however, lasts only 0.2 $t_{\rm ff}$, after which the gas falls back down onto the centre.

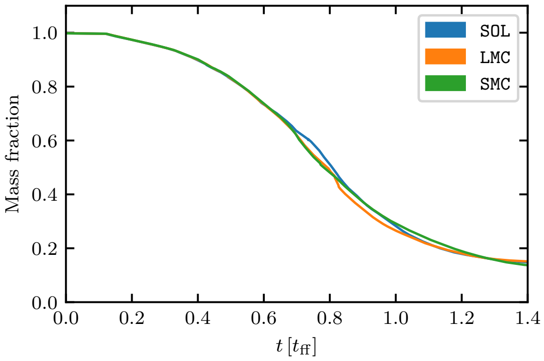

Figure 2. Gas mass present in the computational domain over time based on the initial mass of 150 $\mathrm{M}_{\odot}$. During 0.7 and 0.85 t_{ff}, the `SOL` run shows more unconverted gas mass than the other runs. Here, the principal star repels diffuse gas. Formation of companion stars further reduces the gas mass present in the `LMC` and `SOL` runs compared to the `SMC` run beyond 0.8 t_{ff}.

increased temperatures in between 0.15 t_{ff} and 0.45 t_{ff}. Past 0.6 t_{ff} the Jeans mass reaches values of 1 $M_{\odot}$.

Measuring fragmentation with dendrograms. We examine the degree of fragmentation with the help of dendrograms. Dendrograms allow capturing hierarchical structures in a tree-like way, where leaves refer to structures on the smallest scale. In contrast, branches refer to compositions of multiple leaves and branches viewed on a higher level. For the analysis in this work, we use the python package astrodendro[1]. We show dendrograms for all of our simulations at three comparable times in Fig. 8. Each leaf node is assigned a unique number starting from 0 and points to a local maximum density. At similar times we find more fragmentation in the runs with higher metallicity due to the overall lower temperature and cooling, which enables more fragments to form. The dendrograms show a density structure that is densest in a single location where it forms a single hub. Given that we employ a peaked density profile, $\rho \propto r^{3/2}$, combined with a subvirial velocity field for our initial conditions, a nested dendrogram structure is expected. Interesting, however, is the fact that we find more fragmentation for higher metallicities in this already concentric subvirial structure. We find that this difference allows for the additional formation of companion stars later in the simulation. For leaves in this dendrogram to form sinks, they need to surpass the sink formation density given by the red dashed line in Fig. 8. In addition, fragments that form further out need to be Jeans unstable and collapse sufficiently fast while migrating inwards where they might become radiatively heated and eventually Jeans-stable. Note that radiative heating may indirectly become less effective as the dust-gas coupling is weaker for lower DGRs and thus, metallicities (see Eq. 3.25 of Hollenbach & McKee 1979). We show the total number of leaf nodes against time in Fig. 9. Similarly, higher metallicity runs show more fragments vs. time compared to their lower metallicity counterparts. At 1.0 t_{ff} all runs agree on the number of fragments within a factor of two but the number of fragments is also heavily decreased at this late time below ten.

Comparing to other works. The results of this section are in line with the expectations from the general theory that a lower metallicity will generate less fragmentation and therefore lead to overall more massive clumps due to the lack of cooling (Omukai et al. 2005). However, we show that metallicity directly influences the structure and fragmenting behaviour of an already monolithically collapsing core by its cooling. The work of Chon et al. (2021) discusses similar findings at metallicities 10^{-6} to 0.1 $Z_{\odot}$ for a cloud of 2000 $M_{\odot}$. They find cooling to promote the formation of filamentary structures. In addition, they find a more Chabrier-like initial mass function (Chabrier 2003) with greater metallicities that was otherwise top-heavy. A greater number statistic on simulations with different initial conditions would allow a comparison on the reproduction of the high-mass and of the IMF.

3.2 Metallicity and accretion bursts.

Accretion bursts and metallicity. Fig. 10 shows the accretion rate of the most massive sink particle located in the centre of the potential well for each run. Looking at the accretion rate up to 0.6 t_{ff}, we can identify pronounced spikes in the accretion rate for the runs `SOL` and `LMC`. These spikes in the accretion rate do not appear in the `SMC` run. We suspect the spikes result from smaller fragments that have formed further out and fall onto the central hub. Consequently, mass is accreted in sudden bursts on impact. Because of more fragments forming in the higher metallicity cases (see fig. 9), we see more of these spikes compared to the lower metallicity case. Especially deviations from the rolling average are greater for runs with greater metallicity. We find that the accretion rate is temporarily increased during these bursts, followed by a decrease again. Eventually, the accretion rate relaxes and follows its rolling average. In our simulations, the growth of the central star's mass is not noticeably affected by differences in fragmentation up to a free-fall-time. This can be seen in Fig. 11, where we show the mass of the primary star and the cumulative mass of all companion stars vs time for all three runs. The vertical tick marks on the top indicate the formation of individual sink particles at the corresponding time.

Accretion rate and luminosity. The bursty accretion discussed above may lead to sudden bursts in luminosity. Such a burst in a massive young stellar object (MYSO), G358.93-0.03*, has been observed and analyzed in the work of Stecklum et al. (2021). The observed MYSO is estimated to have a mass of around 10 $\mathrm{M}_{\odot}$ and a pre-burst luminosity of $L^{\mathrm{pre}} = 5000^{+1100}_{-900}\,\mathrm{L}_{\odot}$. During its accretion burst the luminosity reaches $L^{\mathrm{burst}} = 23400^{+4400}_{-3700}\,\mathrm{L}_{\odot}$ and relaxes back to a luminosity $L^{\mathrm{post}} = 12400^{+2000}_{-1700}\,\mathrm{L}_{\odot}$ post-burst. Fig. 10 shows the total luminosity of the most massive stellar object against time in the lower panel for all of our simulations. The higher metallicity runs show more frequent and stronger burst-like luminosity variations by a factor of 2 to 3 at around 0.5 t_{ff}. Later on, we find stronger bursts at around 0.75 t_{ff} causing the luminosity to increase by a factor of 5 to 50. These later bursts, in particular, happen in the lower metallicity runs, `SMC` and `LMC`, where larger clumps that form sink particles in the `SOL` run approach the central star. Smaller bursts in the `SOL` run at later times are caused by fly-bys of sink particles interacting with the central hub. In addition, accretion is suppressed for the time between 0.6 t_{ff} and 0.8 t_{ff} by a factor of two in the `SOL` run due to more efficient RP boosting and therefore preventing fragments from reaching the central star. By direct comparison, we can see the differences among varying metallicities in Fig. 1 show that the gas is expelled from the central region in the `SOL` run. This event, however, is short-lived, and once the material has fallen back down again, we encounter slightly larger accretion rates on average. Looking at Fig. 11 one finds a disagreeing primary stellar masses between the `SOL` run and the `SMC` and `LMC` runs for a brief period around 0.75 t_{ff}.

---

[1] https://github.com/dendrograms/astrodendro/

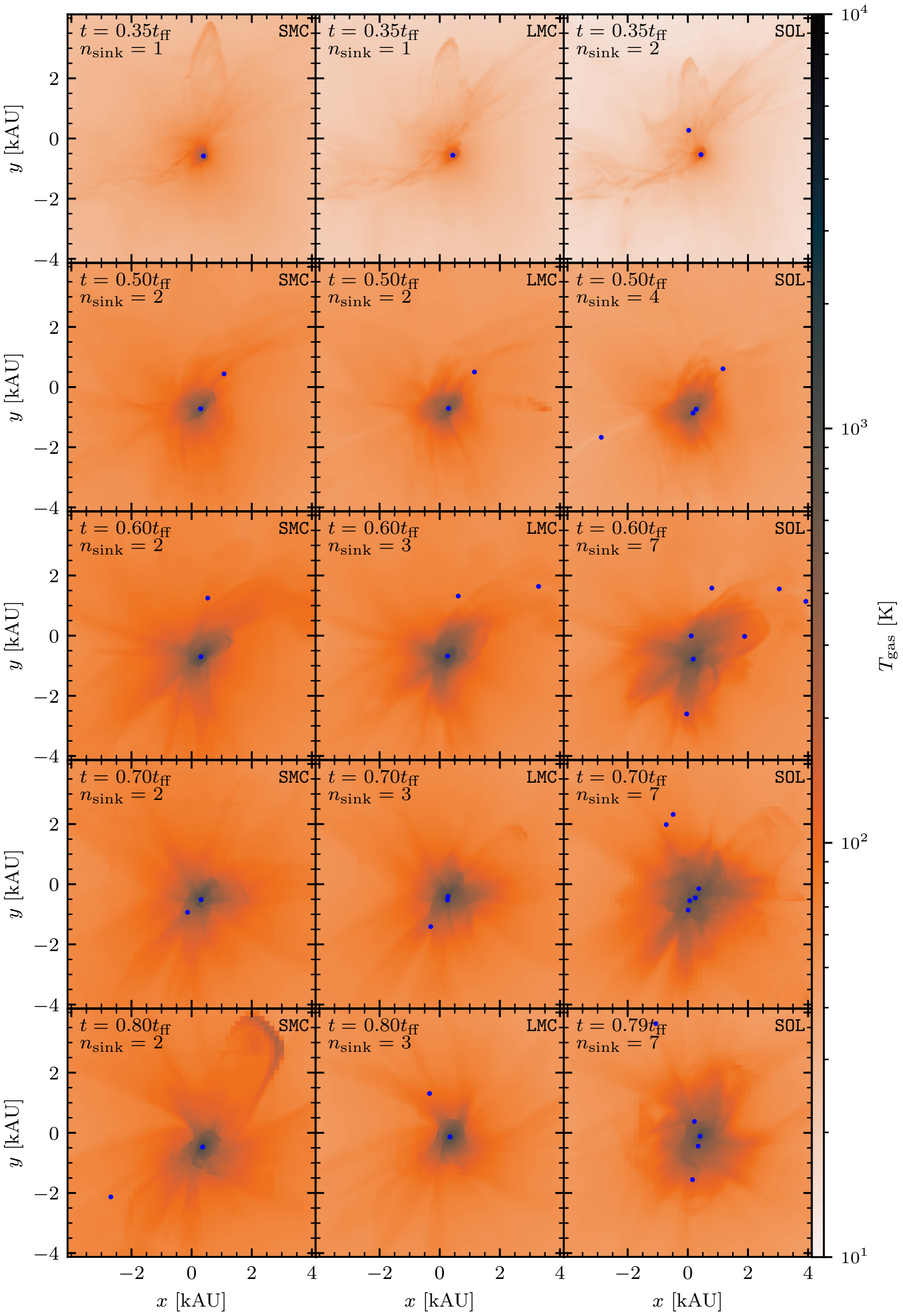

Figure 3. Similar plot to Fig. 1. The ambient medium is hotter for the lower metallicity runs at $t = 0.35\,t_{\rm ff}$ due to less efficient cooling at lower metallicities. The region close to the central hub is hotter in higher metallicity runs due to more effective dust-gas coupling in combination with radiative heating. In addition, the greater dust opacity per unit mass of gas traps the radiation more efficiently causing gas to be hotter at greater distances from the central hub.

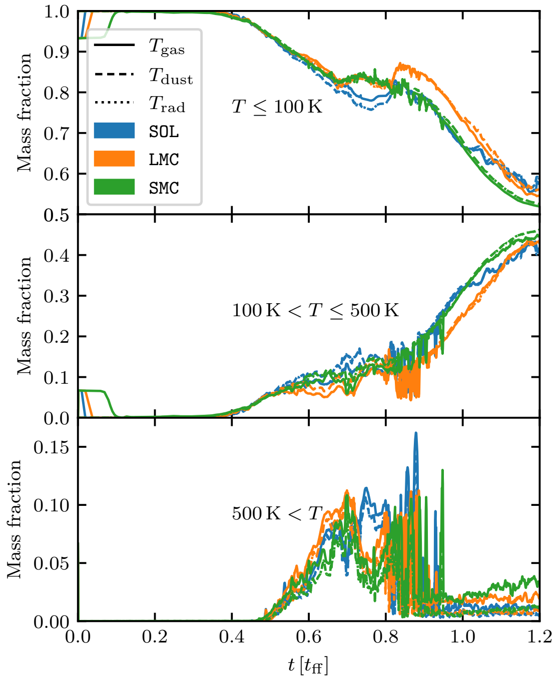

Figure 4. Mass fraction of the total gas mass for cells with a gas, dust or radiation temperature, T, in the intervals $T \leq 100\,{\rm K}$, $100\,{\rm K} < T \leq 500\,{\rm K}$ and $500\,{\rm K} < T$ for our three different runs. We can see that the gas becomes hotter over time, especially after 0.5 $t_{\rm ff}$. Colder temperatures benefit fragmentation in the further course of the simulation.

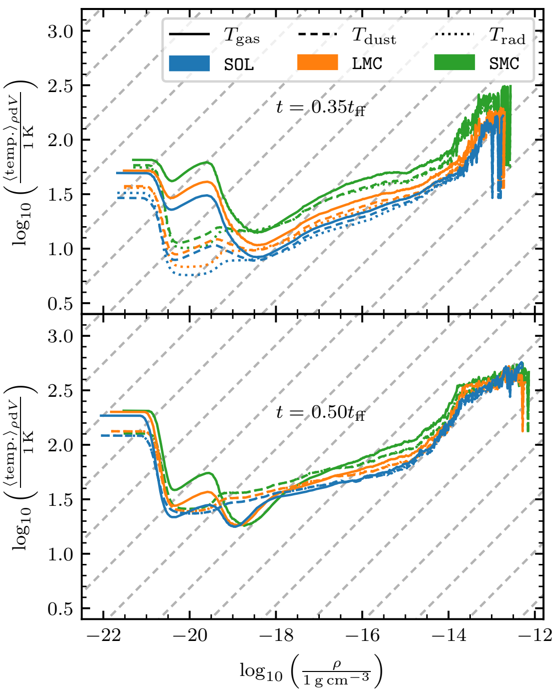

Figure 5. Mass averaged temperature density phase diagrams for the different runs SOL, LMC and SMC at specific times (0.35 and 0.5 $t_{\rm ff}$ from top to bottom). We show the gas, dust and radiation temperatures in solid, dashed and dotted lines, respectively. The grey dashed lines mark adiabatic temperature density relations ($\gamma_{\rm ideal} = 5/3$ for an ideal gas). For early times we find colder gas temperatures for densities above $10^{-18}\,{\rm g\,cm^{-3}}$. The high density regime shows adiabatic behaviour indicating optically thick dust cooling.

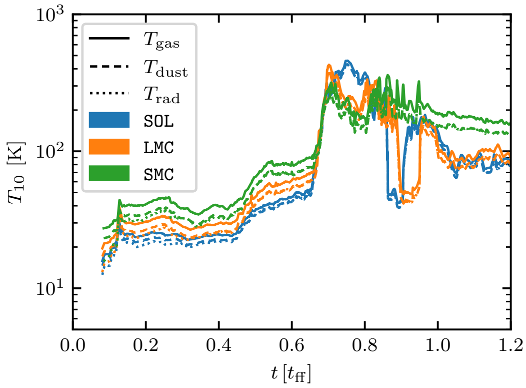

Figure 6. Tenth percentile of gas, dust and radiation temperature, T_{10}, vs. time for the different runs SOL, LMC and SMC. Only mass in gas with $\rho > 10^{-16}{\rm g\,cm^{-3}}$ is taken into consideration. Lower metallicity runs show somewhat higher temperatures during the "main collapse phase" ($t < 0.6\,t_{\rm ff}$) over time. Fragmentation allows for material to cool again.

The gap in mass difference among the runs is closed again by the temporarily increased accretion rate mentioned before.

Companion mass and metallicity. As discussed in §3.1 we find more fragmentation in the higher metallicity runs due to the lower temperature of the gas reached via cooling. This enables the higher metallicity runs to form more companion stars, as shown in Fig. 11. And for stars forming in all runs, we find that the higher metallicity runs form stars slightly earlier (see Fig. 11 at $t = 0.36\,t_{\rm ff}$).

3.3 Comparing Feedback, Thermal Pressure, Gravity and the Centrifugal Force

Ionizing feedback. We find ionizing feedback to be minuscule for the time and spatial scales we consider. Ionising radiation manages to create a hyper compact HII region, which is restricted from expanding due to the pressure generated by the in-falling material. Fig. 13 shows the ionized mass, $M_{\rm HII}$, and the derived size, $r_{\rm HII}$, of the HII region. We calculate, $r_{\rm HII}$, by measuring the ionised volume, $V_{\rm HII}$, in the proximity of the principal star and compute a radius assuming spherical geometry in the following way

$$r_{\rm HII} = \left(\frac{3}{4\pi} V_{\rm HII}\right)^{1/3} . \tag{8}$$

According to the definitions of the work of Kurtz (2005) the HII region can be classified as a hyper-compact HII region with ionised masses at around $10^{-3}\,{\rm M_\odot}$ and sizes of around 10^{-2} pc. The HII re-

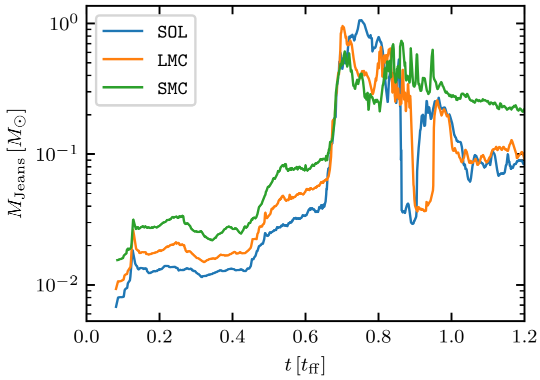

Figure 7. Jeans mass (see Eq. 7) computed with a gas density of $\rho_{\rm sink,\,thresh} = 5.2 \times 10^{-14}\,{\rm g\,cm^{-3}}$ and corresponding gas temperatures from Fig. 6 vs. time. The Jeans mass inversely decreases with metallicity across the 3 different runs. The `SOL` has an almost constant Jeans mass and increases later due to radiative heating. The Jeans mass can be seen as a proxy for fragmentation and shows that less fragmentation can be expected in the lower metallicity runs due to reduced cooling.

gion is unable to expand during the simulation and remains compact. In a similar way, the ionised mass stays below 10^{-2} M$_\odot$.

Radiation pressure. RP manages to generate visible effects on the dynamics of the gas in the `SOL` run. At $t = 0.6\,t_{\rm ff}$ (see Fig. 1) gas is asymmetrically blown towards the positive x-direction and small cavities are generated. Later on, more gas follows to be ejected in all directions forming a spherical imprint of the cavity wall in the projection plot in Fig. 1 at $t = 0.8\,t_{\rm ff}$. The structure, however, is short-lived and begins to fall back down onto the core. Fig. 14 shows the radially outward directed component of the momentum input by RP vs. time for the three different runs `SMC`, `LMC` and `SOL` in olive green respectively. The momentum directly injected by the luminosity (see Eq. 1) is shown as the purple line in each of the panels. We find that the momentum shown by the olive line is boosted compared to the direct RP. This momentum boost is caused by the absorption and reemission of the radiation through the dust. In an effort to model the momentum boost, we plot the black line, which shows the boost factor, β, times the luminosity over c of the most massive star as such:

$$\dot{p}_{\rm boosted,RP} = \beta \times p_{\rm direct}\,. \tag{9}$$

We compute β in the following way:

$$\beta = -\log\left(\frac{1}{N}\sum_{i=1}^{N=192}\exp(-\tau_i)\right), \tag{10}$$

$$\tau_i = \int_0^\infty \rho(\mathbf{r}_{\rm S} + s\mathbf{n}_i)\kappa(\mathbf{r}_{\rm S} + s\mathbf{n}_i){\rm d}s\,, \tag{11}$$

where $\mathbf{r}_{\rm S}$, $\mathbf{n}_i$ and s are the position of the most massive star, the unit vector pointing in the direction of the pixel i generated by the HEALPix algorithm (Górski et al. 2005) and the path length taken by light, respectively. Therefore, τ_i measures the optical depth seen from the central star in an outward direction aligned with pixel i of the HEALPix algorithm.

We can see that the black curve manages to marginally predict the truly boosted momentum (olive green) from the injected momentum (purple). The grey shadow underneath highlights the 1-σ range obtained from the averaging in Eq. 10. Comparing the true radial momentum of the runs with each other, we find that higher metallicity corresponds to a greater momentum boost at comparable times and, therefore, to more radiation pressure. The momentum boost computed by TreeRay/RadPressure decreases again to orders of unity with respect to the direct momentum provided by the luminosity at later times once a disk establishes. The formation of a disk has been previously discussed by Kuiper et al. (2012) with regards to a reduced overall RP in a system with a disk-like geometry compared to a more spherically symmetric mass distribution.

Metallicity and momentum boost. Since the boost factor seems to scale with the metallicity, we can investigate the opacity for the three different runs. Fig. 15 shows a phase diagram of the dust opacity per gramm of gas mass for the runs `SMC`, `LMC` and `SOL` at different times. A greater dust opacity is expected to cause a greater momentum boost because $\beta \propto \tau \propto \kappa$. Looking at Fig. 15 and comparing it to the results of Fig. 14, we recover our expectations that greater opacities at higher metallicities cause greater momentum boosts. We can also see that κ for `SMC` is capped at a lower value than it is for `SOL` due to the max value of the opacity reached at 150 K (see Eq. 3), which contributes to the difference in the measured momentum boosts among different metallicities (see Fig. 14).

Defining other quantities. In the following, we consider other mechanisms that aid the stabilisation of the central hub against gravitational collapse next to RP. These mechanisms include the thermal pressure and centrifugal force caused by rotation. By computing the radial momentum component of either mechanism, we can directly compare their importance for the dynamics of the central hub. We compute the radial momentum input per unit time due to thermal pressure, $\dot{p}_{\rm th}$, gravity, $\dot{p}_{\rm grav}$, and the centrifugal force, $\dot{p}_{\rm centrifugal}$, in the following way

$$\dot{p}_{\rm th} = -\int \mathbf{n}_{\rm star} \cdot (\nabla \cdot P)\,{\rm d}V\,, \tag{12}$$

$$\dot{p}_{\rm grav} = \int \rho\,\mathbf{n}_{\rm star} \cdot \mathbf{a}_{\rm grav}\,{\rm d}V\,, \tag{13}$$

$$\dot{p}_{\rm centrifugal} = \int \frac{\rho(\mathbf{v} - \mathbf{v}\cdot\mathbf{n}_{\rm star})^2}{|\mathbf{r} - \mathbf{r}_{\rm star}|}\,{\rm d}V\,, \tag{14}$$

where $\mathbf{n}_{\rm star}$, P, $\mathbf{a}_{\rm grav}$, $\mathbf{v}$ and $\mathbf{r}_{\rm star}$ are the unit vector pointing towards the most massive star, the thermal pressure, the acceleration due to gravity, the gas velocity and the position of the most massive star, respectively. All quantities are computed locally for each cell. The calculation for the pressure terms is done using the momentum equation of the Euler equations. In all terms, we use the position of the most massive star as the origin because it is the principal source of feedback.

Gravity and centrifugal force. We show $\dot{p}_{\rm grav}$ (green line) and $\dot{p}_{\rm centrifugal}$ (red line) for the three runs in Fig. 16. The results for all three runs show that gravity and the centrifugal force dominate over all other mechanisms influencing the global dynamics. Moreover, given that gravity and the centrifugal force oppose each other, they balance each other out, ultimately forming a disk.

RP vs thermal pressure and ionising feedback. We also show $\dot{p}_{\rm RP}$ (orange line) as well as $\dot{p}_{\rm th}$ (blue line) in Fig. 16. The radiation of the stellar source heats the star's surroundings and hence influences both RP and the momentum generated by thermal pressure. Together, both mechanisms are subordinate when considering the whole core. However, RP is stronger than thermal pressure stabilisation after approximately $0.5\,t_{\rm ff}$. Note that the momentum associated with the D-Type expansion of an HII region is associated with the momentum of the thermal pressure. Since we find an increasing ratio of $\dot{p}_{\rm RP}$ over $\dot{p}_{\rm th}$ with increasing metallicity, we can conclude that the role of

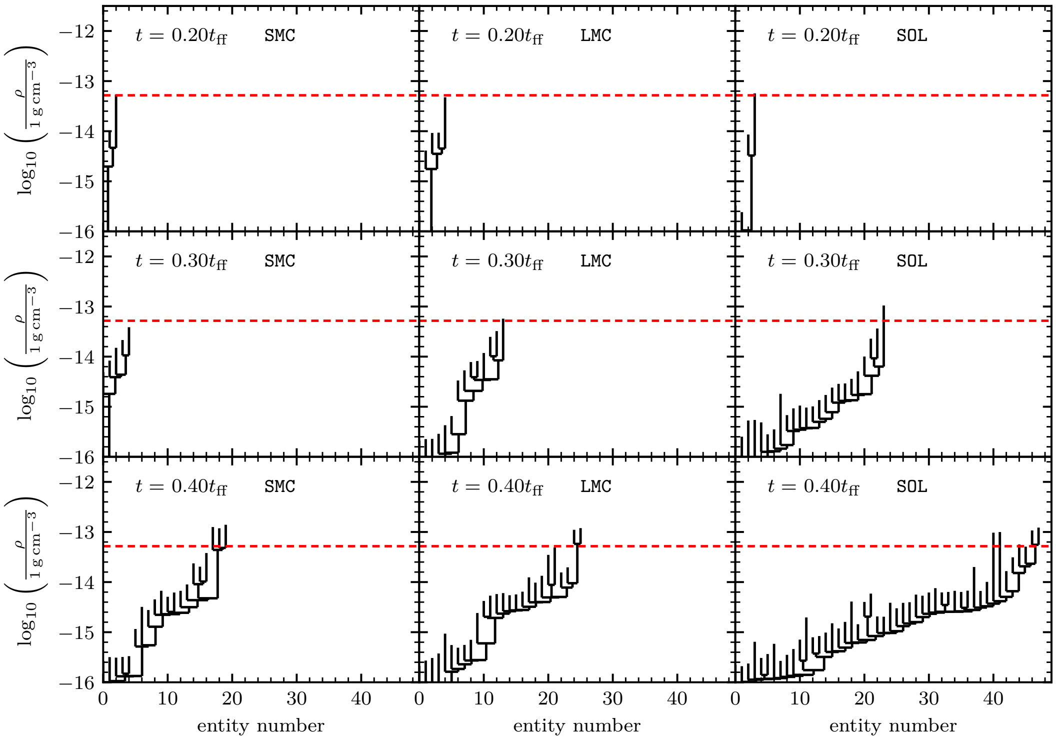

Figure 8. Dendrograms showing hierarchical density structures at different times. From left to right we show the 3 different runs at 0.2, 0.3, 0.4 $t_{\rm ff}$ (top to bottom). The horizontal dashed red line marks the threshold density for sink formation. The dendrograms were computed using the python package ASTRODENDRO. The runs with higher metallicity tend to form more fragments due to better metal and and dust cooling.

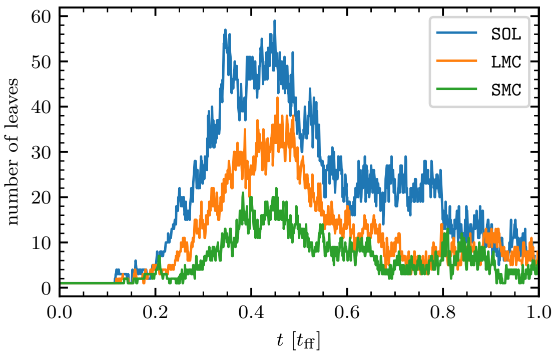

Figure 9. Number of leaves within the dendrogram at different times for the three runs `SOL`, `LMC` and `SMC`. The minimum threshold density is 10^{-16} g cm^{-3} above which we consider contributions towards the dendrogram. The plot shows more leaf nodes forming in the solar metallicity run compared to its lower metallicity counter parts.

RP is more important than ionising feedback for higher metallicities. This finding is similar to the work of Ali (2021) where they find ionising feedback to be stronger than RP while considering overall larger time and spatial scales on the order of 1-10 pc. It is only for the high metallicity run of $Z = 2\,Z_\odot$ metallicity that they find RP to be stronger by a factor of 10 over ionising feedback measured at 0.2 pc distance. In conclusion, they find ionising feedback to dominate globally on large scales.

REMAINING GAS MASS. Gas that has not been converted to stars is shown by Fig. 2. Here, the mass fraction of the initial mass (150M$_\odot$) is shown against time. We find that all runs have similar left over gas. Minor deviations can be linked to a momentary radiation pressure outflow only present in the `SOL` run (0.75 $t_{\rm ff}$) and the formation of companion stars and their accretion (see `LMC` run at, 0.8 $t_{\rm ff}$ and `SOL` run at, 1.0 $t_{\rm ff}$). The difference in metallicity does not affect the conversion of gas mass to stellar mass i.e. the star-formation-efficiency in this highly subvirial configuration.

4 THE FINAL STAGE

DISKS IN MSF. Observations show disks around B-Type stars may range from sizes of 500 AU to 10 kAU where the disk itself may contain masses of 0.1 to 100 M$_\odot$ (see Mitchell et al. 1992; Bernard et al. 1999; Schreyer et al. 2002, 2006). To this day, disks around more massive O-Type stars that are not embedded in their parental core have not been observed. Observations by Cesaroni et al. (2017) show disks around proto-stellar O-Type stars. They conclude that disk detection is sensitive to the evolutionary stage of the young stellar object. Here, we show that disks may arise even for the very massive principal stars in our simulations.

RESULTS FROM SIMULATIONS. In our simulations, we form a disk

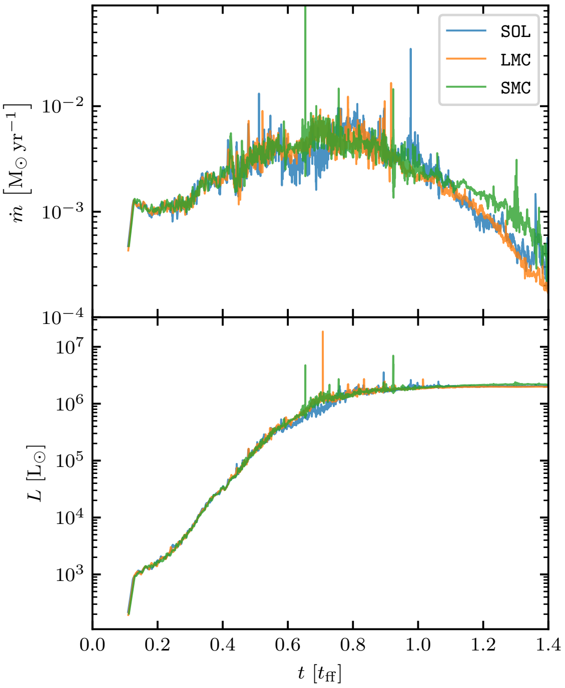

Figure 10. We show the accretion rate of the most massive star vs. time for all simulations in the upper panel and the total luminosity against time in the lower panel. We can see that the lowest metallicity run appears to have a lower deviations from the rolling average over all. This is linked to the generally higher gas temperature suppressing fragmentation and therefore producing a smoother accretion inflow. The higher metallicity run produces in-falling clumps which cause more pronounced spikes in the accretion rate when they interact with the central star. The clumpy accretion causes spikes in the luminosity of the star due to accretion bursts in the lower panel.

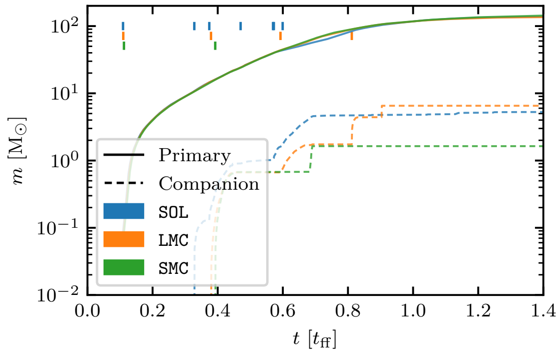

Figure 11. Stellar mass vs. time for all runs of the primary star (solid line) and companion stars (dashed line) forming further out. Sink formation events are marked by small vertical ticks at the top of the plot. We can see that a higher metallicity forms more stellar particles. Stellar particles having counterparts forming in the lower metallicity runs form earlier in the higher metallicity runs (see particle forming at 0.36 t_ff). We find similar masses for the primary stars in each run, while the `SOL` and `LMC` runs form more companion stars.

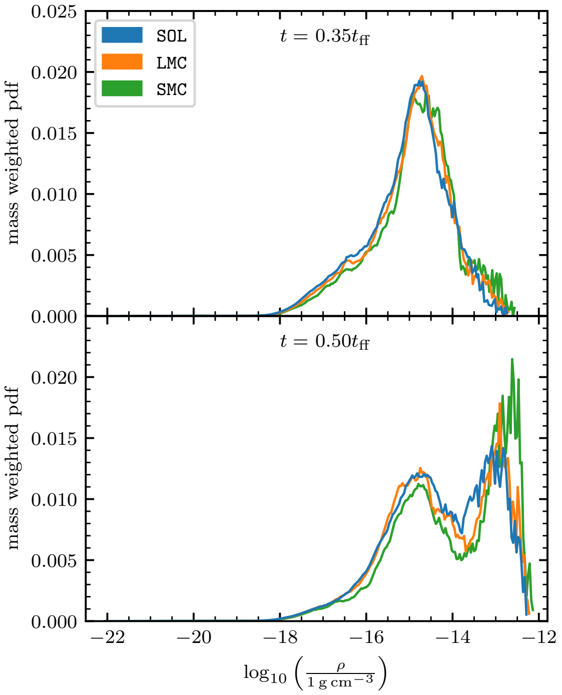

Figure 12. Mass weighted density probability density function (PDF) for 0.35 t_ff and 0.5 t_ff. The lower metallicity runs have more gas at higher densities compared to the higher metallicity runs.

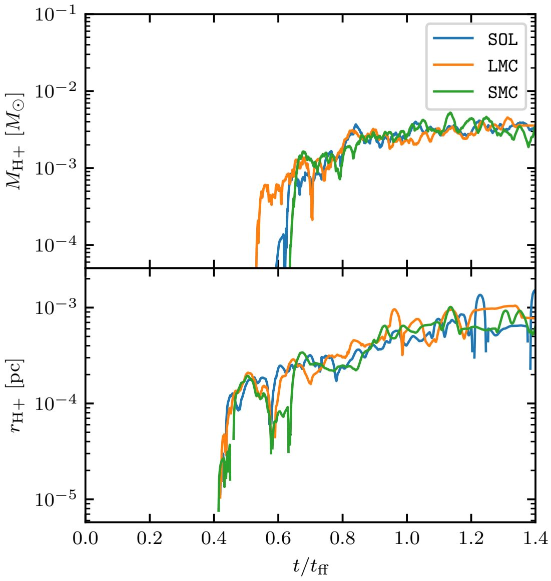

Figure 13. Ionized gas mass (top panel) and derived size of the HII region assuming a spherical volume (bottom panel) against time for the three runs `SMC`, `LMC` and `SOL`. We find comparable sizes and masses across all three runs. Overall the parameters indicate the presence of a hyper-compact HII region on its transition to an ultra-compact HII region.

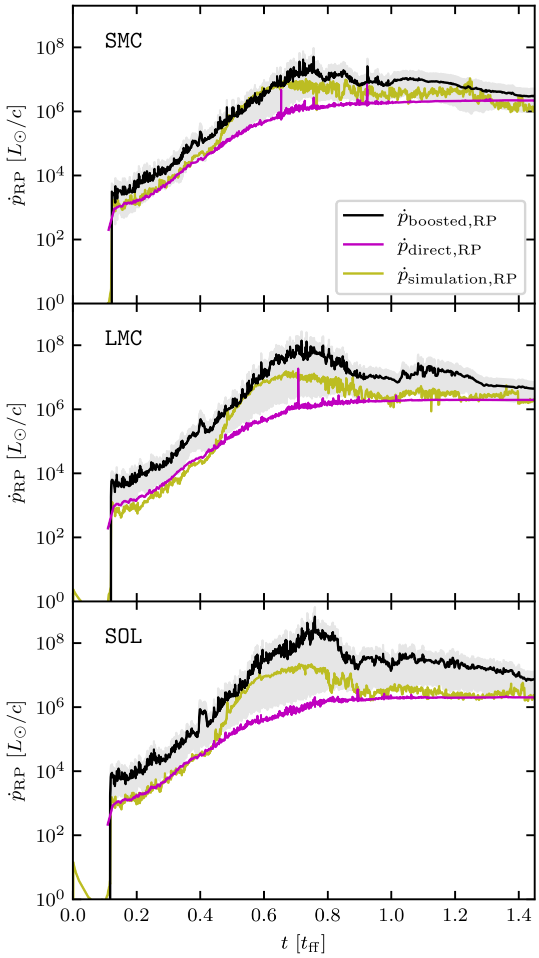

Figure 14. Radial momentum rate acting on dust and gas in the simulation (olive line), momentum input from the most luminous star (purple line, Eq. 1) and boosted RP (black line, Eq. 9) against time. The difference between the direct (purple) and boosted RP (black) curves is credited to the boost factor, that accounts for the direct radiation interacting with the reprocessing medium and therefore generating additional radial momentum through scattering and absorption and reemission.

stabilized by centrifugal forces (see §3.3), from which the star is still accreting mass in all three runs at the end of the simulation. However, this accretion happens slower by a factor of 5 to 10 compared to the initial accretion phase (see Fig. 10 and compare 0.5-1.0 t_{ff} to 1.0-1.25 t_{ff}). We show a collection of volume renderings in Fig. 17 focusing directly on the disk in a slightly elevated edge-on view. Yellow, blue and red colours show molecular, atomic and ionized gas, respectively. The time series shows the evolution of the initial molecular disk. In all simulations, the disk measures about 2 kAU in diameter. The volume renderings show primarily molecular gas at 1.2 t_{ff} where the `SOL` run shows arms or filaments originating from the disk into the ambient medium.

Evacuation of the disk. Following the evolution of the disks, we find RP to clear out gas along the polar direction over time. In particular, greater metallicities rarefy gas along the rotation axis faster. Looking at Fig. 17 one finds atomic gas (blue) for the `LMC` run already at 1.3 t_{ff} while the `SMC` run is still fully molecular. The atomic gas arises from ionized gas being ejected from the UCHII region surrounding the star and recombining to form atomic hydrogen again. Overall, gas is ejected more chaotically in the `LMC` and `SOL` runs compared to the `SMC` run beyond 1.35 t_{ff}. Here, the `SMC` run shows a compact symmetric disk from which gas is ejected in a bipolar fashion. Towards the latest time shown in Fig. 17, gas is still being fed onto the disk, especially for the `SMC` run. Towards the end of the time series shown in Fig. 17, the `SMC` run shows a disk from which atomic gas is ejected in polar directions. A white layer has developed at the boundary of the sideways in-falling gas. The white colour indicates a mixture of molecular and atomic gas in the volume renderings. Similarly, white whispy structures form along the rotation direction. These structures condense to larger blobs and fall back onto the disk again. Once they approach the disk, they could be ejected again. These structures have been described by (Krumholz et al. 2009) as radiative Rayleigh-Taylor instabilities. We find, however, that these structures do not contribute to accretion on the principal star. Instead, the star continues to accrete mass only through the disk in a similar way as described by Kuiper & Yorke (2013). Contrary to the `SMC` run, the higher metallicity runs show a more unstable disk and more structured outflows. The accretion rate of the principal star does not depend on the amount of fragmentation of the infalling gas. Instead, the more pronounced disk accretion, prominently visible in Fig. 17 for the `SMC` run, appears to lead to a greater accretion rate.

Stability of the disk. We show column density plots in the top row of Fig. 18 highlighting the face-on structure of the disk for all three runs. The disk shows more fragmentation for greater metallicities. We also show the (Toomre 1964) criterion for the stability of a disk around a star calculated as

$$Q_{\mathrm{Toomre}} = \frac{c_{\mathrm{s}}\omega}{\pi G \Sigma}, \tag{15}$$

where c_{s}, κ and G are the sound speed, the epicyclic frequency and the gravitational constant, respectively. Fig. 18 shows smaller values than unity for Q_{Toomre} in all three runs indicating that parts of the disks are unstable. However, we find more unstable regions in the disk of the `SOL` run to be present. These unstable regions are linked to the regions with the greatest column densities. From this, one can infer that the disk in the `SOL` run will continue to become more unstable and further fragment. Looking at the `SMC` run, one finds unstable regions not to cover the entire disk but only in the densest part towards the positive y-direction. Overall, the disk shows no fragmentation and appears smooth. The `LMC` run lies in between `SMC` and `SOL` concerning its disk stability. Therefore suggesting higher metallicities to produce more unstable disks.

Influence of metallicity. We consider two mechanisms by which the metallicity and, therefore also, the dust-to-gas ratio may contribute towards the possible outcomes of the respective simulations. First, we consider the boosting of RP due to a greater dust opacity per unit mass of gas, κ_{P}, that is associated with a higher dust-to-gas ratio. One would expect this mechanism to aid in the final removal of the disk around the star due to more momentum being injected due to more scatterings and absorption and reemission events (Hopkins et al. 2011; Krumholz & Thompson 2012, see momentum boost, e.g.). We find, however, that the momentum boost approximately reduces to unity for all three runs. The reduction of the momentum boost has been linked to the flashlight-effect (see, e.g., Kuiper et al. 2011) where in a disk-like geometry radiation can escape along the rotation axis as most matter is concentrated in the disk-plane. Therefore, the impact of the metallicity on RP might be

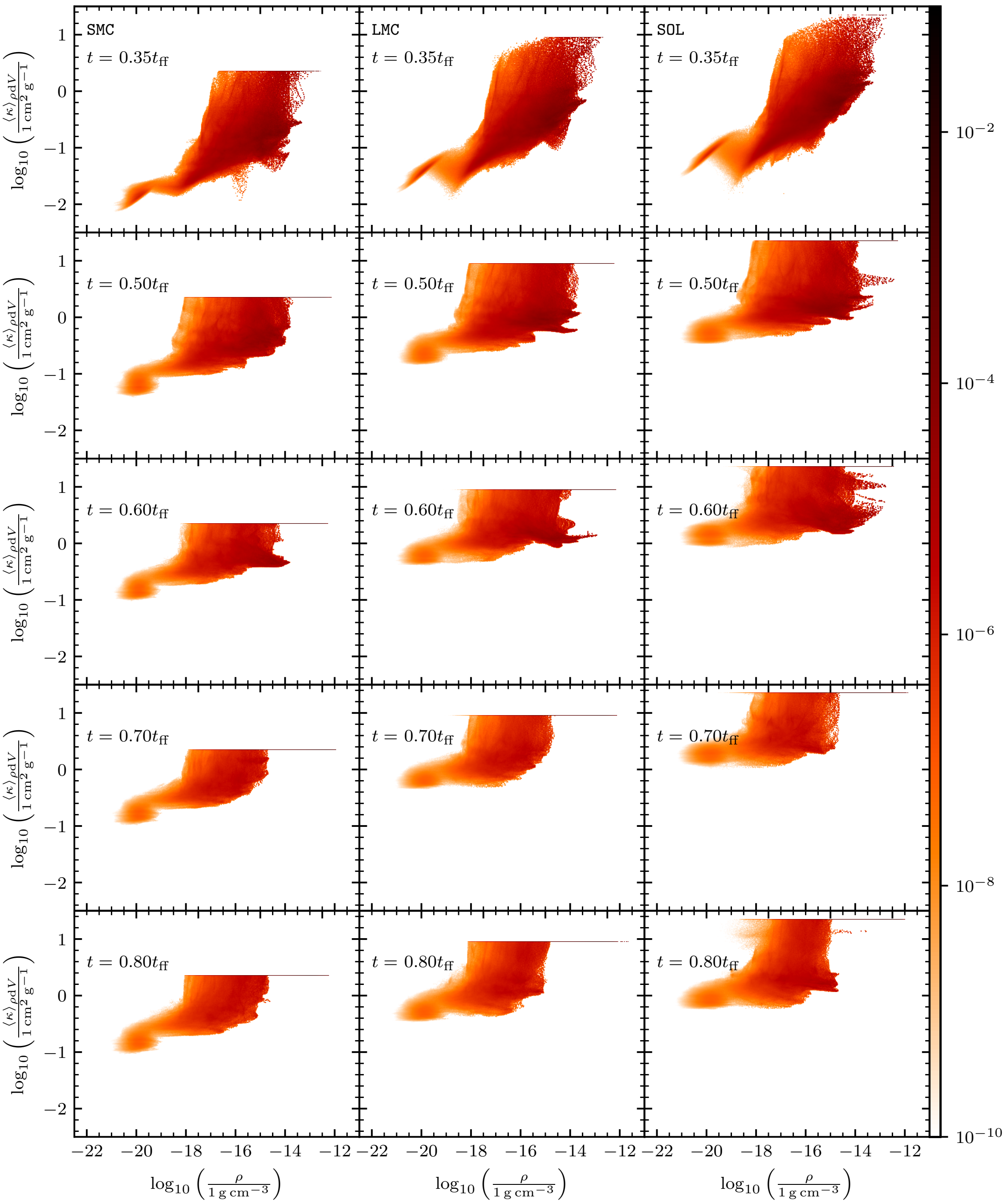

Figure 15. Mass weighted 2D-PDF showing the dust opacity (see Eq. 3) present in the simulation as a function of the gas density. The opacity per gas mass is expected to be a proxy for the momentum boost of RP generated by dust. Due to the lower dust-to-gas ratio, the `SMC` (left column) and `LMC` (middle column) runs should in theory generate less efficient boosting than the `SOL` run (right column). We find this to be the case between 0.4 $t_{\rm ff}$ and 0.8 $t_{\rm ff}$ while looking at Fig. 14. The sharp line at high densities visible in some panels is a result of the opacity model of Eq. 3 for 150 K < $T_{\rm dust}$ < 1500 K, where the opacity is constant.

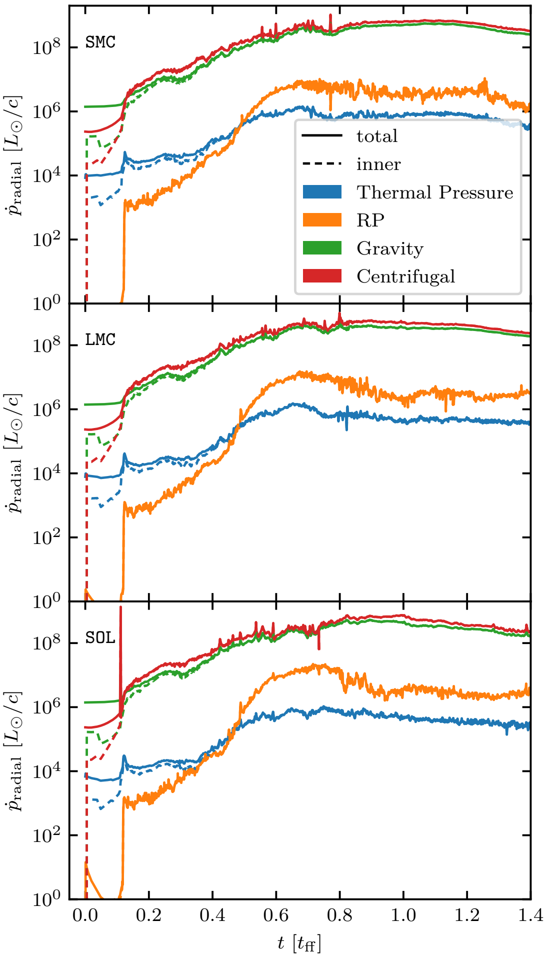

Figure 16. Absolut radial momentum input rate caused by thermal pressure (blue, Eq. 12), RP (orange), gravity (green, Eq. 13) and the centrifugal force (red, Eq. 14). Gravity is mainly opposed by the centrifugal force. While thermal pressure support dominates over RP up to $\approx 0.5\ t_{\mathrm{ff}}$, RP dominates afterwards.

unlikely to play an important role in shaping the outcome of either run. Second, we consider that the enhanced cooling of gas associated with a higher metallicity and dust-to-gas ratio leads to more fragmentation and mass in companion stars (see §3.1). In return, less mass ends up in the disk, which may eventually be destroyed more quickly due to RP and ionizing feedback. Companions stars may cause instabilities in the disk surrounding the most massive star similar to the work of Oliva & Kuiper (2020). These instabilities may lead to further fragmentation of the disk. Both mechanisms by which an increased metallicity influences the dynamics in the simulation can be considered to reduce the mass of the principal star. For the simulated setup, however, the effects do not influence the mass of the central star drastically. Boosting of RP associated with greater metallicities only slightly delays mass accretion. In addition, the formation of low-mass stars only affects the non-star-forming gas mass.

5 CONCLUSION

Summarising the simulations. We examine the role of metallicity for a monolithically collapsing, turbulent 150 $M_\odot$ core in numerical simulations. In total, we investigate three different metallicities, 0.1 $Z_\odot$, 0.4 $Z_\odot$ and 1.0 $Z_\odot$, corresponding to the SMC-like, the LMC-like and the solar neighbourhood conditions, respectively. Gas is allowed to form stars self-consistently while taking into account the stellar feedback from accretion and intrinsic luminosity in the form of RP and ionising radiation. We have modelled radiative heating and the chemical evolution self-consistently with a simple chemical network.

In the following, we will conclude the results of this work.

- Temperature regulated Fragmentation. We examine the role of metallicity on fragmentation in §3.1 and find that a higher metallicity causes more structures to form. The more efficient formation of structures leads to the formation of more low mass stars. Extrapolating this effect to a core initialised with an even greater velocity dispersion, one might find even more structures and therefore more low mass stars
- Accretion burst. We find accretions bursts that lead to a sudden jump in luminosity by a factor of approximately two to ten. These bursts only appear in runs with higher metallicity during the early phase, particularly for the runs with `LMC` and `SOL` metallicity. Among these two runs, we find more bursts in the `SOL` run. We argue that fragmentation associated with higher metallicity leads to accretion of fragments resulting in accretion bursts.
- RP vs ionising feedback. We find RP dominates over ionising feedback in terms of momentum input on the scales presented in this setup. During the cloud's free-fall time, an ultra-compact HII region forms, which is supported by the thermal pressure of the hot ionised gas and RP on gas and dust. Comparing the momentum input of thermal pressure, including the feedback of a D-type expansion, to that of RP, we find that thermal pressure is only stronger in the beginning. Later on, at 0.5 t_{ff}, the momentum input from RP increases and RP becomes greater than that of thermal pressure.
- RP vs thermal pressure and gravity. Overall, the momentum input of gravity dominates over that of RP and thermal pressure by factors of 10 to 100. The rotating disk around the most massive star is mainly stabilised against collapse by the centrifugal force. Given enough time, gas may be removed from the disk so the entire disk may dissolve. Removal of gas from the disk may happen due to accretion and eventually feedback once the central star is massive enough.
- Star formation efficiency and multiplicity. Metallicity does not affect the mass that is converted to stars for the collapse of a sub-virial core shown in this work (see Fig. 2). The number of stars formed and the mass that ends up in low-mass companion stars differ (see Fig. 11). Simulations of less bound structures and less steep density profiles would make for an interesting comparison on the effects of metallicity. The changes in the multiplicity associated with the metallicity might impact the signature of the feedback mechanisms by, for example, forming more low-massive stars.

ACKNOWLEDGEMENTS

AK and SW gratefully acknowledge the European Research Council under the European Community's Framework Programme FP8 via the ERC Starting Grant RADFEEDBACK (project number 679852). AK and SW further thank the Deutsche Forschungsgemeinschaft (DFG) for funding through SFB 956 "The conditions and impact of

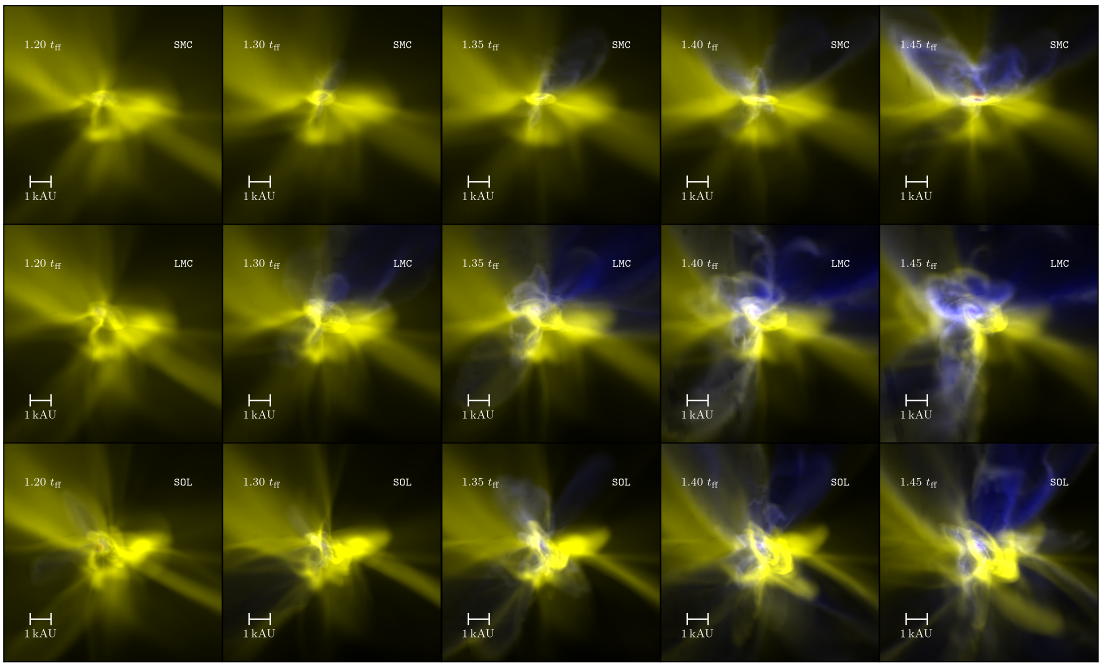

Figure 17. Volume renderings of all three runs at an advanced stage. The runs `SMC`, `LMC` and `SOL` are organized in rows showing different times in columns. Molecular, atomic and ionized gas are shown in yellow, blue and red, respectively. The view of the camera uses a perspective lens such that the scale of 1 kAU in the bottom left of the images are only valid for the plane of the disk. A mixture of atomic and molecular gas is depicted in white colors given the mixing of yellow and blue. During the very late phase, at around 1.4 t_{ff}, one finds molecular gas appearing as condensations above the disk plane. These condensations rain down onto the disk but are removed again, once RP is strong enough near the principal star. Ionized gas is only present very close to the principal star as an UCHII region.

star formation” (sub-project C5). The software used in this work was in part developed by the DOE NNSA-ASC OASCR Flash Center at the University of Chicago. The authors gratefully acknowledge the Gauss Centre for Supercomputing e.V. (www.gauss-centre.eu) for funding this project by providing computing time through the John von Neumann Institute for Computing (NIC) on the GCS Supercomputer JUWELS at Jülich Supercomputing Centre (2021) (JSC). We particularly thank the Regional Computing Center Cologne for providing the computational facilities for this project by hosting our supercomputing cluster "Odin".

DATA AVAILABILITY

The data underlying this article will be shared on reasonable request to the corresponding author.

REFERENCES

Abel T., Bryan G. L., Norman M. L., 2002, Science, 295, 93
Ali A. A., 2021, MNRAS, 501, 4136
Bernard J. P., Dobashi K., Momose M., 1999, A&A, 350, 197
Bestenlehner J. M., et al., 2020, Monthly Notices of the Royal Astronomical Society, 499, 1918–1936
Bromm V., Coppi P. S., Larson R. B., 2002, ApJ, 564, 23
Calvet N., Gullbring E., 1998, ApJ, 509, 802
Cesaroni R., et al., 2017, A&A, 602, A59
Chabrier G., 2003, PASP, 115, 763
Chon S., Omukai K., Schneider R., 2021, MNRAS, 508, 4175
Choudhury S., Subramaniam A., Cole A. A., 2016, MNRAS, 455, 1855
Choudhury S., Subramaniam A., Cole A. A., Sohn Y. J., 2018, MNRAS, 475, 4279
Clark P. C., Glover S. C. O., Klessen R. S., 2008, ApJ, 672, 757
Clarke S. D., Whitworth A. P., Duarte-Cabral A., Hubber D. A., 2017, MNRAS, 468, 2489
Costa T., Rosdahl J., Sijacki D., Haehnelt M. G., 2018, MNRAS, 473, 4197
Dinnbier F., Walch S., 2020, MNRAS, 499, 748
Dopcke G., Glover S. C. O., Clark P. C., Klessen R. S., 2011, ApJ, 729, L3
Doran E. I., et al., 2013, Astronomy & Astrophysics, 558, A134
Federrath C., Banerjee R., Clark P. C., Klessen R. S., 2010, ApJ, 713, 269
Fryxell B., et al., 2000, The Astrophysical Journal Supplement Series, 131, 273
Fujita S., et al., 2021, PASJ, 73, S273
Glover S. C. O., Mac Low M.-M., 2007, ApJS, 169, 239
Górski K. M., Hivon E., Banday A. J., Wandelt B. D., Hansen F. K., Reinecke M., Bartelmann M., 2005, ApJ, 622, 759
Hainich R., et al., 2014, Astronomy & Astrophysics, 565, A27
Hollenbach D., McKee C. F., 1979, ApJS, 41, 555
Hopkins P. F., Quataert E., Murray N., 2011, MNRAS, 417, 950
Jeans J. H., 1902, Philosophical Transactions of the Royal Society of London Series A, 199, 1
Jülich Supercomputing Centre 2021, Journal of large-scale research facilities, 7

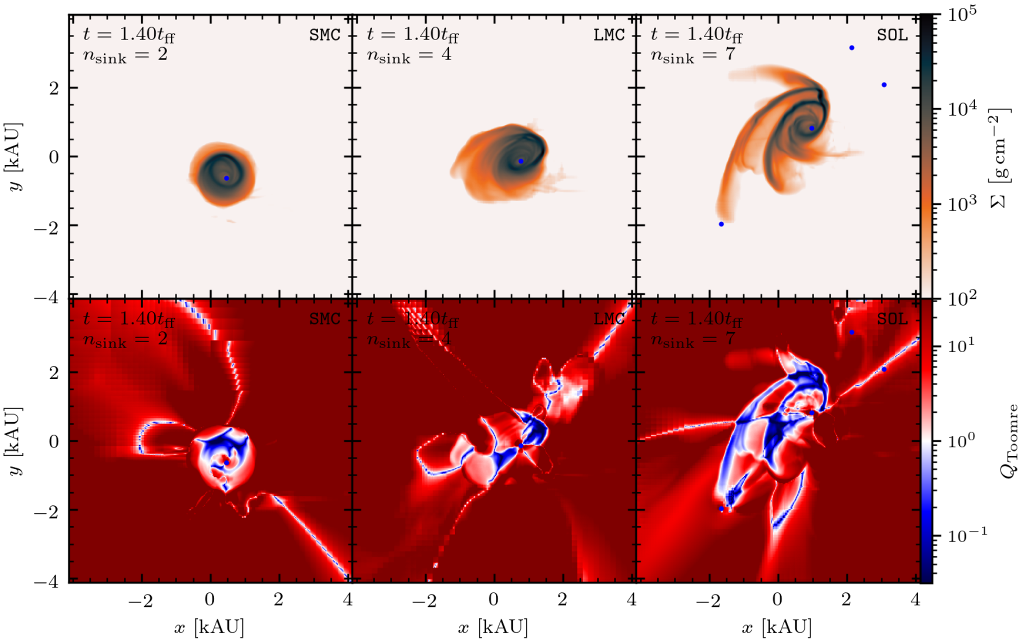

Figure 18. Column density (top row) and Q_{Toomre} (bottom row) for the disk at 1.4 t_{ff} for all three runs (from left to right). The disk shows more fragmentation for greater metallicities and appears to be less stable with increasing metallicity. Q_{Toomre} indicates that the densest parts of the disk are unstable due to values less than 1.

Klassen M., Pudritz R. E., Peters T., 2012, MNRAS, 421, 2861
Klepitko A., Walch S., Wünsch R., Seifried D., Dinnbier F., Haid S., 2023, MNRAS, 521, 160
Kroupa P., 2002, Science, 295, 82
Krumholz M. R., McKee C. F., 2008, Nature, 451, 1082
Krumholz M. R., Thompson T. A., 2012, The Astrophysical Journal, 760, 155
Krumholz M. R., Klein R. I., McKee C. F., Offner S. S. R., Cunningham A. J., 2009, Science, 323, 754
Kuiper R., Yorke H. W., 2013, ApJ, 763, 104
Kuiper R., Klahr H., Beuther H., Henning T., 2011, ApJ, 732, 20
Kuiper R., Klahr H., Beuther H., Henning T., 2012, A&A, 537, A122
Kurtz S., 2005, Proceedings of the International Astronomical Union, 1, 111–119
Matzner C. D., McKee C. F., 2000, ApJ, 545, 364
McKee C. F., Tan J. C., 2003, ApJ, 585, 850
Mitchell G. F., Hasegawa T. I., Schella J., 1992, ApJ, 386, 604
Nelson R. P., Langer W. D., 1997, ApJ, 482, 796
Oliva G. A., Kuiper R., 2020, A&A, 644, A41
Omukai K., 2000, ApJ, 534, 809
Omukai K., Tsuribe T., Schneider R., Ferrara A., 2005, ApJ, 626, 627
Rosen A. L., Li P. S., Zhang Q., Burkhart B., 2019, ApJ, 887, 108
Rosen A. L., Offner S. S. R., Sadavoy S. I., Bhandare A., Vázquez-Semadeni E., Ginsburg A., 2020, Space Sci. Rev., 216, 62
Salpeter E. E., 1955, ApJ, 121, 161
Schneider R., Ferrara A., Salvaterra R., Omukai K., Bromm V., 2003, Nature, 422, 869
Schreyer K., Henning T., van der Tak F. F. S., Boonman A. M. S., van Dishoeck E. F., 2002, A&A, 394, 561
Schreyer K., Semenov D., Henning T., Forbrich J., 2006, ApJ, 637, L129
Semenov D., Henning T., Helling C., Ilgner M., Sedlmayr E., 2003, Astronomy & Astrophysics, 410, 611
Stecklum B., et al., 2021, A&A, 646, A161
Toomre A., 1964, ApJ, 139, 1217
Walch S., et al., 2015, MNRAS, 454, 238
Wood D. O. S., Churchwell E., 1989, ApJS, 69, 831
Wünsch R., Walch S., Dinnbier F., Whitworth A., 2018, MNRAS, 475, 3393
Wünsch R., Walch S., Dinnbier F., Seifried D., Haid S., Klepitko A., Whitworth A. P., Palouš J., 2021, arXiv e-prints, p. arXiv:2105.09644

This paper has been typeset from a TEX/LATEX file prepared by the author.

9

RADIATION PRESSURE BOOST FACTOR

Description. In this chapter, the so-called RP momentum boost factor is studied. The momentum boost factor describes the actual momentum departed by RP taking into account reprocessed radiation with respect to the injected momentum given by the luminosity. Simulations performed in §7 and §8 are utilized to study the momentum boost. In particular, we study whether the novel method developed in §7 can faithfully reproduce the momentum boost. Reprocessed radiation may generate an additional contribution of RP that is expected to boost RP proportional to the optical depth, τ. An additional scheme using the Monte-Carlo approach is presented within this chapter, and a comparison is drawn to TreeRay-RP. The Monte-Carlo method is explained in §9.1. In §9.2, the boost factor is investigated for different opacity models and spherical cloud geometries. The opacity models encompass a constant opacity model, a decreasing opacity model and a realistic opacity model for dust.

9.1

RADMC-3D-RP

Introducing RADMC-3D. RADMC-3D[1] allows the computation of synthetic emission maps of simulations as a post-processing measure. Such post-processing is mandatory to enable better comparison between raw simulation data produced by numerical codes and observations produced by real telescopes. In a way, RADMC-3D takes the role of a telescope by computing RT that results in a physically accurate image. Here, the RT employed by RADMC-3D-RP is sophisticated to the extent that it is certainly unfeasible to be applied on the fly in numerical hydrodynamics simulations. RADMC-3D employs a Monte-Carlo-based RT method allowing to compute radiation mechanisms such as dust continuum thermal emission, scattering and gas line transfer. The methods RADMC-3D is based on are those by Bjorkman and Wood [2001] and Lucy [1999].

Extension to compute RP. For the purpose of this thesis, RADMC-3D had to be extended to compute RP on simulation data generated by flash. The method is based on the work of Klepitko [2016]. However, a fresh implementation starting from *vanilla* RADMC-3D was necessary. Essentially, RADMC-3D is used as an engine for the photon transport inherent to the Monte-Carlo RT method. To compute RP on dust, the implementation builds on the dust continuum RT feature, allowing to model thermal emission and scattering. In the spirit of Monte-Carlo RT, radiation is split into photon packages of equal energy that are launched independently from sources and traverse the computational domain such that their combined dynamics mimic a solution of the RT equation. RP is implemented through the connection that electromagnetic radiation carries momentum and, therefore, momentum is deposited if a particle changes its path. For a photon package with radiative energy,

---

[1] https://www.ita.uni-heidelberg.de/~dullemond/software/radmc-3d/

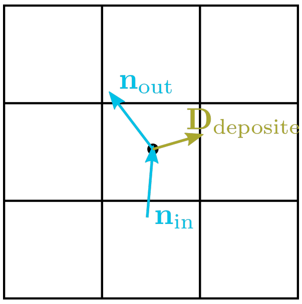
$\mathbf{n}_{\mathrm{out}}$
$\mathbf{D}_{\mathrm{deposite}}$
$\mathbf{n}_{\mathrm{in}}$

Figure 18: Exemplary momentum transfer from a photon package changing its direction within a cell. The incident direction is given by the unit vector $\mathbf{n}_{\mathrm{in}}$ and the outgoing direction by $\mathbf{n}_{\mathrm{out}}$. The deposited momentum, $\mathbf{D}_{\mathrm{deposited}}$, is given shown as the green arrow and results from the change in the direction according to Eq. 9.1.

E_{pkg}, the deposited momentum, $\mathbf{D}_{\mathrm{deposited}}$, is given by

$$\mathbf{D}_{\mathrm{deposited}} = \frac{E_{\mathrm{pkg}}}{c} \times (\mathbf{n}_{\mathrm{out}} - \mathbf{n}_{\mathrm{in}}) \,, \tag{9.1}$$

where $\mathbf{n}_{\mathrm{out}}$ and $\mathbf{n}_{\mathrm{in}}$ are the outgoing and incoming directions of the photon package after and prior to an interaction, respectively. Fig. 18 shows an exemplary interaction of a photon package happening within a cell. The recoil of the interaction corresponds to $\mathbf{D}_{\mathrm{deposit}}$. Throughout the Monte-Carlo scheme, the net momentum generated by sequential interactions combined is stored within each cell and updated accordingly.

Physical processes of RT. RADMC-3D models absorption and scattering during its RT. Each package is assigned a wavelength which may change if the interaction happens to be an absorption. In that instance, the package is absorbed and immediately reemitted at a different wavelength. The underlying dust distribution is given a wavelength-dependent opacity model. Note that multiple individual dust distributions, each with their own opacity model, can be realized in RADMC-3D. However, throughout this thesis, only a single species is employed.

Purpose for this thesis. In the further course of Chapter 9, RADMC-3D is used as an independent method to compute RP on dust. Given that TreeRay-RP does not account for scattering as described in Chapter 7, RADMC-3D makes for an interesting comparison to elaborate on a possible momentum boost generated by absorption and reemission in TreeRay-RP. To compare both methods, the runs of §7 and §8 are used.

9.2
Boost Factor with RADMC3D-RP

Origin of the RP boost. A source of radiation with luminosity, L, can inject a total momentum of, $p_{\mathrm{rad}} = L/c$, through its radiation. Embedded inside a cloud, only a fraction of the luminosity may interact with the cloud if it is optically thin. The total momentum deposited inside the cloud by direct radiation can be expressed as

$$p_{\mathrm{cloud,direct}} = \left(1 - e^{-\tau_{\mathrm{cloud}}}\right) \times \frac{L}{c} \,, \tag{9.2}$$

where τ_{cloud} is the optical depth measured from the position of the source to the

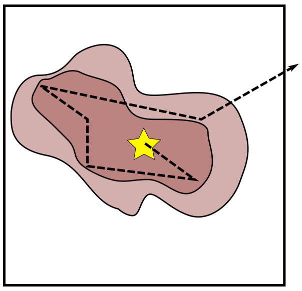

Figure 19: Depiction of a photon package's path emitted by a source embedded in a cloud. The package moves in straight lines until it undergoes an interaction. The interaction may be the result of either scattering or an absorption followed by an immediate reemission. From Eq. 9.1 one can estimate the deposited momentum to be greater than unity with respect to the package's momentum, E_{pkg}/c.

outside of the cloud [see also Klepitko, 2016]. The term direct momentum refers to the momentum generated by the first time radiation interacts with the gas or dust, neglecting subsequent interactions. Eq. 9.2 approaches the limit L/c for increasing τ_{cloud}. However, RP may be boosted and reach multiple accounts as a result of multiple scatterings or absorptions and reemissions along the path of escaping photons. This boost is often called *boost factor* [see e.g. Krumholz and Matzner, 2009, Hopkins et al., 2011, and others], or sometimes also called *radiative trapping*. Fig. 19 shows an exemplary path of a single photon package travelling through dense material. Each interaction deflects the path of the package and therefore causes a recoil leading to the deposition of momentum according to Eq. 9.1. One can model the dynamics of a single photon package to be similar to a random walk [see, e.g., appendix of Hopkins et al., 2011, Costa et al., 2018] with step size, $s = \frac{1}{\rho \kappa}$, where ρ and κ are the mass density and opacity inside a cloud, respectively. Further, for the sake of simplicity, a single opacity and a homogeneous density are assumed. For a given spherical cloud of radius, r_{cloud}, the package is expected to require

$$N = \frac{r_{\mathrm{cloud}}^2}{s^2} = (\tau_{\mathrm{cloud}})^2 \tag{9.3}$$

steps in order to escape the cloud if it was initially launched from the centre. Here, the mean displacement in a random walk must equal r_{cloud}. As pointed out by Costa et al. [2018], packages are reemitted or scattered isotropically in a random walk resulting in momenta cancelling out. The effective momentum departed inside the cloud is

$$p_{\mathrm{cloud}} = \tau_{\mathrm{cloud}} \times \frac{L}{c} \tag{9.4}$$

and not proportional to the number of scatterings alone, $(\tau_{\mathrm{cloud}})^2$ [Costa et al., 2018].

9.2.1

Constant Opacity Case

Description of the idealised setup. In the following, the implementation of RADMC3D-RP is verified on the theoretical expectations of the momentum boost generated for an increasing optical depth. A homogeneous spherical cloud of radius, r_{cloud}, is considered to host a single source of radiation with luminosity, L, in

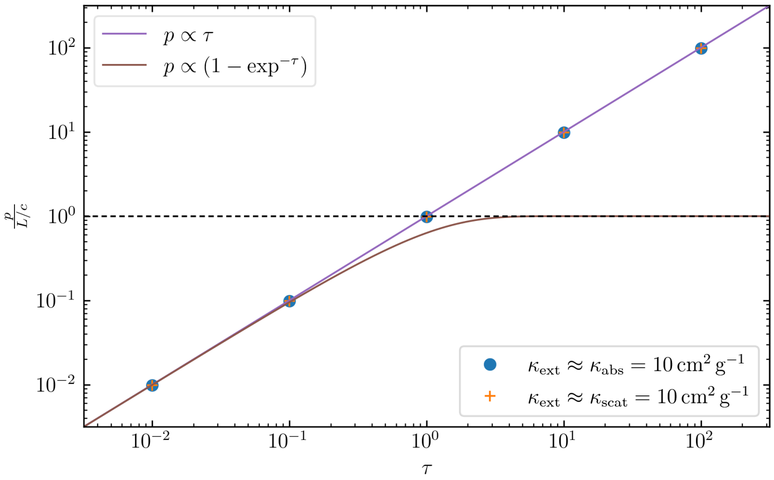

Figure 20: Measured radial momentum normalized to the momentum input vs the optical depth for a homogeneous spherical cloud where the dust has a constant opacity of $10\,{\rm cm^2\,g^{-1}}$. Blue circles and orange crosses show absorption, followed by reemission and scattering only. The purple and brown line show relations according to Eq. 9.4 and 9.2, respectively. Across all optical depths, the deposited momentum in the cloud follows a linear relation. No noticeable difference between absorption and scattering cases can be seen in this setup.

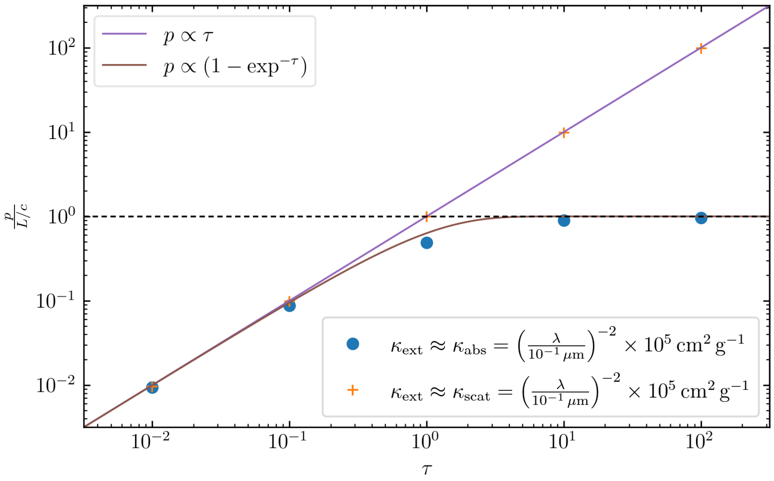

Figure 21: Same as Fig. 20 for an opacity of the form $\kappa_{\rm ext} \propto \lambda^{-2}$ in a low and high albedo case. Blue circles and orange crosses show results for the low and high albedo runs, respectively. In the low albedo case, the radiation interacts ones via absorption with $\kappa_{\rm ext,P}(3 \times 10^4\,{\rm K})$ and escapes after it is emitted at an effectively lower temperature and therefore lower Planck-weighted opacity. In this limit, the profile follows that of direct absorption given by Eq. 9.2 (purple line). The high albedo case follows the profile given by Eq. 9.4. Here, the signature of the initial spectrum is conserved; therefore, the effective opacity stays the same.

its centre. The dust extinction is set to a constant value, $\kappa_{\mathrm{ext}} = 10\,\mathrm{cm}^2\,\mathrm{g}^{-1}$, across all wavelengths. Two groups of runs are initialized: one with $\kappa_{\mathrm{abs}} = 10\,\mathrm{cm}^2\,\mathrm{g}^{-1}$ and $\kappa_{\mathrm{scat}} = 0\,\mathrm{cm}^2\,\mathrm{g}^{-1}$ and another with $\kappa_{\mathrm{scat}} = 10\,\mathrm{cm}^2\,\mathrm{g}^{-1}$ and $\kappa_{\mathrm{abs}} = 0\,\mathrm{cm}^2\,\mathrm{g}^{-1}$. These two groups each represent the case for an albedo, α, of $\alpha = 0$ in the former case and $\alpha = 1$ in the latter case, where the albedo is given as

$$\begin{aligned} \kappa_{\mathrm{ext}} &= \kappa_{\mathrm{abs}} + \kappa_{\mathrm{scat}}\,, \qquad (9.5) \\ \alpha &= \frac{\kappa_{\mathrm{scat}}}{\kappa_{\mathrm{ext}}}\,. \qquad (9.6) \end{aligned}$$

The optical depth measured from the centre to the border of the cloud is varied by increasing the density, ρ, of the cloud while keeping the cloud size constant. The optical depth is given by

$$\tau = r_{\mathrm{cloud}} \rho \kappa_{\mathrm{ext}}\,. \qquad (9.7)$$

Note that the boost factor is scale-free in this strongly idealised setup and only depends on the optical depth. The particular parameters chosen are $\rho(\tau = 1) = 3.24 \times 10^{-20}\,\mathrm{g\,cm}^{-3}$, $r_{\mathrm{cloud}} = 1\,\mathrm{pc}$ and $\kappa_{\mathrm{ext}} = 10\,\mathrm{cm}^2\,\mathrm{g}^{-1}$.

Reproducing the idealised boost factor with RADMC3D-RP. Fig. 20 shows the measured momentum input in the setup above, where blue circles and orange crosses show the resulting momentum of the absorption only and scattering only runs, respectively. Approaching the problem from the low optical depth regime, one can argue that a fraction of the injected luminosity interacts once (scattered or absorbed and reemitted) and leaves the cloud after that. This fraction is given by Eq. 9.2 and is proportional to $(1 - e^{-\tau})$ which gives a behaviour proportional to $\tau + \mathcal{O}(\tau^2)$ in the low optical depth regime. Therefore both curves given by Eq. 9.2 and Eq. 9.4 agree for $\tau << 1$. However, towards large optical depths, $(1 - \exp^{-\tau})$ converges to unity and fails to describe the behaviour of the results in that regime. Here, interactions of reprocessed radiation are not considered. The linear τ-momentum boost relation is well in agreement with all runs.

9.2.2

λ^{-2} Opacity Case and Realistic Opacity Models

Opacity model: $\kappa_{\mathrm{ext}} \propto \lambda^{-2}$. The previous subsection showed that RADMC3D-RP could faithfully reproduce the expected boost factor for RP across a wide range of optical depths. However, the setup on which this behaviour was studied was fairly idealised regarding the constant dust opacity. In the following, an opacity law of the form $\kappa_{\mathrm{ext}} \propto \lambda^{-2}$ is employed where a low and high albedo case is considered again. The absorption and scattering opacities take the form

$$\begin{aligned} \kappa_{\mathrm{abs}} &= \left(\frac{\lambda}{1\,\mu\mathrm{m}}\right)^{-2} \times 10^5\,\mathrm{cm}^2\,\mathrm{g}^{-1}\,, \qquad (9.8) \\ \kappa_{\mathrm{scat}} &= \left(\frac{\lambda}{1\,\mu\mathrm{m}}\right)^{-2} \times 10^5\,\mathrm{cm}^2\,\mathrm{g}^{-1}\,, \qquad (9.9) \end{aligned}$$

for the low and high albedo case, respectively. For both cases, the other opacities (scattering and absorption, respectively) are lower by a factor of 10^{-10}. By doing so, scattering or absorption and reemission are effectively turned off. Since the opacities of Eq. 9.8 and Eq. 9.9 are wavelength dependent now, it is no longer straight forward to compute a single opacity for all wavelengths as described by Eq. 9.7. The Planck-weighted opacity (see Eq. 2.11) provides a suitable way to compute the effective opacity for a given spectrum in this case. For the given relation, one gets

$$\kappa_{\mathrm{ext},P}(T) = 0.9086 \times \left(\frac{T}{100\,\mathrm{K}}\right)^2 \mathrm{cm}^2\,\mathrm{g}^{-1}\,, \tag{9.10}$$

due to the symmetry in κ_{abs} and κ_{scat} where the opacity is measured per mass of dust (not gas). Here, both cases differ in their albedo, which is important for the individual behaviour of the momentum boost in either case. Coming back to the setup of the simple spherical cloud, the initially injected spectrum by the central source is expected to stay unchanged in the case of a high albedo (scattering only) throughout all interactions.

Boost factor for $\kappa_{\mathrm{ext}} \propto \lambda^{-2}$. A star modelled as a Black-Body at temperature, $T_{\mathrm{src}} = 3 \times 10^4\,\mathrm{K}$, generates a spectrum with an effective extinction opacity of $\kappa_{\mathrm{ext},P}(T_{\mathrm{src}}) = 81774.0\,\mathrm{cm}^2\,\mathrm{g}^{-1}$. This statement holds only for an unphysically chosen dust opacity given by Eq. 9.8 and Eq. 9.9. A more realistic model would employ a cutoff beyond a certain temperature for its Planck-weighting [see, e.g. Semenov et al., 2003, Krumholz and Thompson, 2012, for constant κ beyond 150 K]. Moving to the low albedo case, the signature of the initial spectrum would be lost upon absorption, followed by thermal reemission. Therefore, the governing temperature for the Planck-weighted opacity in the low albedo case is given by the local temperatures of the reemitting Black-Bodies, particularly the dust. It can no longer be described by a single temperature as temperatures decrease if they are in a low radiation intensity environment. Both, the low (blue circles) and high (orange crosses) albedo runs are shown in Fig. 21. The only parameter that varied for the different runs was the density. Towards low optical depths ($\tau < 1$), the low (blue circles) and high (orange crosses) albedo runs agree, which is not the case for high optical depths ($\tau > 1$). The main reason for the difference is the absorption and subsequent reemission of the radiation at other wavelengths in the low albedo case. By this mechanism, the effective opacity of the radiation changes such that the cloud is perceived optically thin by the radiation, and it is free to escape. For such a simplified setup, one can estimate the local dust temperature as a function of the flux with the help of Eq. 2.14. In Eq. 2.14, J, the mean radiative intensity, is given by the star's luminosity, L, and distance, R, equating to a dust temperature of

$$T_{\mathrm{dust,\,LTE}}(L, R) = \left(\frac{\pi}{\sigma}\frac{L}{4\pi R^2}\right)^{1/4}\,, \tag{9.11}$$

which holds for dust in local thermal equilibrium (LTE). Combining Eq. 9.11 with Eq. 9.10 allows to estimate the expected extinction opacity in the following way:

$$\kappa_{\mathrm{ext,\,P}}(L, R) = 0.9086 \times \frac{10^5}{(100\,\mathrm{K})^2} \times \left(\frac{\pi}{\sigma}\frac{L}{4\pi R^2}\right)^{1/2} \mathrm{cm}^2\,\mathrm{g}^{-1}\,. \tag{9.12}$$

From Eq. 9.12 one can argue that the temperature of the spectrum emitted by dust decreases with the star's distance as R^{-1}. Further, one would expect a more compact object to have a greater reprocessed radiation temperature and, therefore, greater opacity for its reprocessed radiation while maintaining a similar line of sight optical depths regarding its initially injected stellar spectrum. The latter constraint implies the density to increase by a factor x if the radius shrinks by a factor of x according to Eq. 9.7. Fig. 22 shows three differently sized clouds run at different densities with the low albedo opacities (absorption only). The blue circles show runs of the same size as the previous figures, while orange triangles and green crosses show a ten times larger and smaller cloud, respectively. To match the line of sight optical depth at different sizes, the density is tuned accordingly (see Eq. 9.7). All geometries show matching behaviour for low optical depths up to an optical depth of about one. For $\tau > 1$, the compact clouds show a surplus in the momentum boost compared to the wider ones at a given optical depth. One finds the different cloud sizes to match the reprocessed momentum boost of the respective ten times wider cloud, while the optical depth for the initial spectrum is lower by a factor of 10. The relative differences observed for different cloud sizes in Fig. 22 agree with the idea that the reprocessed spectrum is hotter and therefore reaches a higher opacity. In return, the optical depth of the reprocessed radiation is greater, causing an enhanced momentum boost.

In the following, the total radially departed momentum, p_{total}, is described as two contributions generated by the injected radiation, p_{src}, and the reprocessed radiation, p_{re}. One can describe p_{src} as

$$p_{\text{src}} \quad = \quad \frac{L}{c} \times \left(1 - e^{-R_{\text{cloud}}\kappa_{\text{ext, P}}(T_{\text{src}})\rho}\right) . \tag{9.13}$$

The reprocessed part, however, is sensitive to the spectrum of the reprocessed radiation, which is determined by the underlying dust temperature making its description complicated. The momentum generated by reprocessed radiation becomes relevant once its optical depth, τ_{re}, reaches unity. One can estimate τ_{re} as

$$\tau_{\text{re}} \quad = \quad R_{\text{cloud}}\kappa_{\text{ext, P}}(L_{\text{src}}, R_{\tau_{\text{src}}=1})\rho\,, \tag{9.14}$$

$$R_{\tau_{\text{src}}=1} \quad = \quad \frac{1}{\rho\kappa_{\text{src},P}(T_{\text{src}})}\,, \tag{9.15}$$

where $R_{\tau_{\text{src}}=1}$ is the distance at which the initial spectrum reaches an optical depth of 1, thus marking the distance at which radiation is reprocessed. The distance, $R_{\tau_{\text{src}}=1}$, is crucial for the temperature of the reemitting dust since it determines the incoming intensity and thus gives the radiation its spectral signature. Similar to Eq. 9.13, p_{re} should be proportional to $(1 - \exp(-\tau_{\text{re}}))$, where again τ_{re} marks the optical depth of the reprocessed radiation. For the reprocessed radiation to generate additional boosting, the optical depth of the continuously reprocessed radiation must be larger than one. Otherwise the reprocessed radiation can immediately escape. In radiative equilibrium, the central source injects a rate of energy given by L matching that of the radiation escaping from the cloud. The surface from which radiation can directly escape is given by a diffuse region that measures an optical depth of less than one from the outside. In this simplified setup, the surface is that of a sphere and modelling it as a black body gives

$$T_{\text{escape}} = \left(\frac{L}{\sigma 4\pi R_{\text{escape}}^2}\right)^{1/4} \propto R_{\text{escape}}^{-1/2} \tag{9.16}$$

as its surface temperature. Inside the cloud, the radiation temperature should exceed T_{escape}. By taking T_{escape} as a minimum temperature, one can estimate the minimum opacity of the reprocessed radiation with the Planck weighted mean given by Eq. 9.12. One gets

$$\kappa_{\mathrm{ext,\,P,\,escape}}(R_{\mathrm{escape}}) \propto R_{\mathrm{escape}}^{-1} \tag{9.17}$$

for the opacity of the escaping radiation by combining Eq. 9.16 and Eq. 9.10. The maximum value for R_{escape} is the cloud radius itself. Describing the dependence of R_{escape} on the density would allow us to explain the scaling of the momentum boost concerning the density seen in Fig. 22. One can express R_{escape} as

$$R_{\mathrm{cloud}} - \frac{1}{\rho\kappa_{\mathrm{ext,\,P,\,escape}}(R_{\mathrm{escape}})} = R_{\mathrm{escape}}\,, \tag{9.18}$$

where the fraction involving the density and the Planck-weighted opacity measures one mean free path. Setting $\kappa_{\mathrm{ext,\,P,\,escape}}(R_{\mathrm{escape}}) = kR_{\mathrm{escape}}^{-1}$, where k $\left[\mathrm{g}^{-1}\,\mathrm{cm}^{3}\right]$ is a constant, and solving for R_{escape} yields

$$R_{\mathrm{escape}} = \frac{R_{\mathrm{cloud}}}{1+\frac{1}{\rho k}}\,. \tag{9.19}$$

If $R_{\mathrm{escape}} < R_{\mathrm{cloud}}$, radiation can escape the cloud because it is reprocessed to longer wavelengths resulting in inefficient trapping. Once R_{escape} reaches values comparable to R_{cloud}, the expected scaling of the momentum boost on the density returns to a linear relation. One can see this behaviour building up in Fig. 22 for optical depths greater than 100 with respect to the initial spectrum. The rate at which the momentum boost increases grows with larger optical depths and should approach a linear scaling. As a consequence, a less massive cloud being compact can generate a more efficient momentum boost than a massive extended cloud.

REALISTIC OPACITY MODEL. So far, a constant opacity model as well as a decreasing opacity model ($\kappa_{\mathrm{ext}} \propto \lambda^{-2}$) has been discussed. In the following, a realistic opacity model based on the work of [Weingartner and Draine, 2001b] is considered (hereafter WD01). Looking at Fig. 4 one can see those typical dust models involve a high albedo part transitioning to a low albedo part beyond wavelengths of $10\,\mu$m. The extinction follows a λ^{-2} profile for the low albedo part and is nearly constant below wavelengths of $10\,\mu$m. To describe the boost factor for the WD01 model, one can make use of both aforementioned ideal cases and describe the momentum boost in either its constant regime or its $\propto \lambda^{-2}$ regime. Fig. 23 shows the momentum boost vs. optical depth of the Milky Way dust model (orange crosses) [Weingartner and Draine, 2001b] and the $\kappa_{\mathrm{ext}} \propto \lambda^{-2}$, where the optical depth is measured with respect to the Planck-weighted opacity of the initially injected spectrum at $3 \times 10^4\,$K. Again, both models agree on low optical depths. At $\tau = 1$, the model of WD01 shows a slightly increased momentum boost compared to the λ^{-2} model. This increased momentum boost can be attributed to the difference in albedo, allowing for the high opacity and large albedo at shorter wavelengths to cause scatterings resulting in a more efficient momentum boost. In the limit of scattering only, the momentum boost would continue on the $p \propto \tau$ line as seen in Fig. 21. For greater opacities beyond $\tau = 1$, the model of WD01 shows a more extensive momentum boost compared to the λ^{-2} model at similar optical depths. The model of WD01 shows a scaling of $p \propto \tau$ at optical depths of 10^4 and beyond, indicating that all relevant lines are optically thick for the entire cloud. In particular, R_{escape} has reached the scale of $R_{\mathrm{cloud}} = 1\,$pc.

OPACITY MODEL OF PUBLICATION I. Next, the opacity model used in 7.1 [see

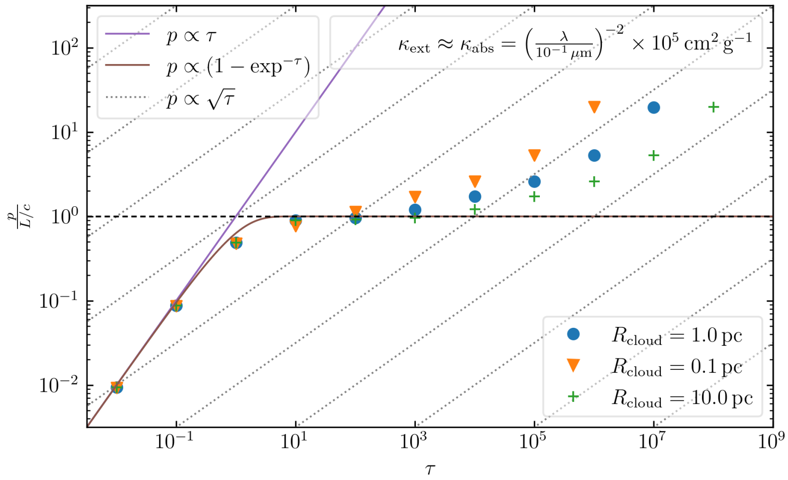

Figure 22: Same as Fig. 20 for an opacity of the form $\kappa_{\text{ext}} \propto \lambda^{-2}$ in a low case. Blue circles, orange triangles and green crosses show results of different cloud of size 1.0 pc, 0.1 pc and 10.0 pc, respectively. More compact clouds transition to the linear momentum boost regime earlier than bigger clouds for corresponding optical depths. This trend is because the maximum wavelength of reprocessed radiation is shorter in compact clouds due to greater minimum radiation temperatures. This allows all reprocessed radiation to become optically thick at comparably lower optical depths with respect to the Planck weighted mean opacity of the initial spectrum.

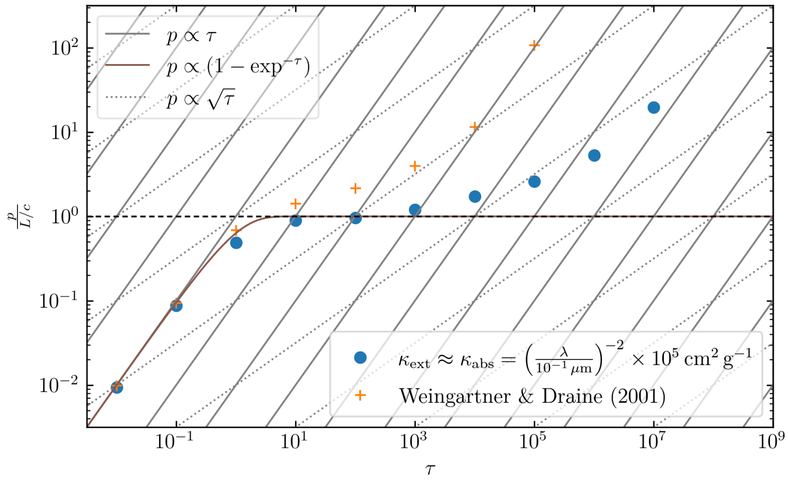

Figure 23: Momentum boost vs optical depth for two different opacity models where the density is varied. The first model is the $\kappa_{\text{ext}} \propto \lambda^{-2}$ model in a low albedo case (blue circles), and the second model is the Milky Way dust model by Weingartner and Draine [2001b] (orange crosses). The optical depth is defined with respect to a Planck weighted mean opacity for 3×10^4 K of either model, respectively. Similar to previous models shown in Fig. 21 and Fig. 22, the Milky Way dust model follows $(1 - \exp(-\tau))$ initially and continues to grow beyond unity for greater optical depths. Compared to the $\kappa_{\text{ext}} \propto \lambda^{-2}$ model, Milky Way dust model starts to grow beyond unity faster and reaches $p \propto \tau$ indicating that all wavelengths are optically thick.

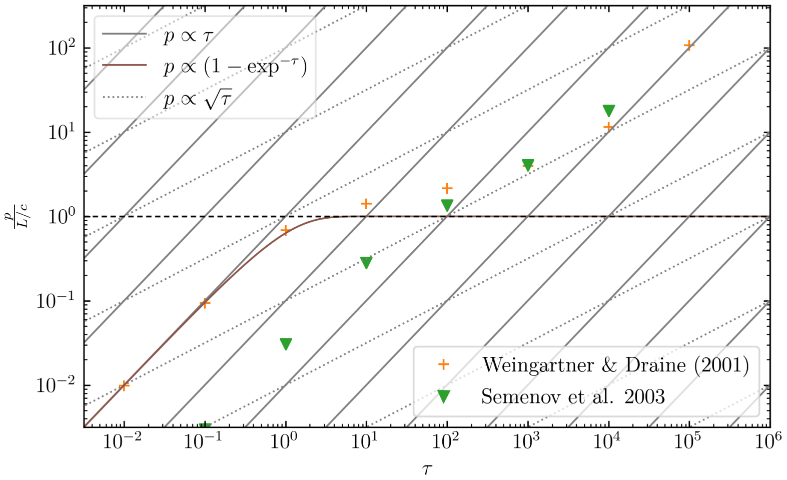

Figure 24: Momentum boost vs optical depth for the realistic Milky Way dust model and the model presented in 9.20. The optical depth is increased incrementally through the density and measured for a black body spectrum of 3×10^{4} K taking the Planck-weighted mean opacity of the Milky Way dust model. In particular, both models have the same normalisation resulting in the horizontal offset at momentum inputs less than unity. Nevertheless, both models agree on greater optical depths.

e.g. Semenov et al., 2003, Krumholz and Thompson, 2012, **Klepitko** et al., 2023] is investigated and compared to the realistic dust model WD01. Assuming a dust-to-gas mass ratio of 1/100, the Planck-weighted opacity model is given as

$$\kappa_{\mathrm{ext,\,P,\,sem}}(T) = 10^{-1}\frac{\mathrm{cm}^2}{1\,\mathrm{K}^2\,\mathrm{g}} \times \begin{cases} T^2 & \text{for } T < 150\,\mathrm{K} \\ (150\,\mathrm{K})^2 & \text{else} \end{cases}, \tag{9.20}$$

where g measures the dust mass in gramms. The model described by Eq. 9.20 is converted to wavelengths by expressing the temperature as a wavelength using Wien's displacement law. This way, one gets

$$\kappa_{\mathrm{ext,\,P,\,sem}}(\lambda) = 2250\frac{(19.32\,\mu\mathrm{m})^2\,\mathrm{cm}^2}{1\,\mathrm{g}} \times \begin{cases} \lambda^{-2} & \text{for } \lambda > 19.32\,\mu\mathrm{m} \\ (19.32\,\mu\mathrm{m})^{-2} & \text{else} \end{cases}, \tag{9.21}$$

where $\kappa_{\mathrm{ext,\,P,\,sem}}$ assumes an albedo of zero and therefore $\kappa_{\mathrm{ext,\,P,\,sem}} = \kappa_{\mathrm{abs,\,P,\,sem}}$. Fig. 24 shows the momentum boost vs. optical depth of the WD01 model and $\kappa_{\mathrm{ext,\,P,\,sem}}$. The optical depth for both models is measured with respect to the initially injected spectrum of the 3×10^{4} K Black-Body for the WD01 model. Moreover, both runs have the same underlying density at respective similar optical depths in Fig. 24. Comparing both models shows that they differ for optical depths smaller than unity, where the radiation temperature is large and therefore dominated by shorter wavelengths. In particular, radiation is not reprocessed yet such that the corresponding difference in opacities with respect to the initial spectrum causes the offset. Once radiation is efficiently reprocessed, however, the boost factor of either model agrees with one another.

Concluding the results. Unlike the constant opacity cases seen in §9.2.1 and the high opacity case seen in Fig. 22, the momentum boost factor does not follow a linear optical depth relation. Instead, the momentum boost flattens in a regime where the reprocessed radiation is in an optically thin limit and can directly escape. Once the cloud is sufficiently optically thick for all wavelengths, the scaling of the momentum boost returns to a linear scaling with respect to the optical depth. The turnover point from a constant to a linear scaling of the boost factor is dependent on the underlying opacity model. The dust model and, in particular, its response to the reprocessed radiation determine the boosting of RP beyond orders of unity.

9.3
Comparing RADMC-3D-RP to TreeRay/RadPressure

Origin of the underlying data. In the following, RADMC-3D-RP is applied to the runs presented in §8 and the computed RP is compared to that of TreeRay. Unlike previous density distributions, the underlying density distributions have formed self-consistently out of an initially turbulent spherical setup. In particular, estimating the boost factor is non-trivial in such a case. Therefore, a comparison to an independent scheme is useful to verify the accuracy of TreeRay/RadPressure.

Measuring RP in TreeRay. TreeRay/RadPressure stores acceleration vectors in units cm s^{-2}, $\mathbf{a}_{\mathrm{RP}}$, at every position. Using $\mathbf{a}_{\mathrm{RP}}$ one can compute the radial projection of the momentum input for the entire domain in the following way

$$\dot{p}_{\mathrm{RP}} = \int \rho \mathbf{a}_{\mathrm{RP}} \cdot \mathbf{n}_{\mathrm{rad}} \mathrm{d}V \,, \tag{9.22}$$

where ρ and $\mathbf{n}_{\mathrm{rad}}$ are the mass density and the radial unit vector pointing away from the point of interest, respectively. The point of interest, in particular, is the central source, a massive star. Similar to the setups shown throughout §9.2, the central star is the principal radiation source. Its momentum input through radiation is expected to be boosted by the interaction of radiation with the surrounding material.

Influence of the chemistry on dust temperatures. The chemistry, as described in §7, determines the dust temperature calculation and, therefore also, the radiation emitted by a corresponding volume element. Mechanisms inherent to the chemistry interact with the temperature of the dust. Therefore, these mechanisms may influence the momentum boost. Figs. 25 to 27 show slices of the dust temperatures for the runs performed by RADMC-3D-RP and TreeRay/RadPressure at different times, respectively. The principal source of radiation is well traced by the hot dust temperatures across all runs shown in the figures. Comparing the dust temperature computed by RADMC-3D-RP to those of TreeRay/RadPressure at early times, where $t \leq 0.35\, t_{\mathrm{ff}}$, one finds hotter dust temperatures in the calculations of RADMC-3D-RP. Comparing only the runs of RADMC-3D-RP for increasing metallicities, e.g. from Fig. 25 to Fig. 26, one finds hotter dust temperatures at greater metallicities due to the increased dust density and therefore greater optical depth. For the same reason, the region very close to the star becomes hotter for increased metallicities, as radiation is trapped more efficiently, resulting in larger regions where dust sublimation occurs. The black contour line encloses the region affected by dust sublimation in each panel. Comparing the runs of TreeRay/RadPressure for $t \leq 0.35 t_{\mathrm{ff}}$, one finds hotter dust temperature for lower metallicities in regions further away. Here, as described in §8, dust is coupled to gas collisionally. Due to the lower abundance of metals, gas is cooled less efficiently, resulting in greater dust temperatures for the ambient medium because of hotter gas. However, these differences in the ambient medium should not influence

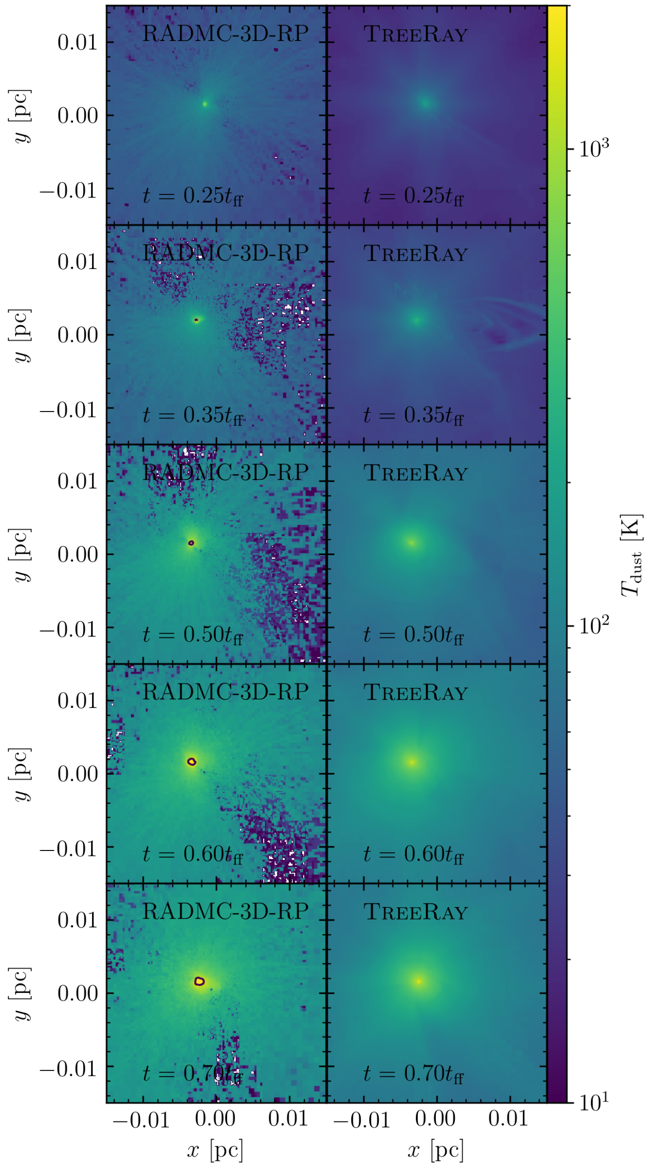

Figure 25: Slices of dust temperatures computed by RADMC-3D-RP and TreeRay/RadPressure at the z-coordinate of the principal star for different times shown in different rows, respectively. The black contours show regions surpassing $T_{\rm dust} > 1500\,\rm K$, where dust is taken to be sublimated. The simulation data is taken from the `SMC` run from §8. White spots correspond to a dust temperature of 0 K. These regions, in particular, had no interactions with photon packages. Comparing the RADMC-3D-RP data to TreeRay shows that RADMC-3D-RP produces hotter dust temperatures than TreeRay.

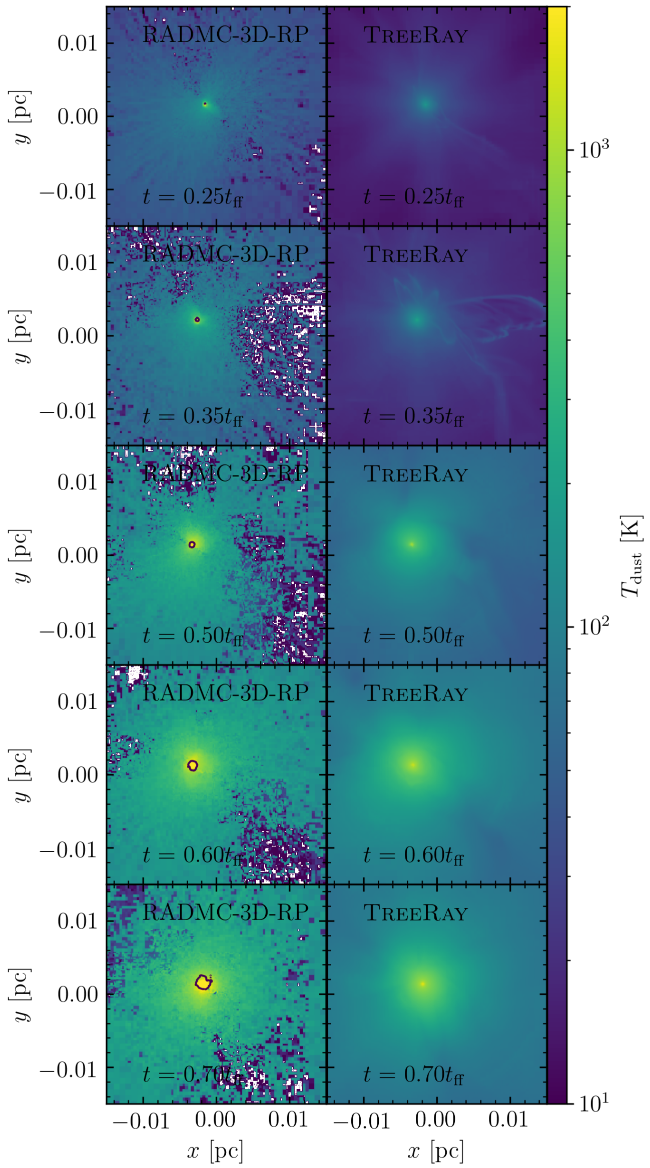

Figure 26: Same as Fig. 25 but for the `LMC` run. The region close to the star is hotter in comparison to Fig. 25 due to the greater metallicity and therefore dust-to-gas ratio. In addition, one finds the region in which dust is sublimated to be larger compared to Fig. 25.

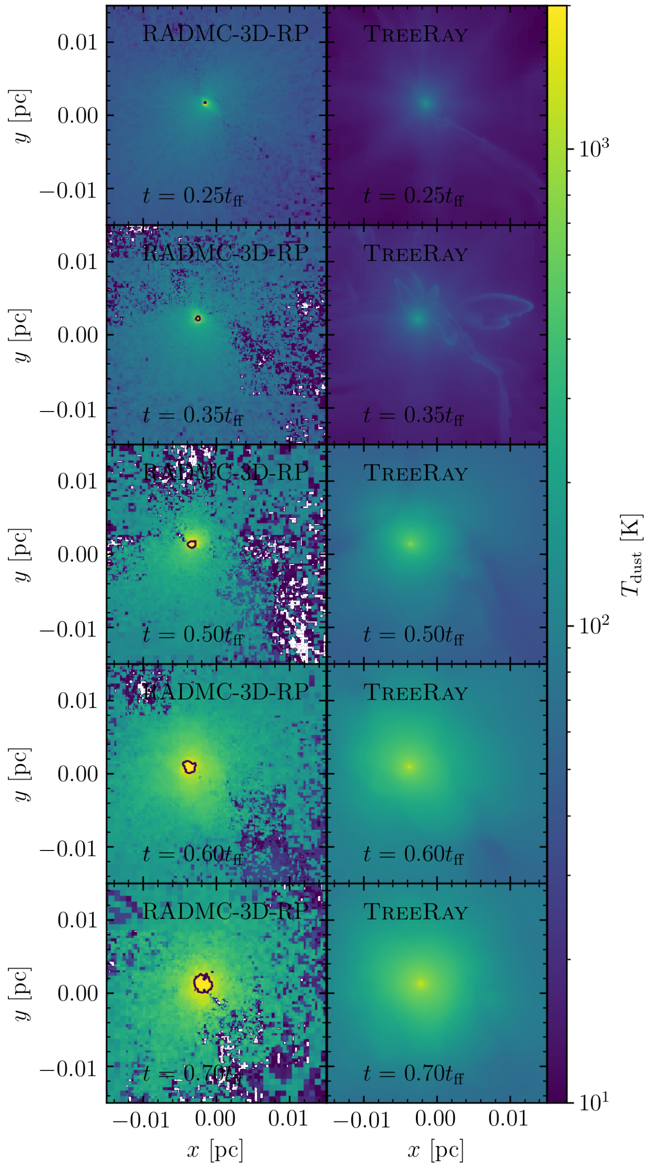

Figure 27: Same as Fig. 25 but for the `SOL` run. In the same way as in Fig. 26, dust close to the principal star is hotter showing an increased region in which dust is sublimated due to the greater dust-to-gas ratio and therefore dust mass.

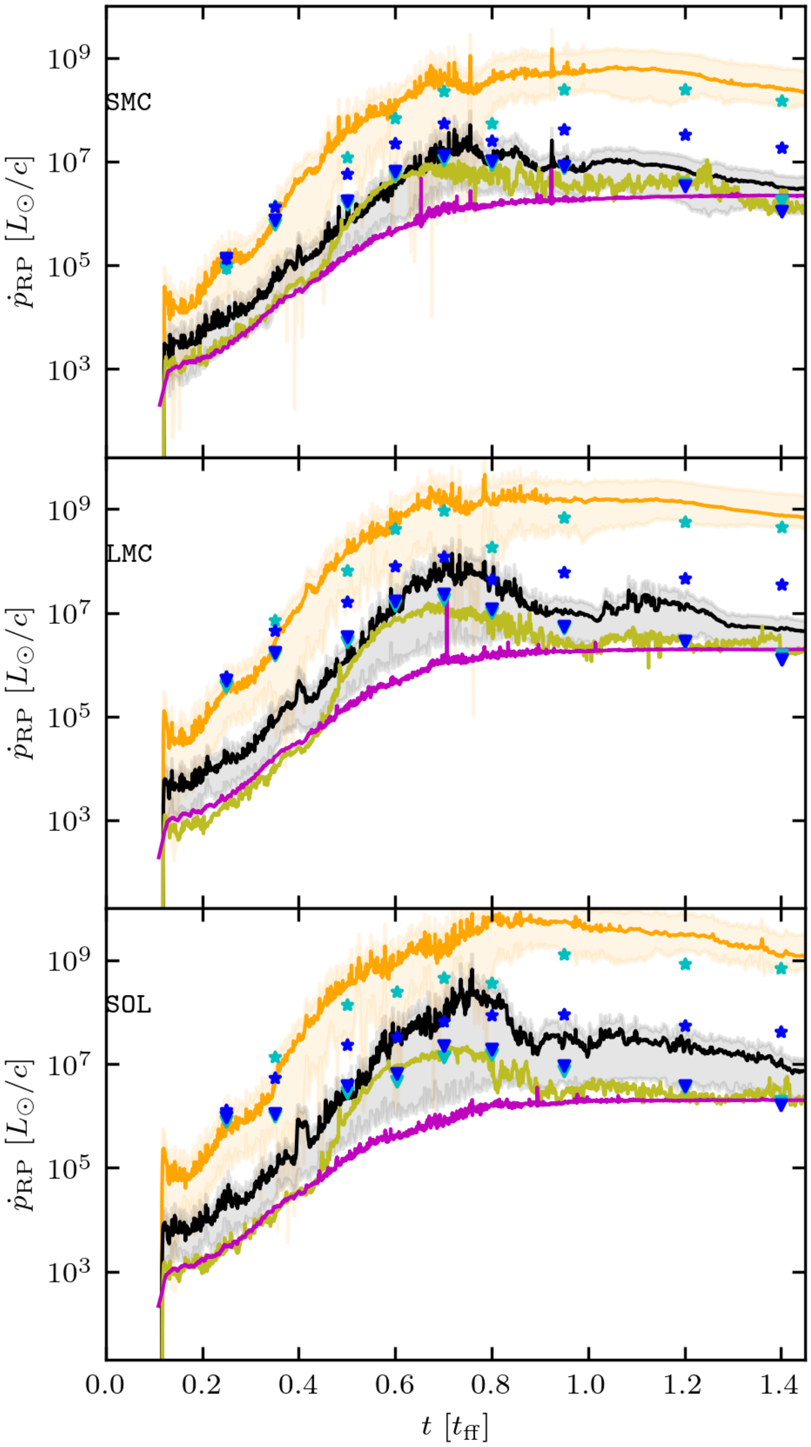

Figure 28: Radiation pressure momentum comparison between RADMC-3D-RP and TreeRay/RadPressure vs. time along with theoretical models (orange and black line). From top to bottom, the runs `SMC`, `LMC` and `SOL` are shown from §8. The purple line shows the direct momentum input by the luminosity of the principal star vs. time. The olive line shows the radial momentum input computed by TreeRay/RadPressure vs. time. Radial momentum input computed by RADMC-3D-RP at corresponding times is shown as scattered points. Blue and cyan points use the opacity model of Weingartner and Draine [2001b] and Semenov et al. [2003], respectively, where the latter follows Eq. 9.21. Triangles account for sublimation by neglecting cells hotter than 1500 K while stars do not.

the radial RP momentum calculated by TreeRay/RadPressure to a large extent as most of the momentum is deposited close to the principal source in hot regions. However, hotter dust temperatures immediately surrounding the star in RADMC-3D-RP compared to TreeRay/RadPressure indicate that TreeRay/RadPressure can not fully model the trapping of radiation. In particular, the sublimation region differs greatly between the two schemes.

Comparing TreeRay/RadPressure and RADMC-3D-RP. Fig. 28 shows the momentum input obtained by RADMC-3D-RP and TreeRay/RadPressure along with theoretical models which are explained in the next paragraph. The main constituent generating RP is the luminosity of the principal star. The purple line shows this luminosity. The olive green line shows the momentum boost directly measured from the simulations of §8 calculated with Eq. 9.22. In other words, the olive green line shows the momentum computed by TreeRay/RadPressure presented in §7. The star and triangle symbols in blue and cyan colour show the radial RP momentum computed with RADMC-3D-RP at given times. Here, the origin from where the radial momentum is measured coincides with that of TreeRay/RadPressure. In addition, all stellar sources present in the simulations of §8 at a given time have been taken into account for the calculations performed by RADMC-3D-RP. In particular, the accretion luminosity and the internal luminosity of each star are modelled by two individual black-body curves in RADMC-3D-RP, respectively. The colors cyan and blue of the RADMC-3D-RP data points indicate whether the [Weingartner and Draine, 2001b] or the [Semenov et al., 2003] (see Eq. 9.21) model is applied, respectively. The triangular or star shape of the points indicate whether the sublimation of dust is accounted for or not, respectively. In the instance where sublimation is taken into account, momentum departed in cells with dust temperatures exceeding 1500 K is neglected during the computation of the radial RP momentum. Here, the data where sublimation is neglected is greater by factors of 10 to 100 than the case where sublimation is accounted for. One finds the WD01 model to generate a bigger boost compared to the model given by Eq. 9.21 in the instance where sublimation is neglected. The greater opacity can explain this difference at shorter wavelengths and the non-zero albedo for the WD01 model. In particular, the idealised setups in §9.2 have shown that opacities with great albedos cause additional boosting. In those instances, the spectrum remains at shorter wavelengths and, therefore, greater opacities for multiple interactions. The difference between sublimation and non-sublimation increases towards later times, once more mass is located near the central star causing the reprocessed spectrum to have a greater temperature as seen in Fig. 25 to 27. This, however, is purely a non-physical remark as the dust would be sublimated at these temperatures anyway. One finds the sublimated data to agree for both models. The RADMC-3D-RP data agrees with the momentum input calculated by TreeRay/RadPressure past free-fall times of 0.5 t_{ff}. For earlier times, however, RADMC-3D-RP shows a difference by a factor of roughly 100 to 500 where both sublimation and no sublimation data points agree with each other.

Theoretical modelling. The boost factor is, to some extent, well described by the theoretical models shown in Fig. 28. All of the models shown in Fig. 28 relate the net input of radial momentum and the injected momentum in radial direction due to RP as a linear relation with an effective optical depth, τ_{eff}. The effective optical depth is computed as a mean of optical depths measured along multiple directions. Here, the individual directions follow the directions of the HEALPix algorithm [Górski et al., 2005] for a total number of 192 directions. Each pixel-aligned optical depth, τ_{pix}, is computed as

$$\begin{aligned}
\tau_{\text{pix},i}\left(R_{\text{star}}\right) &= \int \rho\left(r_{\text{path, pix}\,i}(t)\right)\kappa\left(r_{\text{path, pix}\,i}(t)\right)\frac{\partial r_{\text{path, pix}\,i}(t)}{\partial t}\mathrm{d}t\,, && (9.23)\\
r_{\text{path, pix}\,i}(t) &= 1\,\text{cm}\times t\times r_{\text{pix},i}+R_{\text{star}}\,, && (9.24)
\end{aligned}$$

where R_{star}, ρ, κ and $n_{\text{pix},i}$ are the position of the star, the path-dependent density and opacity, and the unit vector given by HEALPix for a single pixel. The path along which the optical depth is integrated, $r_{\text{path, pix}}(t)$, follows a straight line starting from R_{star} going outwards along the direction of $n_{\text{pix},i}$. The optical depths along individual pixels are calculated based on the densities and dust temperatures generated from TreeRay/RadPressure. Therefore, dust's sublimation is considered by setting the dust opacity to zero. The mean across all directions is computed as

$$\tau_{\text{eff,lin}} = \frac{1}{N_{\text{pix}}}\sum_{i=1}^{N_{\text{pix}}}\tau_{\text{pix},i}\,, \tag{9.25}$$

where N_{pix} is the number of pixels. To predict the momentum boost, the star's luminosity is multiplied by $\tau_{\text{eff,lin}}$ similar to Eq. 9.4. The orange line in Fig. 28 shows the momentum predicted for the effective optical depth of Eq. 9.25. The shadow surrounding the orange line in Fig. 28 is the 1-σ distance of the mean over all pixels. The boost predicted by $\tau_{\text{eff,lin}}$ matches the momentum boost calculated by RADMC-3D-RP at the beginning of the simulations for all runs up to 0.4 t_{ff}. Up to this point, sublimation reduces the momentum input by factors of less than ten. After 0.4 t_{ff} the orange line overestimates the calculated momentum input for both dust opacity models, even in the non-sublimation case (star symbols in Fig. 28). Looking back at the spherically symmetric runs of §9.2, $\tau_{\text{eff,lin}}$ would have predicted the boosted momentum input correctly. Here, however, the setup is not symmetric, allowing radiation to escape along optically thin paths. The idea of radiation leakage has been put forward by Krumholz et al. [2009] [see also Hopkins et al., 2011, Krumholz and Thompson, 2012] in the picture of FLD where radiation escapes through optically thin channels. Optically thin sight-lines need to be given more weight to account for leakage while estimating the effective opacity. Given that the extinction exponentially reduces radiation intensity, one can motivate to choose $\exp(-\tau)$ as an ansatz for the weighting function and thus compute an exponentially weighted mean. This approach yields

$$\tau_{\text{eff,exp}} = -\log\left(\frac{1}{N_{\text{pix}}}\sum_{i=1}^{N_{\text{pix}}}\exp\left(-\tau_{\text{pix},i}\right)\right)\,. \tag{9.26}$$

The effective opacity calculated by 9.26 is shown as the black line in Fig. 28. Together with its shadow being the 1-σ distance of the mean, the black curve describes the momentum input calculated by both schemes well for $0.4\,t_{\text{ff}} < t < 1.4\,t_{\text{ff}}$. Only before 0.4 t_{ff}, the calculated momentum input by both schemes is slightly over- and undershooting the prediction of Eq. 9.26 in the individual case. Compared to the orange line, the black line shows features present in the calculated momenta, such as the local maximum around $t \approx 0.7\,t_{\text{ff}}$.

Varying momentum boost with metallicity. Across different metallicities, the agreement between the black line and the computed RP varies. One would expect the higher metallicities to have a greater momentum boost due to the greater opa-

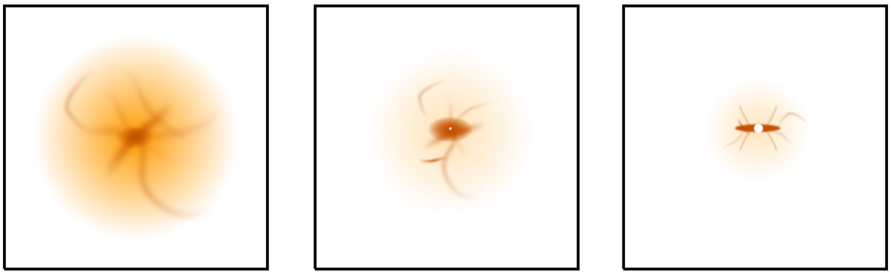

Figure 29: Schematic evolution of the star-forming setup presented in §7 and §8. The initial spherical distribution forms filamentary structures due to the turbulent velocity seed. Fragmentation is more pronounced for higher metallicity runs. Gas migrates to the central hub, where the star potentially accretes it. A small region surrounding the central star shows sublimated dust (white spot in the middle frame). The central hub grows in mass and forms a rotating disk in which the sublimated region grows.

city per gas mass. This behaviour is imprinted in the black curve as it increases relative to the direct L/c momentum. However, the lower metallicity run, `SMC`, shows the best relative agreement with the black line, while the momentum boost for the `SOL` run is slightly off. So other factors must be at play here. Besides the greater opacity per gas mass, the higher metallicity runs show more pronounced fragmentation (see §8). On the contrary, `SMC` is less fragmented, which leads to a more homogeneous appearance. Therefore RP can not escape as easily through optically thin trajectories as it would otherwise be possible in a more fragmented setting. In return, RP may be boosted more efficiently with respect to the available dust mass for the lower metallicity case. In particular, one finds less relative deviation from the black line and the RP calculations between 0.5 - 1.4 t_{ff}. As mentioned before, similar arguments have been made by Hopkins et al. [2011] towards leakage of radiation. Their assumptions towards estimating the boost factor are based on sight lines in a turbulent cloud following a density distribution of a log-normal probability density function (PDF). The mass-weighted PDF shown in §8 indicates that the initial log-normal distribution generates a second peak for the high-density regime in the course of the simulation. This second peak originates from the formation of the central hub, while the initial peak originates from the turbulent velocity seed. The central hub holds angular momentum, which leads to the transition from a spherical object into a flattened disk at later stages. A cartoon of the qualitative evolution of the simulation is shown in Fig. 29 where time increases from left to right. Filamentary structures occur more pronounced for greater metallicities (see §8). In a similar way, the disk shows more fragmentation and instabilities for greater metallicities. Fig. 30 shows column density plots of the disk viewed along the y-axis for all 3 runs presented in §8 at different times. Here, one finds the `SMC` runs to produce a stable disk while the disk in the `SOL` run is more fragmented. In addition, the disk of the latter run shows gravitational instabilities that transport material and angular momentum outwards.

REMOVAL OF GAS. At around 1.2 t_{ff}, gas along the rotation axis of the disk is removed (see §8), decreasing the optical depth for lines of sight along the rotation axis. The decreasing optical depth can be seen in Fig. 28 as shown by the decreasing black and orange lines. At comparable times, the momentum boost calculated by RADMC-3D-RP decreases to unity. At the same time, RP calculated by TREERAY/RADPRESSURE stays close to L/c. Eventually, both schemes may dis-

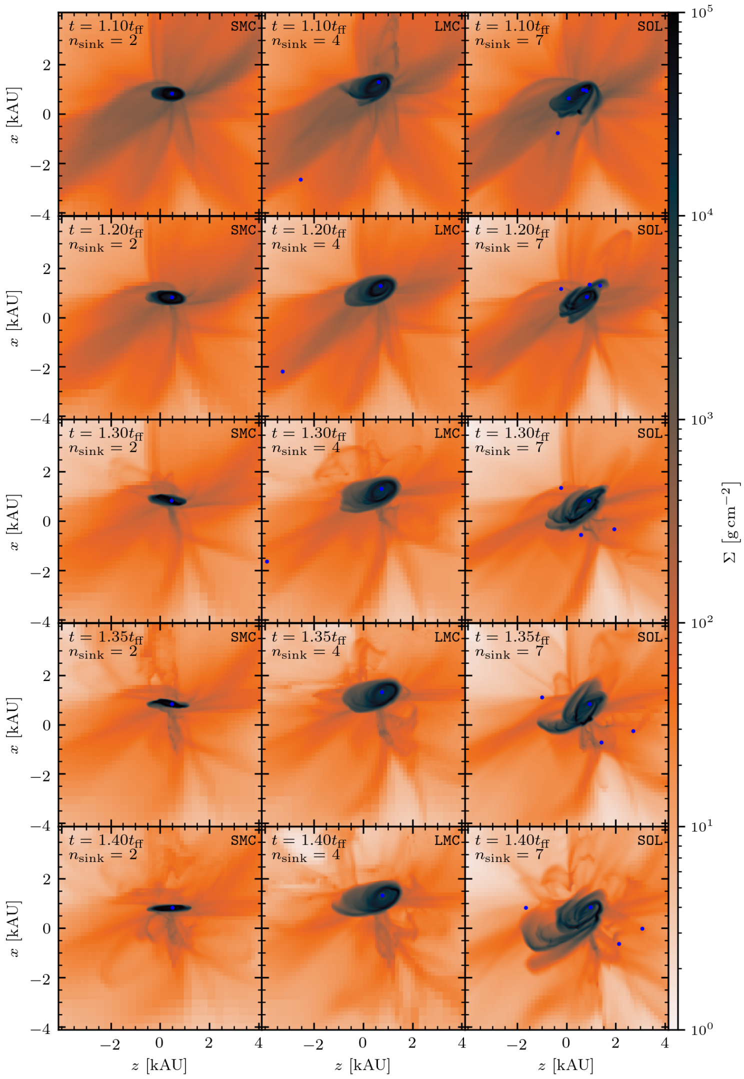

Figure 30: Column density plots in an (almost) edge-on view of the disk for all three runs of different metallicity from §8 at different times. Lower metallicity runs show a less fragmented disk. The fragmentation may be caused by lower temperatures due to better cooling and interactions of other sink particles with the disk. The disk is destroyed by expansion from the inside out by the star as seen for the `LMC` run at 1.4 t_{ff}. At this time, the `SMC` run features a stable disk and the `SOL` run shows gravitational instabilities in the disk.

agree and the resulting difference may be explained by the fact that RADMC-3D-RP calculates RP on dust while TreeRay/RadPressure calculates RP on both dust and gas. At some point, the lines of sight will get optically thin, so radiation no longer interacts with dust. Gas, however, is ionised by radiation, and thus momentum is transferred onto the gas every time gas is reionised after recombination in TreeRay/RadPressure. This additional contribution explains why the two methods may diverge in their results. Despite the additional physics, the computed momentum boost by TreeRay/RadPressure should only amount to at most unity for a configuration optically thin to dust since reprocessed radiation can immediately escape. Therefore, one expects the radial RP to remain around unity until the HII region reaches the computational domain. For the further course of the simulation, one can safely predict more gas to be stripped from the disk and ejected along the rotational direction. This is especially true in the case of the low metallicity run, where the disk is stable. Eventually, the disk might reduce sufficiently in mass so that RP will remove it altogether.

Concluding the comparison. In-between 0.5 t_{ff} and 1.4 t_{ff}, the method developed in §7 is in agreement with the results of RADMC-3D-RP. Here, the RT algorithm developed in the course of this thesis, TreeRay/RadPressure, can successfully compute RP, including the effects of reprocessed radiation. In particular, the differences caused by varying the metallicity are well met and reflected in the momentum boost. Theoretical modelling of the momentum boost agrees partially with the computed one once non-trivial configurations are considered. To accurately determine the momentum boost in a non-trivial configuration, the full RT calculation has to be performed. This statement agrees with Hopkins et al. [2011] where they estimate the momentum boost accounting for leakage based on a statistically motivated optical depth along the lines of sight. Before 0.5 t_{ff}, RADMC-3D-RP yields a greater momentum boost than TreeRay/RadPressure. In a similar way, temperatures around the massive star are hotter in RADMC-3D-RP as well. This may indicate that TreeRay/RadPressure is not modelling the trapping of radiation to the full extent. Certain geometries of the underlying density distribution as, for example, that in the initial phase might be challenging for TreeRay/RadPressure to compute. For the dynamics of the simulation, however, the difference in RP is not relevant, as gravity is stronger by at least three orders of magnitude (see §8).

9.4
Conclusion

Idealised momentum boost. This chapter has succeeded in demonstrating the boost factor with a Monte-Carlo-based RT scheme for idealised and non-idealised setups. Systematic tests in an idealised setting have shown that the momentum boost is sensitive to the setup's underlying opacities and geometry. In particular, the opacities of the reprocessed radiation are important to estimate the momentum boost beyond unity. Furthermore, the generated momentum boost can be accurately estimated for simple geometries by theoretical models taking that only take into account the optical depth along the lines of sight.

Comparison. The comparison between Treeray/RadPressure and RADMC-3D-RP has shown that the method developed in this thesis is capable of computing the momentum boost for non-trivial setups. Treeray/RadPressure accounts for radiation leakage accurately especially for disks. Theoretical models, however, fail to estimate the momentum boost over the full evolution of the simulation. Estimating the effective optical depth by an angular average (see Eq. 9.25) drastically overestimated the momentum boost once the simulation forms a disk. In the beginning, Eq. 9.25 correctly estimates the momentum boost in accordance with RADMC-3D-RP as long as the setup gradually satisfies spherical symmetry.

10

CONCLUSION AND OUTLOOK

10.1
Summary

Novel RT scheme. In §7, the tree-based solver for flash4, TreeRay, is expanded to compute radiative transfer on infrared radiation from dust and point-like sources via backwards ray-tracing. The novel approach is called TreeRay/RadPressure. By design, TreeRay is independent of the number of sources allowing every cell to interact with the radiation field feasibly – through absorption, emission or both. The inherently different treatment of the optically thin and thick matter is key to the accurate computation of the radiation field within TreeRay/RadPressure. The resulting infrared radiation field is coupled to a chemical network, particularly the dust temperature calculation. With that, the dust thermodynamics are significantly improved, allowing dust to shield itself from cooling and being heated by stellar radiation. TreeRay/RadPressure has been benchmarked in various tests for its performance in generating the expected momentum and correct radiation fields.

Metallicity and RP. Moving on to §8, the novel RT scheme is applied in a study towards understanding the role of metallicity in MSF. Here, a highly sub-virial core with different metallicities is modelled to undergo gravitational collapse leading to the formation of a principal MS. The number of companion stars formed around the principal star and fragmentation in the simulation scale with the metallicity. Greater metallicities show a more efficient boosting of RP. The final stage of the simulations shows a more stable disk in the low metallicity run, while the disk shows more fragmentation in the higher metallicity runs. RP is stronger than ionising feedback, and thermal pressure support in terms of radial momentum injected for all three runs after about 0.5 $t_{\rm ff}$ on the simulated scales. RP may become weaker than ionising feedback once the ultra-compact HII region expands.

Comparing the novel RT scheme with an independent method. The momentum boost of RP caused by reprocessed radiation is investigated in §9. The comparison is made by modifying the code RADMC-3D [Dullemond et al., 2012] based on the changes made by Klepitko [2016]. The resulting approach leads to a multi-wavelength Monte-Carlo-based scheme capable of computing RP. The scheme is tested for a simple setup of spherical symmetry to verify its correctness. Here, the novel implementation faithfully reproduces the linear scaling of the momentum boost with optical depth for a wavelength-independent opacity model. Subsequently, the scheme is applied in a study using a simplified $\kappa_{\rm ext} \propto \lambda^{-2}$ opacity model. In one instance, radiation is allowed to be reprocessed by absorption and reemission, changing its wavelength between interactions. In the other instance, radiation does not change its wavelength upon interaction due to being limited to scatterings. Reemission at different wavelengths causes the momentum boost to deviate from the linear slope. Here, the wavelength increases resulting in lower opacities such that radiation can escape the cloud. Once the cloud is optically thick towards even the reprocessed radiation, the momentum boost recovers its linear scaling with the optical depth. Next, the RADMC-3D-based scheme is compared to the novel scheme, TreeRay/RadPressure. Here, the comparison is made using actual simulation data generated in the course of §8. Results from both calculations agree partially throughout the simulations. While TreeRay/RadPressure undershoots the results generated by RADMC-3D-RP, both schemes agree from the intermediate phase onward. The expectation of an increased dust-to-gas ratio yielding an increase in the momentum boost is slightly met by both schemes. Radiation escaping through the dust sublimation region of the disk probably decreases the tendency. However, the tendency is far more drastic in RADMC-3D-RP without consideration of dust sublimation. Theoretical modelling of the boost factor is non-trivial. Simple estimates using averaged optical depths along different lines of sight work well for certain density configurations. Once a disk is established, the momentum boost reaches orders of unity.

10.2
Conclusion

Applicability of the scheme. The novel RT scheme, TreeRay/RadPressure, developed in this thesis works and compares well to an independent method. Backwards ray-tracing forms a third pillar supporting on-the-fly RT computations of reprocessed radiation in demanding HPC simulations. Together with a chemical network, TreeRay/RadPressure enhances the accuracy of dust cooling, taking into account self-shielding and thus cooling and heating accurately. The method has been demonstrated to dampen fragmentation. Thus, the scheme possibly delays star formation or alters the conditions under which stars will form. In particular, the multiplicity of a gravitationally collapsing core may change. Further, fragments forming outside of influential potential minima may be accreted by a hub or a star before they form stars themselves.

Impact of metallicity. Metallicity and the dust-to-gas ratio enhance the cooling of the gas. In return, they benefit fragmentation as seen in §8 and other works before [see, e.g., Omukai, 2000a, Omukai et al., 2005, Chon et al., 2021]. The increasing degree of fragmentation seen in §8 supports the idea of Bromm et al. [2001] that the metallicity and its associated cooling may impact the IMF. They argue that stronger cooling mechanisms enable the condensation of lower-mass clumps, which might form low-mass stars. Similarly, the increased fragmentation allows forming more stars in §8 at greater metallicities. Thus, the results of this thesis support the idea of a metallicity dependent IMF.

Radiation pressure. RP has been put forward as a mechanism to limit the final mass a star is capable of obtaining via accretion [Kahn, 1974]. In return, disks have been proposed to decrease the strength of RP by allowing radiation to escape [Nakano, 1989, Nakano et al., 1995]. The outcome of §8 reveals the formation of disks to decrease RP generated by reprocessed radiation to orders of unity in L/c due to radiation escaping along the rotation axis. These results agree with the work of Kuiper et al. [2010] where they find disk accretion to reduce RP compared to spherical accretion. With those limitations, RP remains unable to suddenly disrupt the disk and fully evacuate the star's surroundings. While simplified predictions following a momentum boost proportional to the mean optical depth would allow for immediate disk destruction (see Fig. 28 with $\dot{p}_{\mathrm{RP}} \approx 10^9 \mathrm{L}/c$ is larger than $\dot{p}_{\mathrm{radial}} \approx 10^8$ of gravity in 8), the calculated momentum input by TreeRay/RadPressure and RADMC-3D-RP are smaller than the critical input required for disk destruction by factors of 10 to 100, respectively. Instead, gas and dust might be removed continuously in the form of bipolar outflows along the rotation axis until the disk has been destroyed. These outflows have also been produced by Kuiper et al. [2010]. Boundary conditions of accretion onto the disk might determine whether the disk surrounding the massive star will grow or shrink in time.

10.3
OUTLOOK AND DISCUSSION

GENERAL RAY-TRACING SCHEME. The scheme presented in this thesis provides a general technique for approaching RT to solve reprocessed radiation. The general concept behind the scheme can be expanded to feasibly solve the reemission of radiation from gas in a feasible manner. TREERAY and its sub-modules show that RT can be approached successfully with backwards ray-tracing [see, e.g. Wünsch et al., 2018, 2021, **Klepitko** et al., 2023, Gaches et al., 2022].

HIGHER MOMENTS FOR MAPPING. So far, TREERAY/RADPRESSURE only tracks the monopole moment on each node. The accuracy of the scheme could be improved by including higher moments during ray-tracing. Higher moments could be stored during the tree build that track anisotropic emission characteristics. Once the tree build is completed, nodes can be mapped onto a single target cell's rays so that higher-level contributions are considered during integration.

MEMORY FOOTPRINT. Complex software almost always allows for further optimization. Optimizations may consider running time performance, the accuracy of the methods or enhancements concerning the memory budget. The improvements regarding higher-level nodes can be matched with enhancements to the accuracy. Indeed, these enhancements require additional storage as additional information has to be stored on the tree. Moving the entire tree on the shared memory of nodes would allow to save additional memory.

GAS-DUST DRIFT. Gas and dust are assumed to be perfectly coupled throughout this work. However, this does not hold in nature; instead, dust and gas may move separately. Accelerations acting on dust would only affect gas via a friction term and vice versa. Additional physics in the form of a gas-dust drift would allow tackling more scientific questions with the scheme. For example, how RP of different bands may impact the dynamics of gas and dust individually.

MORE DEMANDING SIMULATIONS. The strength of TREERAY is its capability to feasibly deal with many sources of radiation. This allows the scheme to perform simulations involving many stars and RT that otherwise would be too expensive to compute with forward ray-tracing.

FINE-TUNING OF THE SCHEME. Besides performance optimizations, accuracy optimizations are viable to explore. In particular, the lack of momentum boost during the early phase ($t < 0.6\, t_{\mathrm{ff}}$) can be further investigated. Following up on this, the difference between both schemes is evident in the dust temperatures. RADMC-3D-RP generates hotter temperatures surrounding the star and presents sites of dust-sublimation, while TREERAY/RADPRESSURE does not. Simply boosting the luminosity of stellar sources in TREERAY/RADPRESSURE according to an estimated trapping factor might increase temperatures and generate an additional momentum boost. This could bring the novel scheme closer to the results of RADMC-3D-RP. Additionally, one would need to verify, whether this approach impacts calculations in the later stage where both schemes agree. It might be the case, that dust-sublimation reduces the efficiency of the momentum boost, for example, by letting radiation escape. To some extent, this effect has been seen in the two sets of runs performed with RADMC-3D-RP where sublimation is considered and where it is not. Certainly, however, the boost should consider only a local region surrounding the star and needs to take into account geometric effects of the underlying density. Otherwise, the momentum boost could be overestimated drastically.

CONCLUDING WORDS. With that said, the current state of TREERAY/RADPRESSURE is on the conservative side of computing RP. The novel scheme reproduces bipolar outflows from disks and a reduction of the momentum boost due to the flashlight effect similar to the work of Kuiper et al. [2011]. The method improves heating and cooling through dust. TREERAY/RADPRESSURE and the method in general is well suited to tackle problems involving many sources of radiation. With that, the scheme developed in this thesis demonstrates a novel approach towards tackling RT of diffuse sources.

VERSICHERUNG AN EIDES STATT

Hiermit versichere ich an Eides statt, dass ich die vorliegende Dissertation selbstständig und ohne die Benutzung anderer als der angegebenen Hilfsmittel und Literatur angefertigt habe. Alle Stellen, die wörtlich oder sinngemäß aus veröffentlichten und nicht veröffentlichten Werken dem Wortlaut oder dem Sinn nach entnommen wurden, sind als solche kenntlich gemacht. Ich versichere an Eides statt, dass diese Dissertation noch keiner anderen Fakultät oder Universität zur Prüfung vorgelegen hat; dass sie - abgesehen von unten angegebenen Teilpublikationen und eingebundenen Artikeln und Manuskripten - noch nicht veröffentlicht worden ist sowie, dass ich eine Veröffentlichung der Dissertation vor Abschluss der Promotion nicht ohne Genehmigung des Promotionsausschusses vornehmen werde. Die Bestimmungen dieser Ordnung sind mir bekannt. Darüber hinaus erkläre ich hiermit, dass ich die Ordnung zur Sicherung guter wissenschaftlicher Praxis und zum Umgang mit wissenschaftlichem Fehlverhalten der Universität zu Köln gelesen und sie bei der Durchführung der Dissertation zugrundeliegenden Arbeiten und der schriftlich verfassten Dissertation beachtet habe und verpflichte mich hiermit, die dort genannten Vorgaben bei allen wissenschaftlichen Tätigkeiten zu beachten und umzusetzen. Ich versichere, dass die eingereichte elektronische Fassung der eingereichten Druckfassung vollständig entspricht.

Teilpublikationen:

- **A. Klepitko**, S. Walch, R. Wünsch, D. Seifried, F. Dinnbier, and S. Haid. Tree-based solvers for adaptive mesh refinement code FLASH - III: a novel scheme for radiation pressure on dust and gas and radiative transfer from diffuse sources. MNRAS, 521(1):160–184, May 2023. doi: 10.1093/mnras/stad385
- **A**. **Klepitko** and S. Walch. The Impact of Metallicity on Massive Star Formation: It is all about the Dust! Unpublished Manuscript, 2022

Klepitko

Köln, den 21.8.2022 (Andre Klepitko)

List of Figures

1 Image showing the heart of the Large Magellanic Cloud, a satellite galaxy of the Milky Way. The Large Magellanic cloud hosts the Tarantula Nebula and is the birthplace of the most massive stars currently known. Dark features in the center are caused by dust. The data of this image was revealed by Josh Lake in Hubble's Hidden Treasures image processing competition. *Credit: ESA/NASA/Hubble* . . 2

2 Schematic overview of Core Accretion (left) and Competitive Accretion (right) in the context of massive star formation. In the model of Core Accretion, individual cores within molecular clouds collapse and form stars where their masses are to some extent determined by the mass of their natal core. This picture changes in the competitive accretion model, where individual stars compete for mass outside of the core they formed in. Stars may combine their mass reservoir to host a cluster of stars. Here, massive stars are preferably located at the potential minimum such that they accrete from the densest parts. 6

3 Looking into the heart of the star-forming region S106 at Sharples 2 reveals hot gas (blue) being expelled from the central young massive star in a horizontal, bipolar fashion. Dust (red) accumulates in a disk surrounding the massive star and squeezes the hot gas into an hourglass shape. *Credit: NASA, ESA, and the Hubble Heritage Team (STScI/AURA)* 10

4 The top panel shows the dust extinction (solid line) and scattering (dotted line) cross sections per grams of dust as a function of the wavelength for two different dust model representing the Milky Way (MW, blue) and the LMC (orange) [Weingartner and Draine, 2001b]. The bottom panel shows the corresponding albedo to for both models. 10

5 Exemplary path of a single photon package during MCRT drawn out by arrows. The package was launched from the central source (star) and permeated the computational domain. During its journey, the photon package changes its direction and associated wavelength (indicated by the color) depending on the nature of the interaction. Finally, the packages leave the computational domain. 18

6 A sketch showing the concepts of forward-ray-tracing on the left and backwards ray-tracing on the right. Both examples include two sources of radiation marked by stars and the material on which the radiation is acting given by the red-brown blob. During forward-ray-tracing, one tries to propagate radiation from the sources via rays, which requires great angular resolutions for distant objects. Backwards ray-tracing casts rays from a target position directed at sources and can obtain results with coarser angular resolutions at greater distances by mapping, for example, multiple sources to a ray. 19

7 Sketch of the finite volume method applied to cells in a one dimensional space with conserved quantities, $\mathbf{h}_j^n$, and fluxes, $\mathbf{f}_{j-1/2}^n$ and $\mathbf{f}_{j+1/2}^n$, where n and j identify the corresponding timestep and cell, respectively. All cells are of width Δx and spaced uniformly apart. . . 21

8 Illustration of the refinement and derefinement process for a block in $N = 2$ dimensions. A single block with eight cells along each dimension is shown on the left side. The red lines highlight the block boundaries. During a refinement process, cell sizes are halved in each direction creating 2^N blocks from the original block. The blue lines highlight each block created during a refinement process. 23

9 Schematic overview of applying adaptive mesh refinement in an astrophysical simulation. Refinement can be put selectively into regions of interest, which are marked by the grey shaded areas. 23

10 Sketch of an octree where data is organized hierarchically on different levels. The root node is labelled 'root' and has eight associated nodes, one level beneath. Each of those nodes may have additional eight children if so desired. Nodes without children are called leaf nodes and are shaded grey. 24

11 Idealized setup of a single clump of angular size, ω_s, sitting between a target point (red dot) and sources of radiation (stars) in a backwards ray-tracing scheme. The ray has a solid angle of size, ω_pix. 62

12 Wall-clock time per timestep vs. the number of shared memory allocations per compute node given by the parameter `tr_sharedGroupSize`. Using fewer shared memory allocations may cause performance issues due to cache conflicts while more processors try to access the same memory space. The performance test was run on the HPE Apollo (HAWK) cluster of the High-Performance Computing Center in Stuttgart running the AMD EPYC$^\mathrm{TM}$ 7742 processors. Overall, the performance is not affected by the number of processors sharing their memory in this example. 63

13 Slices showing the density and three different temperatures for gas, dust and radiation of two runs presented in §7.1. The runs are organized in rows showing the `FIDUCIAL` run and the `NRAD` run in the top and bottom row, respectively. The `FIDUCIAL` run uses TREERAY/RADPRESSURE while `NRAD` does not. With that, dust is allowed to cool in an optically thin manner in the run `NRAD` resulting in colder dust and, thus, colder gas temperatures. Ultimately, the run `NRAD` shows greater densities and finer structure due to lower Jeans masses. 65

14 Diagrams comparing the strength of dust gas coupling and radiative heating and cooling for different pairs of dust and gas temperatures. Different panels show different environmental conditions given by the density and radiation temperature. The qualitative shape of the plot changes for different environmental parameters. The orange lines show the radiation temperature (horizontal) and the dust and gas temperature 1-to-1 line (diagonal), respectively. Regions of equal rates (white) show comparable rates where only the two narrow cones (angel less than 90 degrees) formed by the orange lines are allowed physical solutions. 66

15 Slices showing the radiation temperature of the radiation field for the star forming setup presented in §7.1. The panels are organized in rows for similar times and show runs with different physics included across columns. These runs include a run with all physics (`FIDUCIAL`), a run where accelerations from RP are disabled (`NARP`) and a run where both accelerations from RP and any type of radiation from stars is switched off (`NARPNFE`). The runs `FIDUCIAL` and `NARP` are similar throughout time. `NARPNFE` is similar for $t \leq 0.4t_{\mathrm{ff}}$ but shows lower radiation temperatures throughout for later times. This is especially the case for $t \geq 0.5t_{\mathrm{ff}}$ in the central region once the most massive star located in the center reaches greater luminosities. 69

16 Same as Fig. 15 except that the dust temperature is shown here. Similar to Fig. 16 the run `NARPNFE` appears colder than `FIDUCIAL` and `NARP`. As described in §7.1, the dust temperature is coupled to both the radiation field and the gas. The influence of radiation heating the dust can be seen clearly by comparing the radiation temperatures in Fig. 15 to the corresponding panels of this Fig. 70

17 Same as Fig. 15 but the gas temperature is shown here. Gas is coupled to dust in an exchange of thermal energy which makes it indirectly coupled to the radiation field provided by TREERAY/RADPRESSURE (see §7.1. We can see slightly hotter gas at $t \geq 0.5t_{\mathrm{ff}}$ for the runs that include stellar feedback from the stars (`FIDUCIAL` and `NARP`) compared to the runs that do not include it (`NARPNFE`). However, at times $t \leq 0.4t_{\mathrm{ff}}$ all runs have similar temperatures as the central star is not luminous enough. 71

18 Exemplary momentum transfer from a photon package changing its direction within a cell. The incident direction is given by the unit vector $\mathbf{n}_{\mathrm{in}}$ and the outgoing direction by $\mathbf{n}_{\mathrm{out}}$. The deposited momentum, $\mathbf{D}_{\mathrm{deposited}}$, is given shown as the green arrow and results from the change in the direction according to Eq. 9.1. 90

19 Depiction of a photon package's path emitted by a source embedded in a cloud. The package moves in straight lines until it undergoes an interaction. The interaction may be the result of either scattering or an absorption followed by an immediate reemission. From Eq. 9.1 one can estimate the deposited momentum to be greater than unity with respect to the package's momentum, E_{pkg}/c. 91

20 Measured radial momentum normalized to the momentum input vs the optical depth for a homogeneous spherical cloud where the dust has a constant opacity of $10\,\mathrm{cm}^2\,\mathrm{g}^{-1}$. Blue circles and orange crosses show absorption, followed by reemission and scattering only. The purple and brown line show relations according to Eq. 9.4 and 9.2, respectively. Across all optical depths, the deposited momentum in the cloud follows a linear relation. No noticeable difference between absorption and scattering cases can be seen in this setup. 92

21 Same as Fig. 20 for an opacity of the form $\kappa_{\mathrm{ext}} \propto \lambda^{-2}$ in a low and high albedo case. Blue circles and orange crosses show results for the low and high albedo runs, respectively. In the low albedo case, the radiation interacts ones via absorption with $\kappa_{\mathrm{ext,P}}(3 \times 10^4\,\mathrm{K})$ and escapes after it is emitted at an effectively lower temperature and therefore lower Planck-weighted opacity. In this limit, the profile follows that of direct absorption given by Eq. 9.2 (purple line). The high albedo case follows the profile given by Eq. 9.4. Here, the signature of the initial spectrum is conserved; therefore, the effective opacity stays the same. 92

22 Same as Fig. 20 for an opacity of the form $\kappa_{\mathrm{ext}} \propto \lambda^{-2}$ in a low case. Blue circles, orange triangles and green crosses show results of different cloud of size 1.0 pc, 0.1 pc and 10.0 pc, respectively. More compact clouds transition to the linear momentum boost regime earlier than bigger clouds for corresponding optical depths. This trend is because the maximum wavelength of reprocessed radiation is shorter in compact clouds due to greater minimum radiation temperatures. This allows all reprocessed radiation to become optically thick at comparably lower optical depths with respect to the Planck weighted mean opacity of the initial spectrum. 97

23 Momentum boost vs optical depth for two different opacity models where the density is varied. The first model is the $\kappa_{\mathrm{ext}} \propto \lambda^{-2}$ model in a low albedo case (blue circles), and the second model is the Milky Way dust model by Weingartner and Draine [2001b] (orange crosses). The optical depth is defined with respect to a Planck weighted mean opacity for $3 \times 10^4\,\mathrm{K}$ of either model, respectively. Similar to previous models shown in Fig. 21 and Fig. 22, the Milky Way dust model follows $(1 - \exp(-\tau))$ initially and continues to grow beyond unity for greater optical depths. Compared to the $\kappa_{\mathrm{ext}} \propto \lambda^{-2}$ model, Milky Way dust model starts to grow beyond unity faster and reaches $p \propto \tau$ indicating that all wavelengths are optically thick. 97

24 Momentum boost vs optical depth for the realistic Milky Way dust model and the model presented in 9.20. The optical depth is increased incrementally through the density and measured for a black body spectrum of $3 \times 10^4\,\mathrm{K}$ taking the Planck-weighted mean opacity of the Milky Way dust model. In particular, both models have the same normalisation resulting in the horizontal offset at momentum inputs less than unity. Nevertheless, both models agree on greater optical depths. 98

25 Slices of dust temperatures computed by RADMC-3D-RP and TreeRay/RadPressure at the z-coordinate of the principal star for different times shown in different rows, respectively. The black contours show regions surpassing $T_{\mathrm{dust}} > 1500\,\mathrm{K}$, where dust is taken to be sublimated. The simulation data is taken from the `SMC` run from §8. White spots correspond to a dust temperature of 0 K. These regions, in particular, had no interactions with photon packages. Comparing the RADMC-3D-RP data to TreeRay shows that RADMC-3D-RP produces hotter dust temperatures than TreeRay. 100

26 Same as Fig. 25 but for the `LMC` run. The region close to the star is hotter in comparison to Fig. 25 due to the greater metallicity and therefore dust-to-gas ratio. In addition, one finds the region in which dust is sublimated to be larger compared to Fig. 25. 101

27 Same as Fig. 25 but for the `SOL` run. In the same way as in Fig. 26, dust close to the principal star is hotter showing an increased region in which dust is sublimated due to the greater dust-to-gas ratio and therefore dust mass. 102

28 Radiation pressure momentum comparison between RADMC-3D-RP and TreeRay/RadPressure vs. time along with theoretical models (orange and black line). From top to bottom, the runs `SMC`, `LMC` and `SOL` are shown from §8. The purple line shows the direct momentum input by the luminosity of the principal star vs. time. The olive line shows the radial momentum input computed by TreeRay/RadPressure vs. time. Radial momentum input computed by RADMC-3D-RP at corresponding times is shown as scattered points. Blue and cyan points use the opacity model of Weingartner and Draine [2001b] and Semenov et al. [2003], respectively, where the latter follows Eq. 9.21. Triangles account for sublimation by neglecting cells hotter than 1500 K while stars do not. 103

29 Schematic evolution of the star-forming setup presented in §7 and §8. The initial spherical distribution forms filamentary structures due to the turbulent velocity seed. Fragmentation is more pronounced for higher metallicity runs. Gas migrates to the central hub, where the star potentially accretes it. A small region surrounding the central star shows sublimated dust (white spot in the middle frame). The central hub grows in mass and forms a rotating disk in which the sublimated region grows. 106

30 Column density plots in an (almost) edge-on view of the disk for all three runs of different metallicity from §8 at different times. Lower metallicity runs show a less fragmented disk. The fragmentation may be caused by lower temperatures due to better cooling and interactions of other sink particles with the disk. The disk is destroyed by expansion from the inside out by the star as seen for the `LMC` run at $1.4\,t_{\mathrm{ff}}$. At this time, the `SMC` run features a stable disk and the `SOL` run shows gravitational instabilities in the disk. 107

BIBLIOGRAPHY

Tom Abel and Benjamin D. Wandelt. Adaptive ray tracing for radiative transfer around point sources. MNRAS, 330(3):L53–L56, March 2002. doi: 10.1046/j.1365-8711.2002.05206.x.

Ahmad A. Ali. The growth of H II regions around massive stars: the role of metallicity and dust. MNRAS, 501(3):4136–4147, March 2021. doi: 10.1093/mnras/staa3992.

J. Alves, M. Lombardi, and C. J. Lada. The mass function of dense molecular cores and the origin of the IMF. A&A, 462(1):L17–L21, January 2007. doi: 10.1051/0004-6361:20066389.

Gene Amdahl. Validity of the single processor approach to achieving large scale computing capabilities. *AFIPS spring joint computer conference proceedings*, 1967.

P. André, J. Di Francesco, D. Ward-Thompson, S. I. Inutsuka, R. E. Pudritz, and J. E. Pineda. From Filamentary Networks to Dense Cores in Molecular Clouds: Toward a New Paradigm for Star Formation. In Henrik Beuther, Ralf S. Klessen, Cornelis P. Dullemond, and Thomas Henning, editors, *Protostars and Planets VI*, page 27, January 2014. doi: 10.2458/azu_uapress_9780816531240-ch002.

E. Audit and P. Hennebelle. Thermal condensation in a turbulent atomic hydrogen flow. A&A, 433(1):1–13, April 2005. doi: 10.1051/0004-6361:20041474.

C. Baczynski, S. C. O. Glover, and R. S. Klessen. <monospace>Fervent</monospace>: chemistry-coupled, ionizing and non-ionizing radiative feedback in hydrodynamical simulations. MNRAS, 454(1):380–411, November 2015. doi: 10.1093/mnras/stv1906.

Javier Ballesteros-Paredes, Philippe André, Patrick Hennebelle, Ralf S. Klessen, J. M. Diederik Kruijssen, Mélanie Chevance, Fumitaka Nakamura, Angela Adamo, and Enrique Vázquez-Semadeni. From Diffuse Gas to Dense Molecular Cloud Cores. Space Sci. Rev., 216(5):76, June 2020. doi: 10.1007/s11214-020-00698-3.

T. M. Bania and J. G. Lyon. OB stars and the structure of the interstellar medium - Cloud formation and effects of different equations of state. ApJ, 239:173–192, July 1980. doi: 10.1086/158099.

Ashley T. Barnes, Steven N. Longmore, James E. Dale, Mark R. Krumholz, J. M. Diederik Kruijssen, and Frank Bigiel. Which feedback mechanisms dominate in the high-pressure environment of the central molecular zone? MNRAS, 498(4):4906–4923, November 2020. doi: 10.1093/mnras/staa2719.

Josh Barnes and Piet Hut. A hierarchical O(N log N) force-calculation algorithm. Nature, 324(6096):446–449, December 1986. doi: 10.1038/324446a0.

Frank Bertoldi and Christopher F. McKee. Pressure-confined Clumps in Magnetized Molecular Clouds. ApJ, 395:140, August 1992. doi: 10.1086/171638.

Joachim M Bestenlehner, Paul A Crowther, Saida M Caballero-Nieves, Fabian R N Schneider, Sergio Simón-Díaz, Sarah A Brands, Alex de Koter, Götz Gräfener, Artemio Herrero, Norbert Langer, and et al. The r136 star cluster dissected with hubble space telescope/stis – ii. physical properties of the most massive stars in r136. *Monthly Notices of the Royal Astronomical Society*, 499(2):1918–1936, Sep 2020. ISSN 1365-2966. doi: 10.1093/mnras/staa2801. URL http://dx.doi.org/10.1093/mnras/staa2801.

H. Beuther, P. Schilke, F. Gueth, M. McCaughrean, M. Andersen, T. K. Sridharan, and K. M. Menten. IRAS 05358+3543: Multiple outflows at the earliest stages of massive star formation. A&A, 387:931–943, June 2002a. doi: 10.1051/0004-6361:20020319.

H. Beuther, P. Schilke, T. K. Sridharan, K. M. Menten, C. M. Walmsley, and F. Wyrowski. Massive molecular outflows. A&A, 383:892–904, March 2002b. doi: 10.1051/0004-6361:20011808.

J. E. Bjorkman and Kenneth Wood. Radiative Equilibrium and Temperature Correction in Monte Carlo Radiation Transfer. ApJ, 554(1):615–623, June 2001. doi: 10.1086/321336.

G. N. Blair, II Evans, N. J., P. A. Vanden Bout, and III Peters, W. L. The energetics of molecular clouds. II - The S140 molecular cloud. ApJ, 219:896, February 1978. doi: 10.1086/155853.

L. Blitz, Y. Fukui, A. Kawamura, A. Leroy, N. Mizuno, and E. Rosolowsky. Giant Molecular Clouds in Local Group Galaxies. In Bo Reipurth, David Jewitt, and Klaus Keil, editors, *Protostars and Planets V*, page 81, January 2007.

P. Bodenheimer, G.P. Laughlin, M. Różyczka, and H.W. Yorke. *Numerical Methods in Astrophysics: An Introduction*. Series in Astronomy and Astrophysics. CRC Press, 2006. ISBN 978-0-7503-0883-0.

A. Bonanno, H. Schlattl, and L. Paternò. The age of the Sun and the relativistic corrections in the EOS. A&A, 390:1115–1118, August 2002. doi: 10.1051/0004-6361:20020749.

I. A. Bonnell, M. R. Bate, C. J. Clarke, and J. E. Pringle. Accretion and the stellar mass spectrum in small clusters. MNRAS, 285(1):201–208, February 1997. doi: 10.1093/mnras/285.1.201.

I. A. Bonnell, M. R. Bate, C. J. Clarke, and J. E. Pringle. Competitive accretion in embedded stellar clusters. MNRAS, 323(4):785–794, May 2001. doi: 10.1046/j.1365-8711.2001.04270.x.

Ian A. Bonnell and Matthew R. Bate. Star formation through gravitational collapse and competitive accretion. MNRAS, 370(1):488–494, July 2006. doi: 10.1111/j.1365-2966.2006.10495.x.

Stefano Bovino, Alessandro Lupi, Andrea Giannetti, Giovanni Sabatini, Dominik R. G. Schleicher, Friedrich Wyrowski, and Karl M. Menten. Chemical analysis of prestellar cores in Ophiuchus yields short timescales and rapid collapse. A&A, 654:A34, October 2021. doi: 10.1051/0004-6361/202141252.

V. Bromm, A. Ferrara, P. S. Coppi, and R. B. Larson. The fragmentation of pre-enriched primordial objects. MNRAS, 328(3):969–976, December 2001. doi: 10.1046/j.1365-8711.2001.04915.x.

Blakesley Burkhart, Kye Stalpes, and David C. Collins. The Razor's Edge of Collapse: The Transition Point from Lognormal to Power-Law Distributions in Molecular Clouds. ApJ, 834(1):L1, January 2017. doi: 10.3847/2041-8213/834/1/L1.

Yue Cao, Keping Qiu, Qizhou Zhang, Yuwei Wang, and Yuanming Xiao. Core Mass Function of a Single Giant Molecular Cloud Complex with 10,000 Cores. ApJ, 918 (1):L4, September 2021. doi: 10.3847/2041-8213/ac1947.

F. Casoli and F. Combes. Can giant molecular clouds form in spiral arms. A&A, 110(2):287–294, June 1982.

J. I. Castor, D. C. Abbott, and R. I. Klein. Radiation-driven winds in Of stars. ApJ, 195:157–174, January 1975. doi: 10.1086/153315.

Gilles Chabrier. Galactic Stellar and Substellar Initial Mass Function. PASP, 115 (809):763–795, July 2003. doi: 10.1086/376392.

Sunmyon Chon, Kazuyuki Omukai, and Raffaella Schneider. Transition of the initial mass function in the metal-poor environments. MNRAS, 508(3):4175–4192, December 2021. doi: 10.1093/mnras/stab2497.

Paul C. Clark, Simon C. O. Glover, and Ralf S. Klessen. TreeCol: a novel approach to estimating column densities in astrophysical simulations. MNRAS, 420(1):745–756, February 2012. doi: 10.1111/j.1365-2966.2011.20087.x.

David C. Collins, Alexei G. Kritsuk, Paolo Padoan, Hui Li, Hao Xu, Sergey D. Ustyugov, and Michael L. Norman. The Two States of Star-forming Clouds. ApJ, 750(1):13, May 2012. doi: 10.1088/0004-637X/750/1/13.

Tiago Costa, Joakim Rosdahl, Debora Sijacki, and Martin G. Haehnelt. Driving gas shells with radiation pressure on dust in radiation-hydrodynamic simulations. MNRAS, 473(3):4197–4219, January 2018. doi: 10.1093/mnras/stx2598.

R. Courant, K. Friedrichs, and H. Lewy. Über die partiellen Differenzengleichungen der mathematischen Physik. *Mathematische Annalen*, 100:32–74, January 1928. doi: 10.1007/BF01448839.

T. M. Dame, H. Ungerechts, R. S. Cohen, E. J. de Geus, I. A. Grenier, J. May, D. C. Murphy, L. A. Nyman, and P. Thaddeus. A Composite CO Survey of the Entire Milky Way. ApJ, 322:706, November 1987. doi: 10.1086/165766.

J. R. Dawson, N. M. McClure-Griffiths, A. Kawamura, N. Mizuno, T. Onishi, A. Mizuno, and Y. Fukui. Supershells as Molecular Cloud Factories: Parsec Resolution Observations of H I and ^{12}CO(J = 1-0) in GSH 287+04-17 and GSH 277+00+36. ApJ, 728(2):127, February 2011. doi: 10.1088/0004-637X/728/2/127.

J. R. Dawson, N. M. McClure-Griffiths, T. Wong, John M. Dickey, A. Hughes, Y. Fukui, and A. Kawamura. Supergiant Shells and Molecular Cloud Formation in the Large Magellanic Cloud. ApJ, 763(1):56, January 2013. doi: 10.1088/0004-637X/763/1/56.

C. L. Dobbs. GMC formation by agglomeration and self gravity. MNRAS, 391(2): 844–858, December 2008. doi: 10.1111/j.1365-2966.2008.13939.x.

C. L. Dobbs, M. R. Krumholz, J. Ballesteros-Paredes, A. D. Bolatto, Y. Fukui, M. Heyer, M. M. M. Low, E. C. Ostriker, and E. Vázquez-Semadeni. Formation of Molecular Clouds and Global Conditions for Star Formation. In Henrik Beuther, Ralf S. Klessen, Cornelis P. Dullemond, and Thomas Henning, editors, *Protostars and Planets VI*, page 3, January 2014. doi: 10.2458/azu_uapress_9780816531240-ch001.

Gustavo Dopcke, Simon C. O. Glover, Paul C. Clark, and Ralf S. Klessen. The Effect of Dust Cooling on Low-metallicity Star-forming Clouds. ApJ, 729(1):L3, March 2011. doi: 10.1088/2041-8205/729/1/L3.

E. I. Doran, P. A. Crowther, A. de Koter, C. J. Evans, C. McEvoy, N. R. Walborn, N. Bastian, J. M. Bestenlehner, G. Gräfener, A. Herrero, and et al. The vlt-flames tarantula survey. *Astronomy Astrophysics*, 558:A134, Oct 2013. ISSN 1432-0746. doi: 10.1051/0004-6361/201321824. URL http://dx.doi.org/10.1051/0004-6361/201321824.

Bruce T. Draine. *Physics of the Interstellar and Intergalactic Medium*. 2011.

C. P. Dullemond, A. Juhasz, A. Pohl, F. Sereshti, R. Shetty, T. Peters, B. Commercon, and M. Flock. RADMC-3D: A multi-purpose radiative transfer tool. Astrophysics Source Code Library, record ascl:1202.015, February 2012.

J. E. Dyson and D. A. Williams. *Physics of the interstellar medium*. 1980.

Christoph Federrath, Martin Schrön, Robi Banerjee, and Ralf S. Klessen. Modeling Jet and Outflow Feedback during Star Cluster Formation. ApJ, 790(2):128, August 2014. doi: 10.1088/0004-637X/790/2/128.

G. J. Ferland, R. L. Porter, P. A. M. van Hoof, R. J. R. Williams, N. P. Abel, M. L. Lykins, G. Shaw, W. J. Henney, and P. C. Stancil. The 2013 Release of Cloudy. Rev. Mexicana Astron. Astrofis., 49:137–163, April 2013.

B. Fryxell, K. Olson, P. Ricker, F. X. Timmes, M. Zingale, D. Q. Lamb, P. MacNeice, R. Rosner, J. W. Truran, and H. Tufo. FLASH: An Adaptive Mesh Hydrodynamics Code for Modeling Astrophysical Thermonuclear Flashes. ApJS, 131(1):273–334, November 2000. doi: 10.1086/317361.

Yasuo Fukui, Norikazu Mizuno, Reiko Yamaguchi, Akira Mizuno, and Toshikazu Onishi. On the Mass Spectrum of Giant Molecular Clouds in the Large Magellanic Cloud. PASJ, 53(6):L41–L44, December 2001. doi: 10.1093/pasj/53.6.L41.

B. A. L. Gaches, S. Walch, R. Wünsch, and J. Mackey. Tree-based solvers for adaptive mesh refinement code FLASH - IV: An X-ray radiation scheme to couple discrete and diffuse X-ray emission sources to the thermochemistry of the interstellar medium. Unpublished Manuscript, 2022.

S. Ganguly, S. Walch, S. D. Clarke, and D. Seifried. SILCC-Zoom: the dynamic balance in molecular cloud substructures. *arXiv e-prints*, art. arXiv:2204.02511, April 2022.

G. Garay, D. Mardones, L. Bronfman, K. J. Brooks, L. F. Rodríguez, R. Güsten, L. Å. Nyman, R. Franco-Hernández, and J. M. Moran. Discovery of an energetic bipolar molecular outflow towards IRAS 16547-4247. A&A, 463(1):217–224, February 2007. doi: 10.1051/0004-6361:20065329.

R. Gehrz. Sources of Stardust in the Galaxy. In Louis J. Allamandola and A. G. G. M. Tielens, editors, *Interstellar Dust*, volume 135, page 445, January 1989.

R. Genzel, D. Lutz, E. Sturm, E. Egami, D. Kunze, A. F. M. Moorwood, D. Rigopoulou, H. W. W. Spoon, A. Sternberg, L. E. Tacconi-Garman, L. Tacconi, and N. Thatte. What Powers Ultraluminous IRAS Galaxies? ApJ, 498(2):579–605, May 1998. doi: 10.1086/305576.

Philipp Girichidis, Stefanie Walch, Thorsten Naab, Andrea Gatto, Richard Wünsch, Simon C. O. Glover, Ralf S. Klessen, Paul C. Clark, Thomas Peters, Dominik Derigs, and Christian Baczynski. The SILCC (SImulating the LifeCycle of molecular Clouds) project - II. Dynamical evolution of the supernova-driven ISM and the launching of outflows. MNRAS, 456(4):3432–3455, March 2016. doi: 10.1093/mnras/stv2742.

Simon C. O. Glover and Paul C. Clark. Approximations for modelling CO chemistry in giant molecular clouds: a comparison of approaches. MNRAS, 421(1):116–131, March 2012. doi: 10.1111/j.1365-2966.2011.20260.x.

M. González, E. Audit, and P. Huynh. HERACLES: a three-dimensional radiation hydrodynamics code. A&A, 464(2):429–435, March 2007. doi: 10.1051/0004-6361:20065486.

K. M. Górski, E. Hivon, A. J. Banday, B. D. Wandelt, F. K. Hansen, M. Reinecke, and M. Bartelmann. HEALPix: A Framework for High-Resolution Discretization and Fast Analysis of Data Distributed on the Sphere. ApJ, 622(2):759–771, April 2005. doi: 10.1086/427976.

J. J. Grond, R. M. Woods, J. W. Wadsley, and H. M. P. Couchman. TREVR: A general N $\log^2$N radiative transfer algorithm. MNRAS, 485(3):3681–3695, May 2019. doi: 10.1093/mnras/stz525.

Dávid Guszejnov, Michael Y. Grudić, Stella S. R. Offner, Claude-André Faucher-Giguère, Philip F. Hopkins, and Anna L. Rosen. Effects of the environment and feedback physics on the initial mass function of stars in the STARFORGE simulations. *arXiv e-prints*, art. arXiv:2205.10413, May 2022.

A. Hacar, S Clark, F. Heitsch, J. Kainulainen, G. Panopoulou, D. Seifried, and R. Smith. Initial Conditions for Star Formation: A Physical Description of the Filamentary ISM. *arXiv e-prints*, art. arXiv:2203.09562, March 2022.

S. Haid, S. Walch, D. Seifried, R. Wünsch, F. Dinnbier, and T. Naab. SILCC-Zoom: The early impact of ionizing radiation on forming molecular clouds. MNRAS, 482(3):4062–4083, January 2019. doi: 10.1093/mnras/sty2938.

R. Hainich, U. Rühling, H. Todt, L. M. Oskinova, A. Liermann, G. Gräfener, C. Foellmi, O. Schnurr, and W.-R. Hamann. The wolf-rayet stars in the large magellanic cloud. *Astronomy Astrophysics*, 565:A27, Apr 2014. ISSN 1432-0746. doi: 10.1051/0004-6361/201322696. URL `http://dx.doi.org/10.1051/0004-6361/201322696`.

T. J. Harries, T. J. Haworth, D. Acreman, A. Ali, and T. Douglas. The TORUS radiation transfer code. *Astronomy and Computing*, 27:63, April 2019. doi: 10.1016/j.ascom.2019.03.002.

Tatsuhiko I. Hasegawa, Eric Herbst, and Chun M. Leung. Models of Gas-Grain Chemistry in Dense Interstellar Clouds with Complex Organic Molecules. ApJS, 82:167, September 1992. doi: 10.1086/191713.

Mark Heyer and T. M. Dame. Molecular Clouds in the Milky Way. ARA&A, 53: 583–629, August 2015. doi: 10.1146/annurev-astro-082214-122324.

D. Hollenbach and C. F. McKee. Molecule formation and infrared emission in fast interstellar shocks. I. Physical processes. ApJS, 41:555–592, November 1979. doi: 10.1086/190631.

Philip F. Hopkins, Eliot Quataert, and Norman Murray. Self-regulated star formation in galaxies via momentum input from massive stars. MNRAS, 417(2):950–973, October 2011. doi: 10.1111/j.1365-2966.2011.19306.x.

Takashi Hosokawa, Harold W. Yorke, and Kazuyuki Omukai. Evolution of Massive Protostars Via Disk Accretion. ApJ, 721(1):478–492, September 2010. doi: 10.1088/0004-637X/721/1/478.

Shu-ichiro Inutsuka, Tsuyoshi Inoue, Kazunari Iwasaki, and Takashi Hosokawa. The formation and destruction of molecular clouds and galactic star formation. An origin for the cloud mass function and star formation efficiency. A&A, 580: A49, August 2015. doi: 10.1051/0004-6361/201425584.

J. H. Jeans. The Stability of a Spherical Nebula. *Philosophical Transactions of the Royal Society of London Series A*, 199:1–53, January 1902. doi: 10.1098/rsta.1902.0012.

F. D. Kahn. Cocoons around early-type stars. A&A, 37:149–162, December 1974.

R. S. Kandel and F. Sibille. Anisotropic H II regions with axial symmetry. A&A, 68: 217–228, August 1978.

Rahul Kannan, Mark Vogelsberger, Federico Marinacci, Ryan McKinnon, Rüdiger Pakmor, and Volker Springel. AREPO-RT: radiation hydrodynamics on a moving mesh. MNRAS, 485(1):117–149, May 2019. doi: 10.1093/mnras/stz287.

N. S. Kardashev. Transmission of Information by Extraterrestrial Civilizations. Soviet Ast., 8:217, October 1964.

Jr. Kennicutt, Robert C. The Global Schmidt Law in Star-forming Galaxies. ApJ, 498 (2):541–552, May 1998. doi: 10.1086/305588.

O. Kessel-Deynet and A. Burkert. Ionizing radiation in smoothed particle hydrodynamics. MNRAS, 315(4):713–721, July 2000. doi: 10.1046/j.1365-8711.2000.03451.x.

A. Khokhlov, E. Mueller, and P. Hoeflich. Light curves of type IA supernova models with different explosion mechanisms. A&A, 270:223–248, March 1993.

A. Klepitko and S. Walch. The Impact of Metallicity on Massive Star Formation: It is all about the Dust! Unpublished Manuscript, 2022.

Andre Klepitko. Towards understanding radiation pressure feedback in radiative transfer simulations, Aug 2016.

Andre Klepitko. Radiation pressure first absorption scheme. Master's thesis, University of Cologne, Nov 2018.

A. Klepitko, S. Walch, R. Wünsch, D. Seifried, F. Dinnbier, and S. Haid. Tree-based solvers for adaptive mesh refinement code FLASH - III: a novel scheme for radiation pressure on dust and gas and radiative transfer from diffuse sources. MNRAS, 521(1):160–184, May 2023. doi: 10.1093/mnras/stad385.

R. S. Klessen and P. Hennebelle. Accretion-driven turbulence as universal process: galaxies, molecular clouds, and protostellar disks. A&A, 520:A17, September 2010. doi: 10.1051/0004-6361/200913780.

Kaitlin M. Kratter, Christopher D. Matzner, Mark R. Krumholz, and Richard I. Klein. On the Role of Disks in the Formation of Stellar Systems: A Numerical Parameter Study of Rapid Accretion. ApJ, 708(2):1585–1597, January 2010. doi: 10.1088/0004-637X/708/2/1585.

Pavel Kroupa. The Initial Mass Function of Stars: Evidence for Uniformity in Variable Systems. *Science*, 295(5552):82–91, January 2002. doi: 10.1126/science.1067524.

Mark R. Krumholz and Christopher D. Matzner. The Dynamics of Radiation-pressure-dominated H II Regions. ApJ, 703(2):1352–1362, October 2009. doi: 10.1088/0004-637X/703/2/1352.

Mark R Krumholz and Todd A Thompson. Direct numerical simulation of radiation pressure-driven turbulence and winds in star clusters and galactic disks. *The Astrophysical Journal*, 760(2):155, 2012.

Mark R. Krumholz, Richard I. Klein, Christopher F. McKee, and John Bolstad. Equations and Algorithms for Mixed-frame Flux-limited Diffusion Radiation Hydrodynamics. ApJ, 667(1):626–643, September 2007. doi: 10.1086/520791.

Mark R. Krumholz, Richard I. Klein, Christopher F. McKee, Stella S. R. Offner, and Andrew J. Cunningham. The Formation of Massive Star Systems by Accretion. *Science*, 323(5915):754, February 2009. doi: 10.1126/science.1165857.

R. Kuiper and T. Hosokawa. First hydrodynamics simulations of radiation forces and photoionization feedback in massive star formation. A&A, 616:A101, August 2018. doi: 10.1051/0004-6361/201832638.

Rolf Kuiper, Hubert Klahr, Henrik Beuther, and Thomas Henning. Circumventing the Radiation Pressure Barrier in the Formation of Massive Stars via Disk Accretion. ApJ, 722(2):1556–1576, October 2010. doi: 10.1088/0004-637X/722/2/1556.

Rolf Kuiper, Hubert Klahr, Henrik Beuther, and Thomas Henning. Three-dimensional Simulation of Massive Star Formation in the Disk Accretion Scenario. ApJ, 732(1):20, May 2011. doi: 10.1088/0004-637X/732/1/20.

Rolf Kuiper, Harold W. Yorke, and Andrea Mignone. Makemake + Sedna: A Continuum Radiation Transport and Photoionization Framework for Astrophysical Newtonian Fluid Dynamics. *arXiv e-prints*, art. arXiv:2009.12374, September 2020.

Stan Kurtz. Hypercompact hii regions. *Proceedings of the International Astronomical Union*, 1(S227):111–119, 2005. doi: 10.1017/S1743921305004424.

C. J. Lada. Detailed observations of the M17 molecular cloud complex. ApJS, 32: 603–629, October 1976. doi: 10.1086/190409.

Lachlan Lancaster, Eve C. Ostriker, Jeong-Gyu Kim, and Chang-Goo Kim. Efficiently Cooled Stellar Wind Bubbles in Turbulent Clouds. I. Fractal Theory and Application to Star-forming Clouds. ApJ, 914(2):89, June 2021a. doi: 10.3847/1538-4357/abf8ab.

Lachlan Lancaster, Eve C. Ostriker, Jeong-Gyu Kim, and Chang-Goo Kim. Efficiently Cooled Stellar Wind Bubbles in Turbulent Clouds. II. Validation of Theory with Hydrodynamic Simulations. ApJ, 914(2):90, June 2021b. doi: 10.3847/1538-4357/abf8ac.

R. B. Larson. Turbulence and star formation in molecular clouds. MNRAS, 194: 809–826, March 1981. doi: 10.1093/mnras/194.4.809.

C. D. Levermore. Relating Eddington factors to flux limiters. J. Quant. Spec. Radiat. Transf., 31(2):149–160, February 1984. doi: 10.1016/0022-4073(84)90112-2.

CD Levermore and GC Pomraning. A flux-limited diffusion theory. *The Astrophysical Journal*, 248:321–334, 1981.

Pak Shing Li, Christopher F. McKee, and Richard I. Klein. Magnetized interstellar molecular clouds - I. Comparison between simulations and Zeeman observations. MNRAS, 452(3):2500–2527, September 2015. doi: 10.1093/mnras/stv1437.

Laura A. Lopez, Mark R. Krumholz, Alberto D. Bolatto, J. Xavier Prochaska, Enrico Ramirez-Ruiz, and Daniel Castro. The Role of Stellar Feedback in the Dynamics of H II Regions. ApJ, 795(2):121, November 2014. doi: 10.1088/0004-637X/795/2/121.

Zu-Jia Lu, Veli-Matti Pelkonen, Paolo Padoan, Liubin Pan, Troels Haugbølle, and Åke Nordlund. The Effect of Supernovae on the Turbulence and Dispersal of Molecular Clouds. ApJ, 904(1):58, November 2020. doi: 10.3847/1538-4357/abbd8f.

L. B. Lucy. Computing radiative equilibria with Monte Carlo techniques. A&A, 344:282–288, April 1999.

L. B. Lucy and P. M. Solomon. Mass Loss by Hot Stars. ApJ, 159:879, March 1970. doi: 10.1086/150365.

Michael Marks, Pavel Kroupa, Jörg Dabringhausen, and Marcel S. Pawlowski. Evidence for top-heavy stellar initial mass functions with increasing density and decreasing metallicity. MNRAS, 422(3):2246–2254, May 2012. doi: 10.1111/j.1365-2966.2012.20767.x.

J. S. Mathis, W. Rumpl, and K. H. Nordsieck. The size distribution of interstellar grains. ApJ, 217:425–433, October 1977. doi: 10.1086/155591.

Christopher D. Matzner. On the Role of Massive Stars in the Support and Destruction of Giant Molecular Clouds. ApJ, 566(1):302–314, February 2002. doi: 10.1086/338030.

Richard McCray and Minas Kafatos. Supershells and Propagating Star Formation. ApJ, 317:190, June 1987. doi: 10.1086/165267.

W. H. McCrea and D. McNally. The formation of Population I stars, II. The formation of molecular hydrogen in interstellar matter. MNRAS, 121:238, January 1960. doi: 10.1093/mnras/121.2.238.

Christopher F. McKee and Jonathan C. Tan. The Formation of Massive Stars from Turbulent Cores. ApJ, 585(2):850–871, March 2003. doi: 10.1086/346149.

Shyam H. Menon, Christoph Federrath, and Mark R. Krumholz. Infrared Radiation Feedback Does Not Regulate Star Cluster Formation or Drive Winds. *arXiv e-prints*, art. arXiv:2206.14190, June 2022a.

Shyam H. Menon, Christoph Federrath, Mark R. Krumholz, Rolf Kuiper, Benjamin D. Wibking, and Manuel Jung. VETTAM: a scheme for radiation hydrodynamics with adaptive mesh refinement using the variable Eddington tensor method. MNRAS, 512(1):401–423, May 2022b. doi: 10.1093/mnras/stac485.

Dimitri Mihalas and Barbara Weibel Mihalas. *Foundations of radiation hydrodynamics*. Courier Corporation, 2013.

T. J. Mooney and P. M. Solomon. Star Formation Rates and the Far-Infrared Luminosity of Galactic Molecular Clouds. ApJ, 334:L51, November 1988. doi: 10.1086/185310.

Eric R. Moseley, Romain Teyssier, and B. T. Draine. Dust dynamics in RAMSES – I. Methods and turbulent acceleration. *arXiv e-prints*, art. arXiv:2204.07681, April 2022.

F. Motte and P. André. The circumstellar environment of low-mass protostars: A millimeter continuum mapping survey. A&A, 365:440–464, January 2001. doi: 10.1051/0004-6361:20000072.

F. Motte, P. Andre, and R. Neri. The initial conditions of star formation in the rho Ophiuchi main cloud: wide-field millimeter continuum mapping. A&A, 336: 150–172, August 1998.

Tara Murphy, Martin Cohen, Ronald D. Ekers, Anne J. Green, Robin M. Wark, and Vanessa Moss. Ultra- and hyper-compact HII regions at 20 GHz. MNRAS, 405 (3):1560–1572, July 2010. doi: 10.1111/j.1365-2966.2010.16589.x.

Fumitaka Nakamura and Zhi-Yun Li. Protostellar Turbulence Driven by Collimated Outflows. ApJ, 662(1):395–412, June 2007. doi: 10.1086/517515.

Takenori Nakano. Conditions for the Formation of Massive Stars through Nonspherical Accretion. ApJ, 345:464, October 1989. doi: 10.1086/167919.

Takenori Nakano, Tetsuo Hasegawa, and Colin Norman. The Mass of a Star Formed in a Cloud Core: Theory and Its Application to the Orion A Cloud. ApJ, 450:183, September 1995. doi: 10.1086/176130.

Adi Nusser and Joseph Silk. Regulation of star formation by large-scale gravitoturbulence. MNRAS, 509(2):2979–2993, January 2022. doi: 10.1093/mnras/stab3121.

Takashi Okamoto, Kohji Yoshikawa, and Masayuki Umemura. ARGOT: accelerated radiative transfer on grids using oct-tree. MNRAS, 419(4):2855–2866, February 2012. doi: 10.1111/j.1365-2966.2011.19927.x.

G. André Oliva and R. Kuiper. Modeling disk fragmentation and multiplicity in massive star formation. A&A, 644:A41, December 2020. doi: 10.1051/0004-6361/202038103.

Grace M. Olivier, Laura A. Lopez, Anna L. Rosen, Omnarayani Nayak, Megan Reiter, Mark R. Krumholz, and Alberto D. Bolatto. Evolution of Stellar Feedback in H II Regions. ApJ, 908(1):68, February 2021. doi: 10.3847/1538-4357/abd24a.

K. Omukai, T. Tsuribe, R. Schneider, and A. Ferrara. Thermal and Fragmentation Properties of Star-forming Clouds in Low-Metallicity Environments. ApJ, 626(2): 627–643, June 2005. doi: 10.1086/429955.

Kazuyuki Omukai. Protostellar Collapse with Various Metallicities. ApJ, 534(2): 809–824, May 2000a. doi: 10.1086/308776.

Kazuyuki Omukai. Protostellar Collapse with Various Metallicities. ApJ, 534(2): 809–824, May 2000b. doi: 10.1086/308776.

Jeremiah P. Ostriker and Christopher F. McKee. Astrophysical blastwaves. *Reviews of Modern Physics*, 60(1):1–68, January 1988. doi: 10.1103/RevModPhys.60.1.

Paolo Padoan, Ake Nordlund, and Bernard J. T. Jones. The universality of the stellar initial mass function. MNRAS, 288(1):145–152, June 1997. doi: 10.1093/mnras/288.1.145.

T. G. Phillips, P. J. Huggins, P. G. Wannier, and N. Z. Scoville. Observations of CO(J = 2-1) emission from molecular clouds. ApJ, 231:720–731, August 1979. doi: 10.1086/157237.

G. Praburam and J. Goree. Cosmic Dust Synthesis by Accretion and Coagulation. ApJ, 441:830, March 1995. doi: 10.1086/175406.

R. E. Pudritz, R. Ouyed, Ch. Fendt, and A. Brandenburg. Disk Winds, Jets, and Outflows: Theoretical and Computational Foundations. In Bo Reipurth, David Jewitt, and Klaus Keil, editors, *Protostars and Planets V*, page 277, January 2007.

A. C. Raga, J. Cantó, and L. F. Rodríguez. Analytic and numerical models for the expansion of a compact H II region. MNRAS, 419(1):L39–L43, January 2012. doi: 10.1111/j.1745-3933.2011.01173.x.

G. H. Rieke and F. J. Low. The infrared spectrum of NGC 1068. ApJ, 199:L13–L17, July 1975. doi: 10.1086/181838.

J Rosdahl and R Teyssier. A scheme for radiation pressure and photon diffusion with the m1 closure in ramses-rt. *Monthly Notices of the Royal Astronomical Society*, 449(4):4380–4403, 2015.

A. L. Rosen, M. R. Krumholz, J. S. Oishi, A. T. Lee, and R. I. Klein. Hybrid Adaptive Ray-Moment Method (HARM^2): A highly parallel method for radiation hydrodynamics on adaptive grids. *Journal of Computational Physics*, 330:924–942, February 2017. doi: 10.1016/j.jcp.2016.10.048.

Anna L. Rosen. A Massive Star is Born: How Feedback from Stellar Winds, Radiation Pressure, and Collimated Outflows Limits Accretion onto Massive Stars. *arXiv e-prints*, art. arXiv:2204.09700, April 2022.

Anna L. Rosen and Mark R. Krumholz. The Role of Outflows, Radiation Pressure, and Magnetic Fields in Massive Star Formation. AJ, 160(2):78, August 2020. doi: 10.3847/1538-3881/ab9abf.

Anna L. Rosen, Pak Shing Li, Qizhou Zhang, and Blakesley Burkhart. Massive-star Formation via the Collapse of Subvirial and Virialized Turbulent Massive Cores. ApJ, 887(2):108, December 2019. doi: 10.3847/1538-4357/ab54c6.

Anna L. Rosen, Stella S. R. Offner, Sarah I. Sadavoy, Asmita Bhandare, Enrique Vázquez-Semadeni, and Adam Ginsburg. Zooming in on Individual Star Formation: Low- and High-Mass Stars. Space Sci. Rev., 216(4):62, May 2020. doi: 10.1007/s11214-020-00688-5.

Edwin E. Salpeter. The Luminosity Function and Stellar Evolution. ApJ, 121:161, January 1955. doi: 10.1086/145971.

R. Schneider, A. Ferrara, R. Salvaterra, K. Omukai, and V. Bromm. Low-mass relics of early star formation. Nature, 422(6934):869–871, April 2003. doi: 10.1038/nature01579.

N. Z. Scoville, Min Su Yun, D. P. Clemens, D. B. Sanders, and W. H. Waller. Molecular Clouds and Cloud Cores in the Inner Galaxy. ApJS, 63:821, April 1987. doi: 10.1086/191185.

D. Seifried, R. E. Pudritz, R. Banerjee, D. Duffin, and R. S. Klessen. Magnetic fields during the early stages of massive star formation - II. A generalized outflow criterion. MNRAS, 422(1):347–366, May 2012. doi: 10.1111/j.1365-2966.2012.20610.x.

Dmitry Semenov, Th Henning, Ch Helling, M Ilgner, and E Sedlmayr. Rosseland and planck mean opacities for protoplanetary discs. *Astronomy & Astrophysics*, 410(2):611–621, 2003.

Frank H. Shu, Fred C. Adams, and Susana Lizano. Star formation in molecular clouds: observation and theory. ARA&A, 25:23–81, January 1987. doi: 10.1146/annurev.aa.25.090187.000323.

F. Sibille, J. Bergeat, M. Lunel, and R. Kandel. Infrared observations of Sharpless 2-106, a possible location for star formation. A&A, 40:441–446, May 1975.

M. Aaron Skinner and Eve C. Ostriker. A Two-moment Radiation Hydrodynamics Module in Athena Using a Time-explicit Godunov Method. ApJS, 206(2):21, June 2013. doi: 10.1088/0067-0049/206/2/21.

Aaron Smith, Rahul Kannan, Benny T. H. Tsang, Mark Vogelsberger, and Rüdiger Pakmor. AREPO-MCRT: Monte Carlo Radiation Hydrodynamics on a Moving Mesh. ApJ, 905(1):27, December 2020. doi: 10.3847/1538-4357/abc47e.

Britton Smith, Steinn Sigurdsson, and Tom Abel. Metal cooling in simulations of cosmic structure formation. *Monthly Notices of the Royal Astronomical Society*, 385 (3):1443–1454, 03 2008. ISSN 0035-8711. doi: 10.1111/j.1365-2966.2008.12922.x. URL `https://doi.org/10.1111/j.1365-2966.2008.12922.x`.

P. M. Solomon, A. R. Rivolo, J. Barrett, and A. Yahil. Mass, Luminosity, and Line Width Relations of Galactic Molecular Clouds. ApJ, 319:730, August 1987. doi: 10.1086/165493.

Lyman Spitzer. *Physical processes in the interstellar medium*. 1978. doi: 10.1002/9783527617722.

James M. Stone, Dimitri Mihalas, and Michael L. Norman. ZEUS-2D: A Radiation Magnetohydrodynamics Code for Astrophysical Flows in Two Space Dimensions. III. The Radiation Hydrodynamic Algorithms and Tests. ApJS, 80:819, June 1992. doi: 10.1086/191682.

Bengt Strömgren. The Physical State of Interstellar Hydrogen. ApJ, 89:526, May 1939. doi: 10.1086/144074.

J. C. Tan, M. T. Beltrán, P. Caselli, F. Fontani, A. Fuente, M. R. Krumholz, C. F. McKee, and A. Stolte. Massive Star Formation. In Henrik Beuther, Ralf S. Klessen, Cornelis P. Dullemond, and Thomas Henning, editors, *Protostars and Planets VI*, page 149, January 2014. doi: 10.2458/azu_uapress_9780816531240-ch007.

Kei E. I. Tanaka, Jonathan C. Tan, and Yichen Zhang. The Impact of Feedback During Massive Star Formation by Core Accretion. ApJ, 835(1):32, January 2017. doi: 10.3847/1538-4357/835/1/32.

Leonardo Testi and Anneila I. Sargent. Star Formation in Clusters: A Survey of Compact Millimeter-Wave Sources in the Serpens Core. ApJ, 508(1):L91–L94, November 1998. doi: 10.1086/311724.

Todd A. Thompson, Eliot Quataert, and Norman Murray. Radiation Pressure-supported Starburst Disks and Active Galactic Nucleus Fueling. ApJ, 630(1): 167–185, September 2005. doi: 10.1086/431923.

Alexander GGM Tielens. *The physics and chemistry of the interstellar medium*. Cambridge University Press, 2005. ISBN 978-0-521-82634-1.

Kengo Tomida, Kohji Tomisaka, Tomoaki Matsumoto, Yasunori Hori, Satoshi Okuzumi, Masahiro N. Machida, and Kazuya Saigo. Radiation Magnetohydrodynamic Simulations of Protostellar Collapse: Protostellar Core Formation. ApJ, 763(1):6, January 2013. doi: 10.1088/0004-637X/763/1/6.

Kengo Tomida, Satoshi Okuzumi, and Masahiro N. Machida. Radiation Magnetohydrodynamic Simulations of Protostellar Collapse: Nonideal Magnetohydrodynamic Effects and Early Formation of Circumstellar Disks. ApJ, 801(2):117, March 2015. doi: 10.1088/0004-637X/801/2/117.

A. Toomre. Theories of spiral structure. ARA&A, 15:437–478, January 1977. doi: 10.1146/annurev.aa.15.090177.002253.

Eleuterio F Toro. *Riemann solvers and numerical methods for fluid dynamics: a practical introduction*. Springer Science & Business Media, 2013.

Colin Tudge et al. *Neanderthals, bandits and farmers: how agriculture really began*. Yale University Press, 1999.

Bhargav Vaidya, Christian Fendt, and Henrik Beuther. Accretion Disks Around Massive Stars: Hydrodynamic Structure, Stability, and Dust Sublimation. ApJ, 702(1):567–579, September 2009. doi: 10.1088/0004-637X/702/1/567.

Enrique Vazquez-Semadeni, Thierry Passot, and Annick Pouquet. A Turbulent Model for the Interstellar Medium. I. Threshold Star Formation and Self-Gravity. ApJ, 441:702, March 1995. doi: 10.1086/175393.

Keiichi Wada. Instabilities of Spiral Shocks. II. A Quasi-Steady State in the Multiphase Inhomogeneous ISM. ApJ, 675(1):188–193, March 2008. doi: 10.1086/525037.

S. Walch, P. Girichidis, T. Naab, A. Gatto, S. C. O. Glover, R. Wünsch, R. S. Klessen, P. C. Clark, T. Peters, D. Derigs, and C. Baczynski. The SILCC (SImulating the LifeCycle of molecular Clouds) project - I. Chemical evolution of the supernova-driven ISM. MNRAS, 454(1):238–268, November 2015. doi: 10.1093/mnras/stv1975.

R. Weaver, R. McCray, J. Castor, P. Shapiro, and R. Moore. Interstellar bubbles. II. Structure and evolution. ApJ, 218:377–395, December 1977. doi: 10.1086/155692.

Joseph C. Weingartner and B. T. Draine. Forces on Dust Grains Exposed to Anisotropic Interstellar Radiation Fields. ApJ, 553(2):581–594, June 2001a. doi: 10.1086/320963.

Joseph C. Weingartner and B. T. Draine. Dust Grain-Size Distributions and Extinction in the Milky Way, Large Magellanic Cloud, and Small Magellanic Cloud. ApJ, 548(1):296–309, February 2001b. doi: 10.1086/318651.

D. A. Weitz and M. Oliveria. Fractal structures formed by kinetic aggregation of aqueous gold colloids. Phys. Rev. Lett., 52(16):1433–1436, April 1984. doi: 10.1103/PhysRevLett.52.1433.

A. Whitworth. The erosion and dispersal of massive molecular clouds by young stars. MNRAS, 186:59–67, January 1979. doi: 10.1093/mnras/186.1.59.

R. W. Wilson, K. B. Jefferts, and A. A. Penzias. Carbon Monoxide in the Orion Nebula. ApJ, 161:L43, July 1970. doi: 10.1086/180567.

R. Wünsch, S. Walch, F. Dinnbier, and A. Whitworth. Tree-based solvers for adaptive mesh refinement code FLASH - I: gravity and optical depths. MNRAS, 475(3):3393–3418, April 2018. doi: 10.1093/mnras/sty015.

Richard Wünsch, Stefanie Walch, František Dinnbier, Daniel Seifried, Sebastian Haid, **Andre Klepitko**, Anthony P. Whitworth, and Jan Palouš. Tree-based solvers for adaptive mesh refinement code FLASH - II: radiation transport module TreeRay. MNRAS, 505(3):3730–3754, August 2021. doi: 10.1093/mnras/stab1482.

Harold W. Yorke and Peter Bodenheimer. The Formation of Protostellar Disks. III. The Influence of Gravitationally Induced Angular Momentum Transport on Disk Structure and Appearance. ApJ, 525(1):330–342, November 1999. doi: 10.1086/307867.

DATA AVAILABILITY

The data underlying this thesis will be shared on reasonable request to the supervisor.

ACKNOWLEDGEMENTS

Mein größter Dank gilt meiner Betreuerin, Prof. Dr. Stefanie Walch-Gassner, die mich als Bachelorstudent aufgenommen hat und mir seither die Möglichkeit gegeben hat an spannenden Problemen zu forschen und zu wachsen. Letztendlich ist diese Arbeit nur durch diese vorangestellten Erfahrungen zustandegekommen. Die Entwicklung und Implementation numerischer Applikationen gehen einher mit Höhen und Tiefen. Besonders bei Tiefen konnte mich stets auf die Erfahrung und das Verständnis meiner Betreuerin verlassen, wofür ich sehr dankbar bin.

Des Weiteren möchte ich meinem Zweitgutacher Prof. Dr. Cristiano Porciani und dem Vorsitzenden der Prüfungskomission Prof. Dr. Ulrich Loehnert danken.

Ich danke meinem "Thesis Advisory Comittee" bestehend aus Prof. Dr. Stefanie Walch-Gassner, Prof. Dr. Cristiano Porciani und Prof. Dr. Peter Schilke für ihre Unterstützung und ihren Rat.

Ich möchte Dr. Daniel Seifried, Dr. Brandt Gaches und Shashwata Ganguly herzlichst für das Lesen meiner Arbeit auf Verständlichkeit und Klarheit danken. Ebenso danke ich allen Mitauthoren und dem “Referee“ für ihren Beitrag zur Anfertigung der Teilpuplikationen.

Ich bin froh darüber Teil einer ausgezeichneten Arbeitsgruppe gewesen zu sein, von der ich viel lernen konnte. Es ergaben sich zahlloser Austausch von Ideen und spannende Diskussionen. Besonders möchte ich mich bei Paul, Seamus, Shash, Michael, Daniel, Sebastian S., Sebastian V., Katya, Thorsten und Birka für viele spaßige aber auch konstruktive Momente bedanken.

Meinen gefühlt schon ewigen Freunden Jens, Jonas und Alex bin ich dankbar für tolle Gesellschaft und erfrischende Kaltgetränke am Rhein. Ich möchte mich bei allen Freunden für zahllose virtuelle Abende in der pandemiebedingten Isolation bedanken. Pierre, Konstantin und Timo et al., meinen Freunden aus der Studienzeit, bin ich ebenso sehr dankbar für die tolle Zeit. Sicherlich ist mir der ein oder andere Lösungsvorschlag für ein Problem nach einem geselligen Abend mit Freunden eingefallen.

Ich danke Birka für ihre Unterstützung und liebevolle Art. Gerade in schwierigen Zeiten dieser Arbeit war sie immer für mich da.

Meinen Eltern, Ursula und Günther, die meine Interessen gefördert haben bin ich unendlich dankbar. Sie haben mich in eine Welt gehen lassen, die sie selbst nicht kannten. Ich danke meiner früher größeren – mittlerweile kleineren Schwester Mirella, Oliver und meinen Neffen für spaßige Zeiten jenseits der Arbeit. Ich bin sehr dankbar für meine Familie und ihren Rückhalt.

Andre Klepitko

Curriculum Vitae

I. Physikalisches Institut
University of Cologne
Zülpicher Strasse 77
50937 Cologne
✉ klepitko@ph1.uni-koeln.de

Personal Information

Date of Birth: 15.07.1994

Place of Birth: Leverkusen

Educational Qualification

12/2018 – 10/2022	**PhD**, Universität zu Köln, Cologne, Germany. ○ PhD Thesis: "*Tree-Based Radiative Transfer of Diffuse Sources: A Novel Scheme and its Application in Massive Star Formation*"
10/2017 – 11/2018	**M.Sc.**, Universität zu Köln, Cologne, Germany. ○ Ms.Sc. Thesis: "*Radiation Pressure First Absortpion Scheme*"
10/2013 – 9/2016	**B.Sc.**, Universität zu Köln, Cologne, Germany. ○ B.Sc. Thesis: "*Towards understanding Radiation Pressure*"
2005 – 7/2013	**Allg. Hochschulreife**, Landrad-Lucas-Gymnasium, Leverkusen, Germany.

Publications

A. Klepitko, S. Walch, R. Wünsch, D. Seifried, F. Dinnbier, and S. Haid. Tree-based solvers for adaptive mesh refinement code FLASH - III: a novel scheme for radiation pressure on dust and gas and radiative transfer from diffuse sources. , 521(1):160–184, May 2023. doi: 10.1093/mnras/stad385

A. Klepitko and S. Walch. The Impact of Metallicity on Massive Star Formation: It is all about the Dust! Unpublished Manuscript, 2022

Köln, den 25.06.2023

Klepitko
(Andre Klepitko)